

# Mechanics of Microneedle Penetration into Skin for Drug Delivery

A thesis submitted in partial fulfilment of the requirement for the degree of Doctor of  
Philosophy

Rachael Emma Joyce (M.Eng)

December 2024

Cardiff University

School of Engineering



# ABSTRACT

Microneedle-based drug delivery systems have gained attention as a minimally invasive alternative to conventional hypodermic needles, particularly for vaccination and transdermal drug delivery. Their potential lies in reduced pain, ease of administration, and the ability to bypass the skin's stratum corneum barrier. However, challenges remain in optimising microneedle (MN) designs. This study aimed to develop a validated design tool combining Finite Element Analysis (FEA) and digital volume correlation (DVC) to improve the knowledge of needle-skin biomechanics.

Current literature highlights gaps in the understanding of high-deformation needle insertion mechanics and limited adoption of advanced imaging techniques, such as  $\mu$ -CT and subsequent DVC measurement, for evaluating strain distributions through skin substitute during needle penetration. While existing studies have focused on low strain behaviours or geometric optimisations, their findings often rely on assumptions that do not capture the complexity of needle-skin interactions under high strain. To address these gaps, Ecoflex-30 was validated as a skin substitute through mechanical experiments, and two FEMs were developed. Within FEBio a static, low deformation model focusing on indentation was created, and a second dynamic model incorporating a cohesive zone method was implemented to capture high deformations towards full needle puncture modelling. Work of fracture measurements derived from these experiments were directly incorporated into the simulations.

Micro focus computed tomography ( $\mu$ -CT) scans were used to capture deformation data during the initial needle penetration phases (indentation) with a scaled needle of length 1.1 mm. Two sets of tests were conducted: the first focused on a proof of concept for the DVC, and therefore 6 images were taken at intervals of 75  $\mu$ m to a displacement 375  $\mu$ m. In the second test, 6 images were taken at intervals of 0  $\mu$ m, 350  $\mu$ m, 650  $\mu$ m, 700  $\mu$ m, 750  $\mu$ m and 800  $\mu$ m to a maximum displacement of 800  $\mu$ m, representing the large deformation phase just prior to the identified needle puncture point. The results demonstrated strain concentrations at the needle tip and along its edges, indicating potential failure zones essential for creating insertion pathways. Interpolation of DVC data reduced discrepancies between experimental and computational results. This validated the computational model's initial capabilities and highlighted the benefits of integrating DVC with FEA for evaluating MN designs.

This study establishes a foundation for developing MN optimisation tools that incorporate realistic mechanical behaviours and strain distributions through the integration of advanced imaging techniques and material modelling. The research established Ecoflex-30 as a viable skin substitute, demonstrating mechanical properties closely aligned with published in vivo and ex vivo skin data, particularly in terms of stiffness and elasticity (a stiffness of 3.7251 N/mm, shear modulus of 0.0263 MPa and an initial Young's modulus of 0.0788). By incorporating titanium dioxide particles, the material enables accurate DVC tracking without significantly compromising the mechanical properties (a comparable stiffness of 4.5862 N/mm, shear modulus of 0.0323 MPa and an initial Young's modulus of 0.0970). The findings underscore the importance of considering high strain behaviours to enhance MN geometry and efficacy. Although not yet ready for direct clinical application, the methods introduced in this research represent a significant step towards the creation of reliable and validated MN design tools that could transform drug delivery and reduce preclinical testing burdens.

# ACKNOWLEDGMENTS

I would first like to express my sincere appreciation to my supervisors, Prof. Rhys Pullin, Dr. Hayley Wyatt, Dr. Sion Coulman, and Prof. James Birchall. I also extend my heartfelt thanks to Prof. Sam Evans, who provided invaluable support part way through my first year and stayed as an extra supervisor. The guidance and encouragement you all have offered throughout these four years, particularly during the challenging start during COVID, has been instrumental in enabling me to reach this point. I feel extremely fortunate to have had such an exceptional support system.

I would also like to thank the technicians in the Civil Laboratory at Cardiff University School of Engineering for their support, training, and a listening ear. I am also grateful to Dr Maria Dul at Cardiff University School of Pharmacy for sharing her wisdom and providing support with experiments.

To all my colleagues and friends in the CUSP lab: thank you for being the best support network, as well as wonderful friends.

I would like to thank everyone at NXCT and the University of Southampton for their hospitality during my time in Southampton, and for granting me access to their facility and expertise.

I would like to acknowledge Cardiff University and EPSRC for funding my studies, and SWIEET for providing additional funding for conference experiences.

To my friends and partner: thank you for your unwavering support and understanding over these years. From offering distractions when needed to patiently listening to my rants about research papers and encouraging me to persevere, you have been a vital part of this journey. And to Gryf and Dora for all the late night support.

Finally, to my family, especially my mum: thank you most of all. You have never questioned the reduced visits home during these years and have been the greatest source of encouragement and cheerleaders. Your belief in me has meant everything.

# ***TABLE OF CONTENTS***

---

Abstract.....	III
Acknowledgments.....	IV
List of Figures.....	VIII
List of Tables.....	XX
List of Abbreviations.....	XXII
CHAPTER 1 .....	1
Introduction .....	1
1.1    General Introduction.....	1
1.2    Aims and Objectives.....	5
1.3    Thesis structure.....	6
CHAPTER 2 .....	8
Literature review .....	8
2.1    Microneedles .....	8
2.2    Skin .....	18
2.3    Fracture mechanics.....	32
2.4    Imaging of skin .....	46
2.5    Digital Volume Correlation (DVC).....	57
2.6    Finite element modelling of needle insertion .....	61

2.7	Summary.....	74
CHAPTER 3 .....		76
Development of Experimental Methods for Skin Substitute Evaluation.....		76
3.1	Introduction.....	76
3.2	Material criteria.....	77
3.3	Methods.....	80
3.4	Results .....	96
3.5	Discussion .....	112
3.6	Conclusion.....	118
CHAPTER 4 .....		120
Finite Element Analysis.....		120
4.1	Introduction.....	120
4.2	Method .....	121
4.3	Solution methods.....	141
4.4	Model Studies.....	142
4.5	Mesh convergence study.....	144
4.6	Error analysis .....	145
4.7	Results .....	147
4.8	Discussion .....	166
4.9	Conclusion.....	173

CHAPTER 5 .....	175
Experimental measurements of needle penetration .....	175
5.1 Introduction.....	175
5.2 Method .....	176
5.3 Results .....	198
5.4 Discussion .....	216
5.5 Conclusion .....	227
CHAPTER 6 .....	229
Main Discussion.....	229
CHAPTER 7 .....	246
Main Conclusion .....	246
CHAPTER 8 .....	251
Future work.....	251
References.....	254
Appendix A.....	272
CONFERENCES .....	272
Appendix B.....	274
DVC CODE .....	274
GRAPH CODE.....	290

# ***LIST OF FIGURES***

---

Figure 2-1 - A figure showing the skin layers (epidermis, dermis and hypodermis) and the different transdermal drug delivery methods including topical creams, hypodermic needle, MNAs, and a transdermal patch. .... 9

Figure 2-2 – A figure showing the different drug delivery methods using MNs, indicating how the drug is infused into the skin. These MNs are categorised as solid, hollow, drug coated, dissolvable, and hydrogel (polymer based microneedles that swell upon insertion). The red lines illustrate the drug loading capability of the MN method a) the blue dots illustrate the drug diffusion once the MNs, or patch, has been removed b) ..... 10

Figure 2-3 - Biodegradable MN design with an arrowhead design are shown. The arrowhead breaks off into the skin where the polymer and encapsulated drug dissolves into the blood stream over a set period of time [41] ..... 12

Figure 2-4 - Biodegradable MN design with a bubble which aids in the breaking of the MN tip. The stronger PVA backing enforces the MN to enable insertion into the skin without premature fracturing [42] ..... 13

Figure 2-5 – The structure of human skin, clearly showing the epidermis, dermis and hypodermis and important characteristics of each layer. Sourced from [<https://www.123rf.com>]..... 18

Figure 2-6- Figure of the stress-strain curve of human skin, showing the collagen fibres, and the overall non-linear behaviour of skin [113] ..... 24

Figure 2-7 – The load-displacement-resistance graph from Davis publication [10], illustrating the point of MN insertion can be identified by the sudden drop in skin electrical resistance or applied force ..... 41

Figure 2-8 – The load-displacement graph from Oldfield publication [17], illustrating the five stages of needle insertion that was identified ..... 42

Figure 2-9- The separation-traction graph from Oldfields publication [17], demonstrating the relationship that is utilised for cohesive elements to implement the damage criteria required ..... 44

Figure 2-10 - The load-displacement curves comparing sharp, blunt and cylindrical needles from Boonma’s investigation into MN insertion characteristics [67]. The insertion point is identified for the blunt bevel needles, with the cylindrical needle not puncturing. .... 45

Figure 2-11 – A typical OCT set up, showing how the beam is split from the light source to the reference mirror, the material and to the sensor to be display [154]..... 47

Figure 2-12 - An example of skin thickness found through experimental OCT imaging, showing the epidermis layers and the viable dermis, by Zhang et al. [157]. PAT (Photoacoustic tomography) combines laser-induced ultrasound with OCT to show oxygen saturation or tissue vascularity..... 48

Figure 2-13 – A schematic of the DIC set up for a tension test, showing the speckle pattern area required with a 3D set up using two cameras connected to the control computer ..... 50

Figure 2-14 – A schematic of a CT set up, showing the X-ray source directed at the sample which is connected to a rotating tomography stage. The X-ray photons are then detected, with the computer used to reconstruct the projections..... 53

Figure 2-15 – An example of the number of projections that could be taken of a sample. This shows that increasing the number of projections, for example from 2 to 8 or to 256, increases the accuracy of the filtered back projection reconstruction..... 55

Figure 2-16 – The sketch taken from Assaad [27] publication using the element deletion method, showing the FEM of needle insertion into a cubic gel sample, with

the boundary conditions labelled, and the line of needle insertion denoted by a dotted line..... 68

Figure 2-17 – A sketch taken from the publication of Chen [20], illustrating the multi-layer model investigated using the element deletion method. The boundary conditions are also shown (the tetrahedrons on main geometry). ..... 69

Figure 2-18 – A figure of the FEM created by Oldfield [17], showing the cohesive zone elements along the crack line that illustrates the cohesive zone method developed. .... 71

Figure 2-19 – The cohesive zone method utilised by Mohammadi [206], showing the cohesive zone and needle crack area active forces ..... 72

Figure 3-1 - Silicone mould used for the creation of the silicone samples for the compression and puncture tests ..... 81

Figure 3-2 - Universal test machine used a) and the silicone and conical indenter b) ..... 84

Figure 3-3 – MN and scaled needle used in this study, front view a) and side view b) ..... 85

Figure 3-4 - Tensile test machine set up for puncture tests a) and needle and silicone b)..... 86

Figure 3-5 - Dogbone for tensile tests, with measurements in mm ..... 87

Figure 3-6 – Schematic of the VSG set up used for the tensile test, showing the four dot set up, the area the camera covered, and the connection to the computer..... 89

Figure 3-7 – Physical VSG set up used, showing the camera set up next to the tensile test machine..... 90

Figure 3-8 – Top view of the fixture used for the WoF experiment, identifying the key components such as the fixture arms, clamping plates for the silicone and machine connector ..... 93

Figure 3-9 – The side view of the WoF experimental fixture ..... 93

Figure 3-10 – The silicone sample produced using the initial mould a) the second sample using the thinner mould b) the third sample created using a mould with the width reduced c) the final samples created using the third mould with added groove (pre crack) d)..... 95

Figure 3-11 - Particle size distribution of the averaged sieved (blue line) and un-sieved particles (red line) for TiO<sub>2</sub> ..... 97

Figure 3-12 – Flat indenter load-displacement graph for Material A showing the five cycles and the average (dotted black line) ..... 98

Figure 3-13 – Flat indenter load-displacement data for all material samples tested, showing the average of all 5 cycles. Material A showed the greatest stiffness, with Material C showing the addition of the TiO<sub>2</sub> only had a minor effect on the overall stiffness of the Ecoflex sample. Material D and F (the Ecoflex Gel) was the least stiff of all tested..... 99

Figure 3-14 - Conical indenter load-displacement graph for all material samples tested, showing the average of all 5 cycles. Material A was again the stiffest material, Material E and F shows the change in the manufacturing procedure, whilst minor, does alter the stiffness of the material. .... 99

Figure 3-15 - Puncture test results on Material C using three test speeds, 0.1 mm/s, 0.3 mm/s and 0.5 mm/s to assess the rate-dependent puncture resistance of the silicone. The results show minimal variation in the force-displacement curves, indicating no significant rate-dependence. The average puncture depth and force were 8.09 mm and 3.315 N respectively ..... 101

Figure 3-16 – One term Ogden material model fitting for the VSG results of Material B samples. The experimental data is represented by solid lines, while the Ogden fitting curve is shown with dashed line. .... 103

Figure 3-17 - One term Ogden material model fitting for the TM results of Material B samples. The experimental data is represented by solid lines, while the Ogden fitting curve is shown with dashed line. .... 103

Figure 3-18 – One term Ogden material model fitting for the VSG results of Material C samples. The experimental data is represented by solid lines, while the Ogden fitting curve is shown with dashed line. The results of Material C show a more linear fit than the original Material B. .... 105

Figure 3-19 – One term Ogden material model fitting for the TM results of Material C samples. The experimental data is represented by solid lines, while the Ogden fitting curve is shown with dashed line. .... 106

Figure 3-20 – Comparison of VSG and TM data for Sample One, illustrating the difference in fitting between the one term Ogden material models. The VSG data is slightly lower than the TM, highlighting a slight discrepancy between the two measurement methods. .... 107

Figure 3-21 - Tear test cycles for Material B sample 1 a) sample 2 b) sample 3 c) and sample 4 d). The figure shows the progression of damage during each cycle where unloading was decided by eye, with slight overlaps observed across all samples. Notably, sample 1 and sample 3 required a higher load to progress the first tear compared to the other samples. .... 108

Figure 3-22 - Tearing of Material C samples 1 to 4, highlighting the curved tearing observed during testing, which was not observed with Material B. The addition of the groove through the silicone resulted in improved tearing behaviour of Material C. 109

Figure 3-23 - Tear test cycles for Material C sample 2 a) sample 3 b) and sample 4 c) showing significantly lower load than Material B. The figures also highlight a

substantial overlap in the load-displacement curves for Material C, with a less symmetrical cycle shape than those observed in Material B. .... 110

Figure 3-24 - Fiducial markers of TiO<sub>2</sub> sieved through a 250 micron sieve in Material C. The markers are viewed to enable an assessment of size and distribution to identify the suitability of the TiO<sub>2</sub> for further experiments. .... 112

Figure 4-1 - The needle used in the first, static, model, top view a) bottom view b) side view c) front view d) isometric view e) ..... 123

Figure 4-2 - The needle used for the second, dynamic, model, top view a) bottom view b) side view c) front view d) and isometric view e) ..... 124

Figure 4-3 - Geometry of the silicone solid model (dimensions in mm), showing the outer region (a) and the inner region which had a finer mesh (b). .... 125

Figure 4-4 - The silicone mesh for the first model, which was a full silicone block of 8x8x8 mm dimensions. The needle is also shown (in blue). Isometric view a) top view b) a half slice showing the inside geometry c) close up view of the inside geometry d) ..... 126

Figure 4-5 - The silicone mesh for the second model, which was a quarter model of the same block used for the first model, of dimensions 4x4x8 mm. Isometric view a) top view b) and close up of the side view c) ..... 127

Figure 4-6 - The boundary conditions applied to the silicone blocks, the sides constrained are highlighted in blue. The base of the block constrained in the Z axis a) two sides of the block constrained in the X axis b) and the last two sides constrained in the Y axis c)..... 129

Figure 4-7 - Contacts applied to the needle and silicone showing the primary surface (the needle surface) a) and the secondary surface (the silicone surface) b) ..... 131

Figure 4-8 - Flowchart of the Cohesive Zone Method model creation developed within this study ..... 132

Figure 4-9 - The mesh surface that is chosen (the fracture plane) a) and the shell plane that is created from the surface selected b) ..... 134

Figure 4-10 - The tetrahedrons created in Rhino7 Grasshopper, imported back into FEBio a) and a close up of the tetrahedrons and how they are separated into corner (orange), edges (purple) and centre (yellow) tetrahedrons by partitioning the single elements b) ..... 135

Figure 4-11 - The tetrahedrons fused onto the silicone block showing the isometric view a) side view b) and front view c)..... 136

Figure 4-12 – An example of the linear constraint code within Rhino Grasshopper, showing the boundary condition type ‘linear constraint’ and the corresponding node number that will be inserted ..... 137

Figure 4-13 – An example of the linear constraint code within FEBio notes that shows the node IDs. This code is then automatically added to the .feb file when the model is run ..... 137

Figure 4-14 - Tetrahedron constraints showing the red nodes as the nodes constrained normal to the fracture plane ..... 140

Figure 4-15 - A close up of a single tetrahedron, with the circled yellow nodes the nodes that are constrained normal to the fracture plane and the red circled node the node that is unconstrained and connected to the silicone ..... 140

Figure 4-16 - The rigid wall that is used to recreate the conditions of a full silicone block without constraining the silicone wall fully ..... 141

Figure 4-17 - The load-displacement results for the five meshes investigated. Mesh 3 and 4 are overlapped. .... 148

Figure 4-18 - The load-displacement data for the experimental data (from Section 3.4.3) and the static model with the original Ogden material model parameters .... 149

Figure 4-19 - The load-displacement data comparing the parameter changed, the bulk modulus, against the experimental data to find the best material model fit .....	150
Figure 4-20 - The components of displacement for the static model, X component a) Y component b) Z component c) .....	152
Figure 4-21 - The components of normal Lagrange strain for the static model, Exx component a) Eyy component b) Ezz component c) .....	154
Figure 4-22 - The components of shear Lagrange strain for the static model, Exy component a) Eyz component b) and Exz component c) .....	155
Figure 4-23 - The load-displacement results for the dynamic model parameter study, showing the change with the bulk modulus and the density (in kg/mm <sup>3</sup> ) to reach the experimental output.....	157
Figure 4-24 - The results from the maximum displacement reached by the dynamic model, of 3.8 mm, showing the instability of the mesh and needle placement. The front view a) and side view b) with the needle. ....	158
Figure 4-25 - The results from the maximum displacement reached by the dynamic model, of 3.8 mm, showing the instability of the mesh and needle placement. The isometric view of just the silicone with the mesh a) and without the mesh b). The front view without the needle c) and the side view without the needle d) .....	159
Figure 4-26 - The components of displacement maps for the dynamic model at the maximum needle displacement of 3.8mm, with a mirrored view along the plane of needle symmetry. X component a) Y component b) Z component c).....	161
Figure 4-27 - The load-displacement curve of the dynamic model with the silicone density of 0.1 kg/m <sup>3</sup> used, and the experiment data.....	162
Figure 4-28 - The component of displacement fields for the static and dynamic model (left and right respectively) at the needle displacement of 0.38 mm, similar to that of	

the static model needle displacement. X component a) Y component b) Z component c) .....	164
Figure 4-29 - The load-displacement curves for the final static and dynamic models used within this study .....	165
Figure 5-1 - Versa CT machine used for the first set of scans, showing the X-ray source, detector, tomography stage, and the custom jig .....	177
Figure 5-2 – The custom jig used for first set of scans, with silicone moving upwards .....	177
Figure 5-3 – The custom jig used in both experiments is shown, featuring the jacking screw, Perspex needle, and silicone. In the second experiment, this setup was used with the silicone held stationary while the needle was displaced; in the first experiment, the configuration was reversed, with the needle fixed and the silicone moving upwards. ....	178
Figure 5-4 - Top view of CT scan through Z plane a) side view through X plane b) .....	179
Figure 5-5 - Diondo CT scanner with Perspex needle in the jig a) and close up of the needle in the jig as needle was moved for the second scans b) .....	180
Figure 5-6 - Flow chart of DVC image registration process.....	182
Figure 5-7 - Comparison of voxel placement for the first and last steps to check for anomalies in the data .....	185
Figure 5-8 – This plot helps check the displacement vectors from the DaVis export file within MATLAB. This can be used to spot any gaps in the plot that may not be showing correctly.....	186
Figure 5-9 - Orthoslicer viewing of the Z component of displacement, which was used to select specific slices for further analysis. This tool allows for interactive viewing of 3D datasets by slicing the volume into 2D sections along different axes, in this case the Z component of displacement was chosen. ....	186

Figure 5-10 - CT scan of the first step to assess needle and silicone placement within MATLAB.....	187
Figure 5-11 - Overlay of the needle mesh from FEBio (the red dots) onto the CT image to check rotation and translation of the DVC data .....	187
Figure 5-12 - The whole mesh node position, needle and silicone imported into MATLAB from FEBio (in mm) a) and a close up showing the needle nodes b).....	189
Figure 5-13 - The displacement vectors show the difference in the initial and final nodal positions. ....	189
Figure 5-14 - FEBio displacement magnitudes in MATLAB top view a) and side view b).....	190
Figure 5-15 - Needle mesh nodes from FEBio in MATLAB .....	191
Figure 5-16 - Translation and rotation of the needle nodes to match the top view of the CT scan. The top view of the CT scan a) the initial placement of the needle mesh b) the rotated and translated needle mesh overlaid onto the CT scan image.....	192
Figure 5-17 - Displacement magnitudes of the DVC data prior to rotation and translation (in mm).....	193
Figure 5-18 - The DVC data (the blue rectangle) and FEBio mesh nodes (the pink dots) overlaid. The top view a) and side view b) shows the difference in the two data sets FoV .....	194
Figure 5-19 - The second set of scans needle mesh placement overlaid onto the CT scan.....	195
Figure 5-20 - An example of the search algorithm used to show the nodes placement and the voxel grid.....	196
Figure 5-21 - $\mu$ -CT images of scans one to six a) to f) respectively at the centre slice .....	199

Figure 5-22 - $\mu$ -CT images of scans one to six a) to f) respectively at the centre slice .....	200
Figure 5-23 - Parameter study for the first set of scans test 1 a) test 2 b) test 3 c) test 4 d) test 5 e). The resolution of the tests increase as the voxel size per pass and the FFT pre shift window is decreased and increased respectively. ....	202
Figure 5-24 - Parameter study for the second set of scans, test 1 a) test 2 b) test 3 c) test 4 d) test 5 e) test 6 f) .....	204
Figure 5-25 - Components of the displacement for test 4, X component a) Y component b) Z component c) .....	205
Figure 5-26 - Components of Lagrange normal and shear strain for test 4, Exx (transverse strain) a) Eyy (axial strain) b) Ezz c) Exy (shear strain) d) Exz e) Eyz f) .....	206
Figure 5-27 - X component of displacement at the centre of the needle and 10 slices before a) and after c) to view the displacement fields .....	208
Figure 5-28 - Y component of displacement at the centre of the needle and 10 slices before a) and after c) to view the displacement fields .....	209
Figure 5-29 - Z component of displacement at the centre of the needle and 10 slices before and after to view the displacement fields .....	210
Figure 5-30 - Components of normalised and shear strain for test 4, Exx a) Eyy b) Ezz c) Exy d) Exz e) Eyz f).....	211
Figure 5-31 - The DVC components of displacement for the first large deformation scan step of 3.5 mm, X component a) Y component b) Z component c).....	212
Figure 5-32 - Interpolated DVC data within MATLAB, showing the displacement magnitude at each mesh node .....	213

Figure 5-33 - Interpolated DVC data (the displacement magnitudes) imported into FEBio to view each displacement step of the needle ..... 214

Figure 5-34 - comparison of the experimental steps used for the  $\mu$ -CT scans to the raw DVC data from MATLAB, the interpolated DVC data from MATLAB and the FEA data taken from the centre node ..... 215

# ***LIST OF TABLES***

---

Table 2-1 – The skin properties, including Young’s modulus and stiffness, taken from published papers identifying the different experimental methods used, their anatomical location (if relevant) and sample size .....	25
Table 3-1 - Material naming for all silicones used in this study, detailing which include the TiO <sub>2</sub> particles and the silicones tested by the School of Pharmacy for comparison .....	82
Table 3-2 - Sample number for the two materials tested (material B and material C), and the corresponding sample thickness in mm .....	87
Table 3-3 - Table of the stiffness, shear modulus (G) and Young’s modulus (E) for all materials and the comparison to published data by Groves [23].....	100
Table 3-4 - Needle puncture test results for three speeds and predicted insertion point force and displacement .....	101
Table 3-5 - Ogden material model properties for VSG and TM for Material B.....	102
Table 3-6 - VSG and TM data for the six samples tested showing the Ogden Material Model parameters .....	104
Table 3-7 – The average WoF results for Material B and Material C samples, highlighting the average thickness of the sample .....	111
Table 4-1 - Table of the material parameters initially used in both models for the silicone. All Ogden material model parameters explained in Section 2.2.3 .....	128
Table 4-2 - Table of the material parameters used for the steel needle .....	128
Table 4-3 – Contact properties used for both models, detailing the penalty factors and tolerances.....	131

Table 4-4 - Material model parameters for the tetrahedrons used withing the Cohesive Zone method dynamic model .....	138
Table 4-5 - Analysis steps for the static and dynamic models, including the step sizes, solver applied and if damping was used.....	142
Table 4-6 - The parameter study for the static model with the bulk modulus density changes corresponding to the static model iteration .....	143
Table 4-7 - The parameter study changes applied to the dynamic model silicone density.....	144
Table 4-8 - Salome parameters for the mesh study, including the minimum and maximum size, fineness and growth rate for part one and part two .....	145
Table 4-9 - FEBio details for each Mesh studied, including minimum, maximum and average element size and the number of steps and corresponding computational time .....	145
Table 4-10 - Table showing the RMSE, MAE, and percentage error for the results in Figure 4-27, comparing the experimental displacement and force with the dynamic model to 3.8 displacement magnitude.....	163
Table 4-11 - Table showing the RMSE, MAE, and percentage error for the results in Figure 4-29, comparing the experimental displacement and force with the static model, the dynamic model, and the comparison between the two models .....	166
Table 5-1 - Scan step number with experimental displacement and corresponding FEBio must point time .....	197
Table 5-2 - First scan parameter study test parameters used.....	198
Table 5-3 - Second scan parameter study test parameters used.....	198
Table 5-4 - Input comparisons with their absolute errors per step and overall RMSE, MAE and percentage error for the compared inputs .....	216

# ***LIST OF ABBREVIATIONS***

---

API	Active pharmaceutical ingredients
CT	Computed tomography
DIC	Digital image correlation
DVC	Digital volume correlation
FE	Finite element
FEA	Finite element analysis
FEM	Finite element modelling
FoV	Field of view
OCT	Optical coherence tomography
MAE	Mean absolute error
MAP	Microneedle array patch
MEMs	Micro-electromechanical systems
MNs	Microneedles
MNA	Microneedle arrays
PDMS	Polydimethylsiloxane
RMAE	Root mean absolute error
SC	Stratum corneum
TM	Tensile machine
TiO <sub>2</sub>	Titanium dioxide
VSG	Virtual strain gauge
WoF	Work of fracture
μ-CT	Mirco focus computed tomography

# ***CHAPTER 1***

---

## **INTRODUCTION**

### **1.1 General Introduction**

Microneedle-based drug delivery systems offer significant advantages over conventional injection methods, particularly for transdermal applications. Unlike hypodermic needles, which penetrate deeper into the skin or bloodstream, microneedles (MNs) target the epidermis, without reaching the nerves and blood vessels within the dermis and hypodermis. This makes MNs an ideal alternative for vaccine delivery, as they provide virtually painless insertion, and can be administered by hand (or with an attached applicator) without the need for trained medical personnel. Furthermore, MNs present an innovative mechanism for delivering active pharmaceutical ingredients (APIs) that cannot typically be absorbed through the skin using traditional transdermal dosage forms, such as patches or creams. By introducing microchannels into the skin, MNs overcome the barrier the stratum corneum (SC) imposes on most drug compounds. The SC is the outermost layer of the epidermis [1] and provides a rigid barrier against environmental and physical damage. Composed of dead skin cells, it forms a waterproof layer that can reduce the efficacy of water based creams and solutions from entering the skin.

## Introduction

Despite their potential, MN development has faced challenges, particularly in experimental validation and computational modelling. Much of the literature has focused on experimental and manufacturing techniques. In 2018 approximately 275 papers were published on MNs, and between 2000 and 2020 58% of published papers concentrated on experimental studies [2]. These studies include research on pharmaceutical development of drug flow, deposit or diffuse from the MNs [3], [4], [5], [6], [7], [8], as well as the effects of geometry and array spacing on the insertion force [9], [10], [11], [12], [13], [14], [15] or fracture force [10], [15]. In comparison, only 7% of the published papers focused on modelling MNs.

Laboratory experiments, such as indentation tests and MN puncture tests, can inform key parameters such as the application force required to insert MNs into the skin. Accompanying imaging techniques are typically used to capture the insertion process for a MN. These include light and scanning electron microscopy (with associated histology) and optical coherence tomography (OCT) [16]. These methods usually examine the microchannels in the skin upon or after MN puncture, but do not offer insights into the interaction between the skin and the MNs through the entirety of the insertion process. Finite Element Models (FEMs) have also been used [10], [17], [18], [19], [20], but often don't describe indentation prior to puncture, due to the complexity of the modelling that is required.

There are also challenges associated with experimental techniques using human and porcine skin. Excised skin has a limited timeframe of usability as the tissue integrity degrades from the time of scission, and it is a limited resource necessitating efficient usage. It also requires staining to visualise microchannels, but it is prone to damage during removal and may require stretching to mimic natural conditions. Furthermore, skin biomechanics vary considerably due to factors such as anatomical location, genetics and, environment [21]. Ex vivo samples also become stiffer, with changes in elasticity and compression properties, potentially skewing the predicted insertion forces [22]. The biomechanical differences between in vivo and ex vivo skin properties highlight the challenges researchers face in developing accurate FEMs. Validation of FE models using ex vivo data is intrinsically associated with error, as ex vivo skin behaves differently than in vivo skin due to factors such as dehydration and the loss of physiological tension. However, due to the ethical, cost and clinical recruitment

## Introduction

challenges involved in using in vivo skin, validation of FEAs largely depends on ex vivo skin data, which can limit the effectiveness of these models for pre-clinical MN design.

The limitations of mechanical testing on animal and human skin have highlighted the need for reliable computational models. Finite Element Analysis (FEA) of MNs is an area of research increasing in popularity, with limited publications to date, restricting the development of optimised MNs. There is a noticeable gap in literature concerning accurate needle penetration and skin biomechanics from a modelling perspective with volumetric validation techniques, which this research aims to address. Bridging this gap is essential for advancing knowledge in this field, with more sophisticated software and techniques enabling advances in this research area. FEA plays a crucial role in the development of microneedle patches (MAPs), enabling the rapid investigation of innovative designs at a low cost, reducing the need for animal and human experiments. Recent advances in FEA methods and software have created new opportunities for design optimisation, facilitating the development of more advanced models, including needle insertion simulations. However, FEA still faces challenges such as accurately replicating skin's complex mechanical behaviour and predicting its response to MN insertion.

Accurately modelling the complex mechanical properties of skin and predicting its behaviour during MN insertion remains a significant challenge. There are currently three main modelling approaches. The first is non-invasive modelling, for example indentation prior to puncture [9], [18], [23] or modelling pre-puncture [24], [25], which models the skin as a homogenous, elastic material. Although these methods are useful, they oversimplify the complex structure of skin. The second method, known as the element deletion method, removes elements from the model once a predetermined stress threshold is reached [19], [20], [26], [27], [28]. While this can simulate skin tearing, it can lead to unrealistic representations of material behaviour, such as overestimation of Von Mises stresses [20] or pre strain on the skin [19], affecting overall accuracy. The third approach, cohesive zones, employs cohesive elements to represent skin fracture and separation properties [17]. This method models the progressive failure of skin layers by incorporating fracture and stress properties. It has also been noted that this approach does not always capture the indentation phase and

## Introduction

in some cases does not prevent premature puncture [17], [18], [29]. To overcome these challenges, the development of advanced FEA techniques and more accurate material models is essential. However, the absence of a standard practice for measuring skin biomechanics and MN penetration complicates the use of FEA as a prototyping and design tool.

Global health problems such as Covid-19 have highlighted the need to improve the safe and effective distribution of medication to different populations in a diversity of geographies. MAPs could help increase vaccination rates and / or improve essential medication access in low- and middle- income countries. By enabling self-administration, reducing the need for trained professionals, and simplifying storage and transportation requirements, MNs provide an efficient solution to reaching diverse populations in remote areas. Although clinically safe MAPs are not yet in widespread production, understanding the mechanics of MN puncture can significantly aid the design of small to large microneedle arrays (MNAs). An effective design tool could be used for a range of applications, including doctor training, understanding skin tearing, and aiding tissue regeneration after injury.

This research addresses the challenge of verifying MN models despite the limitations posed when using human skin. The goal is to create a realistic model of needle indentation and subsequent penetration. This model will be validated not just through widely used mechanical experiments, but also by incorporating imaging techniques not yet utilised for high deformation needle penetration model validation, particularly when modelling complex interactions that occur during the initial puncture phase. This research aims to leverage advancements in FEA techniques to develop more realistic and reliable MN models. By combining FEA with micro-focus computed tomography, this study ensures the FEA approaches are based on accurate mechanical behaviours. This allows for the integration of detailed geometrical information to inform boundary conditions, material properties, and structural interactions in the FE simulations. This approach enables the quantification of key metrics such as deformation and strain distributions, force-displacement behaviour and fracture mechanics.

The findings of this study will contribute to the development of more efficient, effective and clinically viable MAPs. The novel aspects of this research lie in its approach to modelling and validation, offering new insights and tools in the field of MN puncture mechanics.

### 1.2 Aims and Objectives

Based on the findings from literature this thesis has two primary aims to guide the research, supported by three objectives:

**Aim 1:** Enhance the fundamental understanding of needle puncture biomechanics by conducting experimental studies to deepen the knowledge of mechanical interactions during needle indentation and puncture. This includes assessing the work of fracture, tension and compression results as well as assessing the material's response to deformation during  $\mu$ -CT imaging and subsequent strain distribution.

**Aim 2:** Develop and validate a finite element model of needle puncture that can be used as an optimisation tool for future MN design

To achieve these aims, the following objectives are outlined:

#### **Objective 1: Identify suitable skin substitutes**

To identify and evaluate suitable skin substitutes with properties closely matching those of human skin, ensuring they are suitable for  $\mu$ -CT imaging. This involves characterising and quantifying the mechanical behaviour and properties of materials under small and large deformations. This includes conducting mechanical testing on silicone-based materials to assess their mechanical response under different deformation scales ensuring they closely mimic human skin. This should also include the addition of characterising the change of mechanical behaviour on the influence of particles required for further testing with Digital Volume Correlation (DVC).

**Objective 2: Develop a finite element model to simulate indentation and puncture of needles**

To create an initial finite element model of needle indentation into silicone-based skin substitutes, incorporating accurate geometry, mesh, material properties, boundary conditions, and contact interactions. In addition, optimisation of the model by predicting the mechanical response of silicone-based skin substitutes under different deformation scenarios, refining mesh and material parameters.

**Objective 3: Develop methods that can be used to validate FE models**

To visualise soft material deformation and needle insertion utilising high-resolution imaging techniques to capture details of skin deformation during needle insertion. Implementing advanced data analysis techniques such as digital volume correlation (DVC) on the captured images to obtain details on the deformation fields and a basis for comparison to finite element model predictions.

### **1.3 Thesis structure**

This section provides a brief overview of the contents of each chapter in this thesis.

Chapter Two contains the literature review, which introduces an overview of drug delivery methods, with a particular focus on transdermal delivery systems. It provides a detailed examination of MNs, covering both the experimental and computational advances in their design and application. The mechanical behaviour of skin is also discussed, including testing methods and constitutive material models. Fracture mechanics and imaging techniques, and DVC are also introduced, with their application to skin research considered. Finally, the current trends and research challenges of MN modelling are highlighted.

Chapter Three outlines the experimental protocol, detailing the material criteria that the skin substitutes must adhere to. It also presents the material property investigations and compares the results against the known properties of skin. The

## Introduction

initial imaging experiment of the particle distribution through silicone is also shown using  $\mu$ -CT.

Chapter Four covers the FEMs that were developed, with both static and dynamic models created. These models incorporate geometry derived from the  $\mu$ -CT scans, as well as a cohesive zone method to simulate needle insertion.

Chapter Five details the subsequent  $\mu$ -CT experiments, focusing on two needle displacements: one at low displacements to establish an initial protocol for DVC, and another at higher displacements to investigate the strain near the predicted puncture points. The image and data processing for DVC, applied to both the first and second sets of scans is then detailed. It highlights the difference in the displacement and strain fields between the two deformation levels, alongside an initial comparison with the FEA from Chapter Three.

Finally, the main discussion, Chapter Six, includes the overall comparison of the FEA results to DVC. Considerations for future MN designs are also discussed. The conclusions and future work are presented in Chapters Seven and Eight.

# ***CHAPTER 2***

---

## **LITERATURE REVIEW**

### **2.1 Microneedles**

#### **2.1.1 *Drug delivery methods***

Methods of delivering drugs into the body have been developed over centuries. Oral medications are one of the most popular methods but the number of drugs that can be delivered using this route is limited. For example, insulin is not compatible with oral delivery systems due to its low absorption rate and enzymatic degradation [30]. Hypodermic needles allow medicines and vaccines to enter the body by a number of routes, including intradermal, subcutaneous, and intramuscular delivery. These needles, which have a large radial tip geometry (diameter ranging from 0.16 mm to 3 mm [31]) penetrate the deeper layers of the skin, namely the dermis and hypodermis. This can lead to side effects such as pain, bleeding, and scarring.

## Literature Review

Transdermal drug delivery methods, such as patches, were initially developed to deliver drugs that can penetrate the skin, allowing for controlled, sustained release while bypassing the gastrointestinal tract. These patches adhere to the top layer of the skin, allowing the drug to be absorbed over time [Figure 2-1]. MNs were invented in 1976 [32] and are tiny (>1000um) needles that can deliver drugs through the skin in a minimally invasive manner. Unlike traditional hypodermic needles, MNs penetrate the outermost layers of the skin without reaching the deeper layers, thus minimising pain and other side effects such as bleeding and bruising.

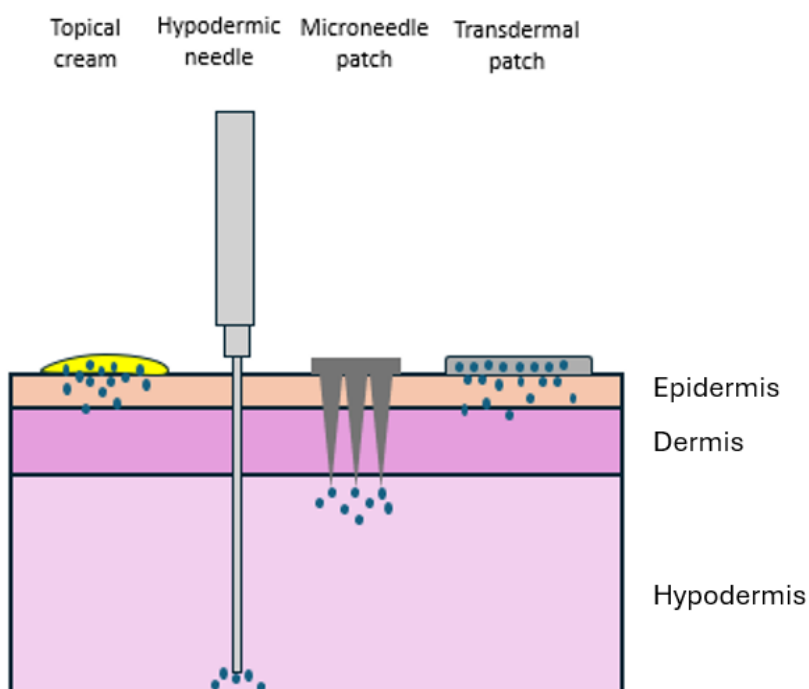


*Figure 2-1 - A figure showing the skin layers (epidermis, dermis and hypodermis) and the different transdermal drug delivery methods including topical creams, hypodermic needle, MNAs, and a transdermal patch.*

Significant advancements in manufacturing methods, especially during the 1990s, led to the development of MNs as a promising method for topically applied drug delivery. The main advantages of MNs include minimally invasive insertion and the potential for self-administration, without the need for a medical professional. These perceived benefits have driven research and development in the field but, despite advancements, MNs are not in routine clinical use.

### 2.1.2 Drug delivery methods using MNs

MNs are typically categorised into the following: solid, coated, hollow, dissolvable and hydrogel [Figure 2-2] [33]. When MNs are collectively arranged on an applicator, or patch, they are referred to as MNAs. These arrays are necessary to achieve the required dose of medication, as a single MN is unlikely to be sufficient in most cases. The number of MNs on an array can range from 5 to over 500 [34].

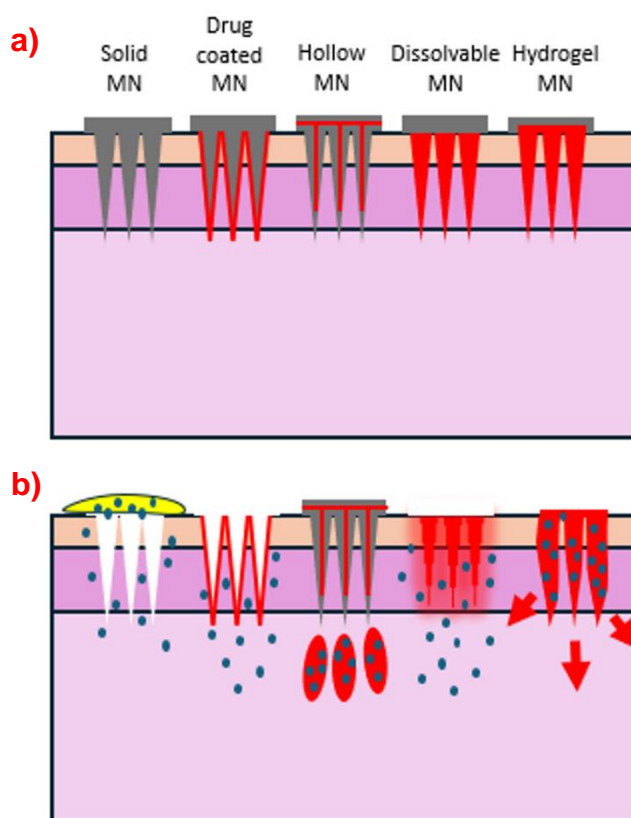


Figure 2-2 – A figure showing the different drug delivery methods using MNs, indicating how the drug is infused into the skin. These MNs are categorised as solid, hollow, drug coated, dissolvable, and hydrogel (polymer based microneedles that swell upon insertion). The red lines illustrate the drug loading capability of the MN method a) the blue dots illustrate the drug diffusion once the MNs, or patch, has been removed b)

Solid MNs, fabricated from materials such as steel and silicon, have been applied in two ways: coat and poke method and a poke and coat method. Firstly, in the coat and poke method, the array of MNs is coated in the specific APIs and then penetrates the SC. The drug diffuses into the skin and the array is then removed. The second solid

## Literature Review

MN method is the poke then coat method. The MNs first penetrate the skin, then a layer of a topical medicine or transdermal patch is applied to the penetration site. Whilst this method is simple, the micron-sized holes on the SC can close within a short period, often within minutes to hours depending on the body's healing response [35] [36]. Both methods produce medical waste, which must be disposed of safely to minimise the risk of reuse or a post-application injury. The two methods are also limited by the potency of the drug coated onto the MN, or within the cream applied to the area following the removal of the array.

Hollow MNs, akin to traditional hypodermic needles, facilitate drug delivery through microchannels within the device. These microchannels offer advantages over conventional solid MNs, notably in their ability to administer microliter volumes of drugs [37]. However, challenges such as needle buckling and fracturing due to their thin walls and sharp tips limit their integration into transdermal patches. Hollow MNs are primarily employed as an alternative to intradermal injections rather than as a comprehensive system for transdermal drug delivery. Additionally, maintaining a constant flow rate is imperative for these devices, which administers a high drug dosage within a required timeframe [38].

Biodegradable MNs, fabricated from diverse biodegradable polymers and dissolvable sugars [39] enable controlled drug release spanning milliseconds to days. Various biodegradable MNs have also been designed to break off in the top layer of the skin, with the skin healing within one to three hours post- penetration [40]. One notable example is a two-tier arrowhead design, Figure 2-3, where the 'arrowhead' rapidly dissolves upon contact with skin fluids, effectuating near-instantaneous drug release. The lower tier of the needle aids with the insertion into the skin due to a higher mechanical strength, and dissolves at a slower rate than the tip. The study by Zhu et al. further refined this design by incorporating a polymer gel layer that dissolves upon contact with bodily fluids, allowing the patch to be removed while leaving MNs embedded in the skin [41].



*Figure 2-3 - Biodegradable MN design with an arrowhead design are shown. The arrowhead breaks off into the skin where the polymer and encapsulated drug dissolves into the blood stream over a set period of time [41]*

One study presented a design for a bubble formation [42] at the interface of the MN and array patch and demonstrated its efficacy in facilitating material fracture and subsequent MN detachment within the skin [Figure 2-4]. Solid arrays tested required over 0.157 N/needle of force to bend the needle and subsequently fracture, and needles with the incorporated bubbles fractured at 0.15 N/needle. It should be noted that the required force to puncture the skin will be dependent on MN geometry and anatomical location, with some studies publishing that this force is less than 0.15 N [28] so, even though the bubbles weaken the mechanical strength of the needle, they can still penetrate the skin. Potential disposal of the patch in general waste reduces the volume of hazardous biomedical waste, underscoring the design's practicality for

self-administration without medical supervision and minimising the likelihood of needle reuse.

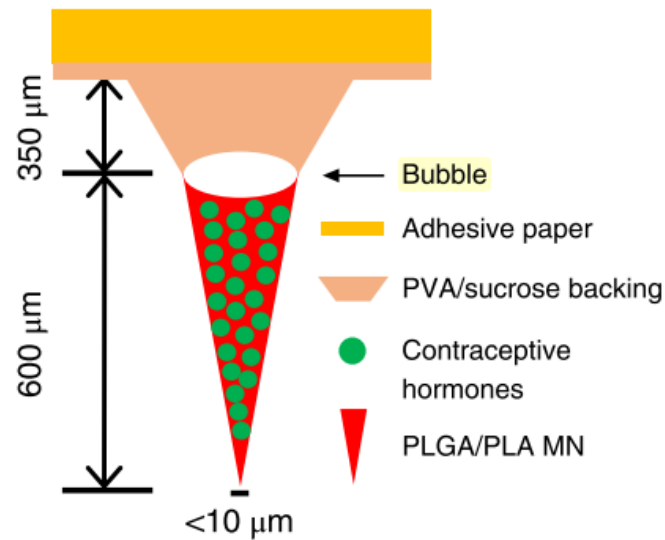


Figure 2-4 - Biodegradable MN design with a bubble which aids in the breaking of the MN tip. The stronger PVA backing enforces the MN to enable insertion into the skin without premature fracturing [42] .

### 2.1.3 Current research and challenges

MNs are at the forefront of transdermal delivery system development. However, it has been reported that only 7% of MN papers published between 2010 and 2020 were based on computational and numerical modelling [2], whereas 26% focused on MN fabrication.

#### 2.1.3.1 MN manufacturing

Significant advances in manufacturing techniques have been made over the past decade, including techniques such as micro-moulding, 3D printing, and laser-assisted fabrication.

Micro-moulding allows for high precision and uniformity in MN production, McAllister in 1998 studied MN performance in human cadaver skin and in vivo using diabetic rats [43] . The study outlined fabrication steps for silicon, metal, polymer, and glass MNs, with most requiring only one to two fabrication steps. Silicon MNs were created

## Literature Review

using sputter deposition and lithography for solid needles and spin-coated polymer photoresist and lithography for hollow needles. Metal MNs were produced by electrodeposition onto polymer or silicon micro-moulds, polymers by melting into PDMS micro-moulds, and glass needles using conventional drawn-glass micropipette techniques. Park et al. detailed the use of micro-electromechanical systems (MEMS) masking and etching to produce MNs with beveled and chisel tips, and lens-based lithography for tapered cones [44]. These were evaluated using mechanical testing of needle failure under axial loading, correlating failure force with Young's modulus, needle base diameter and length. Furthermore, Malek-Khatabi et al. studied the development of using CNC machining and micro-moulding techniques and evaluating their drug delivery capabilities [45].

3D printing offers the flexibility to create complex geometries tailored to specific applications. Techniques such as stereolithography [46], [47], fused deposition modelling, and inkjet printing have also been explored. It has been noted that 3D printing could have the potential to revolutionise MN design and manufacturing, enabling rapid prototyping, [48],[49], and production of personalised MN devices [50]. However, issues such as material efficacy and needle bending can limit the functionality and durability of printed devices. Despite its advantages, the production of reliable, personalised MN device remains a significant challenge, suggesting that widespread clinical use is still some way off. Stereolithography also offers high-resolution control, making it suitable for rapid prototyping of complex designs and the optimisation of needle geometry without requiring significant investment in large-scale manufacturing. Laser-assisted fabrication can also be used to improve the accuracy of MN tips, improving their ability to penetrate the skin effectively [49]. This fabrication could be more suitable where efficacy and consistency are crucial in clinical setting. All methods have been developed to use biocompatible polymers, which is important when considering the development of biodegradable MNs.

Other notable manufacturing methods include the coating of MNs [51] which includes dip-coating, spray-coating, and layer-by-layer coatings. These can determine the drug loading capacity and release profiles of MNs; however more research is required to optimise these techniques for specific drug formulations and applications. Chang et al. investigated optimal fabrication using MEMS and micro-hot embossing techniques

## Literature Review

for four MN designs, finding that optimising the fabrication process, as well as the design, can enhance the structural performance and reliability of MN patches [52]. Biodegradable composite MNs were designed using a mixture of sulfate and gelatin by Yu and were tested for their mechanical strength and their ability to deliver insulin transdermally [53].

### 2.1.3.2 MN and MNA design

The design of MNs is imperative; on average the length of a MN is 150 to 1500  $\mu\text{m}$ , with a tip radius from 1 to 25  $\mu\text{m}$ . The length is crucial; if the MN is too long it may contact the nerves within the dermis. The overall design also significantly impacts the insertion force and penetration depth efficacy. For example, Römgens and Davis highlighted that shorter, sharper needles required lower insertion forces than longer blunt needles [15],[10]. Geometrical design has also been investigated for numerous optimisation outcomes, including insertion force and penetration efficiency [14],[54]. Römgens noted that conical MNs had an insertion force of 0.1 to 0.4 N and beveled needles between 0.15 and 0.45 N. In comparison pyramidal and flat tipped MNs had forces ranging 0.2 to 0.6 N and 0.3 to 0.8 N respectively [15].

Similarly, Oldfield demonstrated that optimising needle shapes such as tapered designs, could reduce insertion force and improve penetration depth [17]. The force required for insertion can vary with needle length, tip diameter, and tip sharpness [10]. Crichton also investigated four MN designs - beveled, chisel-tip, conical and tapered needles -and found that insertion forces were moderately higher than the predictions from Römgens: around 0.8 N for beveled tips, 1.5 N for chisel-tips, a range of 0.6 to 1.3 N depending on the sharpness for conical tips and a range of 0.5 to 0.9 N for tapered needles [55]. Crichton later examined the effect of strain rate (the rate at which the MNA is inserted into the skin) and how this effects the precision of insertion and the corresponding insertion forces. It was noted that a higher strain rate (10 mm/s) caused an increase in force variability, with peaks of 1.5 N, compared to lower strain rates, which can in turn impact the effectiveness of MN delivery systems due to penetration depth [56]. Lim also explored combining different tip geometries for tuneable MN designs, offering flexibility to optimise insertion based on specific applications [57].

## Literature Review

Other design properties such as array interspacing have also been experimentally and computationally investigated [9],[12]. Closer interspacing of MNs increases the insertion force due to the increased skin resistance. This highlights the importance of optimal spacing for penetration efficiency [12].

### 2.1.3.3 Experimental studies

MN insertion is increasingly being tracked via non-invasive imaging techniques, including fluorescence microscopy, confocal microscopy and optical coherence tomography (OCT). OCT provides real-time, high-resolution images of MN insertion, allowing assessment of penetration accuracy and depth; however challenges include resolution, field of view, and alignment remain[16]. More recently, Wang has investigated real time imaging of dissolving MNs, though challenges persist with the resolution and sensitivity of these techniques for detecting fine structural details [58].

Other fundamental experiments for pre-clinical development include skin penetration specifically for drug delivery. Peaton investigated coating methods for plasmid DNA, optimising DNA stability and delivery efficiency by monitoring insertion into human skin [59]. Other drug delivery capabilities were investigated by Zhu and Dul M. Zhu explored the maximum drug loading capabilities of separating MNs, focusing on optimising the amount of drug in the separating mechanism [6]. Dul M used hollow MNs for gene delivery with a hydrodynamic approach (using fluid pressure or flow), enhancing the gene transfer compared to traditional methods (solid or coated MNs) [60]. Ex vivo human skin testing by Birchall demonstrated that DNA and gene expression can be effectively delivered by MNs fabricated using wet-etch techniques [61].

### 2.1.3.4 MN modelling

Whilst modelling previously represented a small percentage of published papers on MNs, this is on the rise, with many notable findings emerging. FEM modelling has explored various aspects, including the influence of geometry on penetration efficiency [29],[28], predicting tissue tearing and the force-displacement behaviour [17], and examining relationships between insertion speed and force [20],[19]. Studies have also investigated array interspacing on insertion forces [9],[62]. Additionally, the

## Literature Review

mechanical performance of MNs has been examined [24]. Quantifying the mechanics of human skin to optimise MN design has also been investigated [13], [23], [63], [64], [65] with other analytical and theoretical models that may aid in the optimisation and design researched [66], [67], [68], [69]. Modelling methods are discussed further in Section 2.6.

### 2.1.3.5 MN applications

MNs are well known for their use in vaccine delivery [70], [71], and the transdermal delivery of small molecules, peptides and proteins as previously noted [72], [73] as well as nano particles [74]. However, numerous other applications have been investigated, demonstrating the diverse range of MN uses. These applications include insulin delivery [75], hormone delivery [76], pain management [77], and cosmetics [78]. Personalised medicinal therapy has been highlighted with the use of MNs for cancer therapy [79], [80], [81], gene therapy [82], and bio sensing [78]. More recently, specific treatments such as wound therapy [83] and scar prevention [84], psoriasis therapy [85], and hair regrowth [86] have also been researched.

Despite the significant advancements in MAP technology, several challenges remain to be addressed. One major issue is scalability for mass production. Many current manufacturing methods, such as micro-moulding and 3D printing, face difficulties in scaling up to the demands of large-scale production while maintaining quality and consistency [20], [54]. Cost effectiveness is also a crucial concern linked to the manufacturing challenges. The high costs associated with the development and production of advanced MNAs can limit their accessibility and widespread use [58], [73]. Reducing these production costs, whilst maintaining high quality especially when dealing with biodegradable needle materials, is essential for ensuring the broader adoption and affordability of MAP technology in healthcare applications.

Regulatory approval presents another significant challenge. The complexity of MN designs and their novel applications necessitate rigorous testing and validation to meet the stringent standards set by regulatory bodies [71]. Ensuring that MNs are safe, effective and compliant with regulatory requirements is also a time-consuming and costly process.

Nevertheless, ongoing research and collaborations between academia, industry, and regulatory agencies are driving the continued advancement of MAP technology. These efforts are aimed at addressing the key challenges and paving the way for its widespread adoption in clinical practice [87].

## 2.2 Skin

The skin is the largest organ of the human body, comprising of three complex layers: the epidermis, dermis, and hypodermis [Figure 2-5]. The primary role of skin is to protect the body and internal organs from damage, including physical, biological, and chemical whilst also maintaining waterproofing. Each layer has its own intricate composition resulting in specific mechanical properties. However, the overall composition of human skin exhibits unique biomechanical properties that ultimately affects its performance in experiments and computational models.

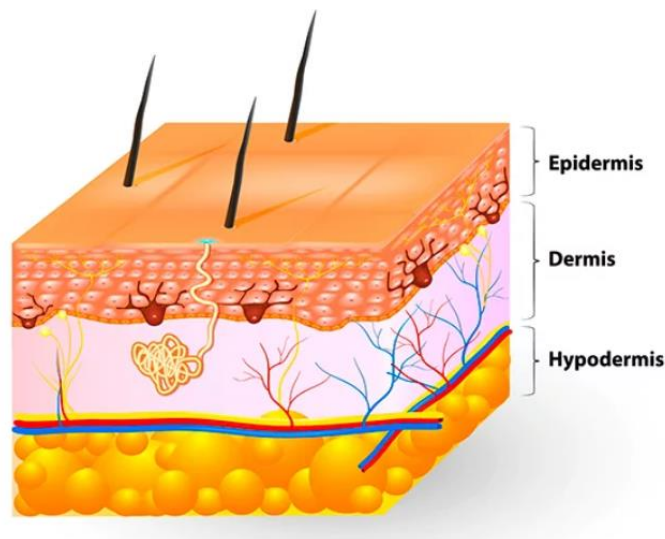


*Figure 2-5 – The structure of human skin, clearly showing the epidermis, dermis and hypodermis and important characteristics of each layer. Sourced from [\[https://www.oncobeta.com/your-health/nmsc-info/the-skin\]](https://www.oncobeta.com/your-health/nmsc-info/the-skin)*

The epidermis, the upper layer of the skin, is further divided into five layers: Stratum corneum (SC), stratum lucidum, stratum granulosum, stratum spinosum, and stratum basale [1]. The SC, the outermost layer, is predominantly composed of dead skin cells surrounded by a lipid matrix, forming a stiff protective layer against environmental,

## Literature Review

physical, and biological damage. Found only on the hands and feet, the stratum lucidum helps create the thickest layers of epidermis, contributing to characteristic ridges such as fingertips.

The thickness of the epidermis, and SC, in certain anatomical sites can pose significant challenges in MN design. A thicker SC requires deeper penetration for effective drug delivery, necessitating a higher insertion force. To address this, needle design may need to be adjusted such as incorporating a sharper tip, using a stiffer material, or making geometric changes to aid in penetration. These modifications are crucial for ensuring the MNs can penetrate the thicker epidermis without buckling or fracturing [88],[89].

The dermis, the middle layer of the skin, comprises two main regions: the papillary region and the reticular region. The papillary region contains blood vessels that nourish the epidermis with the oxygen and nutrients it requires to fight infections and carry away waste products. The reticular region contains nerves, glands, hair follicles, collagen, and elastin fibres. Collagen and elastin directly contribute to the strength and elasticity of skin. Collagen fibres provide tensile strength, supporting the skin's resistance to stretching, while elastin fibres allow for stretchability, helping the skin to accommodate movement. Although elasticity, defined broadly as the ability to return to its original shape after deformation [90], is a limited property in skin, the combined structure of collagen and elastin fibres enables skin to undergo large deformations without tearing. This structure is essential for flexibility and movement, which also increases the overall strength of the dermis [91].

The hypodermis, the deepest layer of the skin, also known as the subcutaneous layer, contains blood vessels, nerves, and layers of fat. Fat plays a crucial role in regulating body temperature and cushioning internal organs and tissues from physical damage. Despite its significance, the hypodermis is often overlooked in skin model studies. However, it directly contributes to skin deformation and MN puncture by providing a supportive, yet deformable, foundation. This layer can affect how the MNs interact with the skin, influencing the depth of penetration and the distribution of forces during insertion [92].

### **2.2.1 Mechanical behaviour of skin**

Skin is inherently an inhomogeneous material that exhibits non-linear, anisotropic and viscous-elastic behaviours, [93],[94], non-linear behaviour refers to the skin's response to stress and strain, where the relationship is not directly proportional, meaning the skin may become stiffer as it is stretched more. Anisotropic behaviour means that the skin's mechanical properties vary depending on the direction of the applied force. This is significant for MN design as the direction of insertion can affect the force required for penetration. Viscoelastic properties describe the skin's ability to stretch, compress and deform in response to an external force which includes both elastic (reversible) and viscous (time dependant) deformation [95], [96]. Additionally, skin exhibits poroelastic behaviour, where the flow of internal liquid through the tissue structure plays a crucial role in its mechanical response, particularly under sustained or repetitive loading.

Studying skin biomechanics presents significant challenges, with key difficulties relating to testing skin in situ and the changes in properties once it is excised. When the skin is in situ, it retains natural hydration and is subject to physiological conditions that can affect its mechanical responses. Once excised, these conditions are altered, which may impact the behaviour observed in testing due to factors like changes in hydration levels or reduced structural integrity. In vitro imaging, such as imaging histology samples, is a popular imaging technique to view skin structure ex vivo. The excision, or biopsy, requires ethical approval, but overall the technique is less complex since the skin is separated from the donor. Histology involves preparing tissue samples for imaging, which can provide detailed structural information but not the mechanical properties needed for biomechanical studies. Imaging of excised samples may reflect altered behaviour due to dehydrations and changes in environmental conditions which could skew interpretations of skins in situ mechanical characteristics.

The lack of standard tests for soft tissue biomechanics leads to considerable variation in how skin properties are quantified and how tissues are treated during testing. This variation has driven the development of computational models to predict skin behaviour which can help predict skin behaviour under various conditions. However, accurate computational modelling requires a thorough understanding of skin

biomechanics and thorough validation with experimental data to ensure their accuracy and reliability.

Skin properties differ from person to person; the thickness and mechanical behaviour of each layer is dependent on various biological and environmental factors [97]. These factors include: age, race, skin thickness, environmental changes (humidity, temperature), and anatomical location. Anisotropy in response to skin fibre orientation and strain rate both affect the ultimate tensile strength of skin, therefore the ultimate failure and tearing of skin can differ due to the way it is punctured or cut [22].

Such variability presents significant challenges for skin modelling and testing. Specifically, the differences in skin properties create an obstacle in developing accurate and reliable computational models. In the context of MN design, the thickness and mechanical behaviour of the skin can impact the efficiency of penetration. For instance, if the MN length is too long, it could penetrate into the reticular dermis causing pain and bleeding, whilst structural inconsistencies can lead to risks of needle fracturing before penetration, and poor reproducibility of puncturing behaviour.

Moreover, the influence of the multiple skin layers on the overall mechanical behaviour of MNs is still relatively unexplored and not widely understood. Most researchers design MNs to ensure they can puncture the skin effectively, and then test their performance empirically. This empirical approach underscores the need for parallel investigations into skin biomechanics and MN design to optimise performance.

### **2.2.2 Testing of skin**

Experimental data on skin mechanics has been collected via multiple methods of varying reliability and precision. To examine the strain dependencies of excised skin, tension tests can be performed. These experiments involve clamping the skin and stretching it to a specific ratio or until failure. The samples are typically rectangular, or dog bone shaped and excised parallel or perpendicular to the skin's natural fibre alignment [22]. These tests assess the stress-strain relationship of skin, highlighting how the material behaves under progressive, uniaxial loading [98]. Strain is often

## Literature Review

measured using optical tracking systems, such as VSG (virtual strain gauge) or DIC (digital image correlation) to ensure accurate local strain measurements. This provides key data on skin's elasticity and tensile strength, and quantifies properties such as Young's modulus, ultimate tensile strength, and strain at failure, which are critical for understanding how skin responds to forces in various directions. Factors such as the rate of strain application, sample thickness and alignment of natural skin fibres can influence the outcome of tensile tests.

Indentation tests involve pressing a probe into the skin (without tearing the skin) to measure its resistance to deformation and recovery, so mechanical properties such as skin stiffness and elasticity can be quantified. This can be performed in both in vivo and ex vivo settings. [88],[99],[100], [101] .

Tear tests involve applying tensile forces to the skin ex vivo, where two edges of the skin are clamped and gradually pulled apart to measure the force required to stretch and then cause a tear. Studies have shown that tear tests can be informative for evaluating skin tensile strength and tear resistance, particularly in wound healing research and clinical assessments [102], [103], [104]. These tests are further talked about in Section 2.3.

Strain imaging such as VSG and DIC, enable non-invasive assessment of skin deformation under mechanical loading. This enables testing of ex vivo skin, or in vivo under certain loading conditions, without damaging the tissue and provides surface deformation measurements. VSG involves recording the material under mechanical loading, with post-analysis of the video frames allowing for the evaluation of strain. In comparison, 2D and 3D DIC requires a random speckle pattern marked on the skin surface. Two to three high-resolution cameras then capture the deformation during mechanical testing (which can include tension, compression, or axial loading). The moving images are compared to the reference (initial) image, enabling the calculation of displacement and strain. Research utilising strain imaging has provided valuable insights into skin elasticity and mechanical response to external forces [105],[106],[107], [22], [108]. OCT (optical coherence tomography) and strain imaging is further discussed in Section 2.4.

## Literature Review

Other methods have also been used to investigate skin properties including suction tests, where a negative pressure (a vacuum) is applied to the skin and as the pressure reduces the skin is sucked up and the deformation and elastic response (the degree to which the skin returns to its original shape) is recorded. [96], [109], [110]. This can provide information about skin elasticity and viscoelastic behaviour and can be used to analyse the contributions of the skin layers to the overall mechanical behaviour. Torsion tests can be used to measure resistance to deformation and skin stiffness in vivo, a device grips the specific area of skin chosen and applies a controlled torque causing the skin to twist. The amount of force required to achieve a certain degree of rotation, as well as the skins ability to return to its original state after the force is removed, is recorded. The degree of resistance to the twisting force provides insights into the mechanical properties of skin, [111], [112].

Unlike simple materials, skin exhibits highly nonlinear, anisotropic, and viscoelastic behaviour, as seen in Figure 2-6. Parameters such as Young's modulus, shear modulus, and stiffness are often reported in studies, but their interpretation requires careful consideration of the experimental set up, loading conditions, and assumptions of the model used. Young's modulus, while commonly used to describe linear elastic materials, is less meaningful for skin due to its nonlinear behaviour. The modulus reported in studies may depend on the strain range, loading rate, and direction of the applied force. Shear modulus, on the other hand, relates to the skin's resistance to deformation under shear stress and is relevant in cases involving torsional and multi-axial loading. Stiffness refers to the load required to achieve a specific displacement or strain, which is inherently dependent on the geometry and boundary conditions of the sample rather than a material property like its modulus. Many studies have adopted more complex, nonlinear, constitutive models to capture the true behaviour of skin, such as Ogden, Mooney-Rivlin, and neo-Hookean models. These material models are explained further in Section 2.2.3.

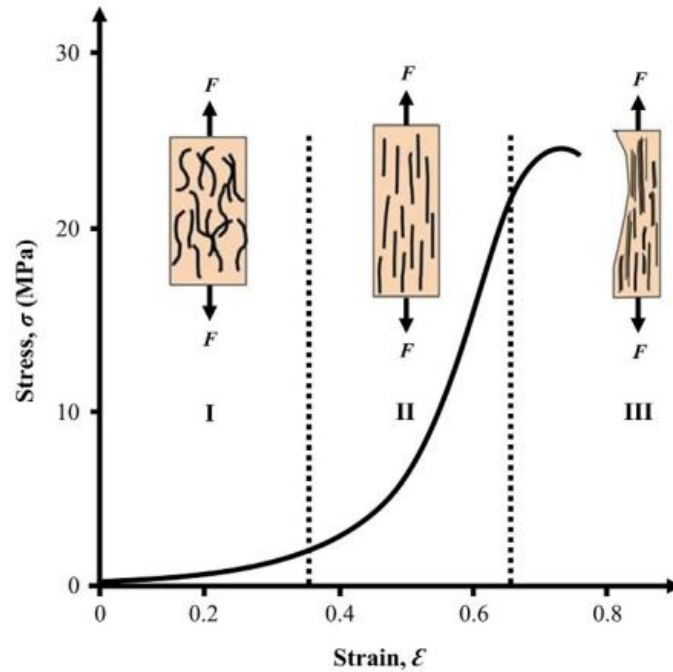


Figure 2-6- Figure of the stress-strain curve of human skin, showing the collagen fibres, and the overall non-linear behaviour of skin [113]

A brief review of the experimental methods discussed within this section and resulting skin properties determined are found in Table 2-1. It should be noted that variations in experimental methods, anatomical location and sample size contribute to the wide range of reported values.

## Literature Review

*Table 2-1 – The skin properties, including Young’s modulus and stiffness, taken from published papers identifying the different experimental methods used, their anatomical location (if relevant) and sample size*

Experimental method	Indenter details	Young’s modulus range (MPa)	Stiffness (N/m)	Anatomical location	Sample size	Reference
<b>Indentation</b>	Spherical (1.5875 mm)	0.03964	63.92	Forearm	7	[69]
	Cylinder (0.5 mm)	0.06586	44.31	Forearm	7	[69]
	Spherical (6.35 mm)	0.0095	25	Forearm	3	[100]
		0.007-0.008	24	Inner forearm	10	[114]
	Conical indenter	0.0125	24	Inner forearm	Not specified	[115]
0.0143			Forearm and thigh	31	[99]	
<b>Suction</b>		0.129 +- 88		Forearm	10	[116]
		0.056		Forearm	13	[109]
		0.3 – 0.6		Forearm	10	[96]
<b>Tension</b>		4.6 – 20		Not specified	Not specified	[98]
<b>Torsion</b>		0.42 – 0.85		Not specified	138	[111]
		0.02-0.1		Forearm	19	[112]
<b>Wave propagation</b>		0.0249 – 0.1012		Forearm	1	[117]
<b>Strain imaging</b>		0.4 – 0.6		Forearm, back of hand, abdomen	10	[107]
		4.02 +- 3.81		Abdomen	Not specified	[22]
		100		Not specified	Not specified	[108]

The reported results from skin biomechanical testing show extreme variability. This variability reflects not only differences in testing methods but also fundamental challenges in standardising testing protocols. For instance, Young’s modulus values span several orders of magnitude across different methods, from 0.007 MPa to 0.0659 MPa for indentation to 100 MPa with strain imaging. Similarly, stiffness values vary significantly, even for tests performed on the same anatomical location, as stiffness reflects the force response to displacement for a given test set up. Such discrepancies

arise from differences in experimental setups, indenter geometries, strain rates, and assumptions about skin behaviour, such as isotropy and linearity. Therefore, the Young's modulus describes the intrinsic material stiffness of skin, independent of its size or shape. It is taken directly from tension or compression tests, with mathematical models used to calculate the results. Stiffness measures the force required to deform a specific sample, meaning it is highly dependent on geometry and test set ups.

For example, suction tests might involve deeper layers of the skin, such as the hypodermis, while tension tests may primarily include superficial layers. In contrast, wave propagation (measuring the speed or attenuation of mechanical or acoustic waves through the tissue) and strain imaging provide insights into the dynamic or layered response of skin, but their results can vary due to testing set up, fibre orientation, or ex vivo skin hydration. Additionally, the choice of experimental method chosen may depend on its relevance to specific scenarios. For instance, suction tests may provide useful data for clinical applications, whereas tension test might be more applicable to computational modelling. Nonlinear methods, such as large-strain tensile testing or bulge tests, which better capture the viscoelastic and anisotropic properties of skin, are underrepresented in Table 2-1, and should be considered alongside the simpler linear models.

While the diversity of testing methods offers complementary perspectives on skin's biomechanical behaviour, it also complicates the development of producing computational models of skin that are accurate for multiple environmental and genetic conditions.

### **2.2.3 Constitutive models for skin**

There are several constitutive models that have been used in recent years to represent the complex behaviour of soft tissues, including human skin. Hyperelastic constitutive material models vary in simplicity and the material constants used to produce an accurate representation of soft tissue biomechanics. They are particularly effective at capturing the nonlinear elastic behaviour of skin, which can undergo large deformations. These models are based on strain-energy functions that describe how

the material stores and dissipates energy during deformation. The most favoured hyperelastic models are Neo-Hookean [118], Mooney-Rivlin [119], [120], Veronda-Westmann [121], and Ogden [122].

The Neo-Hookean material model is the most simplistic, which can make it computationally efficient, however it has limitations in accurately representing the nonlinear behaviour of materials under large strains as it only uses one material constant. The Mooney-Rivlin material model is an extension of the Neo-Hookean model, this model provides a better fit for experimental data over a wider range of deformations compared to the Neo-Hookean model with advantages including its ability to capture nonlinear stress-strain relationships more accurately. However, it still may not be sufficient for extremely large deformations or more complex material behaviours. Finally, the Ogden material model is one of the more versatile and comprehensive of the hyperelastic models. It is used for predicting the nonlinear stress-strain behaviour using multiple material constants [123], allowing the fit of experimental data more precisely across a broad spectrum of strains. This model provides more accuracy for complex materials, however its complexity and need for numerous material constants, such as  $\mu$  and  $\alpha$ , can make it computationally intensive and challenging to implement.

In addition to hyperelastic models, fibre-reinforced material models have gained traction in recent years for representing the anisotropic behaviour of skin, which incorporates fibrous microstructure. These models include the directional properties of collagen and elastin fibres, which significantly influence skin mechanics. Examples include the Holzapfel-Gasser-Ogden model, which combines hyperelasticity with fibre reinforcement to simulate the stress-strain response more realistically [124]. Fibre-reinforced models are particularly important when simulating scenarios involving high anisotropy, such as uniaxial tension or shear in specific directions.

In the study of large deformation mechanics, the Neo-Hookean material model is frequently employed to describe and simulate incompressible materials under various loading conditions. As stated by Groves [92] and Kim [123], the Neo-Hookean material model is an extension of Hooke's law for large deformations, where the initial relationship between the applied stress and strain is assumed to be linear [123]. The

## Literature Review

primary advantage of this model is its simplicity, which makes it computationally efficient. However, it has limitations in accurately representing nonlinear behaviour of materials under large strains as it only uses one material constant.

As explained by Kim [123] and first detailed in [118], the strain energy density, which represents the amount of energy stored in a material, function is given as Equation 1

$$W = C_1(\bar{I}_1 - 3) \quad 1$$

Where  $C_1$  is a material constant and  $\bar{I}_1$  is the first invariant from the Cauchy-Green deformation tensor, representing a scalar measure of the material's deformation. The first invariant is calculated from the tensor and gives insight into the overall stretching or compression without specifying directional details.

In the context of FEBio, an open source biomedical modelling software specifically designed for medical simulations which stores various material models, hyperelastic materials are often modelled using strain energy density functions that incorporate Lamé parameters ( $\mu$  and  $\lambda$ ) to reduce isotropic linear elasticity to small strains. This formulation is given as Equation 2 [118]

$$W = \frac{\mu}{2}(I_1 - 3) - \mu \ln J + \frac{\lambda}{2}(\ln J)^2 \quad 2$$

Where  $\mu$  and  $\lambda$  are the Lamé material parameters from linear elasticity.  $J$  is the determinant of the deformation gradient [125], representing the change in volume. The terms  $\ln J$  and  $(\ln J)^2$  account for the volumetric changes and compressibility, which are important in soft tissue modelling. For compressible materials  $J > 1$ .

The left and right Cauchy-Green deformation tensors are derived from the deformation gradient,  $F$ , which maps the reference configuration to the deformed configuration.

## Literature Review

The right Cauchy-Green tensor,  $C=F^T F$ , describes deformation relative to the initial state, while the left Cauchy-Green tensor,  $B=F F^T$ , is useful for describing deformation relative to the current state. By including these elements in the strain energy density function, these models account for both the materials elastic response, and volumetric changes, during deformation.

The derivatives of the strain energy density ( $W$ ) determine the stress state for a given strain in Equation 3

$$W = W(\bar{I}_1, \bar{I}_2) + U(J) \quad 3$$

The Mooney-Rivlin model allows for multiple parameters within the function, the most popular parameter numbers being two, three, five and nine. The number of parameters chosen is dependent on the suitability of the model and corresponding stress-strain curves. In FEBio, the uncoupled strain energy,  $W$ , is given by Equation 4

$$W = c_1(\bar{I}_1 - 3) + c_2(\bar{I}_2 - 3) + \frac{1}{2}K(\ln J)^2 \quad 4$$

Where the Mooney-Rivlin material coefficients are  $c_1$  and  $c_2$ , and the invariants of the right Cauchy-Green deformation tensor are  $\bar{I}_1$  and  $\bar{I}_2$ .

The Ogden model, introduced in 1972 by Ogden [122] is used for predicting the nonlinear stress-strain behaviour [123] using multiple material constants, allowing the fit of experimental data more precisely across a broad spectrum of strains.

The strain energy density function is expressed as Equation 5

$$W = \sum_{i=1}^N \frac{\mu_i}{\alpha_i} (\lambda_1^{\alpha_i} + \lambda_2^{\alpha_i} + \lambda_3^{\alpha_i} - 3) \quad 5$$

## Literature Review

Where  $\mu_i$  and  $\alpha_i$  are material constants and  $\lambda_j^{\alpha_i}$ , where  $j=1,2,3$ , is the principal stretch ratio of the material. In FEBio, the material constants  $\mu_i$  and  $\alpha_i$  are expressed in the model tree as  $c_i$  and  $m_i^2$ , and the function is described by Equation 6

$$W(\lambda_1, \lambda_2, \lambda_3, J) = \sum_{i=1}^N \frac{c_i}{m_i^2} (\lambda_1^{m_i} + \lambda_2^{m_i} + \lambda_3^{m_i} - 3) + U(J) \quad 6$$

Where  $J$  is the determinant of the deformation gradient, defining  $U(J)$  as the volumetric component.

### **2.2.4 Layer specific properties of the skin.**

Each layer of the skin has distinct mechanical properties which were studied by Groves et al. [23]. Groves et al. investigated the correlation between the indentation depth and the indentation force, examining how the thickness of each skin layer across seven participants influenced their respective mechanical properties [23]. Groves et al. set up an experiment that used two indenters, a spherical and a flat cylindrical indenter, with a displacement depth set to 0.3mm. This depth was chosen based on experiments by Davis et al., which found the minimum force for MN insertion was higher than this depth. A site on the forearm of the participants was chosen, with five cycles per participant, and the average from these five cycles used.

Table 2-2 shows the average Ogden material properties outlined by Groves et al., the two material coefficients  $\mu$  and  $\alpha$ , and the bulk modulus used within the Ogden material model. The set of data chosen as the standard deviation was significant except when comparing the hypodermis  $\alpha$ . The data collected for this study was used to evaluate the material properties of skin using the Ogden model material parameters. Each layer of the skin, the epidermis, dermis, and hypodermis, have specific material properties and thicknesses that differ from one another.

Table 2-2 - The material properties of each skin layer (epidermis, dermis and hypodermis) as specified in Groves [92]

Layer	Thickness (mm)	$\mu$ (MPa)	Standard deviation	$\alpha$	Standard deviation	Bulk modulus (MPa)
<b>Epidermis</b>	0.07	4.0991	0.8382	2.9814	0.9904	4099.1
<b>Dermis</b>	0.84	0.0226	0.00191	3.2876	0.233	22.6
<b>Hypodermis</b>	3	0.0104	0.000715	4.3224	4.3224	10.4

Other studies have also explored key material properties of skin layers. Hendriks et al. explored how different skin layers contribute to the overall mechanical behaviour of skin using suction experiments [96]. They varied cup sizes and combined these with ultrasound and OCT to study the internal deformation during the experiment. The main property investigated was the stiffness of the layers, with the key finding of the experiment showing the significant stiffness differences between the epidermis and dermis. Limitations with this study included the sample size of 10 participants and the lack of in vivo dynamics. A larger sample size would enhance the statistical power of the study, allowing for a more robust conclusions regarding skin differences across individuals.

Single skin layer investigations were conducted by Smalls and Geerligs on the dermis and epidermis respectively. Smalls examined how dermal thickness, tissue composition, and body site affect skin biomechanical properties [126]. Using suction experiments on 20 healthy female participants they demonstrated that skins stiffness varies significantly across body sites due to differences in dermal thickness and tissue composition. These findings emphasise the layered complexity of skin structure and its influence on biomechanical behaviour. On the other hand, Geerlings used in vitro indentation techniques to evaluate the elastic and viscoelastic behaviour of the thin epidermal layers [127]. This study provided insights into the epidermis's role in overall skin mechanics and deformation under force. However, their study only looked at excised skin which can exhibit extreme differences in material properties compared to in vivo skin.

Additionally, Crichton et al. explored the viscoelastic and hyperelastic behaviours of excised skin layers using microscopy at micro and nano scales [128]. They identified

that the dermis exhibited the highest stiffness, producing an elastic modulus of between 7.33 MPa and 13.48 MPa, while the epidermis demonstrated the greatest viscoelasticity. Their work highlighted the scale dependent mechanical properties of skin layers, and the structural contributions of collagen fibres. Again, this study only used excised skin, which poses a limitation as it may exhibit material properties different from in vivo conditions, such as the large stiffness differences.

## **2.3 Fracture mechanics**

### **2.3.1 Background**

Fracture mechanics is a branch of applied mechanics that focuses on the study of the behaviour of materials under the action of external forces, leading to the propagation of cracks or fractures. It is a fundamental field that provides insights into the mechanisms governing fracture processes, as well as methodologies for predicting and preventing structural failures. Fracture mechanics plays a crucial role in various industries, including aerospace, automotive, civil engineering, and biomedical engineering, where understanding the behaviour of materials under loading conditions is essential for ensuring safety and reliability [129].

Fracture mechanics relies on fundamental principles from classical mechanics and solid mechanics to understand the behaviour of materials under loading conditions, particularly when cracks or fractures are present. These principles encompass stress analysis, strain energy considerations, and the mechanics of crack propagation. In the context of this research, fracture mechanics forms the basis of some of the computational modelling discussed further in Section 2.6. Understanding the mechanisms of needle penetration into soft materials, including tearing, is vital for developing more effective and reliable MN designs. By applying the principles of fracture mechanics to create more realistic computational models that simulate MN interactions with skin or soft materials, overall drug delivery designs can be improved.

### 2.3.1.1 Stress Analysis:

Stress analysis is concerned with understanding how forces are distributed within a material. Stress, denoted by  $\sigma$ , represents the force per unit area acting on a material and is typically categorised into normal stress ( $\sigma_n$ ), and shear stress ( $\tau$ ). In fracture mechanics, the focus is often on the stress field near the crack tip, as this region governs crack propagation. The stress field is characterised by high levels of stress concentration, leading to localised deformation and crack growth [130].

### 2.3.1.2 Strain Energy:

Strain energy refers to the internal energy stored within a material due to deformation. When a material is subjected to external forces, it deforms, storing energy in the form of elastic strain. The concept of strain energy is crucial in fracture mechanics, as it provides insight into the energy required to initiate and propagate cracks. In particular, the release of strain energy during crack propagation plays a significant role in determining a material's fracture behaviour [131].

### 2.3.1.3 Crack Propagation:

Crack propagation is the process by which cracks extend through a material under applied loads. It is governed by the balance between the energy required to create new crack surfaces and the energy released by elastic deformation ahead of the crack tip. The critical condition for crack propagation is reached when the energy released by the material surpasses the energy required to create new crack surfaces.

### 2.3.1.4 Strain Energy Release Rate $G$ :

The strain energy release rate, denoted by  $G$ , characterises the rate of energy dissipation due to crack growth. It represents the change in strain energy per unit area as the crack propagates and is a measure of a material's resistance to fracture. The strain energy release rate is often determined experimentally or calculated using analytical or numerical methods and is expressed as Equation 7

$$G = \frac{dU}{dA} \quad 7$$

where  $U$  is the strain energy stored in the material, and  $A$  is the crack surface area [132]. By evaluating the strain energy release rate, engineers and researchers can assess a material's toughness and predict its fracture behaviour under different loading conditions.

#### 2.3.1.5 Work done and work of fracture

The work of fracture (WoF) of soft materials is a crucial parameter to determine the material's resistance to fracture initiation and propagation under specific loading conditions. It represents the energy required to create new crack surfaces as a material undergoes deformation and is a critical factor in understanding the material's fracture behaviour. It is determined experimentally through the analysis of tear formations in material specimens. To determine the WoF, the incremental work-area method, also known as Gurney's method, is commonly employed [133]. This method involves calculating the energy absorbed in creating the new crack surfaces. The crack area is measured using tools such as a travelling microscope, which allows for the precise measurements of the crack dimensions. The energy associated with crack formation is determined from the area under the load-displacement curve, which is obtained from experimental data. This energy is then divided by the area of the new crack to obtain the energy per unit area, or the work of fracture. This method provides direct measurement of the material's resistance to fracture propagation [134], [135], [136].

To calculate the work of fracture ( $W_f$ ), the measured work done ( $W_d$ ) during the fracture process is utilised in Equation 8. This involves summing up the energy expended in overcoming the resistance to crack propagation:

$$W_d = \int_0^d F dx \quad 8$$

where  $F$  is the force applied, and  $d$  is the displacement, and the work of fracture can be expressed as Equation 9

$$W_f = \frac{W_d}{A} \quad 9$$

where  $A$  is the critical crack area.  $A$  is found by Equation 10

$$A = l_c \times t \quad 10$$

Where  $l_c$  is the crack length and  $t$  is the sample thickness.

Exploring the microstructural features and molecular interactions within the material can offer valuable insights into its fracture behaviour. Techniques such as microscopy and spectroscopy enable the visualisation and analysis of internal structures and defects, contributing to a deeper understanding of the mechanisms governing fracture in soft materials [137].

### **2.3.2 Development and advancement of fracture mechanics**

The fracture mechanics of soft materials presents unique challenges due to their viscoelastic nature and complex microstructure. Unlike traditional engineering materials, such as metals or ceramics, soft materials exhibit nonlinear deformation behaviour and may undergo significant changes in mechanical properties under different loading conditions. Consequently, characterising the fracture behaviour of

## Literature Review

soft materials requires specialised experimental techniques and theoretical models tailored to their unique mechanical properties.

The understanding of fracture mechanics has evolved significantly over the years, driven by both theoretical advancements and experimental investigations. Early studies, such as those by Rivlin and Thomas, laid the groundwork for understanding the behaviour of rubber materials, contributing essential theoretical frameworks for elastomer deformation and fracture. The researchers developed a mathematical model describing the elastic behaviour of rubber materials, laying the groundwork for understanding the complex mechanical properties of elastomers [138].

Further work by Broberg in 1975 on stable crack growth contributed significantly to the understanding of fracture mechanics. By examining the conditions under which cracks in materials grow steadily without catastrophic failure, Broberg provides crucial theoretical frameworks for analysing crack propagation phenomena [139].

Mai's study in 1991 focused on the essential work of fracture and J-integral measurements for ductile polymers. By investigating energy dissipation mechanisms during crack propagation, Mai provides valuable insights into the fracture behaviour of polymers under various loading conditions [135]. Following on, Wu and Mai introduced the concept of essential fracture work for measuring the toughness of ductile polymers, offering a comprehensive framework for characterising their fracture behaviour [140].

In 2001 Oyen-Tiesma and Cook introduced a technique for estimating the fracture resistance of cultured neocartilage, a promising approach in tissue engineering [141]. Their work demonstrated the importance of reliable methodologies for assessing the mechanical properties of soft tissues and engineered biomaterials, highlighting how fracture resistance can be quantified in soft, biological materials. This approach laid the foundation for advancements in regenerative medicine and tissue engineering.

A study by Pardoen et al. explored the essential work of fracture compared to traditional fracture mechanics, aiming to develop thickness-independent toughness measures for plane stress conditions [142]. This work contributed to the refinement of fracture assessment methodologies, particularly in thin structures. By focusing on the energy required for crack propagation, this work advanced the understanding of how

## Literature Review

materials fracture under applied stresses. The critical tearing of tire rubber was tested in 2004 by Gdoutos et al. and quantified the material's resistance to tearing and identified factors influencing its mechanical behaviour [143]. This included the roles of temperature, strain rate, and material heterogeneity.

Further studies by Taylor et al. investigated the fracture toughness of soft tissues, a critical aspect in understanding the mechanical behaviour of biological materials [144]. Their research highlighted the relationship between tissue microstructure and fracture resistance, emphasising the viscoelastic nature of soft tissues and their response to crack propagation, including under dynamic loading conditions. This was further studied by Pissarenko's study in 2019, where the study focuses on the toughness of porcine skin, employing quantitative measurements and microstructural characterisation techniques [102]. This research enhanced the understanding of skin biomechanics and fracture resistance, with a particular focus on the role of collagen and elastin fibres in skin's fracture resistance. A subsequent study in 2020 explored the tensile behaviour and structural characterisation of pig dermis, providing insights into the mechanical properties of biological tissues [103].

Spagnoli's comparative study investigated the fracture mechanics in cutting processes, comparing the behaviour of hard and soft polymeric materials [145]. By focusing on cutting mechanisms, Spagnoli's research contributed to understanding the fracture behaviour of polymeric materials during mechanical processes.

The most recent work has included Zhang's research in 2021 examining the relationship between cutting and tearing in soft elastic solids [146]. By explaining the mechanics of cutting processes in these materials, Zhang's study contributes to the understanding of fracture mechanisms in soft elastic solids, such as variations in elasticity and the presence of internal structure. Yin et al. also investigated the essential work of fracture of soft elastomers, aiming to elucidate the fracture mechanics of these versatile materials [147]. By quantifying the energy dissipation during crack propagation, they provided valuable insights into how elastomers absorb and dissipate energy as cracks grow. Specifically, their work highlighted the critical factors influencing the fracture toughness and resilience of elastomers, including their viscoelastic properties, and the role of strain rate in crack propagation.

## Literature Review

Fracture mechanics plays a crucial role in understanding the behaviour of soft materials under needle penetration, as these materials often exhibit complex, nonlinear deformation. In contrast to traditional engineering materials, soft tissues undergo significant mechanical property changes under loading conditions, which complicates the fracture analysis. Needle penetration involves a combination of deformation, fracture, and energy dissipation, and requires an understanding of how these materials resist crack initiation and propagation. The application of fracture mechanics to needle penetration problems involves using theoretical models that account for the material's response to stress concentrations at the tip of the needle. One important concept used is the critical stress intensity factor. This defines the stress intensity at the tip of a crack at which fracture will propagate. Linear elastic fracture mechanics (LEFM) is often applied to model the crack initiation in soft materials during penetration. However, soft materials are typically highly nonlinear, and other models such as nonlinear fracture mechanics or J-integral analysis are also relevant.

Shergold & Fleck [148] developed a model for needle penetration based on the stress intensity factor and elastic-plastic fracture mechanics. Their work applied fracture mechanics theory to predict the penetration force and depth of sharp objects into soft tissues. Their model considered the stress concentration at the needle tip, which induces a crack. By analysing the materials resistance to crack propagation, they showed how the needle geometry, material properties, and loading condition influenced the depth of penetration.

Mattia Bacca [66] further developed the theoretical framework for needle penetration by incorporating plasticity and damage mechanics. Bacca's work highlighted the importance of yield stress and strain hardening in soft tissues during needle penetration. These factors impact the materials ability to resist cracking and deformation, which directly influences the penetration force. The energy release rate and fracture toughness were also explored, providing an understanding of how tissues undergo deformation and fracture under high strain.

### 2.3.3 Analytical models

Numerical models of MN insertion into skin are diverse, focusing on fundamental aspects of skin mechanics such as tearing, cutting, wounding, and penetration. A review of mechanical models for deep penetration into soft solids was conducted by O. Shergold and N. Fleck in 2004 [149]. They presented various mathematical models derived from published experiments and discussed different types of penetration and substrates used including in vivo human skin, human cadaver skin and silicone rubber. They highlighted the use of strain-energy density from the Ogden material model [Section 2.2.3] and concluded that the critical force required for penetrating a soft material depends on the material's stiffness and the needle geometry. Their theory was validated through experiments involving the penetration of silicone rubber and human skin. They found that a one-term Ogden model could provide reasonable approximations [148] but noted that their study did not take into account the initial stages of needle insertion.

Davis explored the MN puncture theory, examining how factors such as wall thickness, angle, and tip radius affect the fracture force using human cadaver skin [10]. Davis differentiated between needle puncture and tear, as described by Pereira et al. [150], by analysing the change in potential energy indicated by the area under the load-displacement curves before skin fracture and relating it to new surfaces created within the skin. Equation 11 relates the work to initiate a crack to the total work inputted

$$G_c = \left( \frac{\delta W}{\delta A} \right) \quad 11$$

Where  $G_c$  is the fracture toughness,  $\delta W$  is the total work to propagate a fracture, and  $\delta A$  is the surface area of the new fracture. The work required is expressed in Equation 12

$$\delta W = \int F dx \quad 12$$

Where  $F$  is the force applied to the needle and  $x$  is the position of the needle. This can be rewritten as Equation 13

$$\int_0^{x_1} F dx = G_p A \quad 13$$

Where  $G_p$  is the puncture fracture toughness and  $x_1$  is the displacement of insertion. Rearranging this gives Equation 14

$$F_1 = \tau G_p A + \theta \quad 14$$

Where  $F_1$  is the force at the point of insertion and  $\theta$  and  $\tau$  are the pre and post exponential constant respectively, allowing  $G_p$  to be determined. The constants are scaling factors that characterise the initial and subsequent changes in force during insertion, showing the material's response over time or under varying conditions. Davis's experiments predicted insertion force, measuring the electrical resistance (using an electrode on the subjects hand) and force during a needle insertion into human skin, shown in Figure 2-7. This reveals a rapid decrease in both skin resistance and force once the needle had penetrated. This experiment provided real-time data on skin impedance changes during the needle insertion.

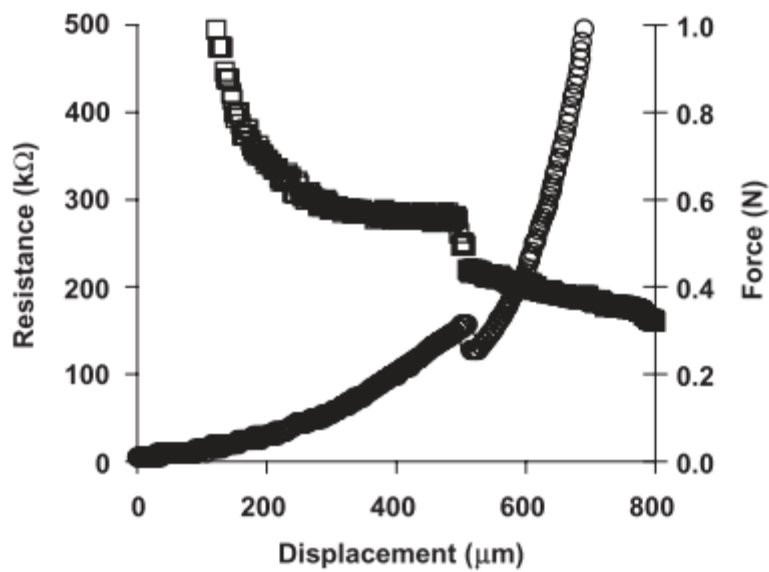


*Figure 2-7 – The load-displacement-resistance graph from Davis publication [10], illustrating the point of MN insertion can be identified by the sudden drop in skin electrical resistance or applied force*

Recent advancements in analytical and theoretical models have further enhanced our understanding of needle insertion mechanics. As mentioned in Section 2.6.4, Oldfield developed a cohesive zone model for penetrating gelatin, noting the overall interaction of needles with soft solids [17]. Oldfield identified five phases of needle insertion [Figure 2-8], with two ‘relaxation’ periods, in contrast to Davis’s observations of a single force drop.

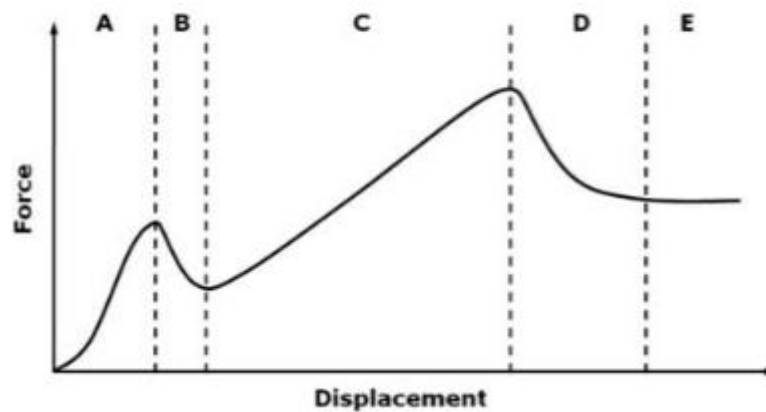


Figure 2-8 – The load-displacement graph from Oldfield publication [17], illustrating the five stages of needle insertion that was identified

Oldfield summarised the work of Azar and Hayward [151], Shergold and Fleck [148] and Misra et al. [152] to create a generic energy balance of Equation 15

$$W_{ext} = W_f + W_\varepsilon + W_{G_c} \quad 15$$

Where  $W_{ext}$  is the external work done by the MN,  $W_f$  is the work to overcome friction,  $W_\varepsilon$  is the work converted to strain energy, and  $W_{G_c}$  is the work required to create the crack. The work to overcome friction can be further explored by Equation 16

$$W_f = \int_0^{U_p} F_F(x) dx \quad 16$$

Where the frictional force,  $F_F$ , is assumed to increase linearly from zero to the maximum insertion value (full penetration),  $x$  is the displacement along the crack axis, and  $U_p$  is the needle tip depth. Ignoring rate-dependant effects, the work to deform the tissue is Equation 17

$$W_{\varepsilon} = \int_0^{U_p} U_{\varepsilon} dx \quad 17$$

Where  $U_{\varepsilon}$  is the strain energy per unit length of crack generated. The insertion depth and reaction forces ( $F_R$ ) give Equation 18

$$W_{ext} = \int_0^{U_p} F_R dx \quad 18$$

And the last component  $W_{G_c}$  is Equation 19

$$W_{G_c} = \int_0^{U_p} G_c w(x) dx \quad 19$$

Where  $w(x)$  is the known crack width and  $G_c$  is the strain energy release rate. This can be used to build a traction-separation relationship in cohesive zone modelling. The strain energy release rate is represented by the area beneath the curve in Figure 2-9. Once the separation exceeds  $\delta_0$ , the cohesive element fails and is removed, or separates, leaving an extended crack line.

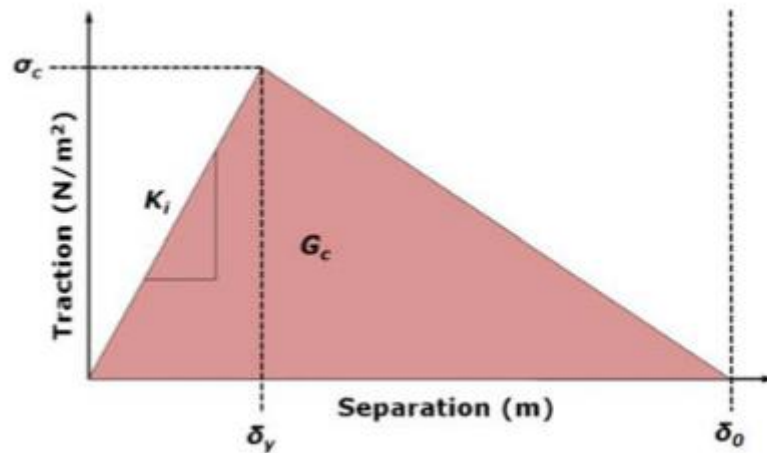


Figure 2-9- The separation-traction graph from Oldfields publication [17], demonstrating the relationship that is utilised for cohesive elements to implement the damage criteria required

Additionally, Boonma's work on analytical modelling of MN apparatuses for biomedical applications shed light on the critical factors affecting MN performance [67]. In their study, a two-stage analytical model was created dividing the needle and skin interaction into pre-puncture and post-puncture. The pre-puncture model used a non-linear relationship between strain and displacement, with the puncture determined by energy changes. Their theory included internal strain energy due to deformation and fracture toughness, as shown in Equation 20

$$Fdx = JdA + d\Delta \quad 20$$

Where  $F$  is the force on the MN,  $dx$  is the MN displacement,  $J$  is the fracture toughness, and  $d\Delta$  is the strain energy. Post puncture insertion force modelling is based on the theory that, when the NM is displaced, the tissue moves perpendicular to the needle surface. The fracture toughness quantifies the ability of a material to resist crack propagation growth under loading. In terms of MN insertion, this is the resistance of the skin to fracturing or tearing when the MN penetrates it. The WoF is closely related to the fracture toughness, but focuses more on the energy required to propagate a

## Literature Review

crack in the material, for example the energy needed for the tissue to fail. When a MN is inserted, it applies stress to the skin, and if the stress exceeds the materials fracture toughness, it will cause the tissue to crack. The WoF then quantifies the energy required for this cracking process.

These analytical models were later represented with a two-step FEM, initially using rubber properties and then extending to a three layer skin model, both with non-linear material properties including the Young's modulus and Poisson's ratio. Experiments validated these models with three needle geometries: sharp bevel, blunt bevel tip and cylindrical (with an external diameter of approximately 230  $\mu\text{m}$ ), with the load-displacement curve results shown in Figure 2-10 .

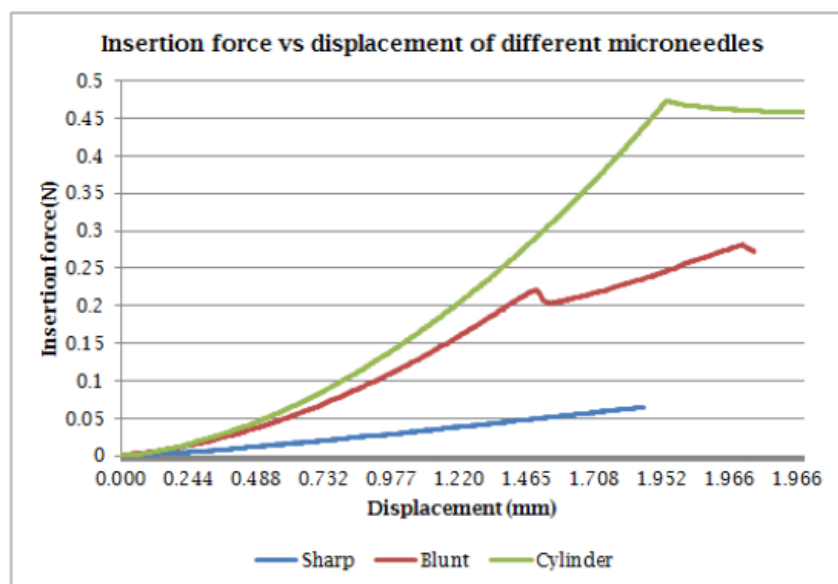


*Figure 2-10 - The load-displacement curves comparing sharp, blunt and cylindrical needles from Boonma's investigation into MN insertion characteristics [67]. The insertion point is identified for the blunt bevel needles, with the cylindrical needle not puncturing.*

The predicted insertion forces were: the sharp needle punctures at 0.23 mm and a force of 0.014 N; the blunt bevel punctured and 1.266 mm and 0.217 N; the cylindrical needle did not puncture under the set experimental parameters. The comparison between their analytical predictions and experimental data showed a good fit.

More recently, Fregonese [66] developed a mechanical theory addressing the pre and post insertion phases of needle penetration into soft materials. In this work, the same incompressible single term Ogden material model was used to describe the hyperelastic behaviour of soft materials. Fregonese detailed a sharp transition from indentation to penetration; this transition was explained using a theory of perfect energy transfer, where the energy for penetration is assumed to be transferred efficiently into the material during the initial phase. However, it was highlighted that frictional forces during penetration can create energy dissipation in a linearly proportional manner, unlike the constant dissipation described by Shergold and Fleck [148]. This distinction is important as it suggests that frictional forces contribute to an increased energy requirement for needle insertion, a factor that has typically been underestimated in simpler models.

By incorporating this proportional dissipation, the model provides a more accurate description of the energy involved in penetration. Despite the added complexity of frictional energy dissipation, Fregonese demonstrates that the critical force required for needle insertion can still be predicted accurately using a simplified version of the material model - specifically a one-term Ogden model instead of a two-term model. This approach maintains predictive accuracy while reducing the computational complexity. This work provides a promising framework for refining and extending needle penetration models. The incorporation of frictional dissipation and the transition from indentation to penetration introduces a more realistic representation of the physical processes involved.

## **2.4 Imaging of skin**

Imaging techniques have revolutionised the study of skin, providing detailed insights into its structure and mechanical properties. Various methods such as Virtual Strain Gauge (VSG), Digital Image Correlation (DIC), Computed Tomography (CT), and Optical Coherence Tomography (OCT) offer unique capabilities for analysing the skin at different levels of detail and depth. These techniques are crucial for advancing our understanding of skin health, disease pathogenesis, and the development of medical

devices, like MNs. Each method offers distinct advantages and limitations, making them suitable for specific applications in both clinical and research settings.

### 2.4.1 OCT

Optical Coherence Tomography (OCT) is a non-invasive imaging technique widely used in medical diagnostics and research to visualise the internal microstructure of biological tissues with high resolution and depth [153]. Developed in the early 1990s, OCT has revolutionised medical imaging by providing cross-sectional and three-dimensional images of tissue morphology in real-time. The principles are explained in further detail in [153], with the general set up shown in Figure 2-11. In simplified terms, OCT uses low-coherence interferometry where light is split into a reference arm and a sample arm. By measuring the interference between light reflected from the tissue and the reference arm, it generates high resolution images of the tissue's microstructure.

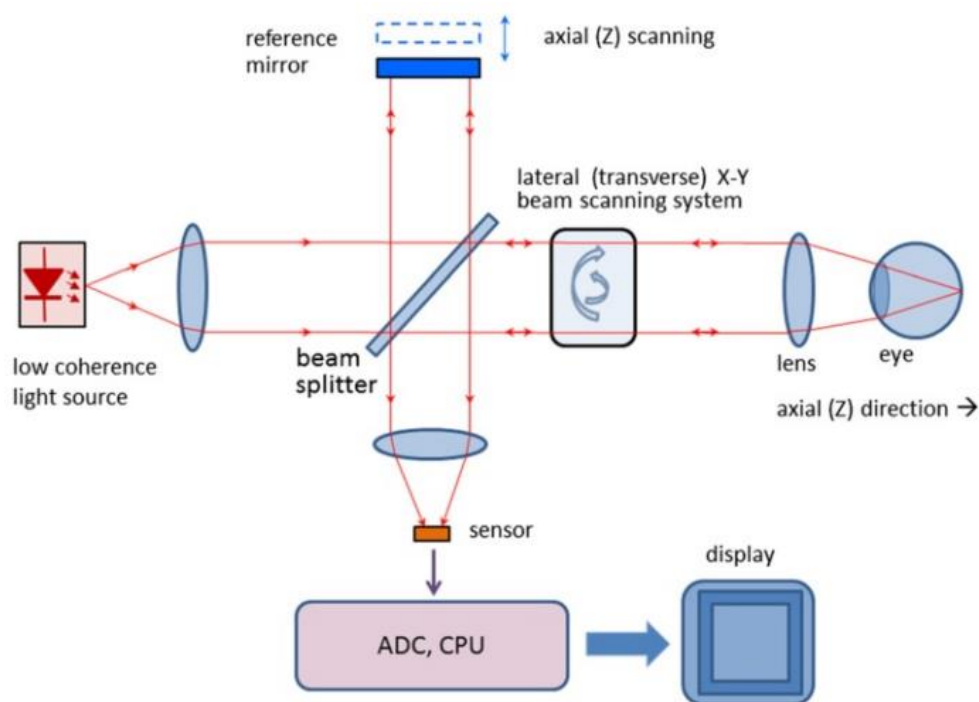


Figure 2-11 – A typical OCT set up, showing how the beam is split from the light source to the reference mirror, the material and to the sensor to be display [154].

## Literature Review

One of the key advantages of OCT is its ability to provide micron-scale resolution imaging at depths of up to 2-3 millimetres in biological tissues [155]. This enables visualisation of various tissue layers, such as the epidermis and dermis with exceptional detail. Additionally, OCT is non-invasive and does not require the use of ionising radiation, making it safe for repeated imaging procedures.

OCT finds widespread applications in various medical fields, including ophthalmology, dermatology, cardiology, and gastroenterology [156]. Studies have allowed for non-destructive optimised viewing of skin depth and MN penetration both in vivo and in situ. Coulman's study demonstrates the application of OCT for real-time imaging of MN insertion into human skin [16]. By providing in vivo and in situ visualisation, the study offers insights into the penetration depth and distribution of MNs within the skin.

Other studies have investigated the use of OCT for 3D morphological skin imaging. Zhang enhanced depth resolution and tissue contrast, facilitating detailed visualisation of skin structures and pathologies [157]. The effects of age, gender, skin type, and anatomical site on epidermal thickness was also investigated by Wang et al. to aid in the understanding of skin physiology and pathology, as well as optimising diagnostic and therapeutic approaches, as shown in Figure 2-12 [21].

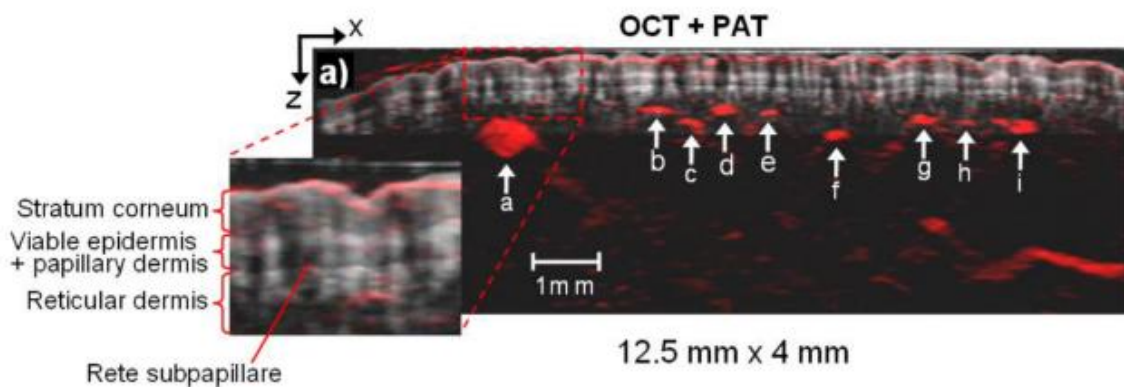


*Figure 2-12 - An example of skin thickness found through experimental OCT imaging, showing the epidermis layers and the viable dermis, by Zhang et al. [157]. PAT (Photoacoustic tomography) combines laser-induced ultrasound with OCT to show oxygen saturation or tissue vascularity.*

### **2.4.2 Optical strain imaging**

Video strain gauge (VSG) is an optical technique used to measure surface displacements and strains. The specimen is recorded under loading with one or two high-resolution cameras, and the features are tracked and analysed in a post processing software. VSG often relies on naturally occurring features rather than an added speckle pattern and utilises a high contrast between the specimen and the background, such as using a black dot on a white background. This method provides direct point-wise measurements but often has limited spatial coverage.

Digital Image Correlation (DIC) is a more advanced non-contact optical technique for quantifying full-field surface displacements and strains. A high-contrast speckle pattern is applied to the specimen, creating unique identifiable regions. Two or more cameras positioned at different angles allows for 3D data collection [Figure 2-13]. During mechanical loading, a series of images are captured, and specialised software compares the initial (reference) image to deformed images. By dividing the surface into smaller regions (subsets) and tracking their movement, the software calculates displacements and strain across the entire surface. Unlike VSG, which relies on point-wise measurements, DIC offers a comprehensive analysis of surface deformation across larger areas, providing a broad understanding of material behaviour [158]. This set up allows for a higher spatial resolution and analysis of more complex deformations compared to VSG [159].

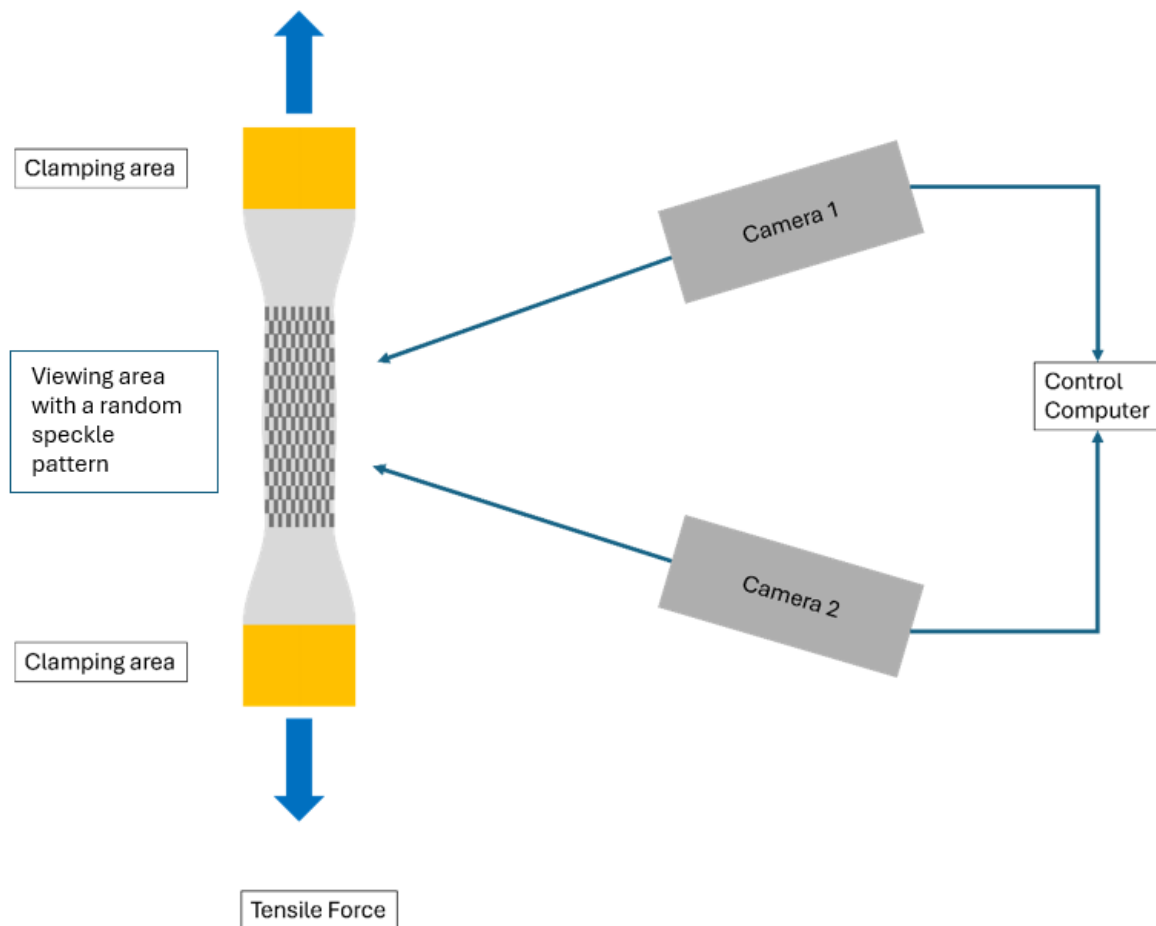


Figure 2-13 – A schematic of the DIC set up for a tension test, showing the speckle pattern area required with a 3D set up using two cameras connected to the control computer

Unlike OCT, which provides depth-resolved imaging of tissue microstructure, DIC focuses on surface deformation analysis. OCT is more suitable for imaging internal tissue layers with high resolution, while DIC excels in quantifying surface strain and displacement [160].

DIC offers several advantages, including high Spatial Resolution. It provides high-resolution displacement and strain measurements across the entire field of view, allowing for detailed analysis of material behaviour and allows for real time monitoring dynamic analysis of mechanical behaviour under varying loading conditions [158]. Additionally, it is a non-invasive imaging technique and does not require physical contact with the specimen, minimising the risk of altering its mechanical properties [159].

## Literature Review

However, there are some major limitations that can affect the use of DIC. For example, DIC requires adequate surface preparation, including speckle pattern application, to ensure accurate tracking of surface features. It also relies on optical access to the specimen surface, limiting its applicability in opaque or inaccessible environments [159]. The processing and analysing of DIC data can be computationally intensive, requiring specialised software and expertise [158]. Additionally, DIC measurements may be affected by changes in lighting conditions, surface reflections, and environmental factors, requiring careful experimental setup and calibration [159].

Despite the limitations of this imaging technique there have been many successful studies focusing on the mechanical properties of biological tissues and the advancement of MN design. There have also been many examples of the integration of DIC and FEA. For example, Evans [107] integrates the use of DIC and computation approaches focusing on the implications of wrinkles. Further studies by Smith et al. [161] focused on the importance of DIC in accurately evaluating scar tissue formation and biomechanics.

The reviews by Palanca et al. [162] and Wang et al. [160] provide overviews of in vivo characterisation of skin mechanical properties using digital image correlation (DIC) and finite element modelling. They show that DIC is capable of capturing strain distributions, but its resolution and accuracy depend on the material properties and experimental set up. The review by Palanca was limited to an overview of biomedical hard and soft tissue, meaning issues such as tearing or needle penetration of skin were not a focus. Oldfield [163] conducted a study focusing on highly resolved strain imaging during needle insertion, using Digital Image Correlation (DIC) techniques. While this allowed for some insights into the mechanical behaviour of tissues during needle penetration, it provided limited information on tissue deformation and strain localisation around the needle. It also highlighted the challenges in capturing real-time behaviour during insertion using surface strains. Although these studies suggest DIC can offer useful insights into strain measurements, the method's ability to fully resolve complex behaviours, such as volumetric measurements during dynamic needle penetration, is still developing.

### **2.4.3 Computed Tomography**

Computed tomography (CT) is a medical imaging technique that has been used within hospitals since the first CT scan on a human in 1971 in London [164]. Medically it is used to view chosen body parts, while in research, it has been applied not only to biological tissues but also on natural materials such as rocks [165], [166] and synthetic materials like carbon fibre [167], [168].

CT imaging operates on the same principles as simple X-ray machines. An X-ray source, connected to an X-ray tube, disperses X-rays across a chosen material. The energy from X-rays is absorbed at different rates by the sample, determined by the density of the sample structure (also known as absorption). For simplicity, denser materials appear lighter (whiter) on the scan. Air, for example, is usually black as the least dense material. A detector on the opposite side of the source picks up the X-rays [Figure 2-14].

The difference between CT and ordinary X-rays is that the CT source and detector rotates around the sample (or the sample rotates) and collect a series of radiographs. These radiographs can then be reconstructed into 3D volume data and further analysed using techniques such as DVC [169].

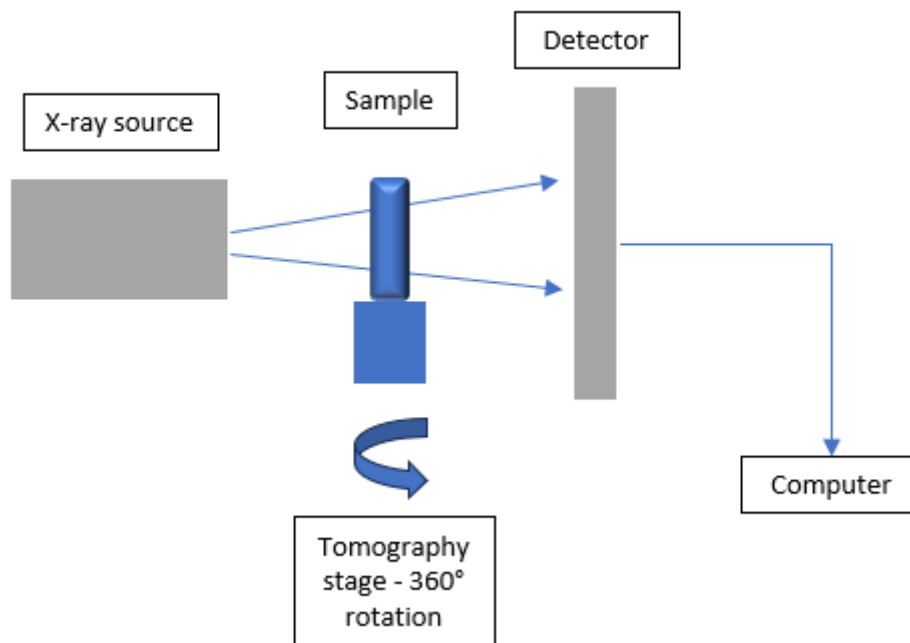


*Figure 2-14 – A schematic of a CT set up, showing the X-ray source directed at the sample which is connected to a rotating tomography stage. The X-ray photons are then detected, with the computer used to reconstruct the projections.*

Micro-computed tomography ( $\mu$ -CT) applies the same principles as CT but on a much smaller scale. This allows to see greater detail in smaller sample sizes. Micro-CT systems can achieve a resolution of a few micrometers or even sub-micrometer levels, enabling detailed visualisation of the internal structure of small samples. Typical dimensions of samples analysed with Micro-CT range from a few millimeters to several centimetres, making it an invaluable tool for high-resolution imaging in fields such as material science and biology, including biological tissues, that are not possible with standard CT.

There are few studies published that involve  $\mu$ -CT and skin due to the limitations previously mentioned, such as high levels of radiation associated with in vivo samples, and the poroelastic nature of skin and dehydration with ex vivo samples. However, it has been used by Urao et al. to assess the vascular structure of mice during wound healing [170]. Post processing was used to evaluate contrast agents, tissue samples, and scanning parameters, enabling 3D reconstructions of the vascular structure.

## Literature Review

Another study by Walton et al. investigated the contrast agents required to visualise the detailed layered structure of human skin [171]. They noted that micro and nano CT could visualise structures at a resolution that previous imaging techniques, such as electron microscopy or histology, could not achieve. However, no observations were made regarding the mechanical behaviour of skin during scanning or staining, as this was outside the scope of their study. Additionally, some studies have explored the imaging of post penetration MNs using  $\mu$ -CT. Loisdou et al. primarily evaluated the post penetration depth and provided 3D visualisations of the MNs, but they did not assess the needles' behaviour pre puncture or during insertion [169].

### **2.4.4 Resolution**

The resolution capability varies depending on machine capabilities and the overall scope of the project. For example, medical and industrial scanners resolutions are usually between 5 and 1000  $\mu\text{m}$ . Micro and nano CT resolutions can go to around 0.5  $\mu\text{m}$  with the possibility of even smaller resolutions [172]. The focal spot size is important, and decreasing the size of the voxels can improve the overall resolution but only to the point where it matches the focal spot size. The voxels can go smaller than that, but it will not improve the resolution.

Binning [173] is a technique whereby adjacent signals (voxels) are combined to produce a larger voxel and the average value is used. This is used to reduce the overall noise and can be applied directly to the detector or during post image processing. However, binning can reduce spatial resolution so the importance of noise to resolution is a significant consideration.

#### 2.4.4.1 Reconstruction

Projections are defined as what is viewed on the detector after the X-rays are transmitted through the object. Projections are used in reconstructions, where the absorption coefficient distribution is back calculated. This can be achieved in various ways including:

- Algebraic reconstruction
- Iterative reconstruction

## Literature Review

- Filtered back projection
- Convolution back projection
- Deep learning reconstruction

Filtered back projection is one of the most common reconstruction methods. This is where forward projections (or radon transformations) are observed, and the absorption coefficient distribution is calculated by back projecting the observed  $p(t,0)$ . This also removes any false absorption data by introducing negative absorptions to provide a uniform absorption spectrum and therefore blur corrections. The accuracy and refinement of the object is improved by increasing the number of projections, as seen in Figure 2-15.

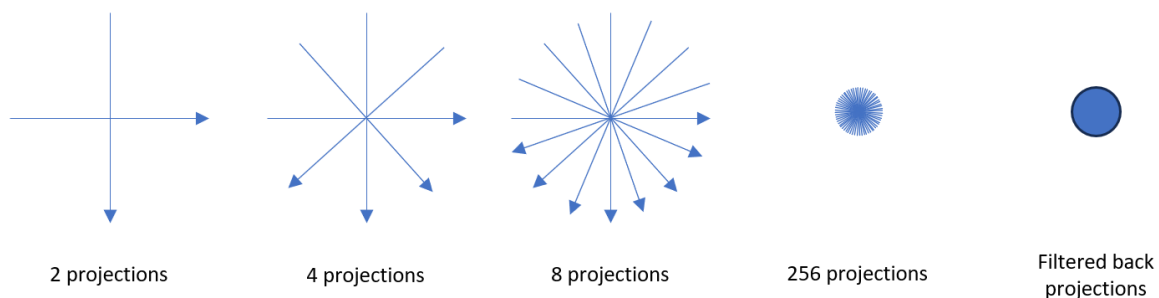


*Figure 2-15 – An example of the number of projections that could be taken of a sample. This shows that increasing the number of projections, for example from 2 to 8 or to 256, increases the accuracy of the filtered back projection reconstruction.*

Equation 21 describes the recommended number of projections

$$N = FoV/Voxel\ size \quad 21$$

The number of angular movements are decided by the number of projections. Typically for cone beam geometries angles between 0-360 are used and 0-180 for parallel beam geometries. The angular movements are used in the forward projections, or radon transformations, to convert the  $(x,y)$  coordinates into  $p(t,0)$  transformations.

### 2.4.4.2 Basic rules and limitations

There are some quite basic rules of CT operation that can reduce problems with reconstruction. The required outcome will determine how these rules are followed and the trade-off that may occur [173]:

1. The object, or at least the focus, must be always in view to get a full and satisfactory model.
2. There must be full penetration through the object at every angular movement. If the transmissions fall below 10% there is not an adequate signal to noise ratio for reconstruction.
3. The number of angles is dependent on the width of the detector.
4. The reconstructed volume size is determined by the width of the detector and how many pixels will 'fill' this width. Most commonly the width of the pixels used is 1.5 times the pixel width of the detector. With machine capabilities nowadays, this is commonly around 3000 pixels.

There are some general limitations that need to be considered when choosing CT as an imaging method. It is a static imaging process; this means that large sample movements can present artifacts. Artifact errors appear on the reconstructed volume, where the voxel is under or overestimated in the results. Artifacts can be related to the source or detector and presented in many ways, such as streaks or bands. Another artifact, more commonly known as noise, is frequently the cause of reduced quality images and is linked to the X-ray tube and resolution used. These errors can be reduced, usually by applying filtering or smoothing to ultimately improve the projections and image processing. Another limitation is the large amount of data storage required. For high spatial resolutions, many slices are required which can also translate to numerous motion steps. Each slice can hold a large amount of data, with one full motion step (one full scan) having the potential to be from 5 to 50GB. This relates back to artifacts, with the greater amount of motion steps requiring more sample relaxation. This can increase the overall scan time from minutes to hours.

The initial objective is paramount in choosing what machine is most appropriate. The voltage and current of the X-ray tubes provide the focus point size, the maximum and minimum resolutions and influence image quality. Image quality is also affected by

factors such as sample quality, exposure time, the detector system and the applied reconstruction algorithm.

## **2.5 Digital Volume Correlation (DVC)**

DVC is a three-dimensional extension of DIC, where DIC tracks surface displacements, DVC operates in 3D by analysing volumetric images. It is a non-destructive method of tracking displacements and strains between a three-dimensional reference scan and subsequent deformed three-dimensional scans. This technique compares voxels, or a set of voxels, from a reference image and tracks the change in displacement of those voxels to the next image (else known as the moving image).

Similarly, to the speckle pattern crucial to DIC, fiducial markers are essential within the substrate to enable tracking of the voxels and are required to be random in size, contrast, distribution, and geometrical shape. Biological soft tissues have a low X-ray absorption, therefore multiple contrast studies have been conducted to investigate suitable contrast agents. Mineralised materials, such as bone and cartilage, have a higher absorption so therefore do not present the same problem.

There are many advantages of DVC, in comparison to strain gauges and DIC. This technique can export full 3D strain maps for comparison to FEA simulation models whereas the pre stated techniques can only export one dimensional measurement. They are more likely to be used on large scale composites and for traditional tension, compression, and buckling experiments. DVC can also use a wide range of scans from the popularly used computed tomography scans to  $\mu$ -CT scans, medical MRI scans and OCT scans.

Limitations of DVC are linked to the procurement of the reference scans. Spatial resolution, field of view, overall displacement as well as environmental factors, scan time and data storage can all effect the scan efficiency. For example, it is recommended for certain software that the overall displacement for DVC (the number of pixels displacement out of the total image size) is not over 5%. Going over this recommendation could render the scans unusable due to large deformations where fiducial marker tracking is not possible.

### **2.5.1 DVC method**

DVC methods can be categorised into Local and Global approaches. Local methods focus on small sub-volumes within the specimen, providing high-resolution displacement measurements, while Global methods analyse the entire volume, offering broader insights into material behaviour [158].

Global DVC methods analyse the entire volume of the specimen, providing a holistic view of deformation behaviour. These methods compute displacement and strain fields across the entire field of view without focusing on specific sub-regions. Global DVC is often employed when studying macroscopic deformations or when high-level trends across the specimen are of interest. Advantages include comprehensive understanding of specimen deformation behaviour by analysing the entire volume, however this can be computationally intensive for large datasets leading to increased processing times. In addition, global methods tend to be easier to implement as they don't have sub region selection. However, they can lack the spatial resolution needed to capture localised deformation on smaller scales within the specimens [174], [175].

Local DVC methods focus on analysing small sub-regions or volumes within the specimen. These methods offer higher spatial resolution and enable the investigation of localised deformation phenomena such as cracks, inclusions, or material heterogeneities. Local DVC is particularly useful for studying microscale or mesoscale deformations within the specimen. It can provide high spatial resolution to analyse small-scale deformation and enables the investigation of localised deformation phenomena, such as material defects or heterogeneities. Local DVC methods offer improved sensitivity to small-scale deformations compared to global approaches. However, Local DVC requires careful selection of sub-regions for analysis, which can be subjective and time-consuming. In addition, analysing small sub-regions may limit the overall field of view, potentially missing global deformation trends [176], [177], [178].

### **2.5.2 Image registration**

Image registration is a process of aligning two or more images of the same scene taken at different times, from different viewpoints, or by different sensors. Both DIC and DVC rely on image registration after image requisition to determine displacements and strains by comparing the reference and deformed images. There are two main types of image registration techniques: intensity-based and feature-based.

**Intensity-based** image registration methods rely on comparing pixel intensities between images to find the best transformation parameters that align them. The objective is to minimise the differences in intensity values between corresponding pixels in the images. This approach is particularly effective when the images being registered have similar content but may vary in terms of scale, rotation, or translation.

Intensity-based methods are robust to changes in lighting conditions and minor variations in image content. They are computationally efficient, making them suitable for real-time or near-real-time applications. Intensity-based methods can be applied to a wide range of image types, including medical images, satellite imagery, and microscopy images.

Intensity-based methods may be sensitive to noise in the images, leading to inaccurate registration results. They may struggle with registering images that contain significant local distortions or deformations. [179], [180].

**Feature-based** image registration methods identify distinctive features, such as corners, edges, or key points, in the images and use them for alignment. These features are selected based on their uniqueness and repeatability across different images. The registration process involves matching corresponding features between the images and estimating the transformation parameters based on these matches.

Feature-based methods are robust to changes in image appearance, such as changes in lighting, contrast, or scale. They enable accurate localisation of corresponding points in the images, even in the presence of noise or occlusions. Feature-based methods can handle complex transformations, including non-linear deformations, by selecting appropriate feature descriptors and matching algorithms.

Feature extraction and matching can be computationally expensive, especially for large images or datasets. The performance of feature-based methods depends heavily on the selection of suitable features and matching criteria, which may require domain-specific knowledge [182], [183].

### **2.5.3 Software**

**DaVis:** DaVis is a software package developed for performing Digital Volume Correlation analysis. It provides tools for image preprocessing, correlation analysis, and visualisation of displacement and strain fields. DaVis is widely used in the field of mechanics and materials science for studying deformation behaviour [158].

**Elastix:** Elastix is an open-source software toolbox for intensity-based medical image registration. It offers a variety of registration algorithms and optimisation strategies, making it suitable for a wide range of registration tasks in medical imaging [183].

**Deep Learning:** Deep learning methods, particularly Convolutional Neural Networks (CNNs), have shown promise in image registration tasks. These methods learn spatial transformations directly from training data and can handle complex registration problems with large deformations or non-linear transformations [184].

### **2.5.4 Applications of DVC**

Medical studies have included force studies for prosthetics [185] to strain mapping biological tissues such as bone. Fu [186] used both OCT and DVC to explore the characterisation of elastic stiffness using three-dimensional full-field deformation focusing on the technique's capabilities for strain mapping. Similarly, Bay [187] and Dall'Ara [188] both investigated the use of DVC to create three dimensional strain maps. Bay discussed the principles as well as highlighting the potential of DVC as a powerful tool for non-invasive, high-resolution characterisation of mechanical behaviour and deformation in three dimensions. Dall'Ara specifically investigated the compromise between spatial resolution and accuracy of strain measurement for bone tissue using a 3D zero-strain study. This study explored the challenges and limitations associated with achieving high spatial resolution while maintaining accuracy in strain

## Literature Review

measurements, particularly focusing on bone tissue mechanics. The study provides valuable insights into the trade-offs involved in selecting appropriate imaging and measurement techniques for studying bone biomechanics and highlights the importance of considering these factors in experimental design and data interpretation. Furthermore, Roberts [189] utilised DVC for characterising bone mechanics, highlighting the methodologies, challenges, and advancements in the field. The review synthesizes findings from various research efforts to illustrate the capabilities and limitations of DVC in bone biomechanics research and its potential for advancing our understanding of bone structure-function relationships. Christen [190] then focused on deformable image registration (DIR) and three-dimensional (3D) strain mapping techniques for the quantitative assessment of cortical bone microdamage. This allowed a comprehensive understanding of bone remodelling, fracture mechanics, and clinical assessment of bone health.

Many applications of DVC have focused on bone assessment and other engineering structures, with human skin being scanned and visually checked but have not yet been assessed using methods such as DVC.

## 2.6 Finite element modelling of needle insertion

This section will explore the various approaches to finite element modelling of needle insertion, discussing the software tools, material models, and computational methods in literature. In the context of transdermal drug delivery, FEM is particularly valuable for predicting MN performance, optimising needle design, and improving the understanding of mechanics involved in skin puncture.

### 2.6.1 Software

To add even further to the complexity of skin modelling there are many softwares available that vary in features and capabilities. Among the plethora of software options available, three prominent options stand out: Abaqus, MATLAB and FEBio.

**Abaqus:** developed by SIMULIA, a subsidiary of Dassault Systèmes, is renowned for its powerful finite element analysis capabilities. It has a rich feature set, encompassing

advanced material models, contact mechanics, and Multiphysics simulations making it a preferred choice for simulating complex mechanical phenomena [191].

**MATLAB:** developed by MathWorks, is a high-level programming language and computing environment. Its extensive library of mathematical functions, and seamless integration with other tools and technologies make it an indispensable asset for prototyping, algorithm development, and data analysis tasks in biomechanics research. MATLAB's versatility extends beyond simulation, encompassing data visualisation, machine learning, and image processing capabilities, thereby offering a holistic solution for researchers with diverse computational requirements [192].

**FEBio:** an open-source finite element analysis software developed by the Musculoskeletal Research Laboratories at the University of Utah, offers a competitive alternative. Its focus on accuracy, efficiency, and user accessibility has gained widespread praise from the biomechanic community. FEBio's robust solver algorithms, coupled with its user-friendly interface and extensive documentation as well as integration with other software, make it an attractive option for researchers seeking a balance between computational rigor and ease of use [193].

The choice of software for skin modelling is often dictated by the specific requirements and objectives of the research project. Factors such as the complexity of the model, the computational resources available, and the expertise of the research team play pivotal roles in determining the most suitable platform. Additionally, considerations such as licensing costs, support services, and the availability of community-driven resources may influence the decision-making process.

### **2.6.2 Assumptions**

The skin is complex to model due to its heterogeneous, anisotropic, and multilayered structure, as well as its nonlinear and viscoelastic behaviour. Each layer of skin, from the stratum corneum to the dermis and hypodermis, has distinct mechanical properties and functional roles, making accurate modelling challenging. Additionally, skin's response to loading is highly dependent on factors such as hydration, temperature, and fibre orientation, which further complicate numerical representation.

## Literature Review

To address these challenges FEMs are often simplified at the expense of the model's accuracy to reduce computational complexity. Some common assumptions in skin FEMs include:

- Single layer representation: simplified structure by modelling just one skin layer, most commonly the epidermis
- Uniform mechanical properties: Assuming the entire epidermis has uniform mechanical properties, often the same properties as the stratum corneum
- Neglecting the hypodermis: some models assume the effect of the hypodermis is negligible
- Simplified material behaviour: Modelling one behaviour, for example isotropy or linear elasticity, despite its inherently complex and anisotropic nature
- Constitutive model simplifications: multiple material constitutive models are used to describe skin's mechanical behaviour, each with their own simplifications

Some studies have highlighted the importance of using a non-linear material model, varying from hyperelastic to viscoplastic. Whilst Neo-Hookean models are still popular, the move to more complex models such as Mooney-Rivlin or Ogden models has increased in recent years.

Several studies have identified these assumptions and their impact on skin modelling and subsequent effect on MN modelling. One key problem is the omission of distinct mechanical properties of individual skin layers. Groves et al. emphasised the importance of considering the distinct mechanical properties of each skin layer and inclusion of the hypodermis to avoid common oversimplifications of assuming uniform properties across the layers [23]. Their findings suggest that these oversights could lead to inaccuracies in modelling overall skin behaviour, such as predictions of MN performance, particularly penetration depth and force-displacement responses. However, these conclusions are based on limited in vivo experiments focused on indentation results, which may not fully represent MN interactions. Leveque investigated how the influence of the stratum corneum affects the mechanics of the skin as a whole, using a non-linear elastic model for all three layers [194]. However, while this approach enhances the realism and aligns with experimental observations of the stratum corneum's stiffness, the assumption of uniform non-linear elasticity

## Literature Review

across all layers introduces inaccuracies. It also neglects the anisotropic and viscoelastic effects of the deeper skin layers, which are crucial for a more comprehensive model.

Moronkeji [65] and Oldfield [163] also looked at the performance and modelling of MNs with the addition of subcutaneous tissue (hypodermis). Their work highlights the importance of considering the hypodermis to better replicate real-world applications as it significantly influences MN penetration depth and resistance. While Moronkeji demonstrated that including the hypodermis improved model accuracy in predicting penetration force, the study assumed simplified mechanical properties for the hypodermis, potentially overlooking its variability in thickness and composition across anatomical locations. Oldfield similarly stressed the necessity of including the subcutaneous layer, but relied heavily on numerical simulations without sufficient sensitivity analysis to determine how changes in hypodermis properties might alter results.

Other studies have looked at modelling the behaviour of individual skin layers. For example, Sasaski modelled skin as an anisotropic, hyperelastic material to reflect its direction dependence, investigating how using an anisotropic model compared to isotropic models [195]. However, by focusing on the dermis layer, and excluding other skin layers, the model's conclusions are limited to scenarios where dermal anisotropy dominates, which could overlook critical interactions between layers during needle insertion. Khatyr conducted a similar study using a viscoelastic material model that brought attention to time-dependent behaviour in skin mechanics [196]. This insight is particularly relevant for applications involving sustained loading. However, like Sasaski, Khatyr's model neglected multi-layer interactions and anisotropy. As a result, while their conclusions about viscoelasticity are valid, they lack generality for scenarios requiring comprehensive understanding of layered behaviour.

Flynn et al. examined the anisotropic response of fibrous tissues using a Neo-Hookean model, offering a simplified framework for capturing directional dependence in soft tissue mechanics [197]. While the study provided some insights into the role of anisotropy in tissue response, the Neo-Hookean model itself is highly simplified, particularly when representing fibrous tissues like skin that exhibit nonlinear behaviour

influenced by collagen alignment. Furthermore, Flynn's work lacked experimental validation with human skin, limiting confidence in the model's predictive capabilities under varying loading conditions for specific MN applications. Further examination of collagen was done by Pond by using a nonlinear hyperelastic model for skin, with variations within the model for the collagen fibres [198]. This approach represents an advancement in capturing biomechanical behaviour of skin more accurately. However, while the model was more realistic, its primary focus was the dermis and collagen fibres, neglecting interactions with other layers like the epidermis and hypodermis, which also play critical roles in the overall mechanics of skin.

Other studies have also investigated numerical methods considering variations due to age, gender, skin type, and anatomical site, providing insights into the relationship between mechanical properties and the wrinkling of skin [197], [199], [200]. This could provide critical context for interpreting MN performance; however, the limited sample sizes and potential biases challenge the generalisation of these insights in modelling for broader populations.

Studies have also investigated the differences in numerical algorithms and modelling approaches providing insights into the capabilities, computational efficiency and ease of use [201]. Coinciding with computational needs, material models often involve simplifications. Kim et al. compared different material models for Chloroprene rubber and highlighted the importance of selecting appropriate material models to avoid inaccurate assumptions [202]. While their work on chloroprene rubber offers transferable insights, direct applicability to skin, with its anisotropic and layered structure, is debatable. This highlights a broader issue that many material models used for skin are adapted from other materials without sufficient validation, and the reliability of these adaptations when applied to complex biological tissues.

### **2.6.3 Modelling needle insertion**

Modelling needle insertion is a complex issue that has been researched at various stages of the MN insertion process. Yadav's article reviews trends and progress in mathematical modelling, simulation, and optimisation of MNs for transdermal drug delivery. Key points include advancements in mathematical models for predicting MN

## Literature Review

behaviour, simulation techniques to optimise needle design and performance, and the evolving landscape of transdermal drug delivery technologies [2].

There are three main MN computational methods that have been published. The first method uses damage mechanism algorithms, such as node separation algorithms. This method uses damage mechanisms on node displacements, allowing the model to simulate needle progression by iteratively separating nodes until the desired insertion depth has been reached. However, this method does not account for actual failure within the elements, meaning it simplifies material behaviour during fracture. These methods often employ parameters like the local effective modulus (LEM) or fracture toughness. The LEM represents a materials stiffness at a localised region under a specific loading condition. It can be experimentally determined by applying a localised linear force-displacement loading, followed by unloading, to quantify the elastic response. While useful for some linear materials, LEM fails to accurately describe the non-linear behaviour of soft tissues like skin. Fracture toughness, on the other hand, is distinct from LEM as it considers the energy required to propagate a crack and crack-tip mechanics that are not addressed by the LEM's stiffness-based framework. Chanthasopeephan et al. proposed a model for surgical training that examines the cutting of soft tissues by a surgical blade, enforcing a 3D, one-layer linear elastic model of the liver [203]. They initially proposed the experiment to outline the parameters required for the LEM and its application within their model. This model was used to look at the varying cutting speeds and angles on the LEM.

The second method is one of the most widely published methods, element deletion. This method emulates the cutting procedure by applying a damage model to the elements within the whole tissue or the cutting zone. The damage model is set up to have a maximum threshold, based on von Mises stress failure, ultimate strength, shear strain threshold etc. The Von Mises stress represents the effective stress at which yielding occurs, and simplifies it into a single scalar value making it computationally efficient and easy to implement. However, as skin and soft tissues are anisotropic, and often fail due to shear or tensile forces, as well as not taking into account the directional dependence, it is not always the best fit for representing skin failure. The ultimate strength is a threshold based on the maximum stress a material can withstand before failure, usually directly tied to experimental measurements. While useful for

## Literature Review

representing failure governed by tensile stresses, it fails to account for other failure modes such as shear stress. The most accurate threshold in relation to MN insertion modelling is the shear strain threshold. This threshold represents failure when the shear strain exceeds a predefined critical value, which can capture behaviour such as sliding or shearing, a common occurrence in skin. It does, however, have limitations, such as requiring specific data which may be challenging to obtain.

In element deletion methods, the needle interacts with the tissue, and once the threshold for that element has been reached, the element is deleted from the model. While in reality, no part of the skin is removed during needle insertion, this method is deemed valid and popular as it commonly uses the threshold values from experiments and can apply a wide range of damage mechanisms based on study requirements. Its popularity is also linked to its ease of implementation and quick generation of results. However, that does not mean the method provides accurate results. This approach underestimates the indentation depth at puncture because it simplifies the tissues response by removing elements once a damage threshold is met, therefore not capturing the gradual deformation of the skin during the initial stages of penetration. Additionally, these models are very dependent on their mesh sizes, with finer meshes giving more accurate results, but still failing to account for the complex behaviour of skin under stress, such as viscoelasticity or anisotropy.

This method has been published mainly simulating 3D models, with a range of studies using one-layer models to three or four layers. Jiang used a bilinear elastoplastic material model to research the insertion of generic medical needles [26]. Flexible neural probes were researched by Singh in a one-layer insertion model, using the Ogden material model, to investigate the optimisation of probe designs [204]. Assaad used the Johnson-cook linear elastic model to investigate how bevel-tipped needles interact with gel, this is illustrated in Figure 2-16 showing the cubic gel sample, the surfaces P1 to P5 and the needle displacement axis [27].

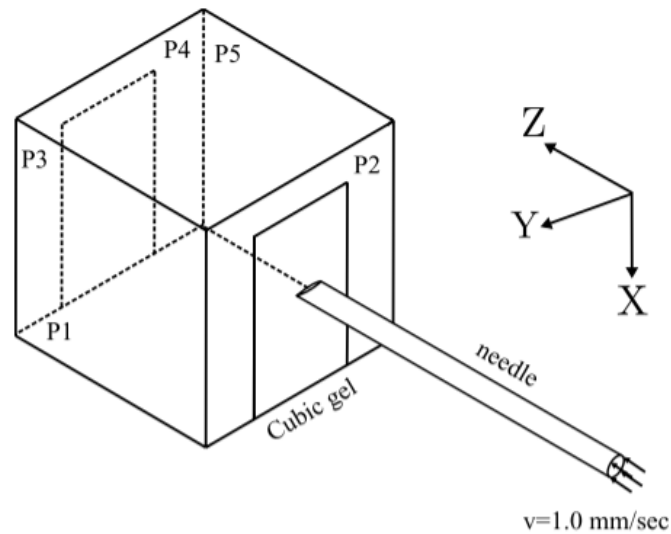


*Figure 2-16 – The sketch taken from Assaad [27] publication using the element deletion method, showing the FEM of needle insertion into a cubic gel sample, with the boundary conditions labelled, and the line of needle insertion denoted by a dotted line.*

More complex models have been investigated by Chen et al. who developed a computational model to analyse MN insertion into four different skin tissue layers using an Ogden material model, as seen in Figure 2-17 with the skin layers coloured [20]. By incorporating tissue biomechanics and MN geometry, the study examines the penetration behaviour and distribution of stresses during the insertion process. Kong studied the insertion of MNs using an elastic and isotropic material model, incorporating three skin layers [28].

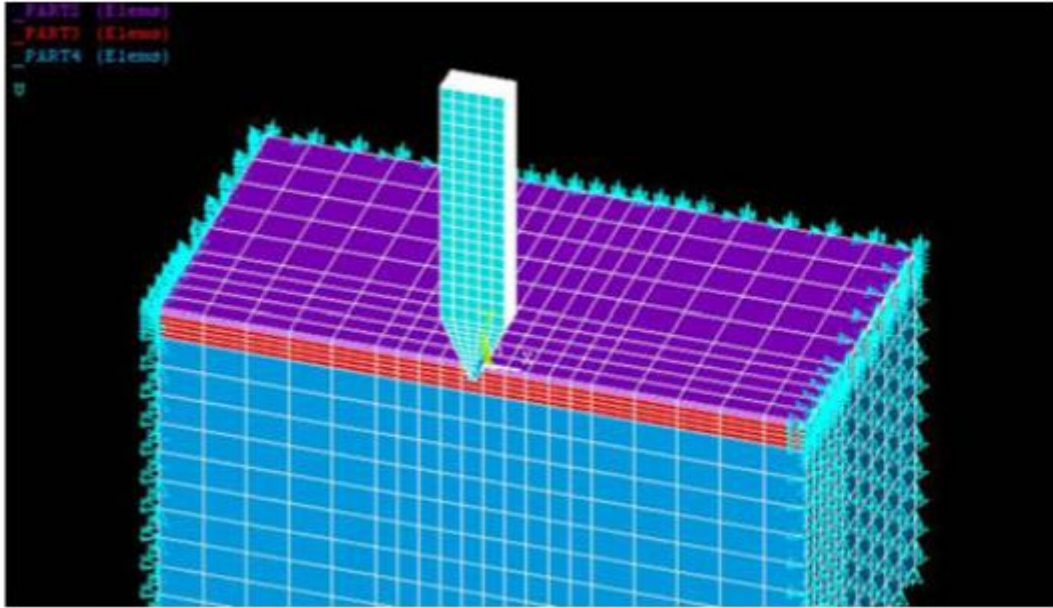


*Figure 2-17 – A sketch taken from the publication of Chen [20], illustrating the multi-layer model investigated using the element deletion method. The boundary conditions are also shown (the tetrahedrons on main geometry).*

More recently a study at the University College Dublin focused on the insertion of MNAs with a model incorporating pretension in a three-layer skin model [19]. The layers used different material models, including Neo-Hookean and Gasser-Ogden-Holzapfel models. The study concluded that modelling a single needle ignores vital boundary conditions that can be mitigated by the addition of an array. However, the element deletion method removed elements entirely in a non-realistic representation of needle penetration, and the initial tension boundary condition had to be reduced because over 10% pre-tension would prematurely delete elements. Results were verified by ex vivo histology of porcine samples, which highlighted limitations due to potential environmental changes in the samples.

The final method that is increasing in popularity is the cohesive zone method. It uses a specific failure mechanism that allows a crack to form during the simulation without removing any material. This damage model uses a traction-separation law (TSL) that relates to the separation of the cohesive surfaces. The most common version is a bilinear TSL, where the cohesive tractions increase linearly with the distance between the cohesive surfaces until the maximum (failure) traction is reached [Figure 2-9]. Once

## Literature Review

this maximum value is hit, the cohesive zone is damaged, and the traction decreases linearly until complete separation of the surfaces. This method simulates material failure at a pre-defined interface, which can be modelled by separating nodes or using special cohesive elements that represent the interface between the two surfaces. This is a similar concept to sticky contact algorithms employed in FEBio. While sticky contacts treat the interface as a frictional contact, where no separation occurs until a threshold is reached, it does not explicitly model the traction-separation relationship. Sticky contact algorithms therefore do not represent the true damage mechanism and progression, whilst cohesive zone models capture the gradual failure and crack propagation.

Oldfield investigated a 2D model using a bilinear TSL, experimentally validated by insertion experiments on a tissue phantom [17]. Three rigid needles were fully inserted into gelatin, with crack width and needle radius measured post insertion. The study identified three main components of the energy required for needle insertion: the strain energy, fracture energy and frictional energy. The study then focused on a finite element model using cohesive elements along the predicted crack path of the needle utilising a defined contact penalty algorithm within Abaqus, the structure used is illustrated in Figure 2-18. Oldfield demonstrated good correlation between experimental and simulated results but noted that calibration of the model was needed to improve the accuracy and simulate the indentation gelatin undergoes prior to needle penetration. At the time of publication, Oldfield acknowledged that the cohesive elements could not prevent penetration. The fundamental issue with this approach is that the sharp needle generates an infinitely high stress concentration if the mesh is sufficiently fine. This means the exact point of penetration is determined by the mesh resolution rather than the materials toughness or resistance to fracture. This method was also used in subsequent publications including studies on rate-dependent models [205].

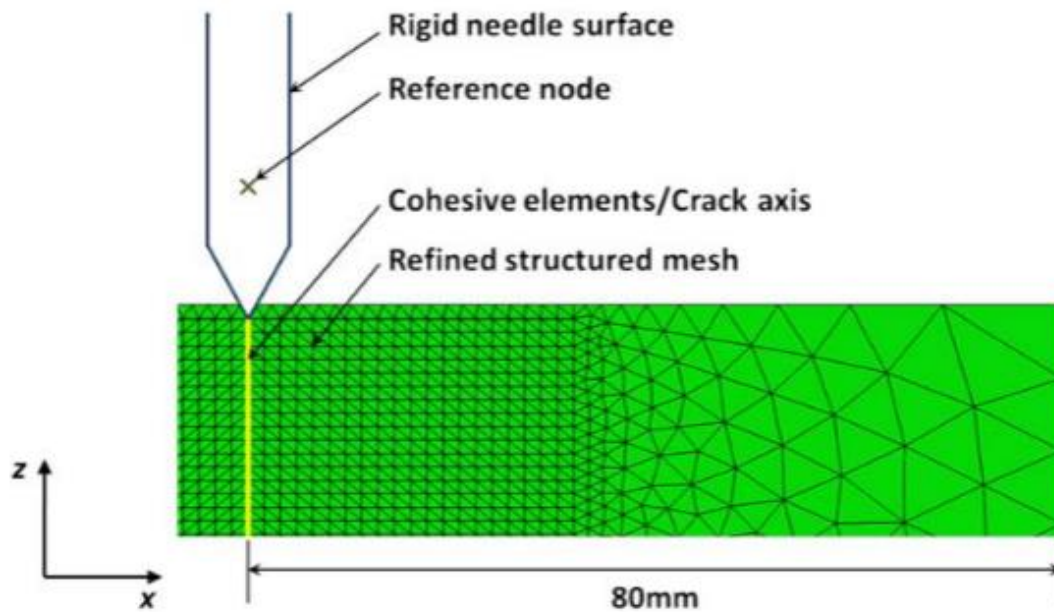


Figure 2-18 – A figure of the FEM created by Oldfield [17], showing the cohesive zone elements along the crack line that illustrates the cohesive zone method developed.

Other studies including Amiri and Mohammadi, have utilised this method. Amiri set up a 3D two-layer Ogden model to investigate the dependency of penetration depth on MN geometry, particularly the MN tip diameter. It was concluded that while the maximum stress decreases as the tip radius increases, the overall force required increases; for example, a radius of 5  $\mu\text{m}$  has a maximum reaction force of 0.06 N, while a 22  $\mu\text{m}$  radius has a force of 1.77 N [29]. Mohammadi initially used this method to analyse needle insertion into human skin, creating a two-dimensional two-layer model with an incompressible, isotropic, first order Ogden material model [Figure 2-19]. The effect of the needle diameter was investigated, supporting Amiri's conclusion that a larger the needle diameter requires greater insertion force [18]. The subsequent study explored other geometrical parameters such as the insertion angle and presented a more thorough energy study [206].

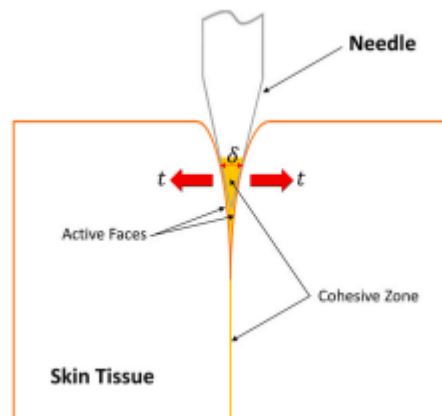


Figure 2-19 – The cohesive zone method utilised by Mohammadi [206], showing the cohesive zone and needle crack area active forces

While the cohesive zone model is more advanced than the element deletion methods, it requires a prediction of the crack line or needle trajectory and remains mesh dependant and challenging to implement in 3D models.

#### 2.6.4 FEA of MNs

Non-invasive methods can be used to look at varying parameters of MNs, without the complex computation of the insertion process. Indentation models are the simplest to create; this is a non-invasive model that focuses on the initial stage of MN insertion, and pre-puncture characteristics such as displacement and strain data up to a pre-determined depth. Groves et al. simulated a 3D, three-layer, quarter skin model employing the Ogden material model for each layer [23]. Mohammadi recently used a one-layer skin model to look at the indentation, then subsequent penetration, of hypodermic needles using the Maxwell material model [18]. The indentation model was predicted using direct experimental data. A more comprehensive overview of needle and skin interaction in the initial indentation stage was completed by Potts et al. in 2023 [9]. Using a three-layer model, and material constants found by Groves et al., the spacing of MNAs, the force acting on the needles and the subsequent skin strain was investigated for three needle geometries.

The other side of non-invasive modelling is pre-puncture models. This type of modelling includes setting out guidelines of where the puncture will be, with no

## Literature Review

damage mechanisms so not actually 'modelling the penetration procedure'. They can be useful when the needle is already in contact with the tissue or embedded within the material, allowing for the analysis of deformation under external load without the need for crack propagation or damage mechanisms. This usually aids in the high computational requirements that non—linear fracture modelling requires. Radhika's study, for instance, employs finite element analysis to assess polymer MNs for transdermal drug delivery using a 3D, one layer model with a linear-elastic material model [24]. The research found that the von Mises stress distribution was key to determining the skin's response and compared these results with experimental force-displacement data of mouse skin penetration. Similarly, Amin et al. investigated needle insertion for insulin therapy using a linear elastic material model, however they used a two-layer skin model [25]. Their study found the differences in skin behaviour when subjected to a needle in a pre-puncture state, focusing on how the needle's characteristics influences stress distribution within the skin layers. By not modelling the puncture directly, these studies were able to focus on needle-tissue interactions and assess the effectiveness of different needle designs, while avoiding the complexities of simulating tissue failure.

Many studies have been created looking at the geometrical effects of MNs on skin penetration. Loizidou's research, for example, evaluated the effects of MN geometry using CT scanning, which allowed for a detailed examination of needle insertion and the resulting tissue deformation. This study aimed to optimise needle design for enhanced drug delivery efficiency by assessing how different needle shapes and sizes influenced penetration depth [169]. Other studies have focused on the efficacy of MN penetration using analytical modelling with subcutaneous tissue representation [65], [67]. These studies emphasised how the mechanical properties of the epidermis and underlying layers influence the penetration force and depth of MNs. Some studies have emphasised the critical failures of skin, such as indentation and penetration points to use as validation tools [66] and interactions between the needles and skin for drug delivery efficiency [29]. These are critical to identify how the skin yields and identifying how penetration occurs under varying conditions.

Moreover, Gittard took a step further and looked at the skin penetration and failure of polymer MNs to analyse how variations in MN geometry – such as needle length,

diameter and tip sharpness - impact penetration depth and structural integrity. This work provided valuable insights into optimising MN design by revealing how changes in needle geometry can affect both the performance of MNs during insertion, and their ability to remain intact through the penetration process [13].

## 2.7 Summary

This chapter has provided a comprehensive overview of the current research trends in transdermal drug delivery, specifically focusing on MNs. It covers the extensive experimental and computational research that has contributed to the design and development of MNs in recent years. Additionally, the challenges that remain in ensuring MNs are clinically safe and effective are highlighted. Key issues have been highlighted, such as the complexities of accurately modelling skin mechanics, the limitations of existing material models, and the need for improved needle-tissue interaction simulations.

The literature review also examines the importance of the mechanical behaviour of skin, including experimental properties, testing methods, layer specific characteristics and constitutive material models. While various constitutive material models have been proposed to represent skin's behaviour, there is still a gap in achieving models that adequately account for skin's anisotropy, viscoelasticity, and non-linear responses during MN insertion. Furthermore, the chapter reviews the challenges in modelling skin tearing and fracture during needle penetration, especially the limitations of current analytical techniques, including tearing, cutting and wounding.

Imaging techniques such as OCT and CT are reviewed, alongside their capabilities for strain measurements such as DIC and DVC, which are relevant to the study of skin deformation and improving the understanding of the mechanical interactions between MNs and skin. The introduction of DVC also outlines the methods, softwares and applications used in this technique. The limitations for these techniques, such as the resolution requirements and experimental setups, are also evaluated in relation to imaging biological tissues.

## Literature Review

Finally, the chapter reviews the finite element modelling of needle insertion, emphasising the difficulties associated with mesh sensitivity, material assumptions, and the need for improved validation methods. While the current FEM approaches provide useful insights into the mechanics of needle insertion, they often oversimplify the complex tissue behaviour, leading to inaccurate predictions of penetration depth and force responses. As computational methods evolve, incorporating more realistic material models and fracture mechanics is critical to advancing the accuracy of MN simulations.

# ***CHAPTER 3***

---

## **DEVELOPMENT OF EXPERIMENTAL METHODS FOR SKIN SUBSTITUTE EVALUATION**

### **3.1 Introduction**

The mechanical behaviour of skin is inherently complex and challenging to characterise experimentally, with various studies offering insights into its non-linear, anisotropic, and inhomogeneous behaviours. Due to the limitations surrounding using in vivo or excised skin, this chapter describes the aims to evaluate the suitability of a skin substitute for subsequent DVC analysis and FEA modelling, detailed within Section 3.4.

The chapter begins by detailing the experimental procedures for using a skin substitute, emphasising the use of  $\mu$ -CT and subsequent DVC techniques, which have not yet been applied, to the authors knowledge, to continuous deformation measurements in skin. It outlines the criteria for selecting the skin substitute material

and describes the testing methods, including compression, insertion, and tear tests. These tests are designed to ensure the chosen skin substitute has material properties comparable to those reported in the literature. The tear tests build upon previous work conducted by third year students at Cardiff University School of Engineering, with these properties incorporated into the FEA models discussed in Chapter 4.

### **3.2 Material criteria**

For this study it was decided to forgo the use of porcine or human skin for numerous reasons. Firstly, the use of skin in experiments requires several ethical considerations. These ethical considerations also determine the laboratories that could be used for experiments. Another consideration when using human or animal skin is the change in mechanical properties for in vivo or ex vivo experiments. Excised skin, which also require ethical approval, could exhibit significant changes in mechanical properties due to dehydration, freezing and thawing and even damage due to the way it was removed. However, a skin substitute needs to replicate key characteristics of real skin to ensure the developed methods in this study can be effectively applied to actual skin. Therefore, material criteria were developed.

#### **1. Appropriate stiffness**

The silicone material should exhibit appropriate stiffness and a high strain to failure capacity, allowing it to endure large deformations without permanent damage. Groves reported a shear modulus of 0.069 MPa for human skin, which provides a useful reference for selecting materials with similar stiffness characteristics [23]. Values can vary due to factors such as anatomical location, age, and testing method, so this figure can be considered a reasonable reference but may be conservative in some contexts.

#### **2. Comparable mechanical behaviour to skin including, Young's modulus, tensile and compressive strength**

The silicone should effectively mimic the behaviour of skin under different loading conditions, making it suitable for use in experimental and computational studies aimed at understanding skin mechanics and facilitating meaningful comparisons. These will

allow for a comprehensive comparison of the materials failure point in relation to human skin. While Young's modulus and shear modulus alone do not fully capture the complex, non-linear mechanical behaviour of skin (shown in Figure 2-6), including these parameters ensures that the silicone's material properties are comparable to those reported in existing publications. Additionally, the stiffness values are useful for examining the material's behaviour under both small and large deformations, providing a broader understanding of how the skin substitute responds across a range of loading conditions. Publications have reported a mix of Young's modulus results from varying in vivo tests, listed in Section 2.2.2. For this study, only the data from forearms will be listed, so the range should be between 0.007 – 0.01 MPa. The stiffness should also be within a range of 24 N/m to 64 N/m.

Gallagher [207] collated a review of the dynamic testing published, listing three tests on human skin, seven tests on porcine and rat skin, and a comparison to their own results. The tensile strength for their dynamic test on ex vivo back skin is between 17.9 – 36.5 MPa.

Shergold investigated a one parameter Ogden material model, noting  $\mu$  as 0.11 MPa for human hands and  $\alpha$  at 9, however the two silicones they investigated experimentally had  $\mu$  of 2.7 and 0.4 MPa and  $\alpha$  as 2.5 and 3.0. Therefore, the parameters should be between 0.1 and 2.5 MPa for  $\mu$  and 2.5 and 9 for  $\alpha$  [148], [149].

### 3. Compatibility with experimental methods

The material should be compatible with various experimental methods used in skin biomechanics research allowing for seamless integration into existing protocol and enabling accurate comparisons with human and porcine skin. It will need to have a high contrast between fiducial markers and the sample to allow for DVC tracking. It should also be easily manufactured into different sample sizes required for different tests, for example dog bone samples for tensile tests, square blocks for compression tests.

4. The inclusion of fiducial markers does not impact the criteria outlined in points 1 –4.

## Development of Experimental Methods for Skin Substitute Evaluation

The fiducial marker size required is dependent on the  $\mu$ -CT parameters, for example a larger field of view would require larger fiducial markers within the sample material. If the FoV is set to 2 mm or 2000 pixels, the markers should be approximately 10 to 20 microns, but with enough size distribution to still count as random distribution. For DVC, both the spatial resolution of the fiducial markers and the expected displacement between time steps must be considered. A general guideline is that displacement between frames should not exceed 5% of the field of view, in pixels. To ensure accurate correlation, fiducial markers should span approximately 3–5 pixels in diameter. For a voxel size of 1  $\mu\text{m}$  and a field of view of 2000 pixels, this corresponds to marker sizes of around 10–20  $\mu\text{m}$ . This ensures that the markers are large enough to be resolved while maintaining a random and distributed pattern suitable for DVC tracking. This is further explained in Section 5.2.1.

Silicone, or silicone rubber, is a family of elastomer which experiences high elasticity under large strains. Silicone is a relatively inexpensive and readily available material, with some silicones exhibiting material properties that are similar in behaviour to skin. The choice of silicone will be dependent on the application, for example if it is required to represent the skin layers individually, or as a whole. The application can also make an impact on the choice, for example if the surface or volume deformation is being tracked the sample colour may be important, but for a simple tear test this is insignificant. The aim of using a skin substitute is to investigate which experimental methods and modelling techniques could be interchangeable when used with human skin. Criteria four is tailored to the silicone experiments as fiducial markers cannot be embedded into skin. This limitation underscores the importance of selecting materials that enable accurate measurement techniques, which could eventually be adapted for use with skin. Some publications have previously cited the use of stains as a viable alternative for marking skin, though their impact on skin properties have been reported in prior studies [19], [22], [205].

### 3.3 Methods

Within this section the different methods used to extract material parameters from three different silicones for testing against the material criteria outlined are described. This includes the investigation into how these parameters change with the manufacturing process and how the silicones may differ when adding particles that are required for further data processing for DVC.

#### 3.3.1 *Silicone production*

Three silicones have been used within this study, Technovent Tek-sil 25 [208], Ecoflex-30 [209] and Ecoflex Gel [210]. Technovent Tek-sil 25 was readily available within the University to initially outline method protocols, with the two Ecoflex silicones identified by the School of Pharmacy as potentially good property match to skin.

**Tek-sil 25** The silicone initially used within this study was Technovent Tek-sil 25 [208]. Digital scales (Kern EMS, Max 3000g, d=0.01g) were used to weigh each ingredient. As specified by the manufacturer's instructions, a 9:1 ratio of resin to hardener was used. For this study 50 g was used, 45 g resin to 5 g hardener. This would allow for a sufficient depth (over 10 mm so as to mitigate external conditions affecting the mechanical properties) in the plastic mould; the mould's width was approximately 25 mm, and shown in Figure 3-1. The two ingredients were weighed and then mixed by hand initially for 30 seconds. Afterwards, to ensure a thorough mix of both components, a Speed Mixer (Hauschild DAC800.1 FVZ) was used for 2 minutes at 1200 rpm. Once the liquid silicone was removed from the Speed Mixer, it was placed inside a vacuum chamber. The vacuum chamber was degassed -1 bar to remove air pockets (bubbles) within the liquid and visually inspected after 10 minutes to determine when all air pockets were removed, and the process could finish. Air pockets encased in hardened silicone would cause discrepancies in experimental results, and the specimen would be classed as flawed, increasing product wastage.

The moulds were placed in a room temperature environment, away from direct sunlight, and allowed to cure for 24 hours. Once the allotted time had passed, the silicone was removed from its mould and visually checked for flaws. The samples were

then stored in individual, airtight, plastic bags. This minimises the risk of further contamination, physical damage, and changes in the material properties over time.

**Ecoflex-30 and Ecoflex Gel** The same method as above was used, the two parts were weighed on a digital scale and then hand mixed. This silicone was mixed with a ratio 1:1 Part A (25 g) to Part B (25 g). the same timings for both the speed mixer and vacuum chamber were used.

**Ecoflex-30 with titanium dioxide** Titanium dioxide ( $\text{TiO}_2$ ) particles (Sigma Aldrich Titanium (IV) oxide anatase powder, -325 mesh [211]) were added to the Ecoflex silicones. The  $\text{TiO}_2$  has an average particle size of 10 microns and agglomerate size up to 300 microns and was sieved through a 250-micron sieve to reduce the number of agglomerates present. A 4:1 silicone (50 g) to  $\text{TiO}_2$  particle (10 g) mix was made. Further discussion on the addition of the  $\text{TiO}_2$  is in Section 3.3.2.

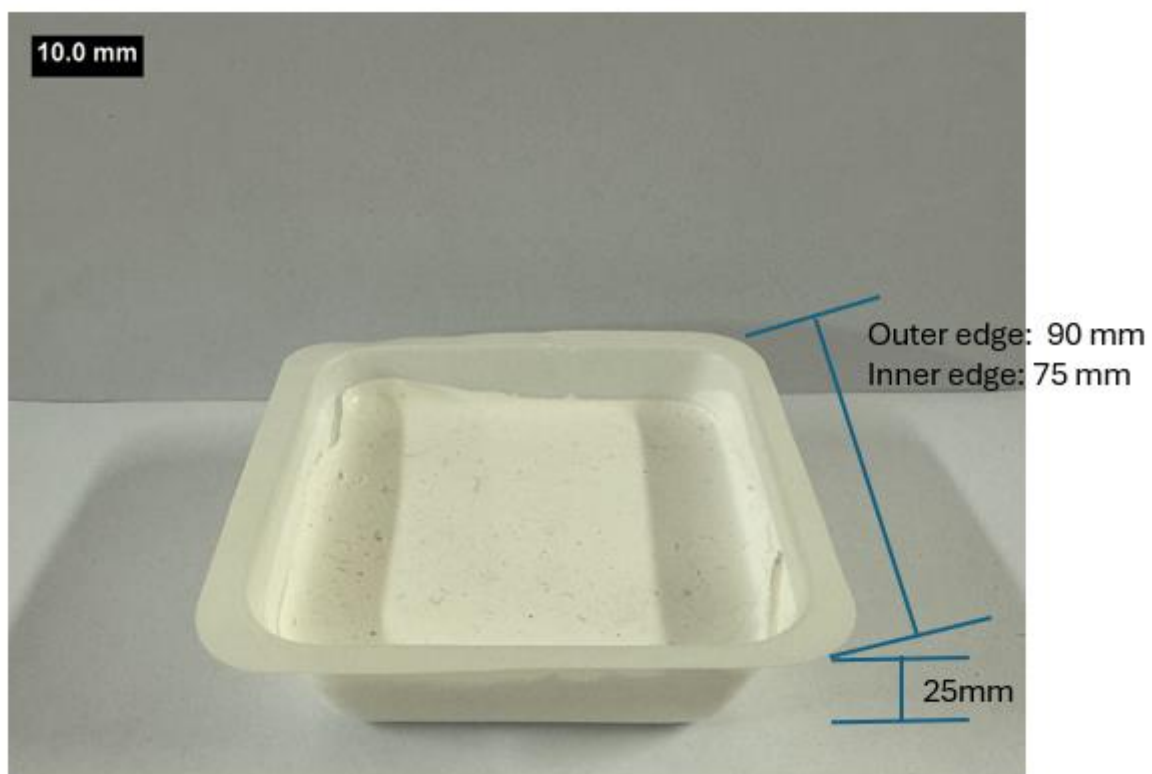


*Figure 3-1 - Silicone mould used for the creation of the silicone samples for the compression and puncture tests*

For comparison, Ecoflex-30 and Ecoflex gel samples were made in the School of Pharmacy with the same ratio mix, but only mixed by hand (no vacuum chamber or

speed mixer used). This approach allows for a comparison of how the mechanical properties were influenced by the silicone production method, as hand mixing may introduce microbubbles that affect the material's consistency. Table 3-1 details the names the silicone will be referred to from here on.

*Table 3-1 - Material naming for all silicones used in this study, detailing which include the TiO<sub>2</sub> particles and the silicones tested by the School of Pharmacy for comparison*

<b>Original Material</b>	<b>Material name</b>
<b>Technovent Tek-sil 25</b>	Material A
<b>Ecoflex-30</b>	Material B
<b>Ecoflex-30 with TiO<sub>2</sub></b>	Material C
<b>Ecoflex Gel with TiO<sub>2</sub></b>	Material D
<b>Ecoflex-30 (School of Pharmacy)</b>	Material E
<b>Ecoflex Gel (School of Pharmacy)</b>	Material F

### **3.3.2 Particle size and distribution**

TiO<sub>2</sub> was chosen as it would fit into the criterion outlined in Section 3.2 with the manufacturing guide specifying the average particle size of 10 microns. Whilst the original particles are a size deemed appropriate for the field of view and resolution desired, the particles also naturally form agglomerates. These agglomerates, ranging to the maximum size of 316 microns, allows for the range of size and shape also required.

The average size of the particles was also checked at the School of Pharmacy using a Malvern Mastersizer 2000. This machine is a laser diffraction particle sizer that can give highly accurate wet and dry particle dispersions of particles from 0.02 to 2000 microns. 100 g of un-sieved TiO<sub>2</sub> was placed into the Mastersizer 2000 and run through the diffraction lasers 3 times. Next, 100 g TiO<sub>2</sub> was sieved through a 250-micron sieve. These sieved particles were passed through a Mastersizer 2000 three times.

### 3.3.3 Compression test

All six material samples were tested using a servohydraulic testing machine (Zwick, Zwick Testing Machines) with a 10 N load cell (Interface) was used. Two indenters were chosen to test, a flat indenter and a conical indenter. The flat indenter has a radius of 7 mm and the conical indenter had a tip radius of 0.5 mm. These indenters and loading conditions were chosen to ensure consistency with previous studies, particularly the work by Groves et al, and ongoing testing within the School of Pharmacy. Using the same experimental configuration allowed for direct comparison of results without the need to replicate their original experiments. A point close to the centre of the silicone was chosen and the indenter was displaced 5 times in the same spot at a constant speed of 1.67 mm/s (100 mm/min). The silicone was resting on the machine bed, with no attachments to reduce the chances of pre-stress across the silicone [Figure 3-2]. Two different loads were used for the different indenters, 8 N for the flat indenter and 2 N for the conical indenter. The same loads were initially used by the School of Pharmacy for other testing; using the same method allowed these results to be directly compared without repeating their original tests. This also allowed for the investigation of the addition of the vacuum chamber and speed mixer in the mixing process to be evaluated.

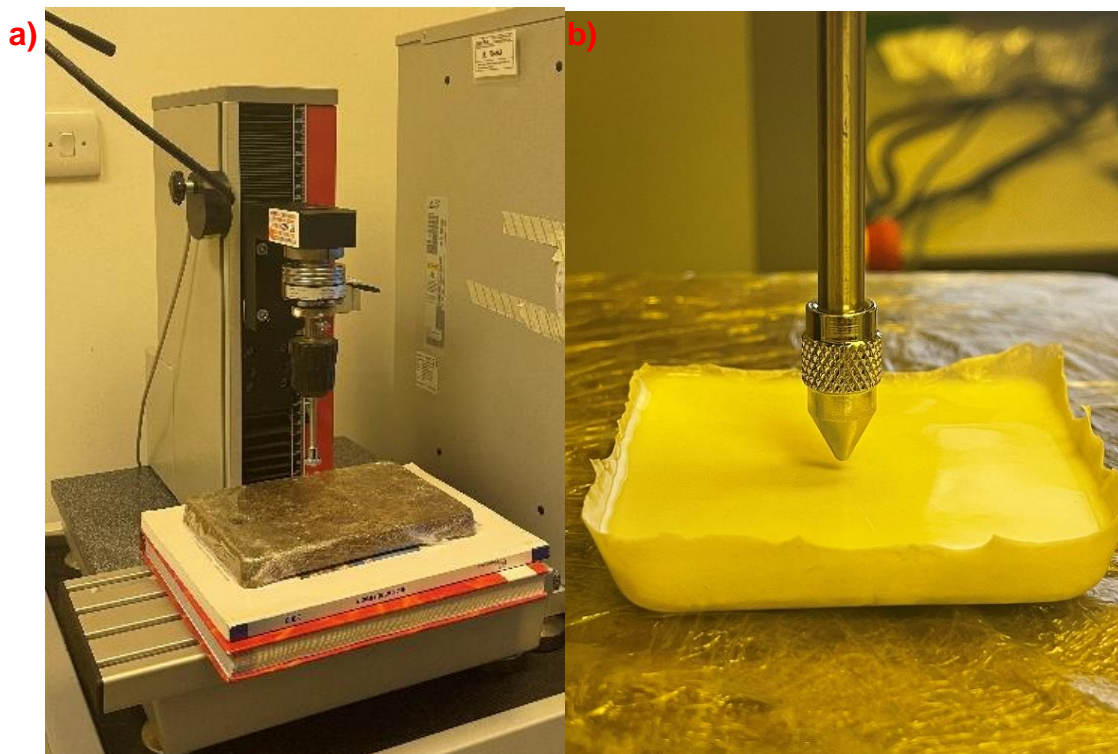


*Figure 3-2 - Universal test machine used a) and the silicone and conical indenter b)*

For the flat indenter indentation results, the main values that are being examined within this section are the compressive stiffness, which provides a measure of resistance to compressive deformation under indentation. This can be influenced by the shear modulus and the Young's modulus. The Shear modulus,  $G_s$ , is calculated by Equation 22 [212]

$$G_s = \frac{K(1 - \nu)}{4r\kappa} \quad 22$$

Where  $K$  is the stiffness of the material, this can be found from the gradient of the force-displacement graphs,  $\nu$  is the Poisson's ratio of the material,  $r$  is the radius of the indenter used and  $\kappa$  is a mathematical parameter.  $\kappa$  is taken from Hayes publication on indentation tests where the values for a range of  $a/h$  and  $\nu$  values, where  $a/h$  is the ratio between the contact radius and the thickness of the silicone [212]. For this study  $\kappa$  was valued at 2.533 and  $\nu$  was assumed to be 0.5 as it represents an ideal incompressible material for calculation simplification. This is then used to calculate the Young's modulus in Equation 23

$$E = 2G_s(1 + \nu) \quad 23$$

Assuming a Poisson's ratio of 0.5 simplifies calculations by treating the material as incompressible, which is reasonable for soft tissues like silicone or skin, but may slightly overestimate stiffness since real tissues are not perfectly incompressible.

### 3.3.3.1 Puncture test

A single needle was manufactured from stainless steel using wire EDM (electrical discharge machining) for a pharmaceutical project [Figure 3-3]. This needle had

## Development of Experimental Methods for Skin Substitute Evaluation

dimensions of 1.1 mm length and a 0.3 mm x 0.5 mm square base, it was attached to a larger base that allows an attachment to standard tensile test machine. A scaled single needle was also fabricated from stainless steel using a CNC milling machine, that was 10x bigger than the original MN. Identical copies of this single needle were also fabricated from Perspex for use in  $\mu$ -CT imaging using the same manufacturing process.

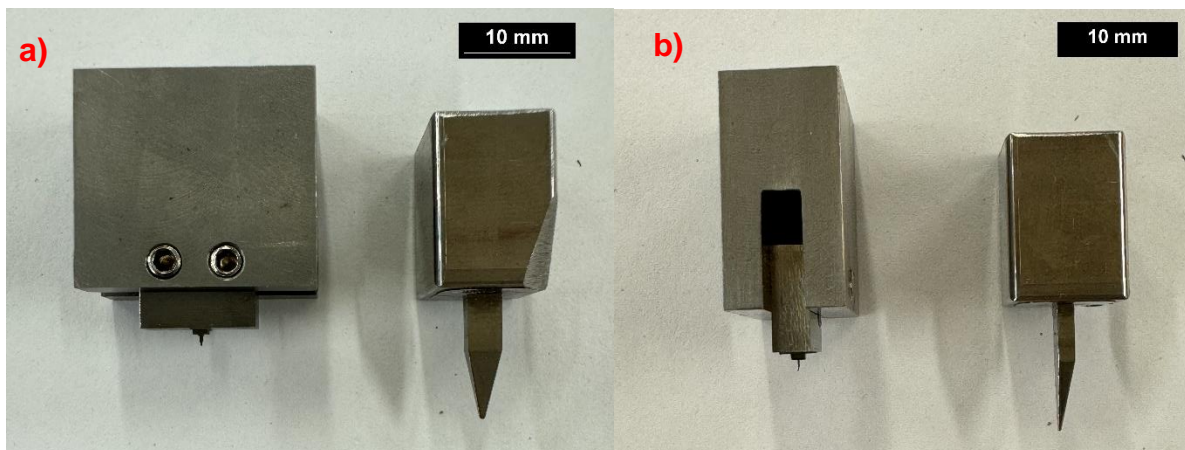


*Figure 3-3 – MN and scaled needle used in this study, front view a) and side view b)*

To assess the puncture point of this needle, an insertion test was performed with the Ecoflex-30 TiO<sub>2</sub> silicone. The needle penetration point was then measured at speeds of 0.1 mm/s, 0.3 mm/s and 0.5 mm/s. This was completed using a servohydraulic testing machine (Losenhausen, with an MTS FlexTest GT controller) with a 10 N load cell (Interface). These speeds were selected to represent a range of quasi-static insertion rates used in previous microneedle studies, ensuring sufficient contrast in force response while remaining within the limits of typical experimental setups. The puncture was tested on three different areas of the silicone, once in the centre and two randomly placed closer to the edge of the sample [Figure 3-4].

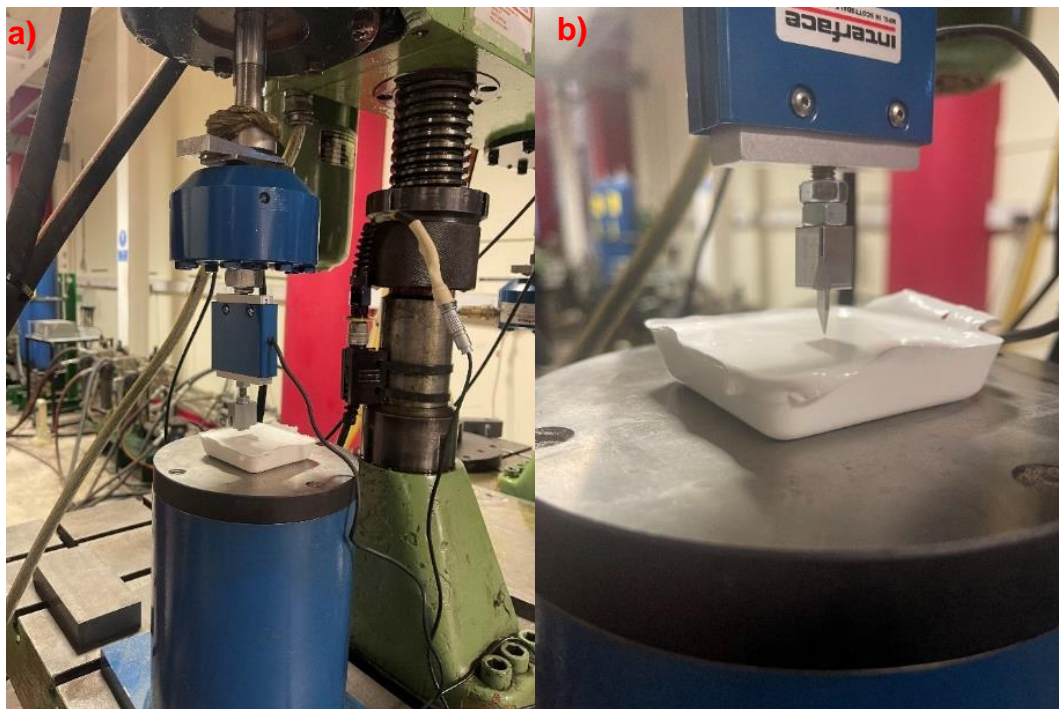


Figure 3-4 - Tensile test machine set up for puncture tests a) and needle and silicone b)

It has been previously published that the puncture point into skin is identified on the force-displacement curve by a significant reduction in force [10]. In addition, choosing three different speeds to investigate allowed for an evaluation of speed dependence of needle puncturing.

### 3.3.4 Tensile test

A mould for tensile test dog bone specimens was created and 3D printed using a PLA filament and standard machine settings [Figure 3-5]. Six samples were made using Material B and a further six samples of Material C as other materials were ruled out in the compression test. The same procedure previously stated was followed, by pouring into the dog bone moulds and leaving to cure for 24 hours. The thicknesses of the samples are given in Table 3-2.

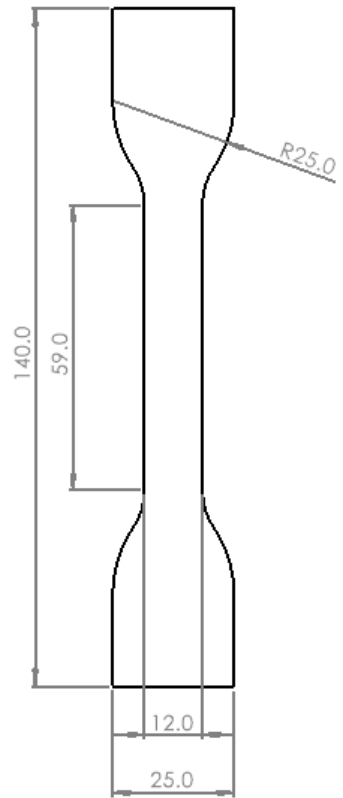


Figure 3-5 - Dogbone for tensile tests, with measurements in mm

Table 3-2 - Sample number for the two materials tested (material B and material C), and the corresponding sample thickness in mm

Material	Sample Number	Thickness average (mm)
<b>Material B</b>	1	1.79
	2	1.70
	3	1.48
	4	2.37
	5	2.23
	6	2.16
<b>Material C</b>	1	3.00
	2	2.91
	3	3.14
	4	1.88
	5	1.60
	6	1.47

## Development of Experimental Methods for Skin Substitute Evaluation

Whilst a tensile test is considered relatively simple to carry out and further calculate material properties, the highly elastic properties of soft materials allow for large deformations and strains that can make traditional testing difficult. To combat these limitations, direct strain measurement on the specimen is essential, and is typically done using an extensometer. In this study a video strain gauge (VSG) was chosen to allow for uniaxial maximum principal strains or localised strains across a chosen grid to be viewed and facilitate further calculations, such as the use within the Ogden material model or tensile strength, to be made. However, virtual strain gauges do have some limitations, including sensitivity to environmental vibrations and lighting conditions and they can be sensitive when measuring large deformations. For this experiment a Zwick/Roell Z050 machine with a 1 kN load cell was used, all tests were completed with a constant speed of 3 mm/s. The larger load cell was used in anticipation of higher strain loads.

The sample had two dots marked on the top of the sample in black Sandtex Exterior paint, and two marked on the bottom approximately 60 mm (the top and bottom dots) and 20 mm (the centre dots) distance apart. These were used by the VSG to track the deformation of the sample by tracking the distance the dots displaced. The four dots were used to measure the strain across two areas, however the outer dots were used for further data analysis as they covered the largest surface area.

To measure the strain during testing, an IMT-CAM028 camera [GigE PoE 15fps 2452 x 2056 with a IMT-LENS-GP002 General purpose lens with 8 mm focal length] was set up 920 mm distance from the sample, chosen due to the focal range of the cameras used. A white board was placed on the opposite side of the machine to minimise background disturbances, and an additional light was placed behind the camera to illuminate the sample. The camera was connected to the computer which allowed the force, displacement and strain data to be recorded within the video strain gauge software [Imetrum Video Gauge version 5.3.5.4951] [Figure 3-6, Figure 3-7]. The force and displacement data was also directly exported from the tensile test machine for comparison or VSG anomaly removal. After the first test it was found that the VSG set up could not be used through to material failure as the system crashed, it was theorised that as the equipment is outdated and with such large deformation occurring the dots also stretched, causing the system to lose track. A newer version of this

## Development of Experimental Methods for Skin Substitute Evaluation

software could potentially improve the tracking capabilities, but is uncertain it would fully resolve the issue of dot stretching which fundamentally affects tracking reliability. Once the strain reached 400% the VSG software was paused, and then material was taken to failure to allow image analysis of material tearing only.

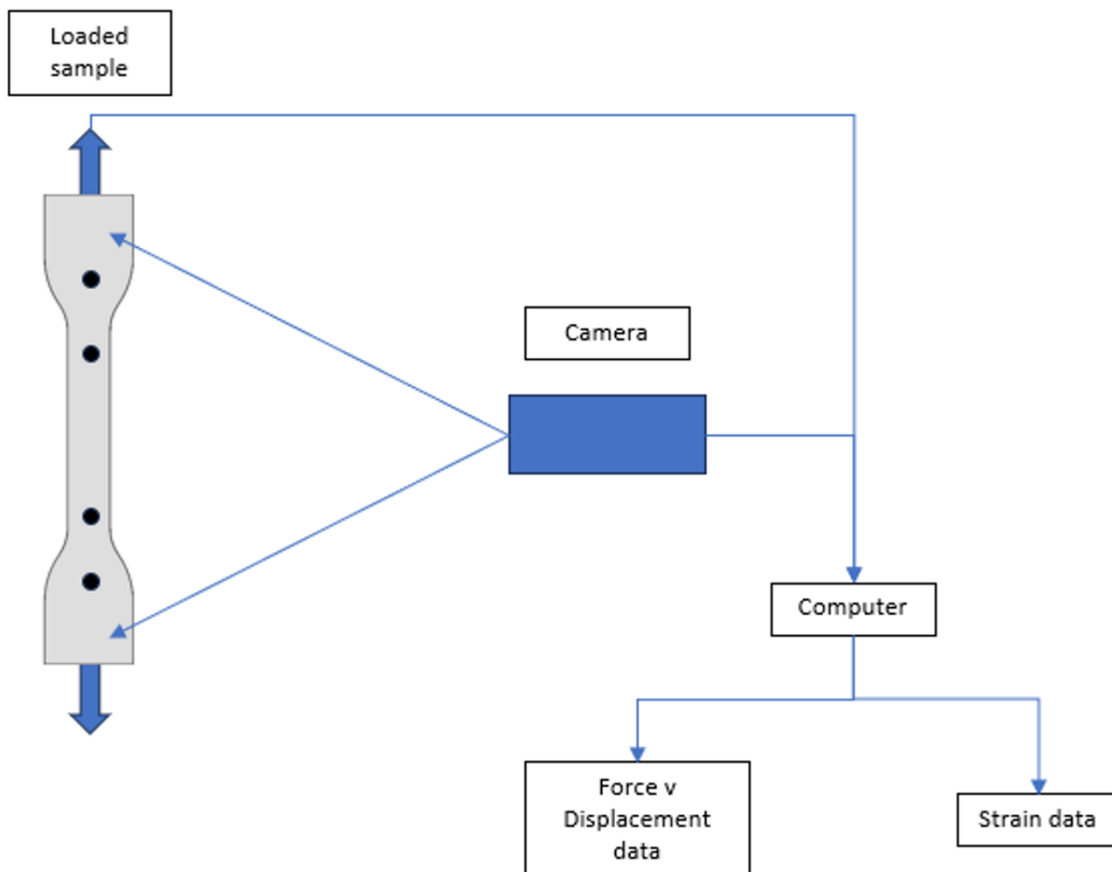


*Figure 3-6 – Schematic of the VSG set up used for the tensile test, showing the four dot set up, the area the camera covered, and the connection to the computer.*

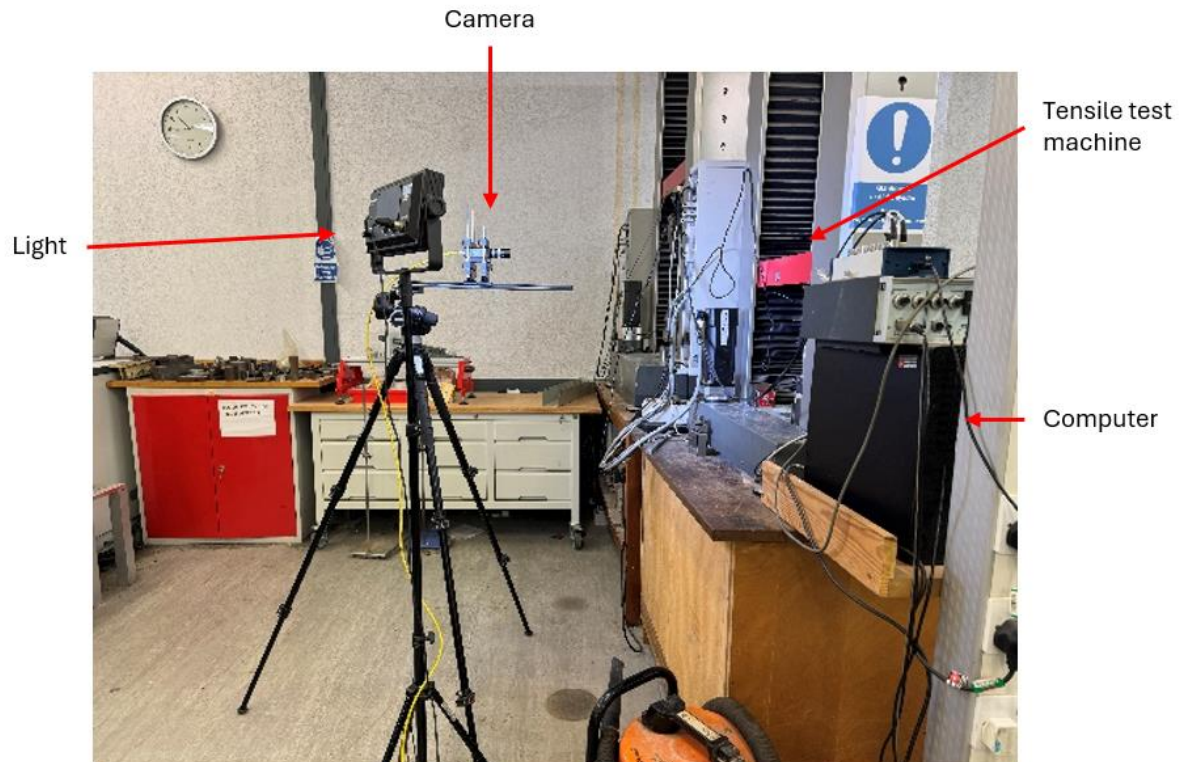


*Figure 3-7 – Physical VSG set up used, showing the camera set up next to the tensile test machine*

The force displacement data was then processed in Matlab to enable a fit to the Ogden material model explained in Section 2.2.3. This processed the engineering strain to principal stretch,  $\lambda$ , and the data fit allowed for the extraction of material properties  $\mu$  and  $\alpha$  in Equation 24

$$\lambda = \left( \frac{\varepsilon}{100} \right) + 1 \quad 24$$

Where  $\varepsilon$  is the engineering strain. The optimisation is performed by iteratively choosing the input  $\mu$  and  $\alpha$  and the sum of squares is used to determine the final iterative. This iteration process was completed in MATLAB using an Ogden Material

model code. The total sum of squares, Equation 25 and the residual sum of squares is used, shown in Equation 26

$$SS_{tot} = \sum_{i=1}^n (y_i - y_m)^2 \quad 25$$

Where  $y_i$  is the observed value and  $y_m$  is the mean of the observed values.

$$SS_{res} = \sum_{i=1}^n (y_i - \hat{y}_i)^2 \quad 26$$

Where  $\hat{y}_i$  is the fitted value from the model. These are then used to determine  $R^2$  by Equation 27

$$R^2 = 1 - \frac{SS_{res}}{SS_{tot}} \quad 27$$

### 3.3.5 *Work of Fracture*

For this experiment, A Losenhausen servohydraulic testing machine equipped with an MTS FlexTest GT controller was used. This machine offered the capability to measure both loading and unloading, crucial for fracture mechanics analysis. The silicone materials under examination were Material B and Material C. These selections allowed the fracture behaviour of the material with and without TiO<sub>2</sub> to be explored.

The initial crack of approximately 10 mm was created using a scalpel, ensuring a consistent starting point for each test. This crack length was chosen so that a minimum

## Development of Experimental Methods for Skin Substitute Evaluation

of four crack increments could be measured across the sample. A traveling microscope was used to accurately track crack propagation, which enabled precise measurements of crack length.

The initial fixture was created and adapted by third year students at Cardiff University School of Engineering [213]. For this study, adaptations were made to the silicone moulding process to allow for fixture functionality and relevance to this study.

Figure 3-8 and Figure 3-9 show the fixture used for this study. It was 3D printed out of six parts, with the three flexible arms laser cut to size. The distances from the silicone clamp to the fixture arm pivot point were decreased from the initial experiments by a third-year student at Cardiff University [214] to decrease the overall force exerted on the sample. This modification was imperative, as the load cell on the testing machine had a maximum capacity of 10 N, which was being approached during crack propagation tests. The last big modification to the fixture was the arm connector between the two fixture halves. This was redesigned to be thinner at the centre, enhancing flexibility and laser cut to size. This adjustment facilitated smoother movement during testing, reducing the risk of unintended stress concentrations and potential structural failures.

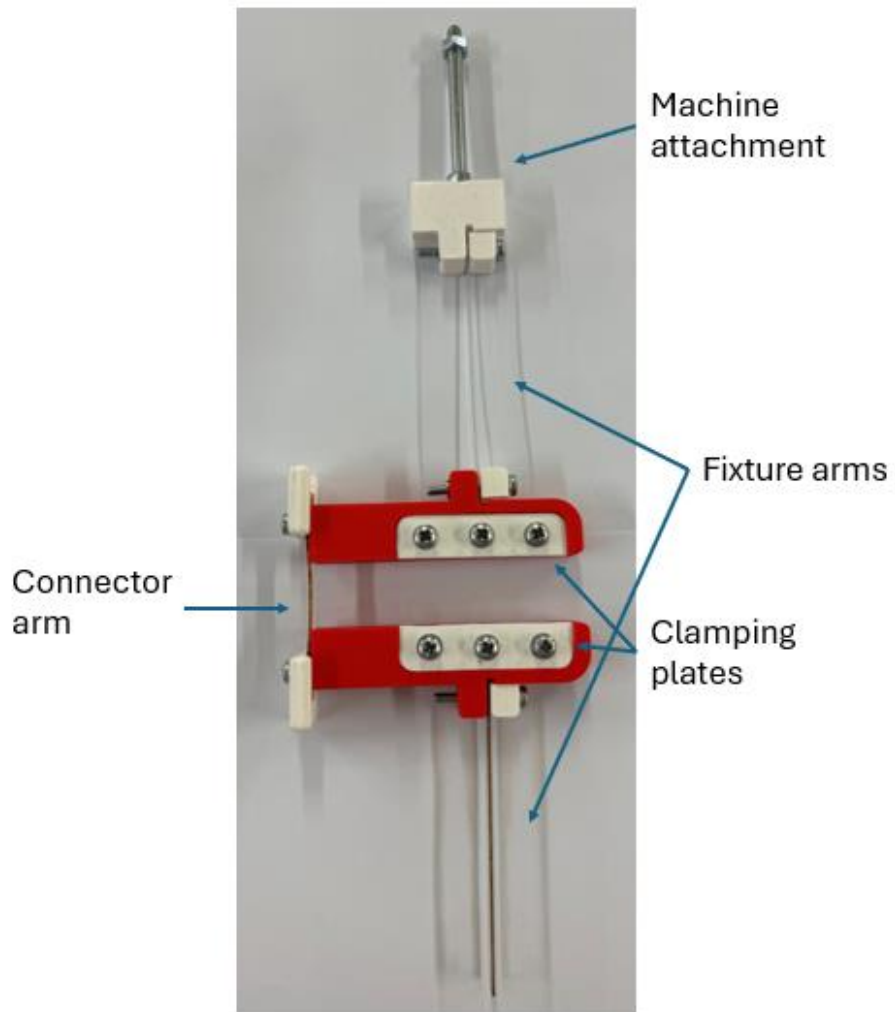


*Figure 3-8 – Top view of the fixture used for the WoF experiment, identifying the key components such as the fixture arms, clamping plates for the silicone and machine connector*

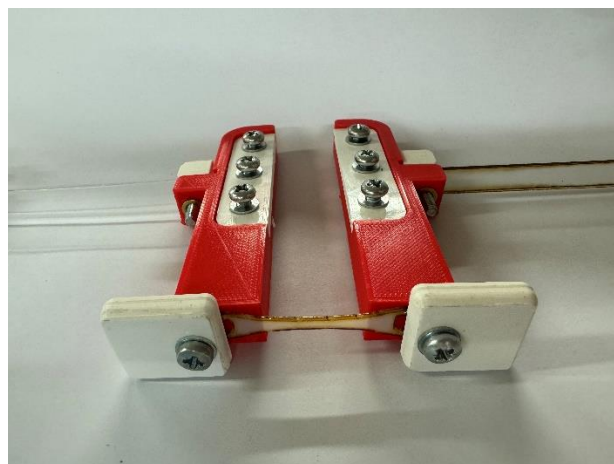


*Figure 3-9 – The side view of the WoF experimental fixture*

## Development of Experimental Methods for Skin Substitute Evaluation

The Ecoflex-30 samples were made with the original sample mould, however some issues arose when using this mould for the Ecoflex-30 with TiO<sub>2</sub> samples. The tensile test machine has a 10 N load cell connected, and when using this with these samples it reached the maximum load without initiating a tear. This resulted in a curve on the sample [Figure 3-10 a)]. To reduce the load required to tear the sample and get the sample tearing in the correct direction three new moulds were created:

1. Thinner sample mould
2. Thinner sample mould with reduced sample width
3. Same as 2, but with a groove to guide the crack

Mould 1 was 3D printed and had the same shape as the original but was thinner (2.5 mm to 1.5 mm) to try and reduce the overall thickness of the sample. This resulted in a reduced load, but the crack continued to curve upwards as it initiated a tear [Figure 3-10 b)]. The next step taken was to create mould 2, where the reduced thickness was kept but then the width of the sample was also reduced. This again kept the reduced load seen for mould 1 but the tear was still moving up the sample instead of across [Figure 3-10 c)]. Therefore, the final try was to create the third mould but with a groove across the sample to try and force the crack to follow a given path across the sample instead of deviating upwards [Figure 3-10 d)].

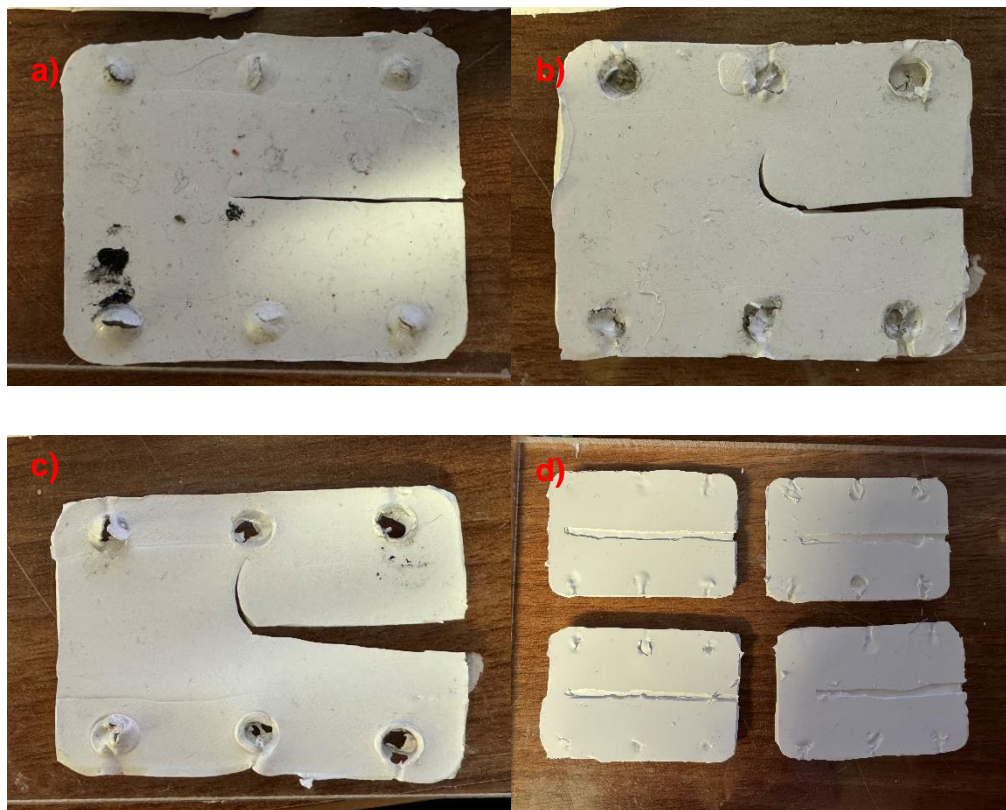


*Figure 3-10 – The silicone sample produced using the initial mould a) the second sample using the thinner mould b) the third sample created using a mould with the width reduced c) the final samples created using the third mould with added groove (pre crack) d)*

### 3.3.5.1 Experimental Procedure

With the optimised fixture in place, the experimental procedure followed a systematic approach. Each of the silicone samples were carefully prepared and mounted onto the testing fixture, ensuring proper alignment and clamping. It was found that the best procedure was to fix the middle screw first to ensure the silicone was evenly clamped and spread out through the fixture. Uneven clamping could result in uneven crack propagation due to the change in material thickness. Using a scalpel, an initial crack, of approximately 10 mm, was cut at the predetermined location on the silicone sample. This was then more accurately measured on the travelling microscope.

The testing machine was programmed to apply controlled loading and unloading cycles to the silicone sample, allowing us to observe crack propagation behaviour, at a constant speed of 0.1 mm/s. This was done by eye, once tearing was observed, the

machine was stopped, and an unloading cycle could begin until 0 N force was reached. The sample was then removed from the machine and the whole crack length measured. These steps were repeated until at least four cycles were completed, without causing a complete tearing of the material. The force-displacement data for each cycle was then exported, these data along with the crack length were used to calculate the Work of Fracture (WoF). The work done and WoF calculations are detailed in Section 2.3.1.5.

### **3.3.6 Particle dispersion**

Whilst the particle size was separately tested, the distribution and particle size when embedded within the silicone required inspection. As previously stated, the TiO<sub>2</sub> was added to the Ecoflex-30 to provide fiducial markers for DVC. Fiducial markers have certain requirements, for example random size and random distribution. TiO<sub>2</sub>, whilst having a manufacturing particle size of 10 microns, can clump together to cause agglomerates. This can fulfil the random size criterion for fiducial markers but could also cause those markers to be larger than the  $\mu$ -CT resolution requires.

To assess the fiducial markers, two samples were scanned at the University of Southampton n-XCT laboratory [215],[216]. Sample one included TiO<sub>2</sub> that was sieved through a 250 micron sieve prior to mixing into the Ecoflex-30 silicone. Sample two included the particles that were sieved through a 45 micron sieve. A biopsy needle was used to remove a small sample of the silicone and this was placed in the scanner. This sample was scanned at 110 kVp 10W using a 160 kVp Zeiss Xradia Versa 510 (Carl Zeiss GmbH, Germany) at 1  $\mu$ m voxel resolution.

## **3.4 Results**

This section presents the data from all experiments conducted on the selected silicones in accordance with the material criteria detailed in Section 3.2, an overview of the particle size and distribution of the TiO<sub>2</sub> are provided. The silicone compression characteristics are outlined, with comparisons made to published skin data and the exclusion of certain silicones based on this comparison. Subsequently, the load-

displacement curves from tension and tear tests are examined, and further calculations, including Young's modulus and Ogden material model properties, are presented. Finally, the application of the chosen silicones in  $\mu$ -CT tests for visual assessment is shown, along with their use in further data processing as outlined in Chapter 5.

### 3.4.1 Particle size and distribution

The particle size and distribution for both un-sieved and sieved  $\text{TiO}_2$  are presented. The average distributions from the three repeat tests are shown in Figure 3-11.

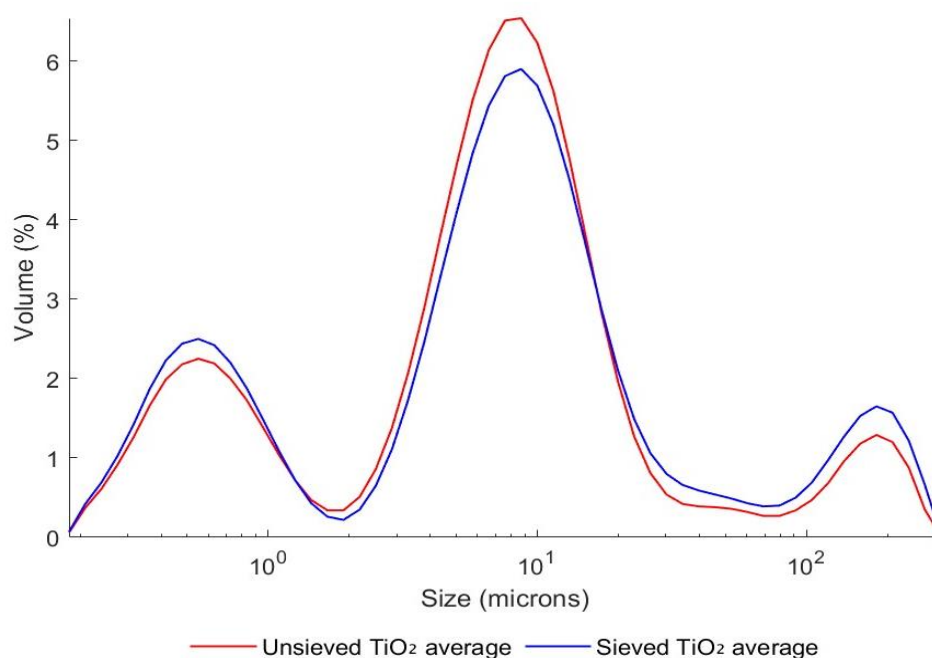


*Figure 3-11 - Particle size distribution of the averaged sieved (blue line) and un-sieved particles (red line) for  $\text{TiO}_2$  showing the three peaks. These peaks show the highest volume distribution.*

The average particle size was found to be 7.586 microns for the un-sieved  $\text{TiO}_2$  and 8.710 microns for the sieved  $\text{TiO}_2$ . However, the size dispersion of the sieved particles was greater than that of the un-sieved particles: the height of the central peak was lower (5.9% vs 7.2%) while the two peaks at the extremes of the distribution were larger. Interestingly, both the sieved and un-sieved particles exhibited a strange distribution of three distinct peaks.

### 3.4.2 Compression test

Measurements of the indenter force to the indenter depth for both the flat and spherical indenter are presented for all six silicones. The average of the five cycles performed on each silicone was taken for the two indenters.

Figure 3-12 shows the variation across Material A, the little variation between the five cycles shows the appropriateness of taking the average of the cycles.

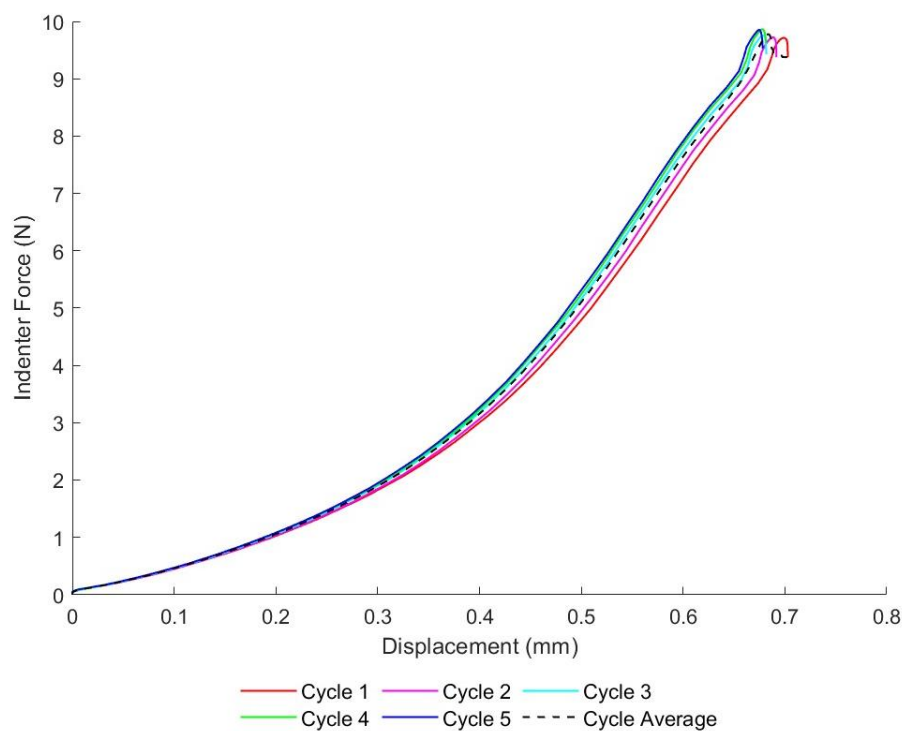


Figure 3-12 – Flat indenter load-displacement graph for Material A showing the five cycles on the same sample and the average (dotted black line)

Figure 3-13 and Figure 3-14 illustrates the load- displacement average for all six silicones for the flat and spherical indenter respectively. These plots show that the stiffest silicone was Material A, as the greatest load was applied with the corresponding lowest indenter depth. In comparison, Materials D and F were the least stiff.

## Development of Experimental Methods for Skin Substitute Evaluation

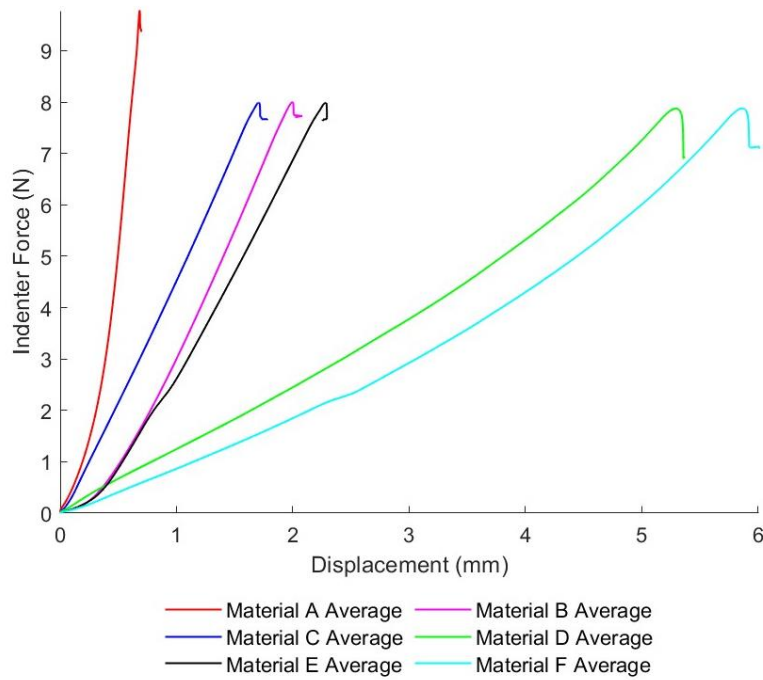


Figure 3-13 – Flat indenter load-displacement data for all material samples tested, showing the average of all 5 cycles. Material A showed the greatest stiffness, with Material C showing the addition of the  $TiO_2$  only had a minor effect on the overall stiffness of the Ecoflex sample. Material D and F (the Ecoflex Gel) was the least stiff of all tested.

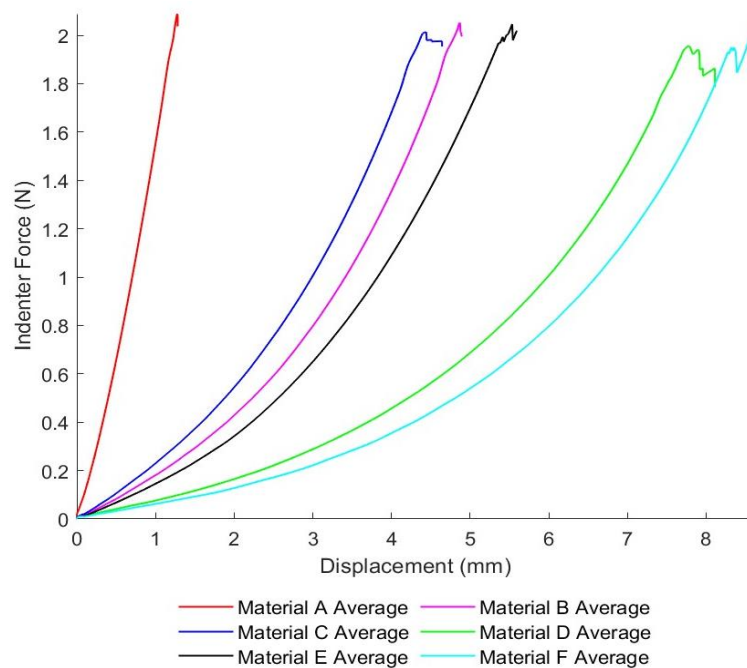


Figure 3-14 - Conical indenter load-displacement graph for all material samples tested, showing the average of all 5 cycles. Material A was again the stiffest material, Material E and F shows the change in the manufacturing procedure, whilst minor, does alter the stiffness of the material.

Silicone, like skin, displays non-linear stress-strain characteristics. In this study, the Young's modulus at small deformations can be compared to other published studies. For these results the initial, linear part of the stress strain curve (between 0.5 and 2 N) was used, with the gradient of the graph between these forces representing the stiffness, K. however, it is important to note that this range exceeds the initial elastic region where Young's modulus is most accurately defined (usually to <0.05 N). As the same indenters were used, the data from Groves is compared in Table 3-3.

*Table 3-3 - Table of the stiffness, shear modulus (G) and Young's modulus (E) for all materials and the comparison to published data by Groves [23]*

<b>Material</b>	<b>Vacuum chamber?</b>	<b>K (N/mm)</b>	<b>G (MPa)</b>	<b>E (MPa)</b>
<b>Skin average (Groves et al.)</b>	N/A	0.04431	0.0396	0.0659
<b>Material A</b>	Yes	7.2526	0.0511	0.1533
<b>Material B</b>	Yes	3.7261	0.0263	0.0788
<b>Material C</b>	Yes	4.5862	0.0323	0.0970
<b>Material D</b>	Yes	1.2694	0.0089	0.0268
<b>Material E</b>	No	3.7062	0.0261	0.0784
<b>Material F</b>	No	0.9665	0.0068	0.0204

### **3.4.3 Puncture test**

The scaled needle was displaced into the silicone three times, with the average force and displacement at each speed shown on Figure 3-15.

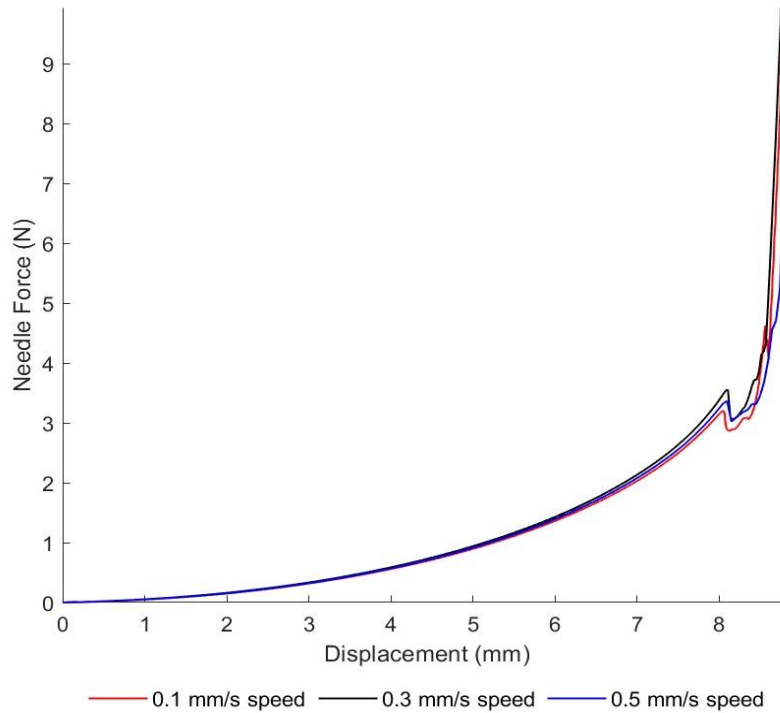


*Figure 3-15 - Puncture test results on Material C using three test speeds, 0.1 mm/s, 0.3 mm/s and 0.5 mm/s to assess the rate-dependent puncture resistance of the silicone. The results show minimal variation in the force-displacement curves, indicating no significant rate-dependence. The average puncture depth and force were 8.09 mm and 3.315 N respectively*

Visually, the difference in the overall force at which the needle inserted into the silicone at each speed is somewhat negligible, with only a difference of 0.32 N from 0.1 mm/s to 0.3 mm/s. The displacement of the needle at the point of suspected puncture, however, has a greater difference between 0.1 mm/s and 0.3 mm/s, at 0.537 mm, and 0.188 mm between speeds 0.3 mm/s and 0.5 mm/s. The suspected puncture force and displacement is detailed in Table 3-4.

*Table 3-4 - Needle puncture test results for three speeds and predicted insertion point force and displacement*

Speed (mm/s)	Displacement (mm)	Force (N)
<b>0.1</b>	8.075	3.020
<b>0.3</b>	8.107	3.557
<b>0.5</b>	8.098	3.369

### 3.4.4 Tensile test

All 6 tensile specimens were tested for the two silicones identified in Section 3.3.4. Table 3-5 shows the optimised VSG and tensile test machine results when fitted to the Ogden material model for Material B. This uses the highest recorded  $R^2$  found for each sample. The VSG data average was further used in Chapter 4.

Table 3-5 - Ogden material model properties including the standard deviation, for VSG and TM for Material B

Data output	Sample	$R^2$	$\mu$ (MPa)	$\alpha$	$\mu_0$ (MPa)
<b>VSG</b>	1	0.8303	0.1193	1.6342	0.0975
	2	0.9003	0.0831	1.9007	0.0790
	3	-	-	-	-
	4	0.9430	0.0558	2.1024	0.0586
	5	0.9408	0.0582	2.0877	0.0607
	6	0.9409	0.0574	2.1132	0.0606
	Average	-	0.0748	1.9677	0.0713
	SD	-	0.0273	0.2058	0.0168
<b>TM</b>	1	0.8196	0.1315	1.5360	0.1010
	2	0.9046	0.0905	1.8120	0.0820
	3	0.8748	0.0809	1.6522	0.0668
	4	0.9485	0.0616	2.0167	0.0621
	5	0.9538	0.0556	2.1135	0.0588
	6	0.9630	0.0469	2.2531	0.0529
	Average	-	0.0778	1.8973	0.0706
	SD	-	0.0309	0.2777	0.0179

The thinner samples, sample 1 to 3, had higher  $\mu$  and lower  $\alpha$  values than the thicker samples, sample 4 to 6. The thinner samples also had a lower  $R^2$  values than the thicker samples. The Ogden material model fit for each sample of Material B tested is shown in Figure 3-16 and Figure 3-17. The VSG data has five samples as the third sample tore prior to the 400% strain limit. The tensile test machine data has all six samples. The trend of both results is similar, with the thinner material initially being a lot stiffer but not requiring as large a force to tear as the thicker samples do. The thinner material appeared stiffer initially due to reduced compliance and less material deformation under the same strain, leading to a higher stress response in the early stages of loading.

## Development of Experimental Methods for Skin Substitute Evaluation

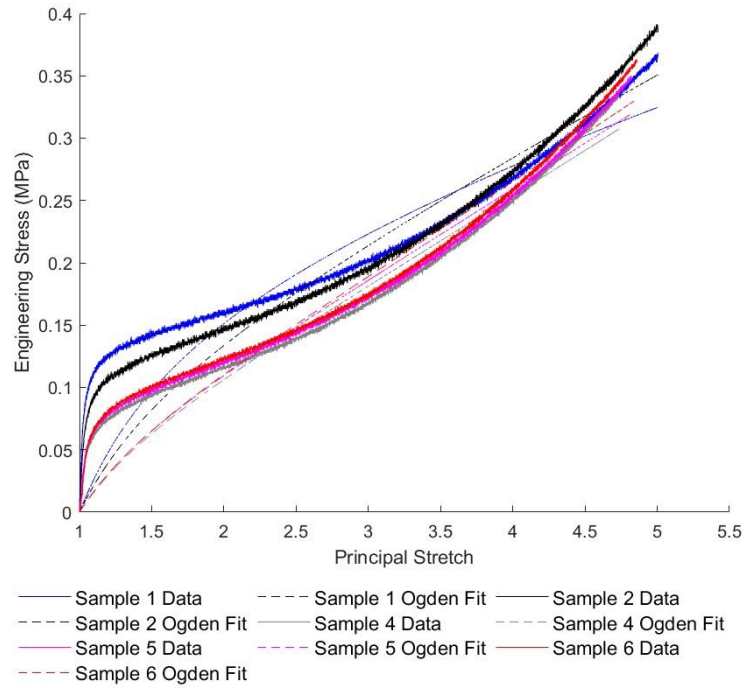


Figure 3-16 – One term Ogden material model fitting for the VSG results of Material B samples. The experimental data is represented by solid lines, while the Ogden fitting curve is shown with dashed line.

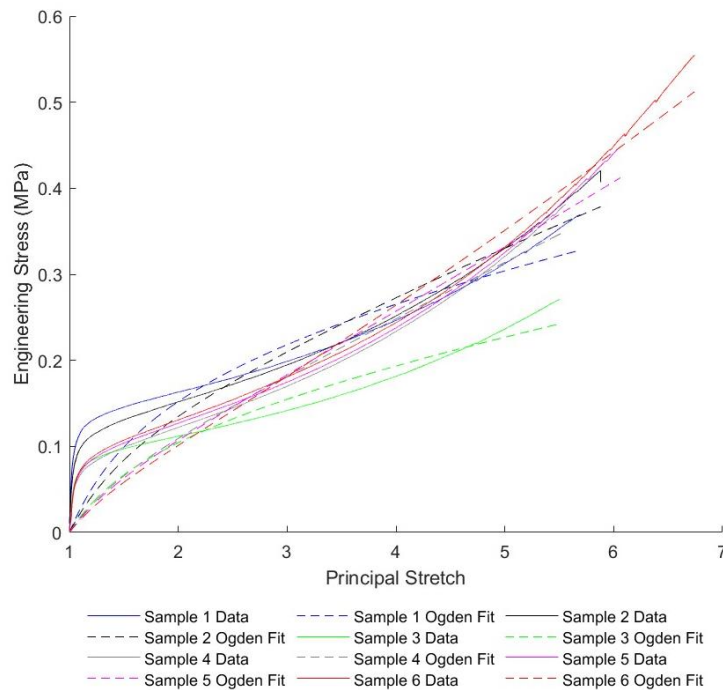


Figure 3-17 - One term Ogden material model fitting for the TM results of Material B samples. The experimental data is represented by solid lines, while the Ogden fitting curve is shown with dashed line.

Table 3-6 shows the optimised VSG and tensile test machine data for Material C. The thinner samples, samples 1 to 3, show larger  $\mu$  and lower  $\alpha$  values for both the VSG and TM data outputs, and also exhibit greater variability, with  $\mu$  standard deviations of 0.0256 MPa (VSG) and 0.0269 MPa (TM), and  $\alpha$  standard deviations of 0.1335 (VSG) and 0.1393 (TM), compared to just 0.0012 MPa and 0.0074 MPa for  $\mu$ , and 0.0143 and 0.0105 for  $\alpha$  in the thicker samples (4–6).

*Table 3-6 - VSG and TM data, and standard deviation, for the six samples tested showing the Ogden Material Model parameters for Material C*

Data output	Sample	$R^2$	$\mu$ (MPa)	$\alpha$	$\mu_0$ (MPa)
<b>VSG</b>	1	-	-	-	-
	2	0.9982	0.0646	2.4283	0.0785
	3	0.9985	0.0781	2.4793	0.0968
	4	0.9912	0.0235	3.1027	0.0364
	5	0.9968	0.0352	2.8992	0.0511
	6	0.9960	0.0349	2.8595	0.0498
	Average	-	0.04726	2.7538	0.0625
	SD	-	0.02299	0.2895	0.02452
<b>TM</b>	1	0.9991	0.0760	2.4135	0.0917
	2	0.9993	0.0765	2.3802	0.0910
	3	0.9989	0.0890	2.3717	0.1055
	4	0.9965	0.0251	2.6104	0.0328
	5	0.9974	0.0321	2.5124	0.0403
	6	0.9960	0.0309	2.5668	0.0309
	Average	-	0.05072	2.4883	0.0601
	SD	-	0.02849	0.1016	0.03417

Figure 3-18 shows engineering stress compared to the principal stretch for the VSG data, fitted to the Ogden material model for the five samples successfully recorded. All samples show a linear relationship compared to Material B with no distinct difference between the thinner and thicker samples.

## Development of Experimental Methods for Skin Substitute Evaluation

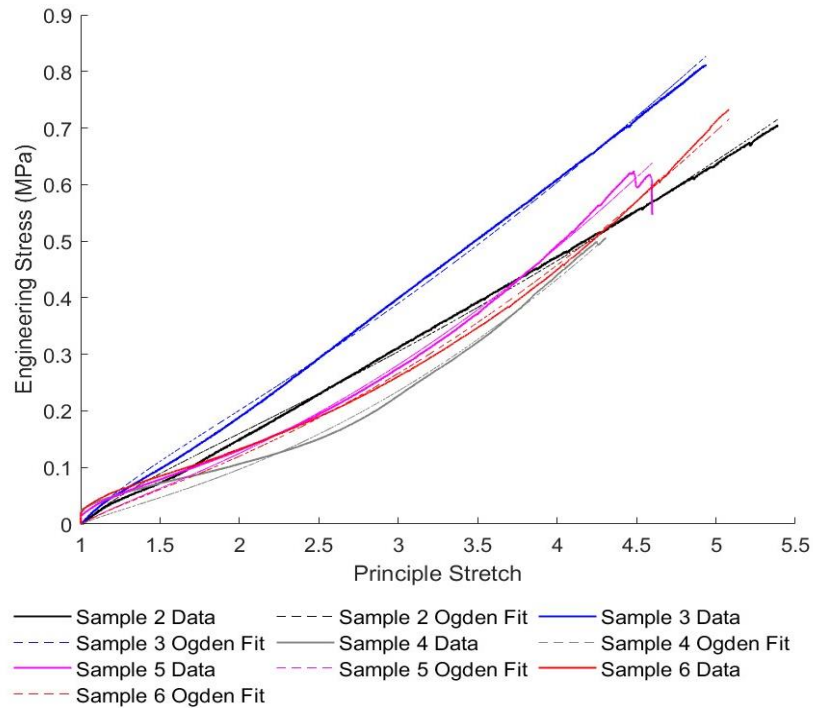


*Figure 3-18 – One term Ogden material model fitting for the VSG results of Material C samples. The experimental data is represented by solid lines, while the Ogden fitting curve is shown with dashed line. The results of Material C show a more linear fit than the original Material B.*

The tensile test machine data shows that the material failure point is higher than the point at which the VSG was ended. The VSG software was paused at 400 to 500 % strain, but the actual material failure point observed for the thinner samples (sample 4 to 6) was over 600% strain, with sample 6 observed at over 700% strain [Figure 3-19].

## Development of Experimental Methods for Skin Substitute Evaluation

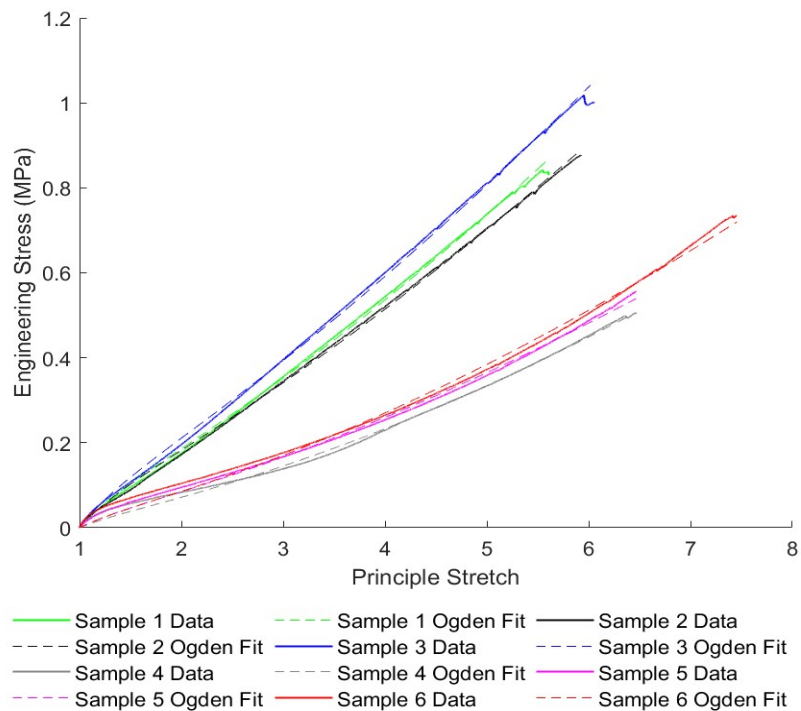


*Figure 3-19 – One term Ogden material model fitting for the TM results of Material C samples. The experimental data is represented by solid lines, while the Ogden fitting curve is shown with dashed line.*

The difference between the VSG and TM data is shown in Figure 3-20. This highlights the slight underestimation from the VSG data compared to what is recorded by the test machine.

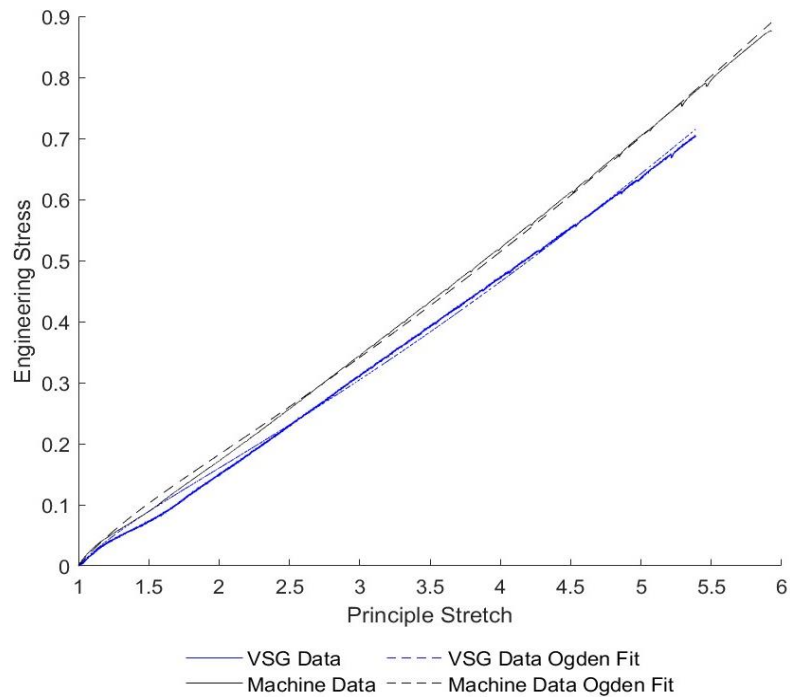


Figure 3-20 – Comparison of VSG and tensile machine data for Sample One, illustrating the difference in fitting between the one term Ogden material models. The VSG data is slightly lower than the TM, highlighting a slight discrepancy between the two measurement methods.

### 3.4.5 Work of Fracture

For the purpose of this section of the study, the tear tests of Material B and Material C were examined to compare the material properties with the addition of the TiO<sub>2</sub> particles, and to the toughness of skin.

Four samples were successfully tested for Material B, with a minimum of four crack increments for each sample. Figure 3-21 shows load-displacement curves for the four samples. The initialising of the material tear can be seen at the peak of the crack cycle.

## Development of Experimental Methods for Skin Substitute Evaluation

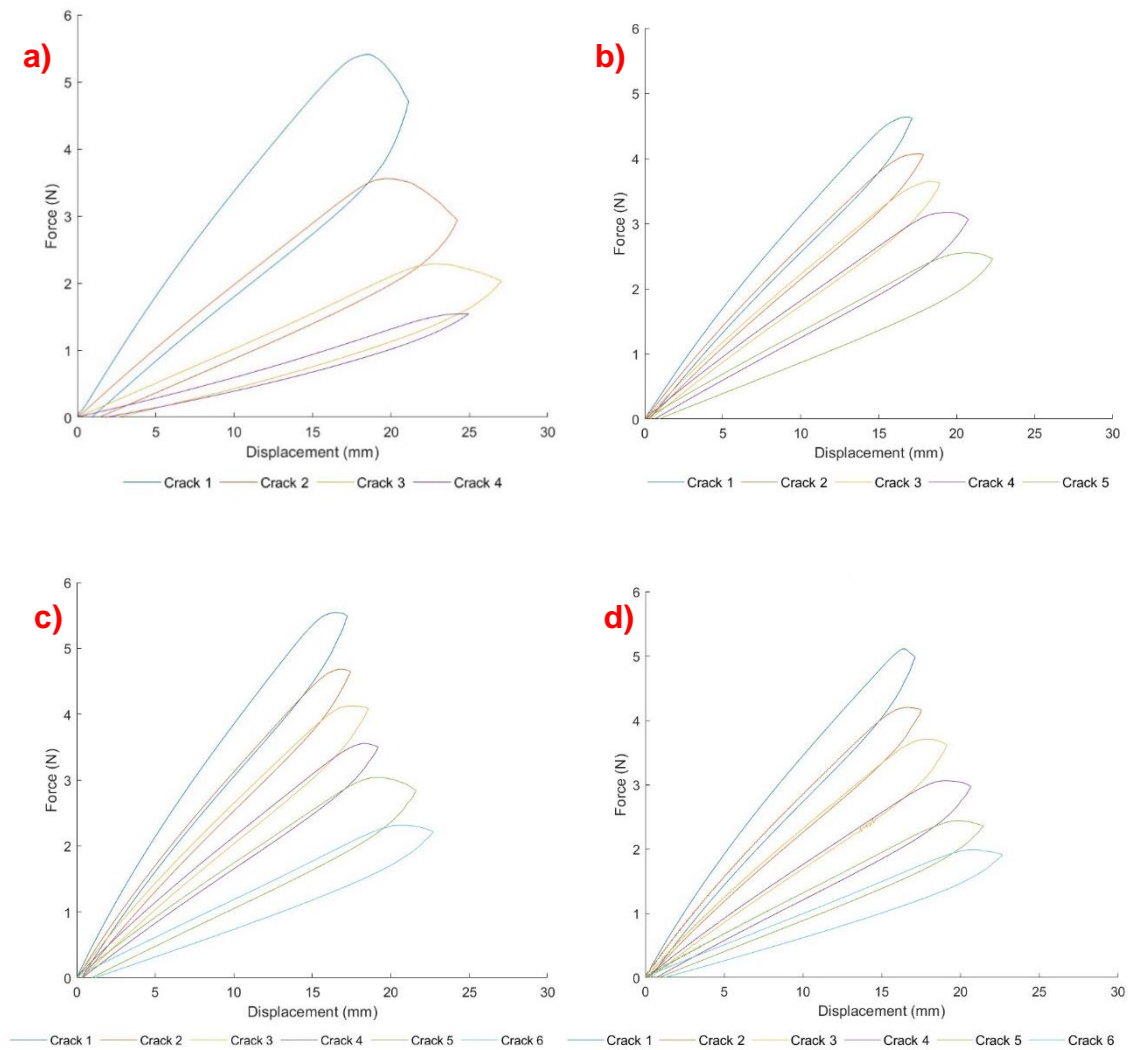


*Figure 3-21 - Tear test cycles for Material B sample 1 a) sample 2 b) sample 3 c) and sample 4 d). The figure shows the progression of damage during each cycle where unloading was decided by eye, with slight overlaps observed across all samples. Notably, sample 1 and sample 3 required a higher load to progress the first tear compared to the other samples.*

Material C had only three successful samples when using the final mould detailed in Section 3.3.5. It can be seen in Figure 3-22 that the crack propagation was not linear, although it did attempt to follow the groove created in the silicone.

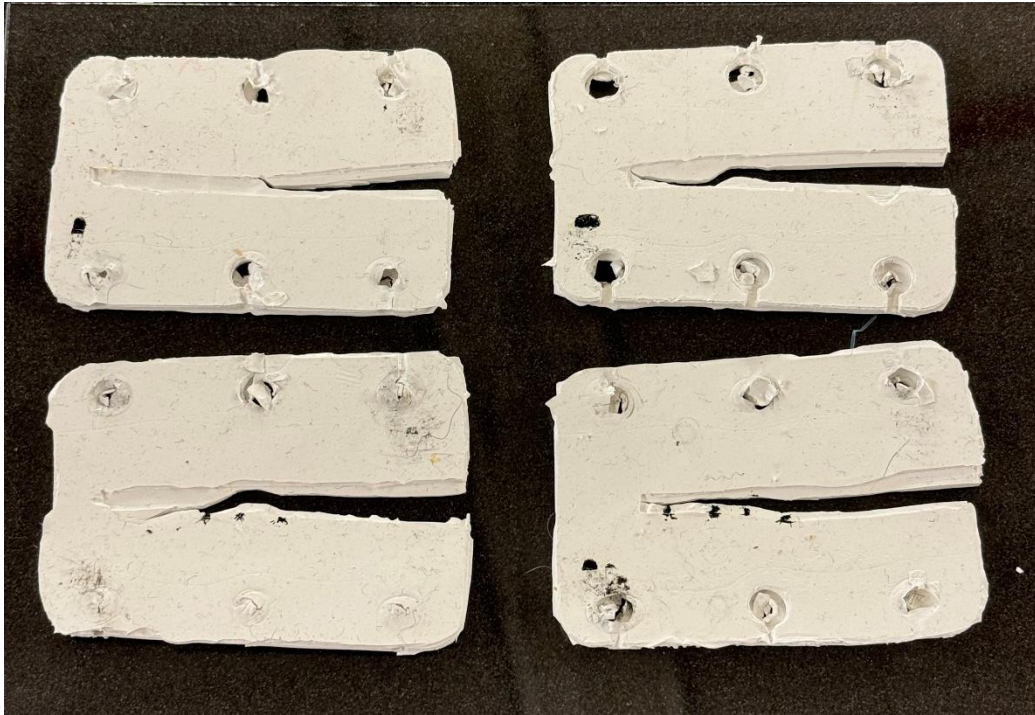


*Figure 3-22 - Tearing of Material C samples 1 to 4, highlighting the curved tearing observed during testing, which was not observed with Material B. The addition of the groove through the silicone resulted in improved tearing behaviour of Material C.*

Figure 3-23 shows the load-displacement curve for each sample and the crack formation cycles. The maximum displacement for each sample is over 25 mm, in comparison to Material B's maximum displacement reached over 20 mm on the final two crack tears. The maximum force observed for Material C is also significantly less than Material B, only reaching over 3 N on one tear cycle.

## Development of Experimental Methods for Skin Substitute Evaluation

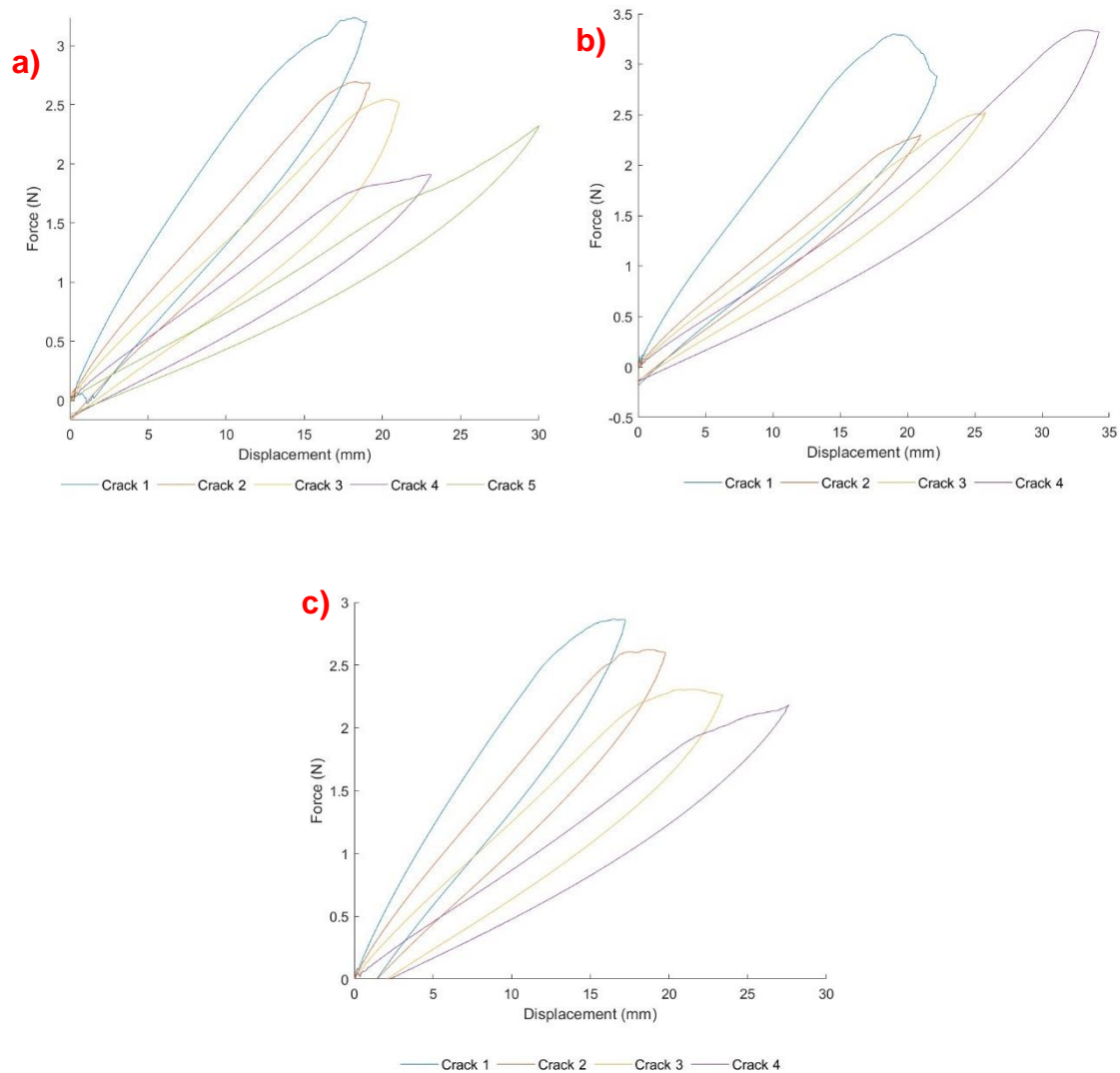


*Figure 3-23 - Tear test cycles for Material C sample 2 a) sample 3 b) and sample 4 c) showing significantly lower load than Material B. The figures also highlight a substantial overlap in the load-displacement curves for Material C, with a less symmetrical cycle shape than those observed in Material B.*

The data from the load-displacement curves were then used to calculate the work done for each crack cycle. As detailed in Section 3.3.5, the work done and area of the crack (using the sample thickness and each crack length) is used to calculate the WoF detailed in Table 3-7. The WoF for Material B had a maximum of  $1006 \text{ J/mm}^2$  and minimum of  $658 \text{ J/mm}^2$ . Material C exhibited a higher WoF compared to the other materials. The sample of thickness 1 mm had a WoF of  $2696 \text{ J/mm}^2$  and the thickest

sample at 1.57 mm had a WoF of 1241 J/mm<sup>2</sup>. These results suggest that as the sample thickness increased, the WoF decreased, which could be indicative of the influence of material thickness on its fracture resistance. However, given the high variation observed in Material C, particularly with WoF ranging from 1241 to 2696 J/mm<sup>2</sup>, this trend should be interpreted cautiously. This decrease in WoF could also be related to the presence and distribution of TiO<sub>2</sub> particles, or the presence of agglomerates from the silicone setting, which might affect the fracture behaviour in the thicker samples.

*Table 3-7 – The average WoF results for Material B and Material C samples, highlighting the average thickness of the sample*

<b>Material</b>	<b>Sample</b>	<b>Average thickness (mm)</b>	<b>WoF Average (J/mm<sup>2</sup>)</b>
<b>Material B</b>	1	2.5	1006.652
	2	2.4	722.6633
	3	2.7	738.4418
	4	2.5	658.3798
<b>Material C</b>	1	-	-
	2	1.43	1704.081
	3	1	2696.815
	4	1.57	1241.43

### **3.4.6 $\mu$ -CT**

As part of this study the initial steps for  $\mu$ -CT were conducted. The main observations included the particle distribution through the chosen silicone, and visualising the deformation of silicone during the initial stages of needle puncturing. As discussed previously, the success of this method is pivotal for the next steps detailed in Chapter 5.

Whilst the particle distribution, in Section 3.3.2, shows the size ranges of particles it also provides the percentage of each particle size showing the proportion of particles in different size ranges. However, the addition of these particles in the silicone could cause the formation of agglomerates and therefore change the size distributions.

## Development of Experimental Methods for Skin Substitute Evaluation

Figure 3-24 shows the particle distribution through the silicone, where agglomerates can be seen. This is a maximum intensity projection of 100 slices showing the variation of TiO<sub>2</sub> particles dispersed through a 100x100 pixel region.

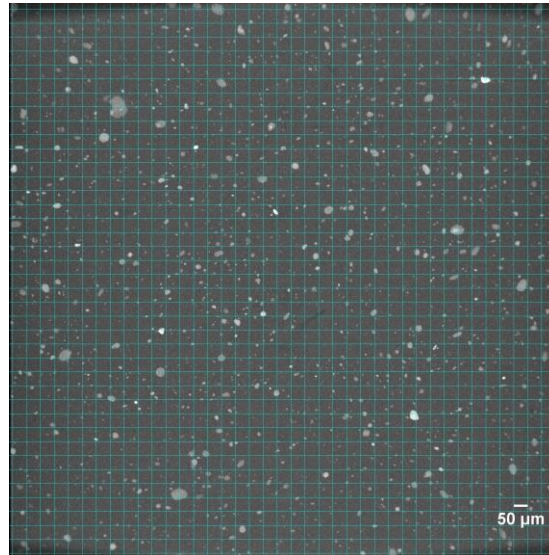


*Figure 3-24 - Fiducial markers of TiO<sub>2</sub> sieved through a 250 micron sieve in Material C. The markers are viewed to enable an assessment of size and distribution to identify the suitability of the TiO<sub>2</sub> for further experiments.*

The fiducial markers were in line with the requirements, randomly dispersed and randomly sized, with particles ranging from 10 microns to 100 microns.

### **3.5 Discussion**

This study evaluated multiple material samples against a set of material criteria to assess their potential as skin substitutes in further experiments. The criteria were chosen based on existing published data about human skin. Three different silicones were selected for testing: these were readily available and currently being used by the School of Pharmacy in their study to find suitable skin substitutes. Additionally, a compression test was conducted to evaluate the material properties of specimens produced using the proposed manufacturing process, which involved a speed mixer and a vacuum chamber. It was observed that vacuum degassing the samples

increased their stiffness. Figure 3-13 presents the average results of the compression tests for all six silicone variations. Material A exhibited the highest stiffness when tested with both the flat and conical indenters, with a Young's modulus of 0.1533 MPa. This is much higher than 0.0659 MPa reported for human skin by Groves et al. and so this material was eliminated.

On the other hand, Material D and F (Ecoflex Gel) showed stiffness values closer to those recorded by Groves et al. (0.069 N/mm) [69], at 1.2694 N/mm and 0.9665 N/mm, respectively. However, their shear modulus and Young's modulus [Table 3-3] were too low to meet the criteria. Material C displayed the closest shear modulus at 0.0323 MPa, though its Young's modulus was higher than that of Material's B and E. Among the three Ecoflex30 materials, Material B and E demonstrated the lowest stiffness values, at 3.7261N/mm and 3.7062N/mm respectively. This suggests that addition of the vacuum chamber and speed mixer does influence the materials stiffness, but not significantly. This finding is consistent with the shear modulus and Young's modulus, where differences were just 0.5% and 0.8%, respectively.

Material C exhibited a higher stiffness and Young's modulus than Material B and E, which could be attributed to the addition of the TiO<sub>2</sub> particles. Although the stiffness of Material C does not fall within the range specified by the material criteria in Section 3.2, the shear and Young's modulus do. Therefore, Material B and C (both Ecoflex-30 but with and without the particles) were selected for further experiments. This choice was made to allow a detailed comparison of how the addition of TiO<sub>2</sub> affects other material properties, as Material C was required for all  $\mu$ -CT experiments for data processing with DVC, as detailed in Chapter 5.

A puncture test was conducted to predict the puncture point of the scaled needle, building on the published work of Davis [10] and Oldfield [17]. Davis explained that a drop in material electrical resistance and needle force during MN displacement can identify the point of needle insertion into human skin. Similarly, Oldfield outlined a five-step process for needle insertion, where the load-displacement curve identifies two periods of force 'relaxation'. Accordingly, a puncture experiment with the scaled needle was carried out for Material C, which would be used in the  $\mu$ -CT scans. Three different

speeds were also investigated to determine if speed affected the puncturing process. Figure 3-15 illustrates the differences in puncturing parameters at each speed.

It was determined that the speed of indentation, 0.1 mm/s, 0.3 mm/s and 0.5 mm/s, had a small effect over the range measured, with only a 0.54 N difference between the slowest and fastest speeds, equating to 9.81% of the peak force. Whilst the force at 0.3 mm/s was slightly higher than both 0.1 mm/s and 0.5 mm/s, the variation across speeds does not follow a clear trend, suggesting that the difference may be due to natural variability in the data rather than a consistent relationship between speed and insertion force. Additionally, the predicted needle insertion point (defined as the maximum force prior to the force drop) showed a displacement difference of just 0.032 mm between the 0.1 mm/s and 0.3 mm/s speeds. The average displacement was 8.093 mm, and the average force at 3.315 N. These findings were subsequently used for the second phase of  $\mu$ -CT scans, where the needle displacement was set to 8mm, just before the point where the needle would begin puncturing the silicone.

After the compression tests, Material B and C were selected for further testing because their results were closest to the published parameters outlined in Section 3.2. These materials were examined to assess their tensile and tearing properties, which was important because silicone, like skin, is a homogenous material whose properties are generally isotropic. However, they can exhibit variations in behaviour under different loading conditions such as compression and tension. Additionally, investigating the behaviour changes between Material B and C, where the only difference is the presence of  $\text{TiO}_2$ , was considered a useful comparison.

To test the tensile properties, a tension test using VSG was set up to track the strain between two points on the dog bone samples, outputting surface strain changes up to the materials failure point. However, the VSG software struggled to track the silicone at strains beyond 400%. At the point of failure, the software crashed, losing the data. As a result, the decision was made to stop the software at 400% strain to prevent data loss (primarily caused by the stretching of the tracking dots beyond the software's capability). Tensile test machine data were also collected to compare to the VSG data, ensuring accuracy and checking for any under-or- over estimation from the strain gauge.

Six samples each were tested for both Material B and Material C. In Material B, the third sample failed before reaching 400% (at around 380%), while the first sample of Material C failed at 390%, preventing the collection of VSG data for these two samples. The five successful samples from each material were used for curve fitting against the Ogden material model to derive the required parameters,  $\mu$  and  $\alpha$ . The algorithm used to fit this material model required initial inputs of  $\mu$  and  $\alpha$  and then iteratively processed the final parameters, using the  $R^2$  value to assess the best model fit. These initial parameters were then applied to each sample in MATLAB. As six samples were tested for each material, three were classified as 'thinner' and three as 'thicker,' to investigate how thickness affects the material behaviour.

For Material B, the thinner samples failed at approximately 400% strain, with sample 3 failing slightly earlier, just before reaching 400%. The thinner samples also exhibited higher initial stiffness, exceeding 0.1 MPa, before their linear increase up to the material failure point. In contrast, the thicker samples (samples four to six) demonstrated linear stress-strain curve at values below 0.1 MPa, with very similar material properties across these samples. Table 3-5 presents the Ogden material parameters for all six samples. For the thicker samples, there was a 4.2% variation in the  $\mu$  parameter and a 1.2% variation in the  $\alpha$  parameter. However, in comparison, the thinner samples (samples one and two) exhibited a greater variation, with a 35.8% difference in  $\mu$  and a 15.1% difference in  $\alpha$ . This variation could be due to the smaller cross-sectional area making them more sensitive to stress concentrations. Inconsistencies within the material, or surface imperfections, could lead to defects and the premature failure seen in this experiment. When comparing the VSG data with the tensile test machine data, there was a slight overestimation of  $\mu$  and a slight underestimation of  $\alpha$ . While neither method is perfect, the close similarity between the two confirms the reliability of the VSG testing setup.

For Material C, the Ogden material model displayed a more linear stress-strain curve across all samples, with an improved  $R^2$  value exceeding 0.99 for each sample, indicating a better fit compared to Material B. It was observed that the thinner samples of Material B had higher  $\mu$  values and lower  $\alpha$  values than any other samples. Furthermore, there was a greater disparity in the parameters between the thicker and thinner samples in Material B compared to Material C. Both Material B and Material C

exhibited similar material parameters among their thicker samples, than seen with the thinner samples tested. Overall, it can be concluded that the thickness of the samples significantly affects the material failure properties. Thinner samples tended to fail at a lower strain, and the addition of TiO<sub>2</sub> particles increased the overall stiffness of the material. This addition resulted in more linear stretching behaviour, requiring a higher strain to tear the material; increasing from 5.5-7 % stretch to tear Material B to 5.75-7.5 % stretch to tear Material C. The average  $\mu$  and  $\alpha$  values for Material C were ultimately used in the computational models, as detailed in Section 4.2.3.

Following the tensile tests, the tearing properties of Materials B and C were investigated in greater detail by examining the work required to propagate a tear, which corresponds to the material's WoF. These properties are not only important to finding a comparable skin substitute, but also essential for input into computational models that rely on WoF data, such as those using cohesive zone methods, along with the Ogden material properties derived from the tensile tests. The average WoF for Material B was found to be 781.53 J/mm<sup>2</sup>, with a 41.8% difference between the largest and smallest WoF values observed in samples 1 and 4. This difference could be due to material defects obtained during preparation, or the experimental variation in load cycles from sample 1 to sample 4.

For Material C, only three samples were tested due to the challenges discussed in Section 3.3.5. The mould had to be modified to accommodate the increased load required to tear Material C, as a 10 N load cell was used. When the load approached the maximum limit, the tear began propagating vertically instead of horizontally. To address this, a groove was introduced across the sample to guide the crack horizontally. The groove resulted in an average thickness reduction of 1.25 mm, preventing the load from reaching 10 N. Unfortunately, the first sample failed when the crack propagated beyond the groove line. However, the following three samples were successful, as shown in Figure 3-16. Although the tears in Material C did not propagate perfectly horizontally and sometimes curved vertically, the tests were largely successful. Figure 3-18 illustrates the loading and unloading cycles for the three successful samples. Compared to Material B, these cycles showed more overlap, likely due to the vertical curving of the cracks. Sample 4, which exhibited the most horizontal tearing, had the most symmetrical loading and unloading cycles.

## Development of Experimental Methods for Skin Substitute Evaluation

The average WoF for Material C was 1880.775 J/mm<sup>2</sup>, which is 82.6% higher than that of Material B. However, there was a 74% difference between the highest WoF (sample 3) and the lowest (sample 4), a larger variation than seen in Material B's samples. There is limited data on acceptable ranges of WoF variability in soft synthetic materials, but previous studies such as Taylor et al. [144] report standard deviations of up to 30% across comparable tests. In this context, the 74% variation seen in Material C is unusually high, potentially due to inhomogeneities introduced by TiO<sub>2</sub> clustering.

The large variation in WoF results is primarily due to differences in material tearing, with the cycles overlapping and the tearing of the material sometimes occurring vertically rather than horizontally, as observed with Material B. Similar to the tensile test results, the increased force required to tear Material C, along with its higher stiffness, is attributed to the addition of TiO<sub>2</sub> particles. The challenges with vertical tearing in earlier samples may be due to agglomerates of TiO<sub>2</sub> forming within the silicone, which created obstacles that influenced the path of the tear. It is also acknowledged that the reduction in material thickness introduced by the groove may have altered the local stress states, contributing to some of the variability observed in the tearing behaviour; however, the impact of this change is not explored further within the scope of this project.

The final phase of this study explored the use of Material C in an imaging study designed to investigate small and large deformations during needle indentation, just before needle insertion. This was aligned with material criteria four and five, which required that the TiO<sub>2</sub> be compatible with  $\mu$ -CT experiments. Specifically, the fiducial markers used for Digital Volume Correlation (DVC) processing needed to be randomly sized and distributed, and suitable for the field of view (FoV) to be used. The fiducial marker size was first evaluated using a dry particle Mastersizer, comparing the particle size and distribution of both sieved and non-sieved particles. Figure 3-11 shows that both distributions peaked around a particle size of 10 microns, which was deemed ideal for a 2 mm FoV. The sieved particles demonstrated a more consistent size distribution, though they contained a higher volume of both smaller (0.1–1 micron) and larger (over 100 microns) particles.

To assess potential agglomeration and ensure random distribution within the silicone, a  $\mu$ -CT test was performed at the University of Southampton, scanning just the silicone (without the needle) using 100 projections. Figure 3-24 displays the resulting image, showing an average particle diameter ranging between 10 and 50 microns, which satisfied material criterion four. Following this preliminary scan, a small needle indentation experiment was performed on the same Versa CT scanner, with the experimental protocol outlined in Section 5.2.1.

This study initially evaluated multiple material samples to assess their suitability as skin substitutes for further experiments. Materials B and C, both made from Ecoflex-30 silicone, were chosen as their properties were closest to human skin. Material C in particular, with the addition of  $\text{TiO}_2$ , had the closest shear modulus and Young's modulus compared to other materials despite its stiffness being slightly above the human skin range. Material B and C were tested further in various experiments including puncture, tensile, tear tests and  $\mu$ -CT, and showed promise in replicating the mechanical properties of human skin under various loading conditions. Material C, specifically, exhibited a more linear stress-strain curve and higher stiffness, which is more representative of skin's behaviour under deformation. The addition of the  $\text{TiO}_2$  particles did introduce some challenges in material behaviour, such as increased variation in tearing properties which could affect its consistency as a skin substitute.

Overall, there was variability in the stiffness, shear modulus and tear resistance in the samples tested suggesting that silicone may not fully replicate skin. However, it is important to note that skin is also inconsistent as evidenced with the results in published data, which presents a challenge in identifying a suitable skin substitute. Despite these challenges, Materials B and C showed sufficient potential, with Material C ultimately selected for further experiments due to its suitability for  $\mu$ -CT and DVC analysis.

### **3.6 Conclusion**

This chapter has demonstrated the feasibility of using skin substitutes, such as silicone, for controlled and more accessible experiments, which could be applied to

## Development of Experimental Methods for Skin Substitute Evaluation

future studies including skin. Specific skin behaviours have been examined based on past literature to identify the type of silicone that matches the mechanical characteristics of skin. Parameters extracted from these experiments, such as Young's modulus, stiffness, and shear modulus, have been compared to those of skin and utilised in Chapter 4 to inform the Ogden material model parameters in FEA.

While findings suggest that silicone, particularly Material C, can replicate key mechanical properties of human skin, challenges such as variability in material behaviour and consistency remain. These factors will need to be addressed in future studies to refine the material selection and experimental techniques. However, the suitability of the material selected for DVC in Chapter 5 has been addressed and compared to the original material, ensuring its applicability.

# ***CHAPTER 4***

---

## **FINITE ELEMENT ANALYSIS**

### **4.1 Introduction**

As detailed in Chapter 2, the FEM modelling and analysis of needle insertion is a challenging and complex area of MN research. Understanding the mechanics of needle insertion is critical for improving the design and performance of FEMs. While experimental methods, such as DVC, allow for the direct observation of material deformation, computational models provide a valuable complementary tool for predicting and simulating needle behaviour under various conditions. Several factors influence the type and design of the FEM, including computational time, material models and needle geometry and array design.

Given the complexity of the interactions involved with needle puncture, two FEM approaches were investigated in this study. This chapter outlines these approaches to modelling both small and large deformations and to simulate the steps of needle indentation prior to puncturing. The first model is a static analysis for small deformations, which addresses the initial contact and deformation behaviours. It was also used to perform a mesh analysis which is vital to assess the FEM performance

and mesh dependence. The second model is a dynamic analysis for large deformations, capturing more complex interactions and material responses just prior to material tearing. Both models were developed with the intention of validating and refining them using the experimental DVC data, as discussed in Chapter 5. By comparing the model predictions with the actual observed deformations from the experiments, the FEM can be fine-tuned to more accurately reflect real-world behaviours.

## **4.2 Method**

### **4.2.1 Software**

FEBio is a finite element software specifically designed for FEA applications in biomechanics by the University of Utah [217]. For this study, version (2.6.0) of FEBio Studio was used. FEBio was chosen as it is an open-source software, which has the flexibility to integrate with MATLAB and the ability to add user-defined code. It also provides a wide range of applicable material models suited for complex material behaviours.

The two needles for this study were created using segmentation via Simpleware ScanIP. Simpleware ScanIP is a software package used for processing and analysing 3D image data from various imaging techniques, including  $\mu$ -CT and MRI. It offers a range of tools for image segmentation, mesh generation, and simulation setup. Consequently, the needles are accurately modelled and can be directly used with the DVC detailed in Chapter 5 for model validation.

Solidworks was then used to create the silicone parts. Whilst FEBio facilitates simple meshing, this was outsourced to Salome, an open-source software that allows for advanced meshing capabilities, including parameter adjustments such as growth rate particularly useful for the silicone meshing.

Another software that has contributed to the development of a large strain FEM is Rhino7 with Grasshopper. This software assisted in coding the linear constraints model [Section 4.2.6] by identifying areas from FEBio logfiles and reordering node coordinates for input back into FEBio.

### **4.2.2 Geometry and mesh**

#### 4.2.2.1 Needle geometry and mesh

The needles for both models were created by a segmentation process, which involves several steps to extract the needle from the  $\mu$ -CT image, with the image collection process explained in Section 3.4.6, and to prepare them for further use within the two models studied. This allowed for an accurate representation of the experiment in the FE models. The main differences between the CT needles and the original CAD needles is the needle length due to the  $\mu$ -CT FoV.

Firstly,  $\mu$ -CT stacks (the reference images) were imported into Simpleware ScanIP, these images contain both the needle and silicone and therefore required some further processing to separate the two structures. To complete this, an initial mask was created. Masks are binary images that define regions of interest or specific features within the  $\mu$ -CT image stack [218]. They consist of pixel values representing either the presence or absence of the material of interest. In the context of  $\mu$ -CT segmentation for DVC and FEA modelling of a needle and silicone, masks are used to isolate the needle and silicone from the background and each other. A threshold of 60 to 250 greyscale intensity values is applied to this first mask segmented, the silicone from the background, with the box for keeping only the largest island ticked. A second mask was then applied, where the threshold of 0 to 60 greyscale values segments the silicone and the needle. The thresholds were determined by looking at the greyscale histogram (ranging from 0 to 250) and looking at the imported scan geometry boundaries.

Once the needle is outlined, any gaps or discontinuities in the segmented needle mask were closed to ensure a continuous representation of the needle geometry using the 'fill gaps' function. Any internal voids or cavities were then filled within the needle, with a recursive Gaussian smoothing filter applied after to ensure any noise or artifacts were removed from the segmented needle. The filter was left at the default settings of 1 pixel for X, Y and Z sigma, referring to the Gaussian smoothing used. The final step was to generate a volume mesh from the segmented masks. To create this, the 'set up model' option was chosen, this allows options such as general, surface optimisation and mesh refinement to be chosen for a specific mask. The option of

## Finite Element Analysis

model type and export type is also given within this model set up. This converted the 3D mask data into a mesh .stl file, set at the ScanIP coarseness of -25 for the first needle (somewhat fine to show some features) and -50 for the second needle (close to the maximum fineness of -100) and adjusted by eye, suitable to import into FEBio. The static model needle was exported with 1781 elements and the dynamic model needle had 59616 elements. There were no convergence studies conducted on the needle, however the mesh densities were determined as sufficient needle geometry was captured.

This step was repeated for both sets of  $\mu$ -CT scans to allow for a direct feature comparison to the DVC scans. The needles were then imported into FEBio. Both needles are symmetrical in only one plane. The needle used for small strain modelling is depicted in Figure 4-1 and the larger needle for large strain modelling in Figure 4-2.

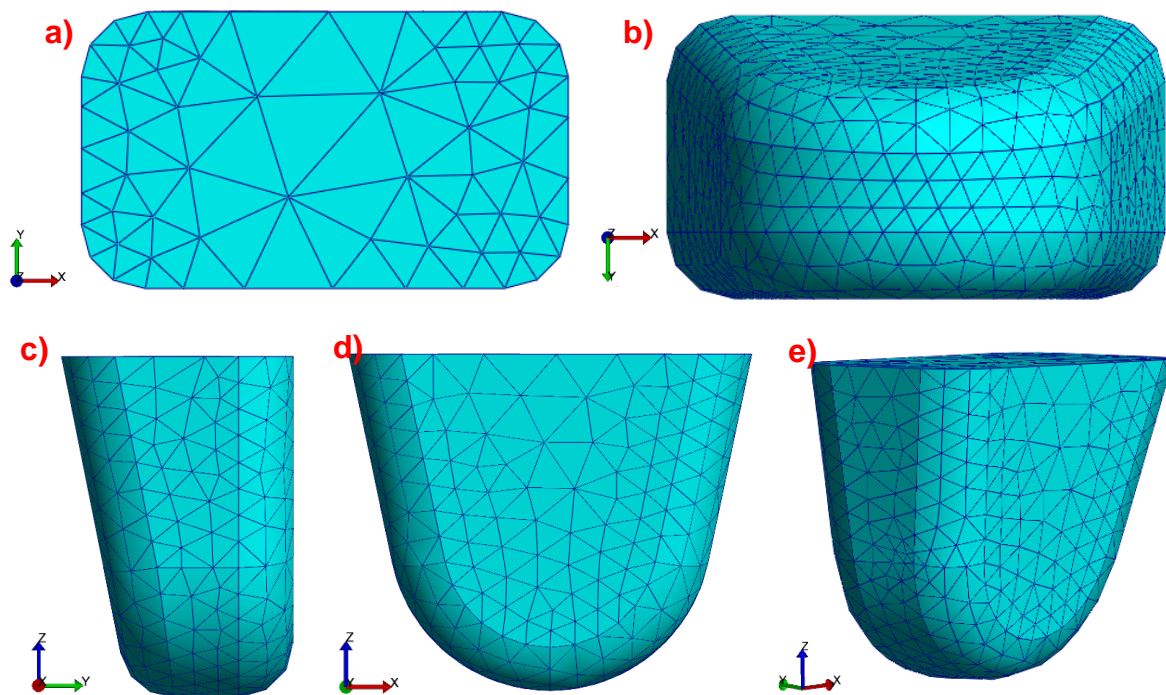


Figure 4-1 - The needle used in the first, static, model, top view a) bottom view b) side view c) front view d) isometric view e)

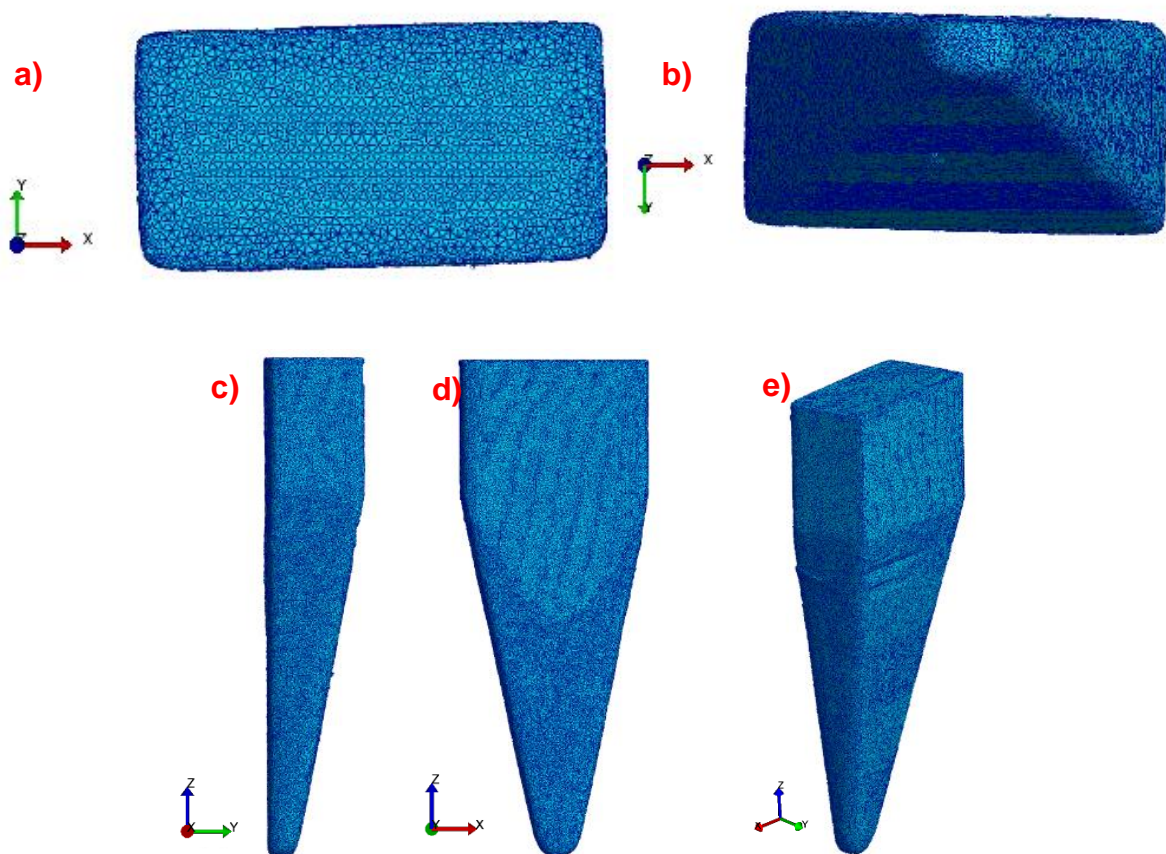


Figure 4-2 - The needle used for the second, dynamic, model, top view a) bottom view b) side view c) front view d) and isometric view e)

#### 4.2.2.2 Silicone mesh and geometry

A quarter part of silicone, with dimensions 4x4x8 mm was created in Solidworks. This silicone block was then separated into two parts [Figure 4-3]. These parts were then imported into Salome 9.7 as a .step file, where a 4 node tetrahedron mesh was created. This allowed a finer mesh to be created on the smaller block (where the needle tip would have the most contact) with the larger blocks supporting a low mesh growth rate, the Salome settings are detailed in Table 4-8, Mesh 4 was used. This allowed for a refined mesh in the areas of interest, and a low-density mesh in areas of less interest, situated further from the needle. the result was a lower number of elements in the model, reducing the time required for the model to run. The mesh block was then imported into FEBio as a .unv file, this is a universal file format used for importing between different FEA tools.

## Finite Element Analysis

For the first indentation model, the quarter mesh was mirrored within Salome to create a full block with dimensions 8 x 8 x 8 mm [Figure 4-4]. The second model used the quarter geometry only, of dimension 4 x 4 x 8 mm [Figure 4-5]. Although the needle used in this study is not symmetrical, the quarter model was chosen to simplify the model due to computational requirements and align with the scope of this project, which was to develop an initial pre-penetration model with potential for future expansion. While a full silicone block would better account for the displacements and strains caused by the needles non-symmetry, computational limitations made this approach infeasible. This assumption is justified for the initial stages of model development but should be revisited in future studies to assess its impact on the accuracy of strain and displacement predictions.

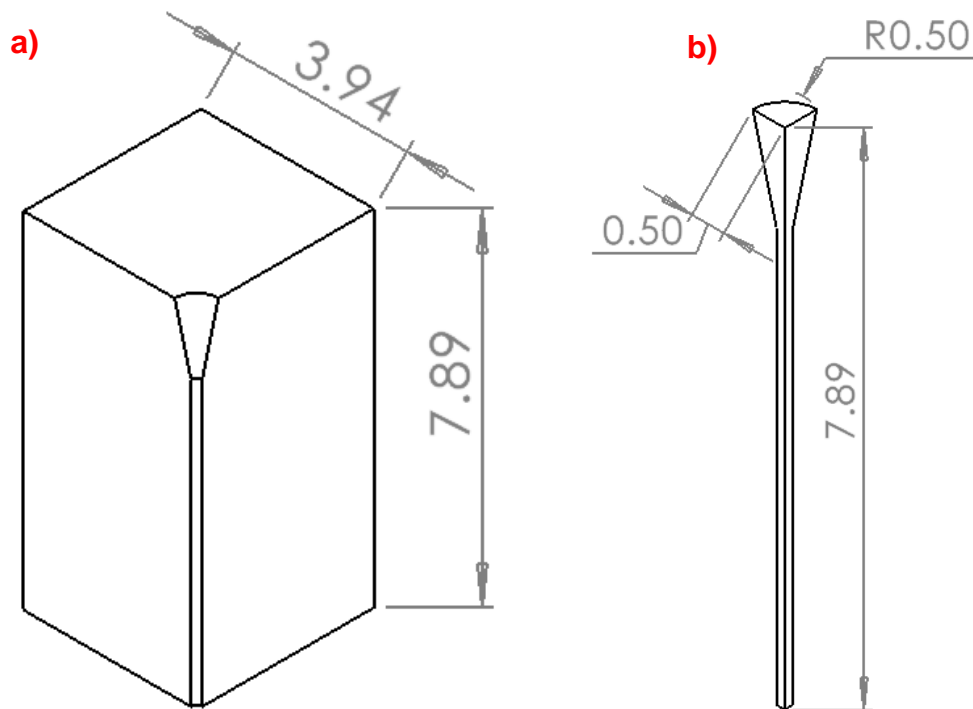


Figure 4-3 - Geometry of the silicone solid model (dimensions in mm), showing the outer region (a) and the inner region which had a finer mesh (b).

## Finite Element Analysis

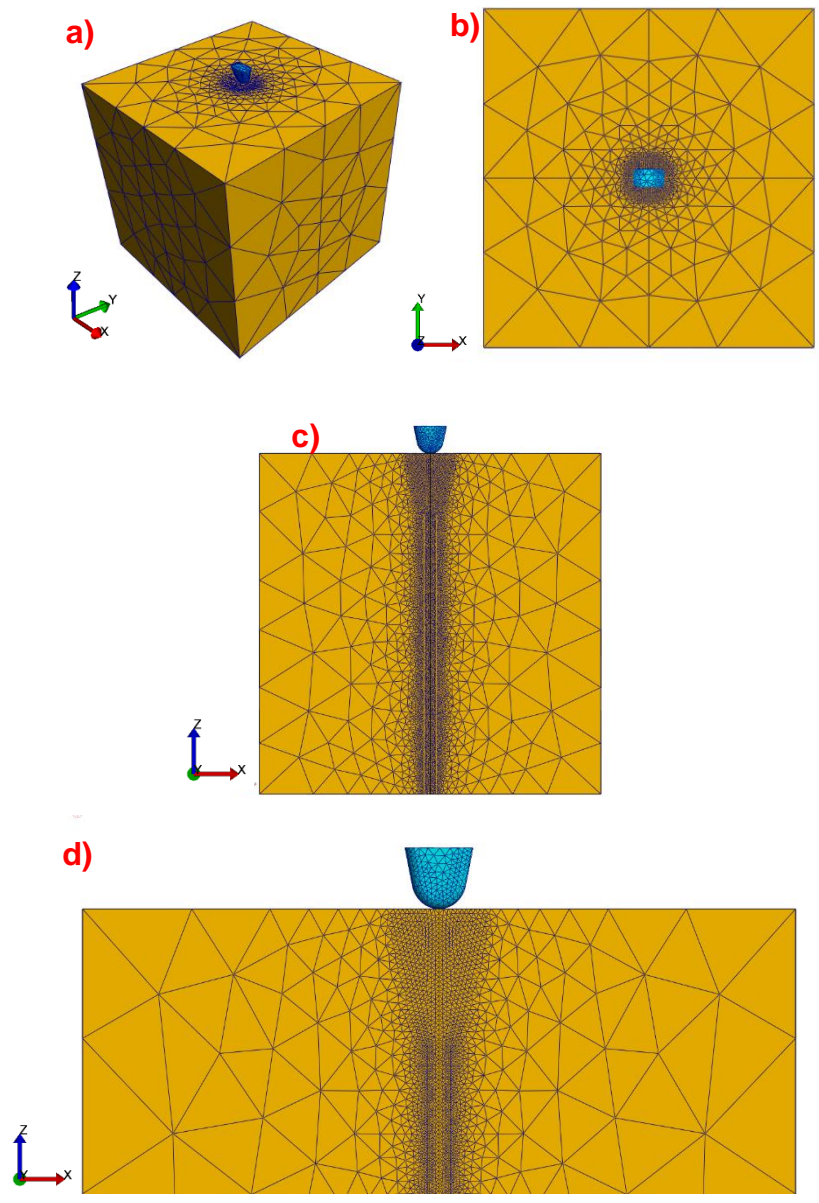


Figure 4-4 - The silicone mesh for the first model, which was a full silicone block of 8x8x8 mm dimensions. The needle is also shown (in blue). Isometric view a) top view b) a half slice showing the inside geometry c) close up view of the inside geometry d)

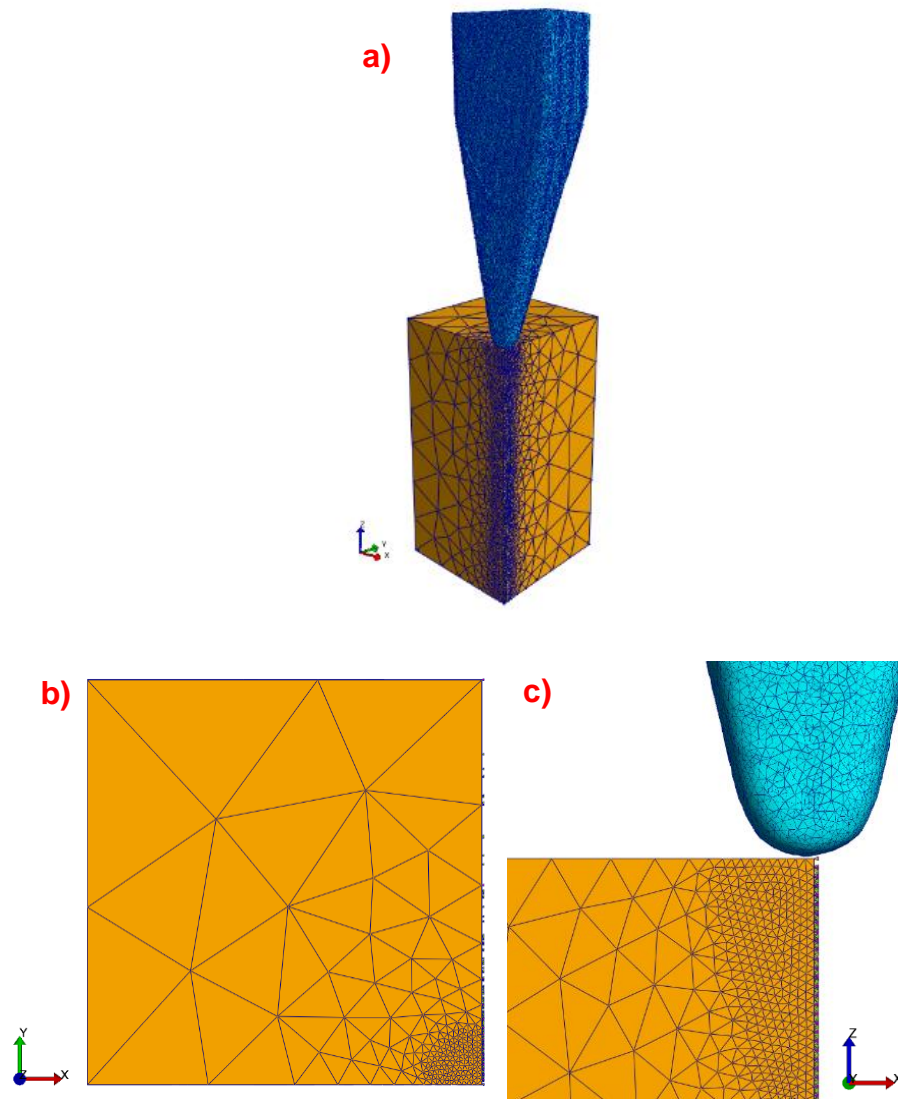


Figure 4-5 - The silicone mesh for the second model, which was a quarter model of the same block used for the first model, of dimensions 4x4x8 mm. Isometric view a) top view b) and close up of the side view c)

#### 4.2.3 Materials

An Ogden material model was used for the silicone block. This material model (as explained in Section 2.2.3) used multiple material constants such as the  $\mu$ ,  $\alpha$  and the bulk modulus (K). These properties were found by tensile testing of Ecoflex-30 with the TiO<sub>2</sub> particles, all work with VSG and the tensile tests are detailed in Section 3.4.4 [Table 4-1]. K was determined by multiplying  $\alpha$  by 1000. The low strain model is a static model, and therefore is not density dependent and remained as the default setting by

FEBio. However, the high strain model is dynamic and therefore is density dependent. This is later investigated in Section 4.4.

*Table 4-1 - Table of the material parameters initially used in both models for the silicone. All Ogden material model parameters explained in Section 2.2.3*

<b>Geometry</b>	<b>Material model</b>	<b>Density (kg/mm<sup>2</sup>)</b>	<b><math>\mu</math> (MPa)</b>	<b><math>\alpha</math></b>	<b>k (MPa)</b>
<b>Silicone</b>	Ogden	1	0.04726	2.7538	47.26

The needles are made of stainless steel with known material properties [219]. For this FEM, it was classed as a rigid body . The density, Poisson ratio and Young’s modulus for steel are detailed in Table 4-2.

*Table 4-2 - Table of the material parameters used for the steel needle*

<b>Geometry</b>	<b>Material model</b>	<b>Density (kg/mm<sup>2</sup>)</b>	<b>Young’s modulus (MPa)</b>	<b>Poisson’s ratio</b>
<b>Needle</b>	Rigid Body	1	200	0.25

#### **4.2.4 Boundary conditions**

Two rigid body constraints were applied to the needle. The first constrained the displacement of the needle in the x and y direction (the axes are defined in Figure 4-5). It also removed the possibility of rotation in all directions (x, y and z). The second constraint, the prescribed displacement, acted along the z axis to allow the displacement of 0.375 mm.

The boundary conditions for the silicone blocks were chosen to replicate the testing conditions and simplified to take advantage of model symmetry. The base of the silicone [Figure 4-6 a)] was constrained in the Z direction, the same direction that the needle will be displaced in. This simulates the silicone resting on the test rig. The two sides of the silicone were then constrained in the x axis [Figure 4-6 b)], and the last

## Finite Element Analysis

two sides constrained in the y axis [Figure 4-6 c)], these were the symmetry boundary conditions representing the rest of the silicone. The top of the silicone was left unconstrained. The same boundary conditions were used for both the small deformation and large deformation models, the only change for the high deformation model was that only one side of the silicone was constrained in the X axis, the other was left unconstrained due to the addition of the tetrahedrons explained further in Section 4.2.6.

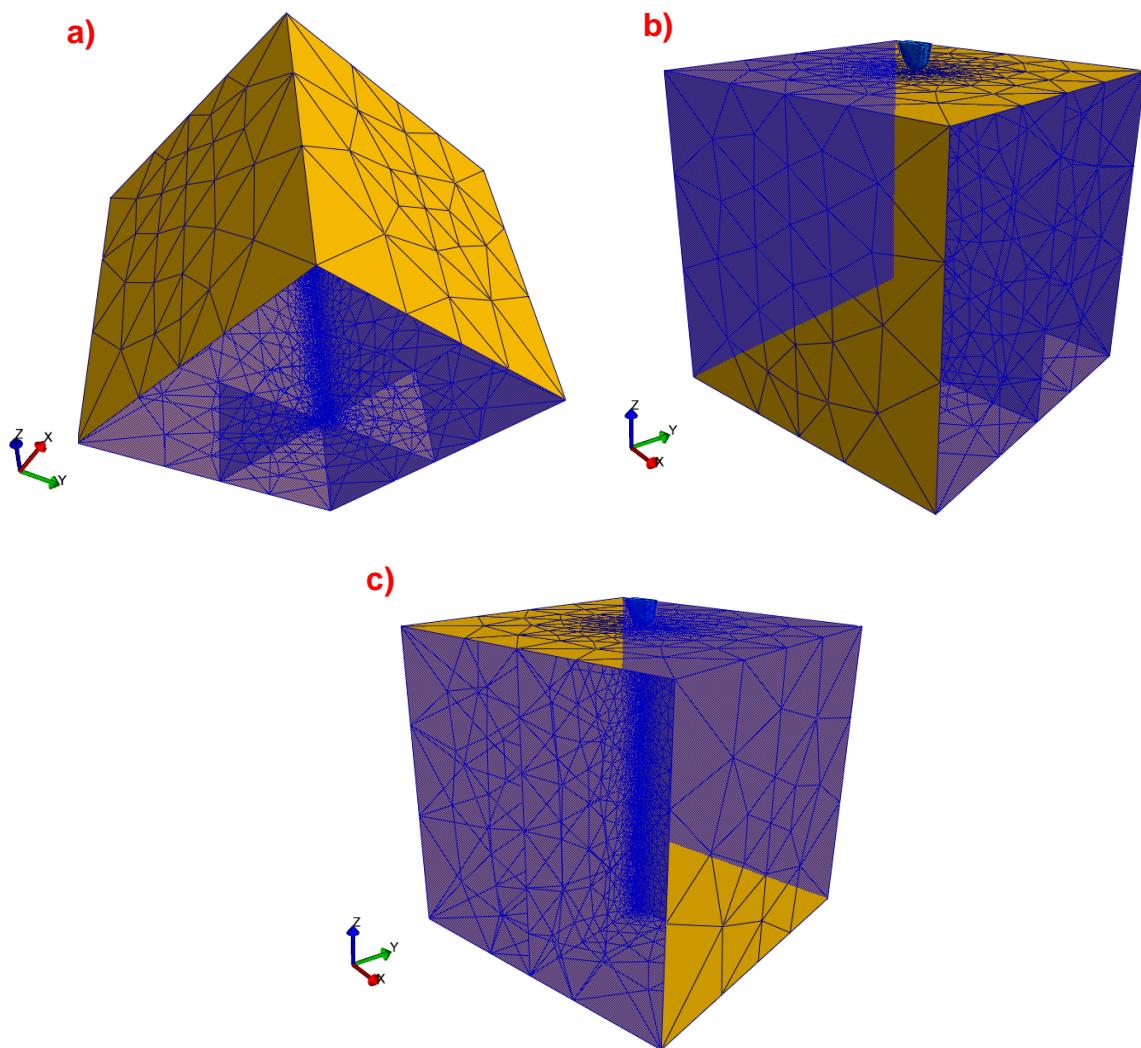


*Figure 4-6 - The boundary conditions applied to the silicone blocks, the sides constrained are highlighted in blue. The base of the block constrained in the Z axis a) two sides of the block constrained in the X axis b) and the last two sides constrained in the Y axis c)*

#### **4.2.5 Contacts**

The contacts used between the needle surfaces and the silicone surfaces in this study were sliding contacts, namely the sliding facet on facet algorithm in FEBio. A facet-to-facet sliding contact algorithm was used to implement a non-penetration constraint between two or more surfaces. This means that the two surfaces will move over one another in the direction set by the boundary conditions. Compared to the additional two algorithms available, this contact has been shown to have added stability and higher convergence rates [220]. The contact used implemented a penalty factor method. The penalty factor is dependent on material properties as well as mesh and element dimensions. The penalty factor was determined using a trial and error approach, low penalty factor will cause the sliding contact to not work; for example, in this study the needle will penetrate through the silicone without indenting the silicone surface. If the penalty factor is too high, the model will fail to converge.

The primary and secondary surfaces were selected; for this model the primary surface was the surface of the silicone [Figure 4-7 a)] and the secondary was the needle surface [Figure 4-7 b)]. FEBio's advice is for the secondary surface to be the rigid body, or higher mesh dense geometry. It should be noted that no other contact properties were altered from the default settings in FEBio; the properties that were changed are shown in Table 4-3.

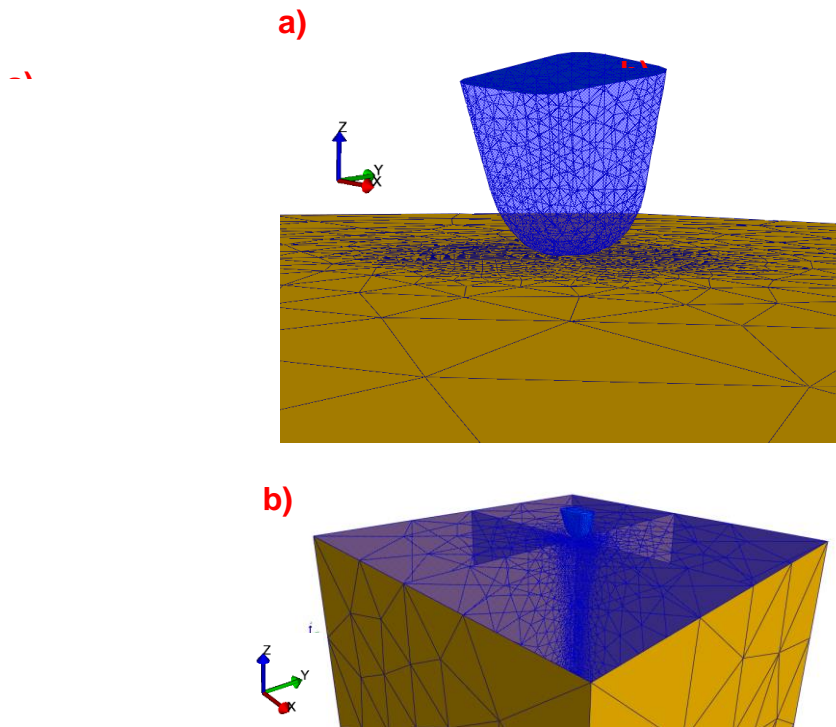


Figure 4-7 - Contacts applied to the needle and silicone showing the primary surface (the needle surface) a) and the secondary surface (the silicone surface) b)

Table 4-3 – Contact properties used for both models, detailing the penalty factors and tolerances

Model	Enforcement parameter	Penalty	Tolerance	Search tolerance	Search radius
1	Penalty	100	0.1	0.02	0.2
2	Penalty	10000	0.1	0.02	0.2

#### 4.2.6 Cohesive zone model

Prior to needle penetration, the skin undergoes high deformation and large strains during indentation. To simulate the tearing of the silicone, a novel cohesive zone method developed by Matthew Potts at Cardiff University was used [No reference as unpublished]. Figure 4-8 details the creation of the model using this method, with the sections expanded later within this section and further supporting images included.

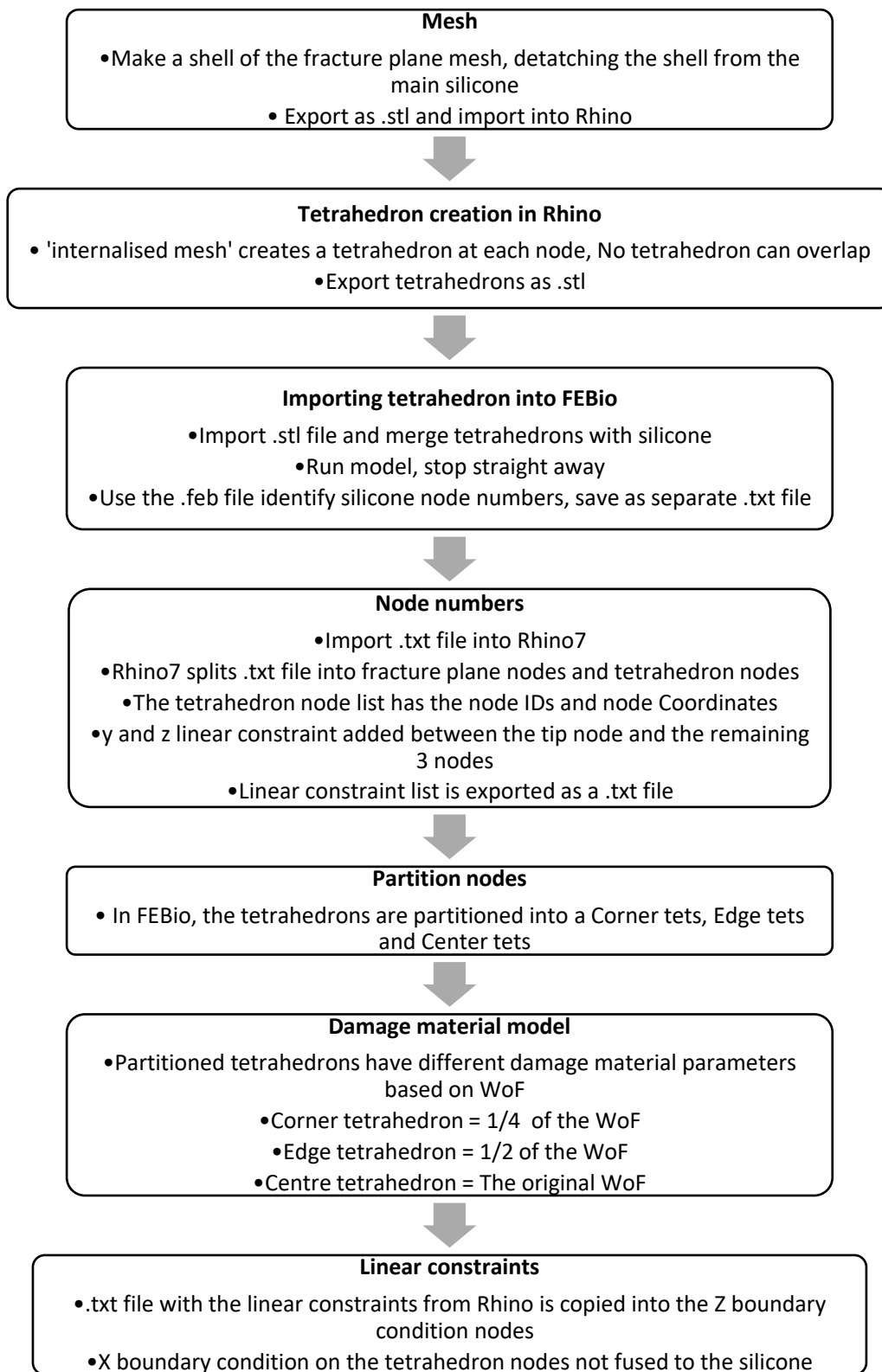


Figure 4-8 - Flowchart of the Cohesive Zone Method model creation developed within this study

## Finite Element Analysis

At each node on the fracture plane mesh, a tetrahedron was created. These tetrahedrons were made by generating a shell of the fracture plane mesh, detaching the shell from the main silicone mesh using 'detach elements' and exporting this shell as a .stl file into Rhino7 [Figure 4-9].

The code within Rhino Grasshopper then created its own version of the imported mesh by 'internalising' the data, and then creating a tetrahedron at each node point on that mesh. The tetrahedron size is also adjustable within the code, as it is paramount that no tetrahedrons overlap as this will create an error within FEBio. The tetrahedrons were then imported as a .stl file back into FEBio [Figure 4-10], meshed with the meshing function, and fused onto the silicone mesh using the 'merge objects' function, with the default (from FEBio) weld tolerance of  $1e-6$  used [Figure 4-11]. Next, the .txt file of the mesh node numbers for the silicone was imported back into Rhino, with the code in Rhino Grasshopper then identifying the nodes for the fracture plane mesh and the tetrahedrons from the input file and separating them into two lists. The first list is the node IDs and the second list is the corresponding coordinates of the node IDs.

The next section of code extracts the node IDs that correspond to the tip and rear nodes of each tetrahedron (the tetrahedron geometry is still within the Rhino viewport to aid this). Next, the code creates a y and z linear constraint contact code between the tip node of each tetrahedron and the three nodes defining the rear triangular surface of the tetrahedron [Figure 4-14]. These constraints are defined in the local coordinate system of each element, ensuring accurate contact behaviour as the geometry deforms. Finally, the linear constraints code, the contact type and parameter value, is blocked using brackets, an example of this code is illustrated in Figure 4-12. This code is then saved into a blank .txt file and copied into the notes section of FEBio bound condition Z, shown in Figure 4-13, this automatically adds the linear constraint code into the .feb file when the model is run.

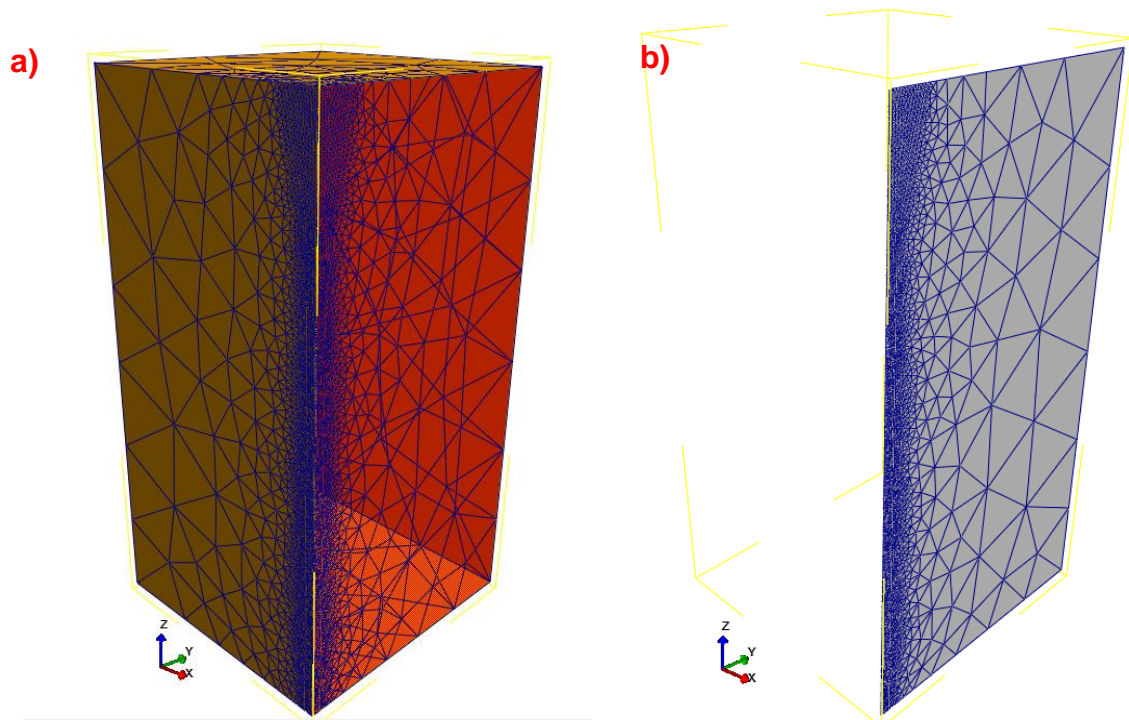


*Figure 4-9 - The mesh surface that is chosen (the fracture plane) a) and the shell plane that is created from the surface selected b)*

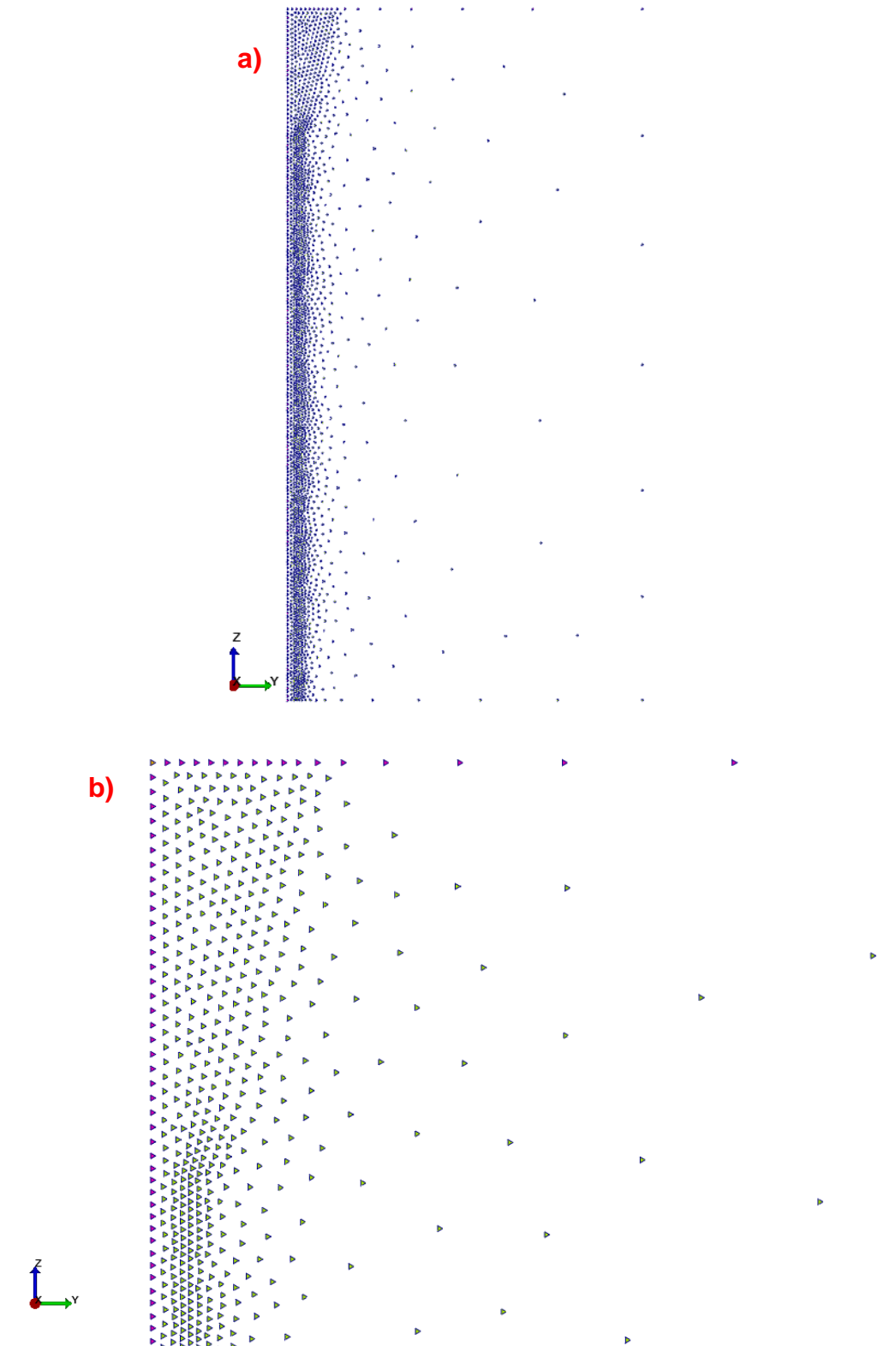


Figure 4-10 - The tetrahedrons created in Rhino7 Grasshopper, imported back into FEBio a) and a close up of the tetrahedrons and how they are separated into corner (orange), edges (purple) and centre (yellow) tetrahedrons by partitioning the single elements b)

# Finite Element Analysis

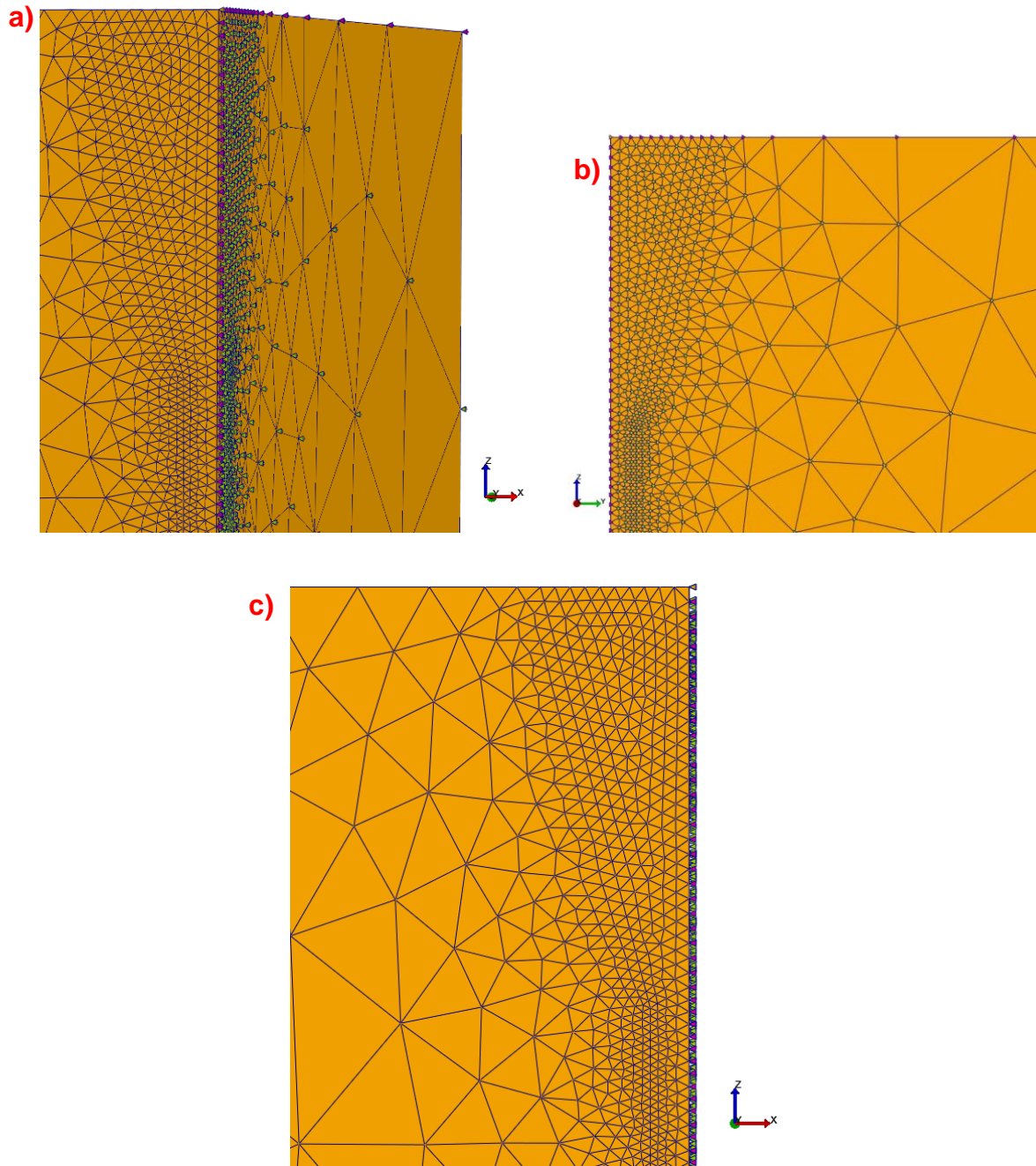


Figure 4-11 - The tetrahedrons fused onto the silicone block showing the isometric view a) side view b) and front view c)

## Finite Element Analysis

```
<bc type="linear constraint"><node></node><dof>y</dof><child_dof><node></node><dof>y</dof><value>1</value></child_dof></bc>
<bc type="linear constraint"><node></node><dof>y</dof><child_dof><node></node><dof>y</dof><value>1</value></child_dof></bc>
<bc type="linear constraint"><node></node><dof>y</dof><child_dof><node></node><dof>y</dof><value>1</value></child_dof></bc>
<bc type="linear constraint"><node></node><dof>z</dof><child_dof><node></node><dof>z</dof><value>1</value></child_dof></bc>
<bc type="linear constraint"><node></node><dof>z</dof><child_dof><node></node><dof>z</dof><value>1</value></child_dof></bc>
<bc type="linear constraint"><node></node><dof>z</dof><child_dof><node></node><dof>z</dof><value>1</value></child_dof></bc>
```

Figure 4-12 – An example of the linear constraint code within Rhino Grasshopper, showing the boundary condition type ‘linear constraint’ and the corresponding node number that will be inserted

```
Notes
Notes for: 1SFZ (zero displacement)
-->
<bc type="linear constraint"><node>50070</node><dof>y</dof><child_dof><node>50072</
node><dof>y</dof><value>1</value></child_dof></bc>
<bc type="linear constraint"><node>50066</node><dof>y</dof><child_dof><node>50068</
node><dof>y</dof><value>1</value></child_dof></bc>
<bc type="linear constraint"><node>50062</node><dof>y</dof><child_dof><node>50064</
node><dof>y</dof><value>1</value></child_dof></bc>
<bc type="linear constraint"><node>50058</node><dof>y</dof><child_dof><node>50060</
node><dof>y</dof><value>1</value></child_dof></bc>
<bc type="linear constraint"><node>50054</node><dof>y</dof><child_dof><node>50056</
node><dof>y</dof><value>1</value></child_dof></bc>
```

Figure 4-13 – An example of the linear constraint code within FEBio notes that shows the node IDs. This code is then automatically added to the .feb file when the model is run

The corner, edges and interior were then partitioned [Figure 4-10] within the FEBio mesh editor so that the elastic damage model with different Young’s moduli in Table 4-4 could be applied.

Table 4-4 - Material model parameters for the tetrahedrons used within the Cohesive Zone method dynamic model

Tetrahedron	Density (J/mm <sup>3</sup> )	Elastic		Damage – CDF Weibull			Criterion
		Density (J/mm <sup>3</sup> )	Young's Modulus (MPa)	Dmax	$\alpha$	$\mu$	
<b>Corner</b>	10	1	5640	1	2.5	0.2	DC max normal Lagrange
<b>Edges</b>			2820				
<b>Centre</b>			1410				

The next step was to apply specific material properties to the partitioned tetrahedrons, this includes a damage material model. Damage material refers to the material model and accounts for how the material changes due to the load or stress applied. The parameters applied to these damage materials include the initial material properties and how the damage progresses. In FEBio this explains the damage variable (the extent of the damage in the material), threshold (the point the damage starts to accumulate) and the function (how the damage progresses with loading). The damage material applied to tetrahedrons reproduce a force-separation boundary condition at each node, which reproduces the mechanical behaviour of material failure in a more realistic manner during tearing.

The work of fracture is then determined by the Weibull cumulative damage function. This function describes the probability of failure based on the stress or strain of the material, providing a statistical approach to how the material will fail. Within FEBio's user manual, the material parameters  $\mu$  and  $\alpha$  are detailed, with alpha regulating the rate of the damage and therefore the greater alpha is the more rapid the damage is [221]. For this purpose, alpha explains that when a tetrahedron is stretched, a force displacement graph is produced. The area under said graph and the surface area of the tetrahedron [Equation 8 and 9] determines the WoF. The Young's modulus dictates the fracture energy and therefore was adjusted on the tetrahedrons to reflect the effective material representation by each element. For the tetrahedrons fused to the elements at the edges, the Young's modulus was set to half the value used for the interior tetrahedrons. The corner tetrahedron was assigned a Young's modulus of one

## Finite Element Analysis

quarter the interior value. This adjustment ensures that each element accurately represents the amount of material it occupies

The second step was the application of the linear constraints. These constraints help enforce specific conditions on a model, for this study this is the restriction of movement for the tetrahedrons and therefore the crack plane of the silicone. This was done in two ways. The first was with the coding within Rhino7 Grasshopper connecting two tetrahedron nodes with a 'linear constraint' boundary condition. This code identifies a parent node involved in the constraint whose degrees of freedom are constrained in the vertical direction, acting as a reference point for deformation. It then identifies a child node of the same tetrahedron, which is related to the parent node already identified and linked by a factor of one. Therefore, any vertical displacement applied to the parent node will be exactly replicated by the child node. Next, the nodes on the tetrahedrons that were not fused to the silicone [Figure 4-14] had a boundary condition where they were constrained normal to the fracture plane. This gives the tetrahedron some freedom to move in two planes, enforcing the symmetry conditions, and also provides some stability.

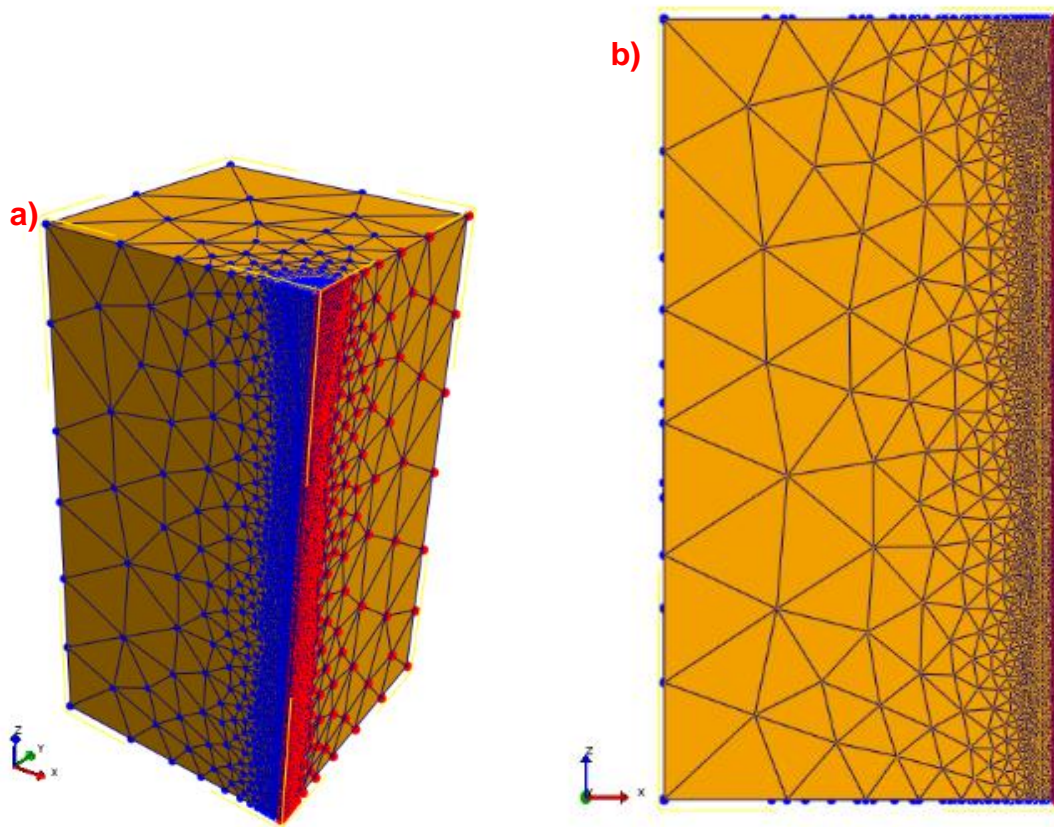


Figure 4-14 - Tetrahedron constraints showing the red nodes as the nodes constrained normal to the fracture plane

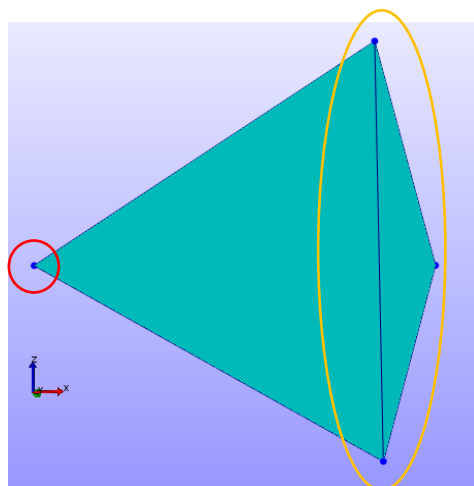
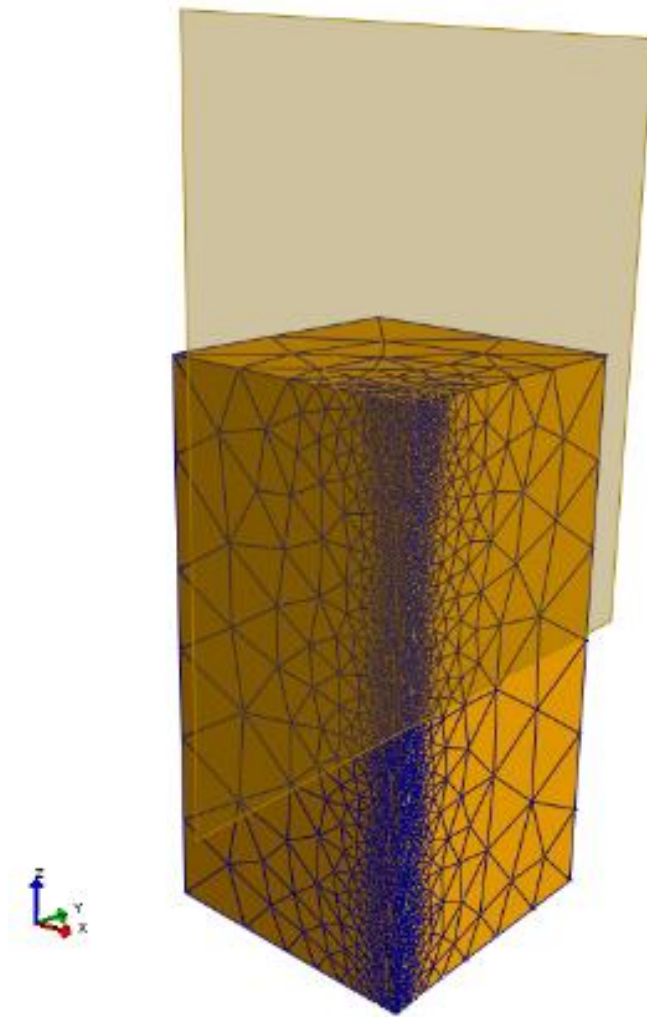


Figure 4-15 - A close up of a single tetrahedron, with the circled yellow nodes the nodes that are constrained normal to the fracture plane and the red circled node the node that is unconstrained and connected to the silicone

## Finite Element Analysis

The final model condition added to the simulation was a rigid wall against the fracture plane [Figure 4-16]. This ensured that when the silicone deforms, it behaves as if the model were a full model rather than just a quarter, preventing it from pushing past the fracture line.



*Figure 4-16 - The rigid wall that is used to recreate the conditions of a full silicone block without constraining the silicone wall fully*

### 4.3 Solution methods

As discussed previously, the two models studied are static and dynamic, both of which are dependent on different parameters. They also require different solvers and

## Finite Element Analysis

analysis steps. Table 4-5 details the analysis steps used for both FEMs, including the number of timesteps, the step size and the damping (if used).

*Table 4-5 - Analysis steps for the static and dynamic models, including the step sizes, solver applied and if damping was used*

<b>Model</b>	<b>Analysis</b>	<b>Time steps</b>	<b>Step size</b>	<b>Auto time step?</b>	<b>Solver</b>	<b>Damping</b>
<b>1</b>	Static	100	0.01	Default	Solid	N/A
<b>2</b>	Dynamic	2e6	1e-5	No	Explicit solver	0.9999

The low-deformation model utilised a static analysis solver, more specifically the solid solver. This solver was appropriate given the low level of displacement being investigated, where deformations remain small and quasi-static.

The dynamic model utilised the explicit dynamic solver within FEBio; this solver uses a lumped mass algorithm. A mass matrix explains how mass within the elements is distributed through the model. Using a 'lumped' algorithm simplifies these calculations to improve computational efficiency. This mass matrix is a diagonal matrix, explained by FEBio as one in which the off-diagonal terms which represent interactions between the different elements, are zero. There are two lumping matrices offered by FEBio currently, Row-Sum Lumping and HRZ-lumping [222]. For this model the Row-sum lumping method was used. This method is explained by FEBio [223], and for simplicity means the lumped mass at each node is the total mass that was originally distributed to that node and its neighbouring nodes. This is implemented by using 1 under Mass\_Lumping within the explicit solver tree of the steps section.

## 4.4 Model Studies

To investigate the dependencies of both the static and dynamic models an investigation into one parameter per model was conducted. This was also done to help match the load-displacement output of the FEM to the experimental data collected via

## Finite Element Analysis

the puncture tests in Section 3.4.3. For the static model, where it is not density dependent (previously discussed in Section 4.2.3) the bulk modulus was changed [Table 4-6].

*Table 4-6 - The parameter study for the static model with the bulk modulus density changes corresponding to the static model iteration*

<b>Static model Number</b>	<b>Bulk modulus Density (MPa)</b>
<b>1</b>	47.26
<b>2</b>	10
<b>3</b>	1
<b>4</b>	0.1

In the dynamic model, the load-displacement characteristics showed no dependency on the bulk modulus, as shown in Section 4.7.3, where varying K between 0.1 and 0.01 MPa did not change these characteristics compared to the static model and the experimental data. Therefore, for the dynamic model, the silicone density was adjusted rather than the bulk modulus, as shown in Table 4-7. While the static model, being non-density dependent, used a density of 1 kg/mm<sup>3</sup> the dynamic model required a reduced density of 0.01 kg/mm<sup>3</sup>.

For context, biological substances such as skin are referenced at around 1000 kg/m<sup>3</sup> due to the large amount of water within the material [224]. For explicit dynamic models increasing or decreasing the density is likened to adapting the damping of the model. For example, decreasing the density acts as an artificial dampener where the mass effects of the model are minimised to offer some stability. This can also minimise the inertia effects across the silicone, which can help create a static like model with some dynamic features. However, decreasing the density close to the real value of 1000 kg/m<sup>3</sup> (1x10<sup>-6</sup> kg/mm<sup>3</sup>) would increase model instability increasing the running time.

*Table 4-7 - The parameter study changes applied to the dynamic model silicone density*

<b>Dynamic Model Number</b>	<b>Silicone density (kg/mm<sup>3</sup>)</b>
<b>1</b>	1
<b>2</b>	0.1
<b>3</b>	0.01

## 4.5 Mesh convergence study

To determine the mesh that was chosen has a balance of computational cost versus solution precision, a mesh convergence study was conducted. A mesh convergence study is critical to ensure the accuracy and reliability of simulations. By systematically varying the mesh density and evaluating the results, the optimal mesh size that captures the essential details of the model can be determined. This process also helps identify and mitigate potential errors due to mesh dependency and can reveal model sensitivity to different levels of detail and critical regions that may require a higher resolution.

To decide on the mesh density, the minimum and maximum growth rate (how the mesh elements increase in size as they move away from the specified feature) in Salome was varied, as shown in Table 4-8. This then determined the number of elements and the corresponding minimum and maximum element volume within FEBio. Five meshes were generated as shown in Table 4-9; the minimum number of elements was in Mesh 1 3,108 which had just a single element under the needle tip. The results of this study are shown in section 4.7.1, and Mesh 4 was chosen for further investigation. It can be seen that as the number of elements increased, the computational time also increased, however, all results were returned within a reasonable time frame and thus the variable does not need to be considered further within this study.

## Finite Element Analysis

*Table 4-8 - Salome parameters for the mesh study, including the minimum and maximum size, fineness and growth rate for part one and part two*

Mesh ID	Part 1				Part 2			
	Max. size	Min. Size	Fineness	Growth rate	Max. size	Min. Size	Fineness	Growth rate
Mesh 1	0.2	0.0006	Moderate	0.3	0.005	0.0005	Moderate	0.3
Mesh 2	0.2	6e-5	Moderate	0.3	0.0005	0.0002	Fine	0.2
Mesh 3	0.2	6e-5	Moderate	0.3	5e-5	4e-5	Fine	0.2
Mesh 4	0.2	6e-5	Moderate	0.3	5e-5	2e-5	Very fine	0.1
Mesh 5	0.2	6e-5	Moderate	0.3	2.5e-5	5e-6	Very fine	0.1

*Table 4-9 - FEBio details for each Mesh studied, including minimum, maximum and average element size and the number of steps and corresponding computational time*

Mesh ID	No. of elements	Min element volume	Max element volume	Average element volume	Number of steps	Running time (s)
Mesh 1	3,108	1.40856e-12	2.32557e-09	1.61918e-10	16	2
Mesh 2	12,376	1.00241e-14	1.35407e-09	4.06626e-11	16	5
Mesh 3	107,640	6.70497e-15	1.5936e-09	4.67521e-12	17	60
Mesh 4	257,704	1.29647e-15	1.71566e-09	1.9527e-12	17	156
Mesh 5	484,496	8.74762e-16	1.12213e-09	1.03869e-12	25	752

The main area of focus for this mesh study was outputting the rigid body force, and comparing the load-displacement graphs to identify the mesh where the results stabilise. At this point the model should not be mesh dependent.

### 4.6 Error analysis

To evaluate the differences between the low and high deformation models, and the DVC results within Chapter 5, error analysis was performed to identify absolute errors

between the data inputs. The overall RMSE (root mean square), MAE (mean absolute error), and percentage errors were also calculated.

The step error is the absolute difference between the corresponding displacements in two distinct data sets for individual steps [225], shown in Equation 28

$$\text{Step Error}_i = |\text{Data1}_i - \text{Data2}_i| \quad 28$$

Where  $i$  is the step of the two data sets. The RMSE measures the overall magnitude of the error by computing the square root of the average of the squared step errors across all steps, Equation 29. This is particularly useful when large areas are more heavily penalised

$$\text{RMSE} = \sqrt{\frac{1}{n} \sum_{i=1}^n (\text{Data1}_i - \text{Data2}_i)^2} \quad 29$$

Where  $n$  is the number of steps. The MAE is the average of the absolute differences (or step errors) across all steps. It provides a straightforward interpretation of the average error magnitude, as shown in Equation 30

$$\text{MAE} = \frac{1}{n} \sum_{i=1}^n |\text{Data1}_i - \text{Data2}_i| \quad 30$$

## 4.7 Results

### 4.7.1 *Mesh study results*

To ensure the accuracy and reliability of the FEM, a mesh study was conducted to evaluate the effect of mesh densities on the displacement magnitude and force output. Five different meshes were analysed, each with varying levels of refinement [Table 4-8]. Figure 4-17 shows the load-displacement graphs for the five meshes investigated. Meshes 1 and 2 were excluded due to their excessively high force values, overestimating the stiffness of the silicone, with potential contacts not working efficiently due to the large elements. Meshes 3, 4 and 5 demonstrated similar trends in their overall force increase and displacement magnitude. Mesh 3 and Mesh 4 had overlapping load-displacement outputs; however, Mesh 4 was selected for subsequent simulations as it offers an optimal compromise between computational time and result precision, and a more ideal element size when considering its use within the dynamic model.

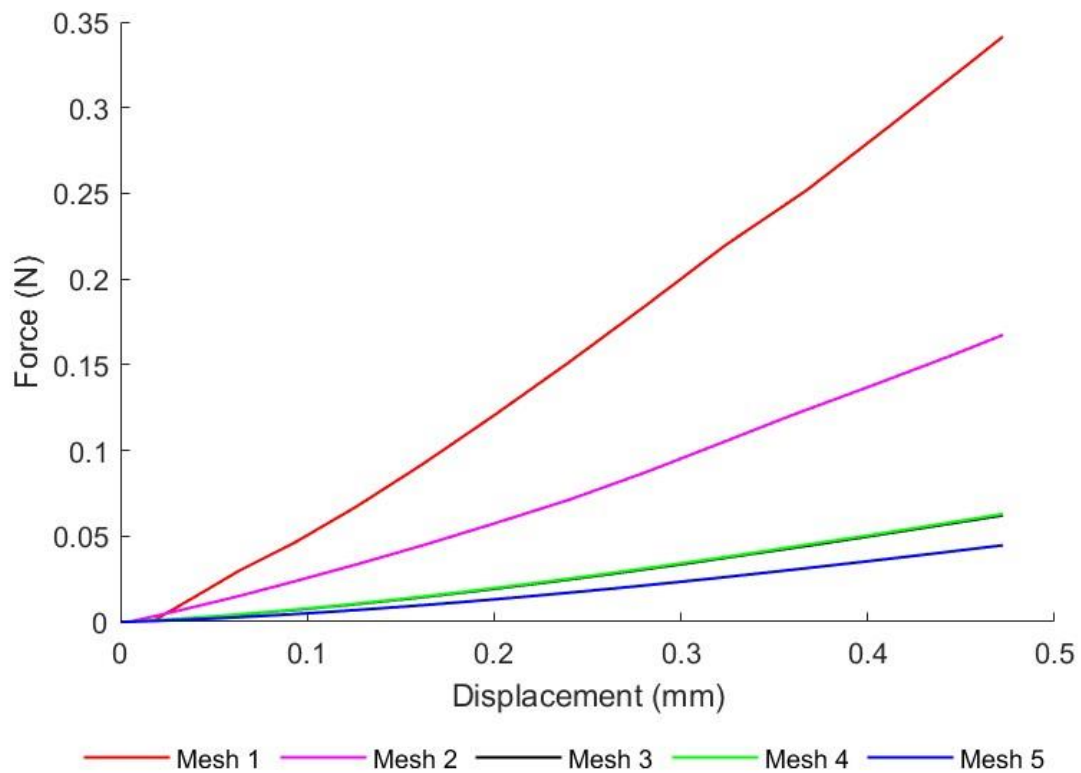


Figure 4-17 - The load-displacement results for the five meshes investigated. Mesh 3 and 4 are overlapped.

#### 4.7.2 Static model

The initial static model incorporated the Ogden material model parameters detailed in Section 2.2.3, with a bulk modulus of 47.6 MPa. However, as illustrated in Figure 4-18, the load-displacement curve (using mesh 4 from Figure 4-18) deviates from the experimental data obtained from the puncture test, as described in Section 3.4.3.

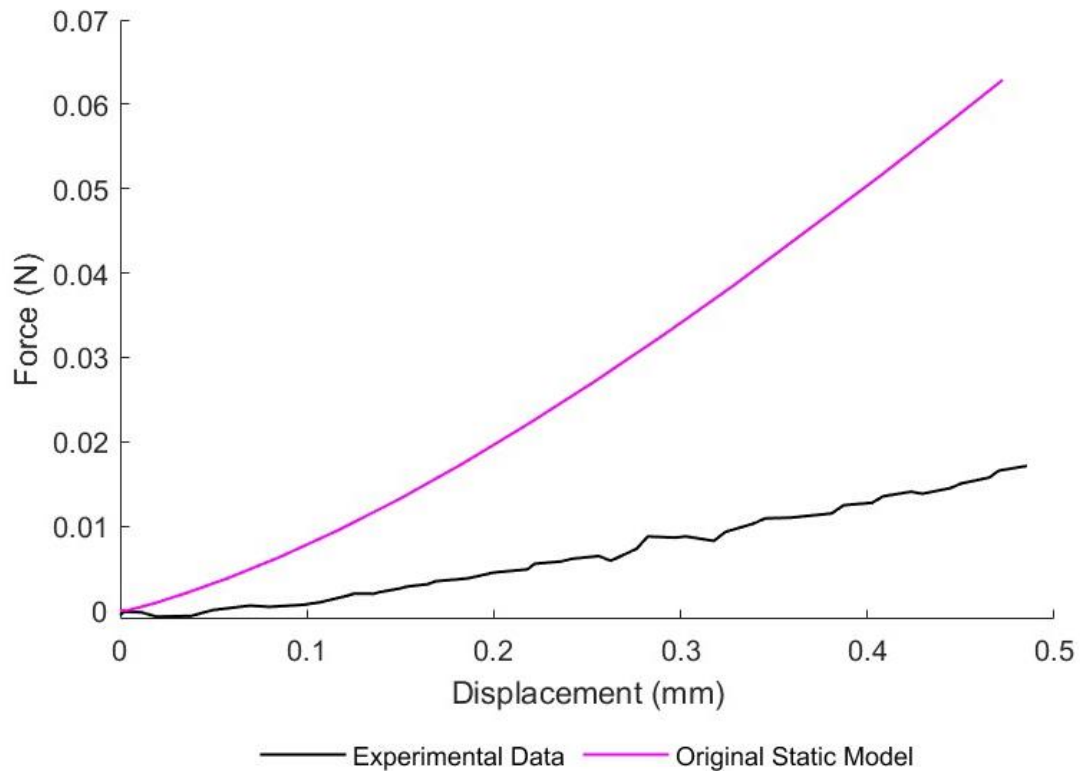


Figure 4-18 - The load-displacement data for the experimental data (from Section 3.4.3) and the static model with the original Ogden material model parameters

This mismatch suggests that the static model may not adequately capture the non-linear behaviour observed during the physical experiment, potentially due to limitations in the Ogden parameters used. To improve the correlation with the experimental results, alternative adjustments to the material model were investigated. Table 4-6 summarises the changes to the bulk modulus explored. Figure 4-19 illustrates the resulting load-displacement curves following these changes, compared to the original static model and the experimental data. The closest fit to the experimental data is observed when the bulk modulus is 0.1 MPa, suggesting that this value most accurately represents the material behaviour in the static model.

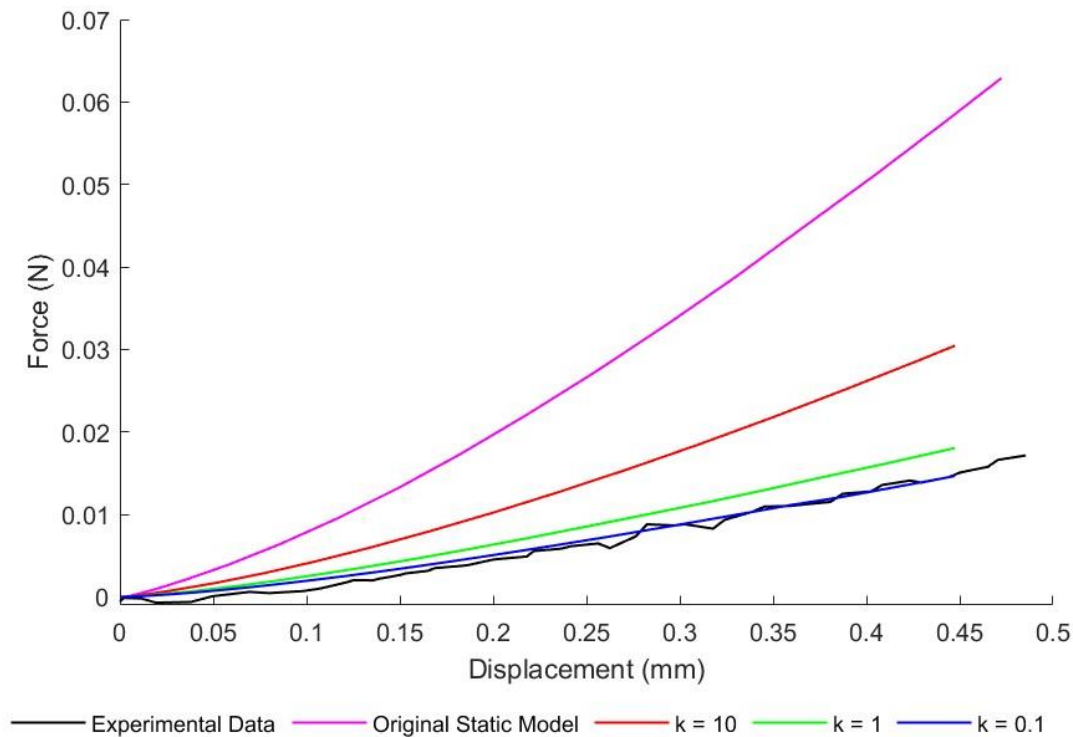


Figure 4-19 - The load-displacement data comparing the parameter changed, the bulk modulus, against the experimental data to find the best material model fit

In addition to the load-displacement curves, the individual components of displacement were also analysed. Displaying the displacement in its X, Y, and Z components, rather than the overall displacement magnitude, allows for direct comparison to the DVC results, as detailed in Section 5.3.4.

The colour scales used in the figures highlight regions of maximum compression and tension, with red representing the highest positive displacements and blue representing the largest negative displacements. The fracture line of the silicone is the origin, with the arrows of the axis showing the positive direction. These extremes provide a visual representation of the silicone's deformation in each plane.

The X component, illustrated in Figure 4-20, shows two distinct positive and negative fields on either side of the needle, with values ranging from 0.048 mm to -0.048 mm. The Y component of displacement displays a similar field pattern to the X component but in the Y plane. The displacement ranged from a maximum of 0.0393 mm to a

## Finite Element Analysis

minimum of -0.0475 mm around the needle tip. This suggests that the asymmetry of the needle affects the Y component more, as the displacement field radiates further through the silicone in this direction. A smaller cluster is also observed around the edge of the needle at the silicone's surface for both the X and Y components. However, the notable clustering of high displacement values near the needle tip suggests concentrated deformation in this region, reflecting the material's response to the localised force applied by the needle.

The Z component of the displacement, however, reveals a more homogeneous and symmetrical displacement field across the X and Y planes, despite the needle's asymmetry. The minimum displacement in the Z component is -0.373 mm [Figure 4-20 c)]. Compared to the X and Y components, this suggests that the silicone's deformation is more heavily influenced by the Z component and that the material undergoes more uniform compression along the Z axis.

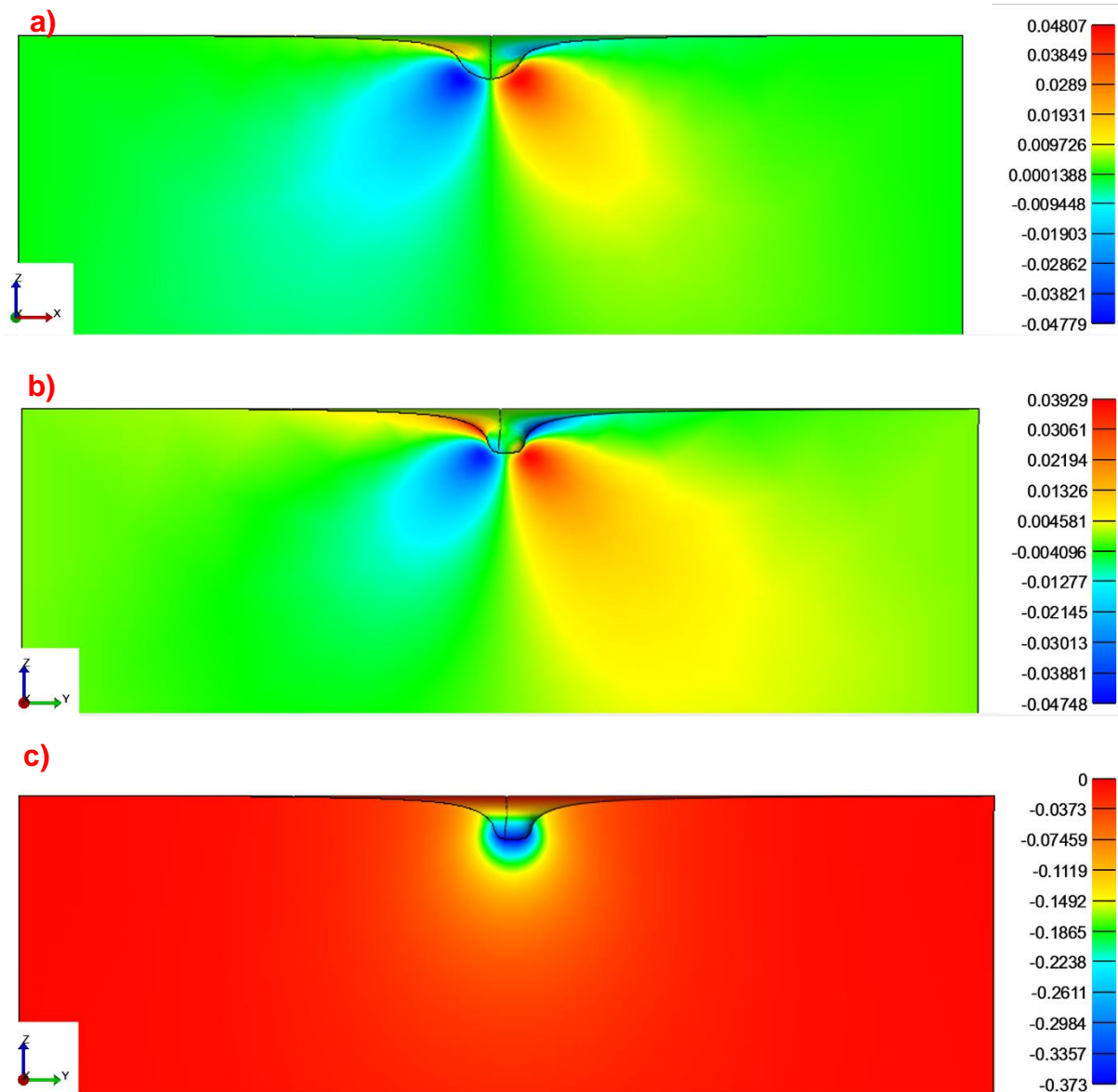


Figure 4-20 - The components of displacement for the static model, X component a) Y component b) Z component c)

The normalised Lagrange strain is shown in Figure 4-21 a) to c), and the shear Lagrange strain in Figure 4-22 a) to c). This allows for the visualisation of material behaviour and identification of which component represents the maximum deformation caused by the needle. It is important to note that these strains are Lagrange strains, meaning they are measured in directions that rotate with the material rather than in a fixed local x, y, z directions.

## Finite Element Analysis

$E_{xx}$  and  $E_{yy}$  have a maximum deformation of 0.4794 and 0.4856, respectively, with minimums of -0.07972 and -0.06873. In comparison,  $E_{zz}$  has a maximum of 0.0181 and a minimum of -0.3966, indicating that the majority of the compression is attributed to the  $E_{zz}$  component. Visually, the normal strain is concentrated around the needle tip.

On the other hand, the shear strains are significantly lower, with  $E_{xy}$  range from 0.1173 to -0.1179,  $E_{yz}$  from 0.2424 to -0.2442, and  $E_{zx}$  from 0.2256 to -0.2246. All three components exhibit symmetry in the numerical results between the minimum and maximum values. Additionally, there is a visual comparison of each component through the X and Y planes. The  $E_{yz}$  and  $E_{zx}$  components show bands of compression and tension around the needle edge highlighting that these two components are most affected by the needle indentation, which could be directly compared to the experimental results in Section 5.3.4.

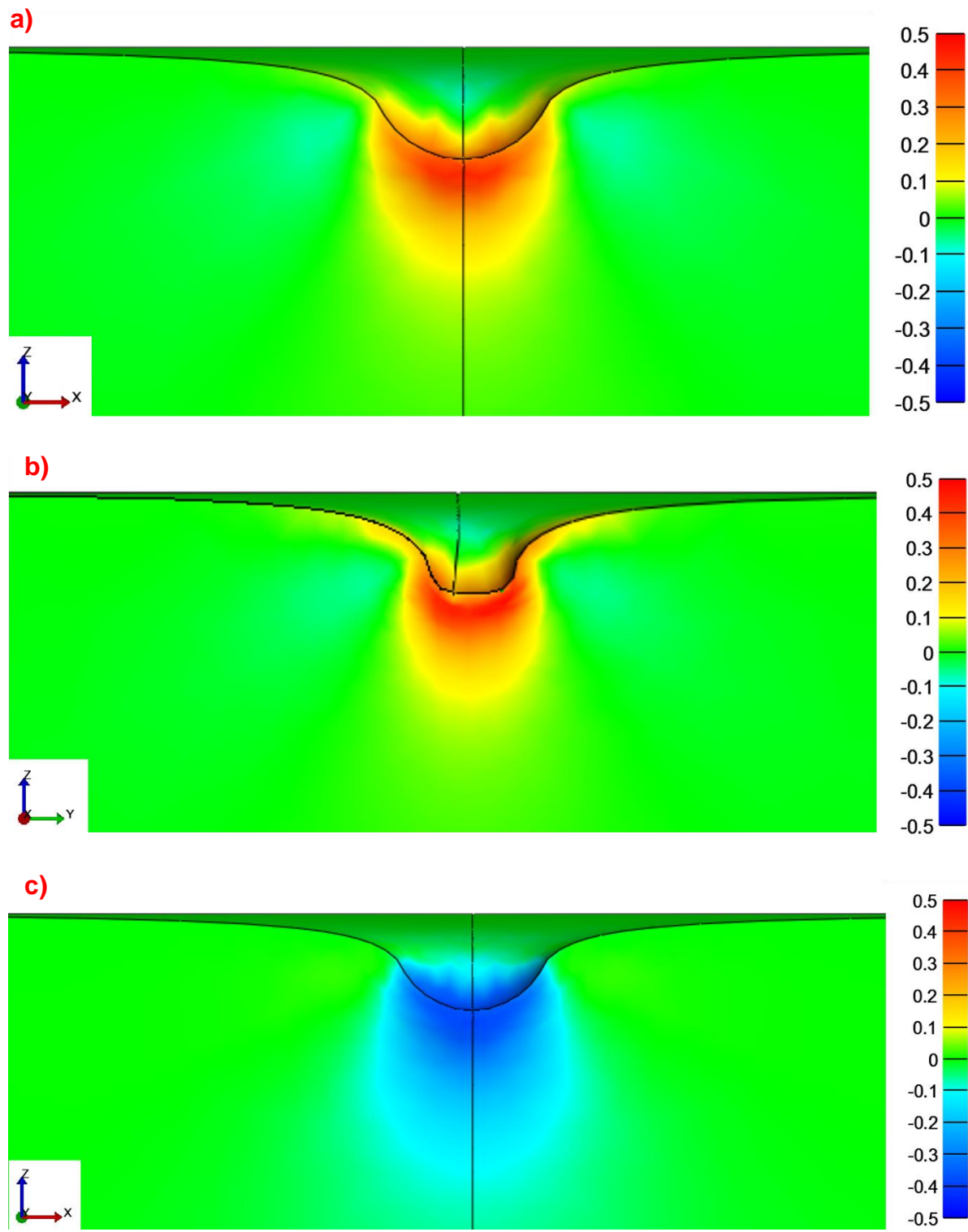


Figure 4-21 - The components of normal Lagrange strain for the static model,  $E_{xx}$  component a)  $E_{yy}$  component b)  $E_{zz}$  component c)

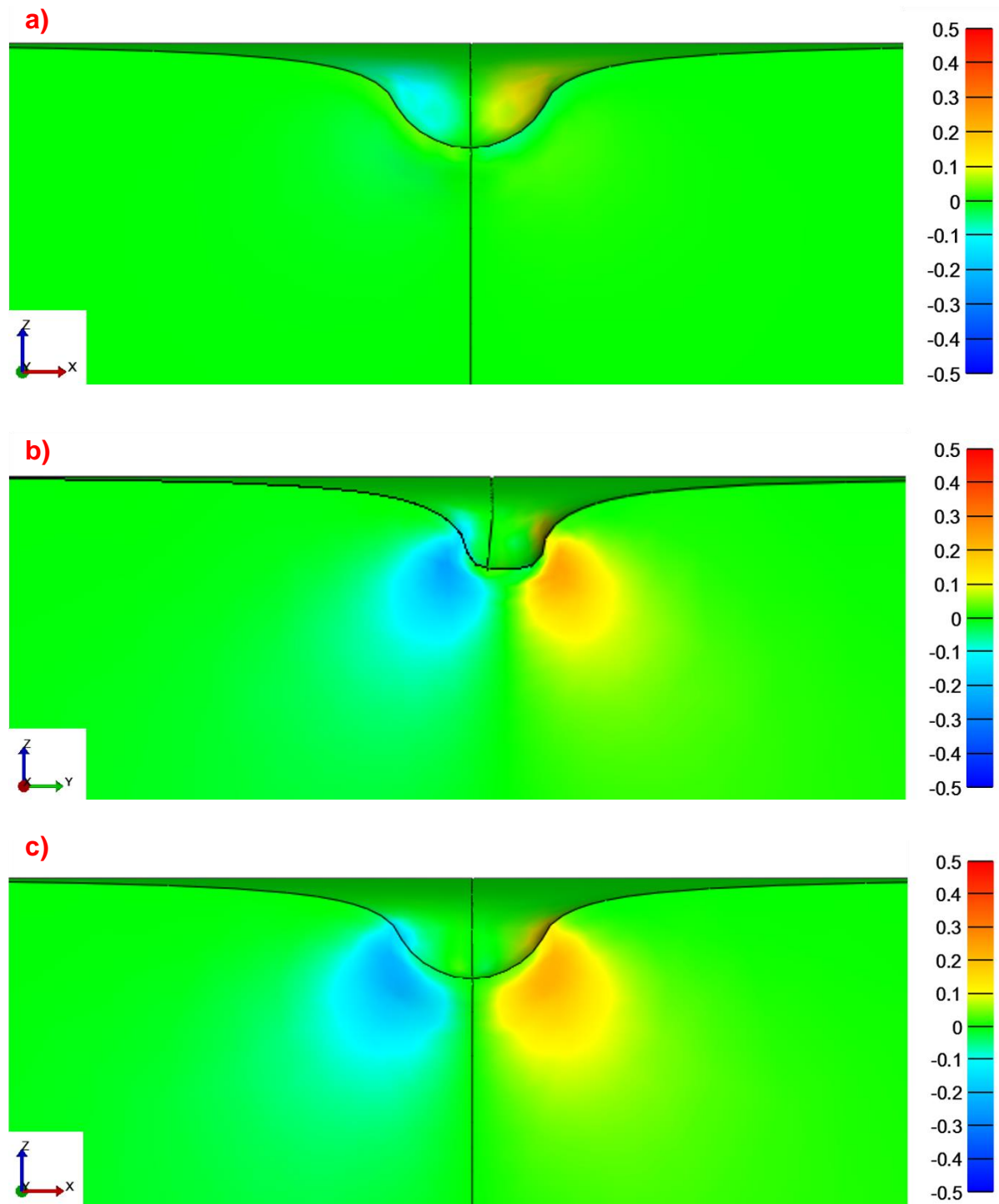


Figure 4-22 - The components of shear Lagrange strain for the static model,  $E_{xy}$  component a)  $E_{yz}$  component b) and  $E_{xz}$  component c)

### **4.7.3 Dynamic model**

Although the static model provided insight into the material's deformation under steady state conditions, it was limited in handling the large deformations and unstable tearing associated with needle penetration. To overcome these challenges, a model using an explicit solver was developed. The explicit solver was chosen because it handles complex, non-linear behaviour such as the high deformation and tearing in the silicone that the implicit solver could not manage effectively. This model was not designed as a full dynamic analysis of time-dependent or inertial effects, as realistic density and damping values were not applied. Instead, the explicit solver provided a stable framework for evaluating load-displacement behaviour and capturing detailed displacement fields despite the computational difficulties posed by large deformations. The influence of parameters such as bulk modulus, density, and the inclusion of cohesive zone methods and WoF values have on the load-displacement behaviour and visual displacement fields were also investigated

Firstly, to investigate the parameters the dynamic model is dependent on, two bulk modulus values and two densities were investigated as outlined in Section 4.4. It can be observed that changing the bulk modulus from 0.1 MPa, as used in the static model, to 0.01 MPa had little effect on the load-displacement curve of the dynamic model. Therefore, two densities were compared. Initially, a density of 1 kg/mm<sup>3</sup> was used, as in the original static model, and then decreased to 0.1 kg/mm<sup>3</sup> and 0.01 kg/mm<sup>3</sup>. These two densities, as shown on Figure 4-23, slightly overestimate and underestimate the load-displacement characteristics, respectively. However, it was determined that a density of 0.1 kg/mm<sup>3</sup> was sufficiently close to the experimental values to proceed with this parameter.

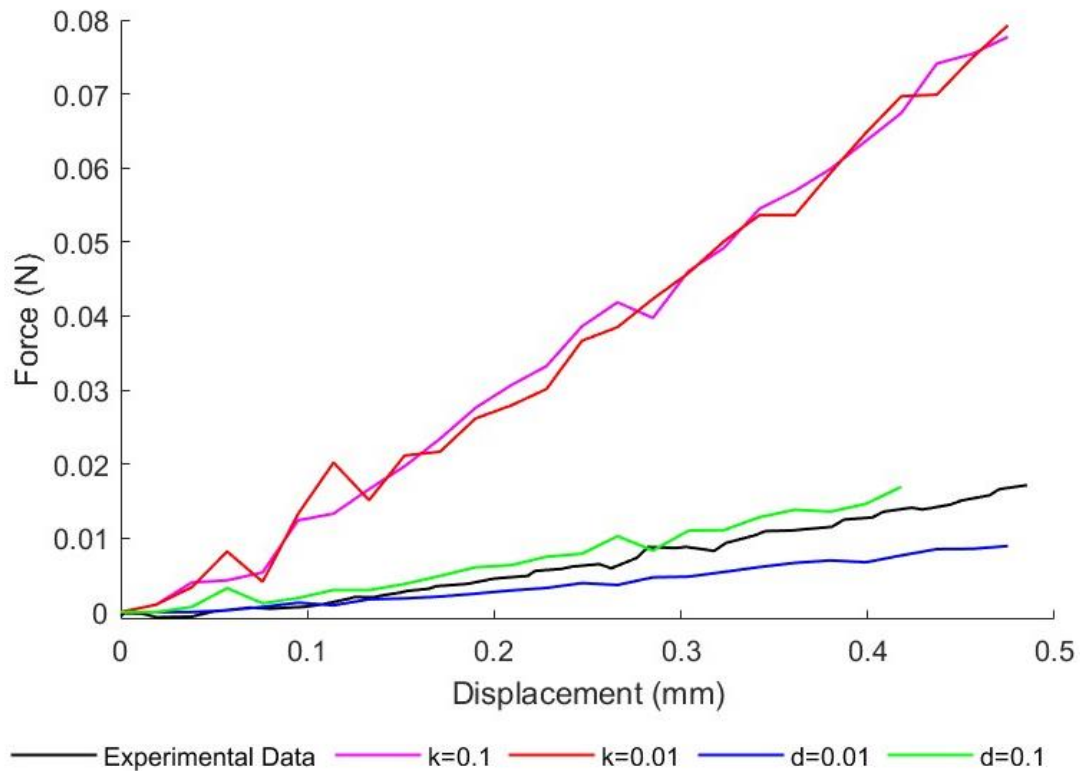
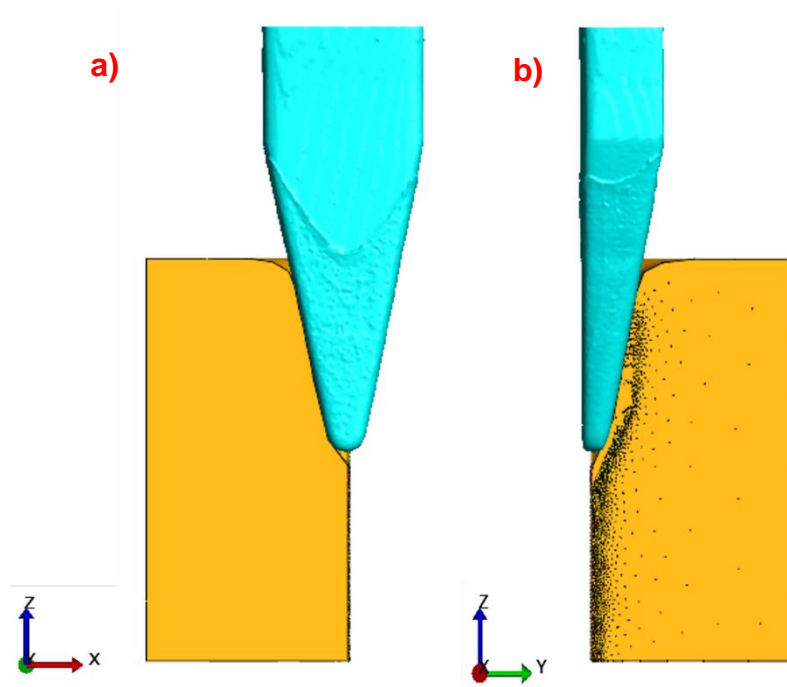


Figure 4-23 - The load-displacement results for the dynamic model parameter study, showing the change with the bulk modulus and the density (in  $\text{kg}/\text{mm}^3$ ) to reach the experimental output

As explained in Section 4.2.2, the dynamic model utilised the same mesh as the static model, allowing for direct comparison of the outputs. Initially, the model was run to the maximum displacement achievable with the parameters in Table 4-1 and Table 4-6. Visually, the stability of the mesh can be assessed based on when the model becomes mesh-dependent. Figure 4-25 a) and b) show the indentation of the segmented needle up to a displacement of 3.8 mm, without the mesh visible to highlight the deformation around the needle. Figure 4-25 a) and b) provide an isometric view of the full displacement magnitude of the needle with and without the mesh. It is evident that the elements surrounding the needle tip are overstretched and no longer deform properly. Additionally, Figure 4-25 c) and d) shows the front and side view of the mesh without the needle visible, highlighting the compression of the elements beneath the needle tip and the stretching of the needle surface elements around the sides of the needle.

## Finite Element Analysis



*Figure 4-24 - The results from the maximum displacement reached by the dynamic model, of 3.8 mm, showing the instability of the mesh and needle placement. The front view a) and side view b) with the needle.*

Finite Element Analysis

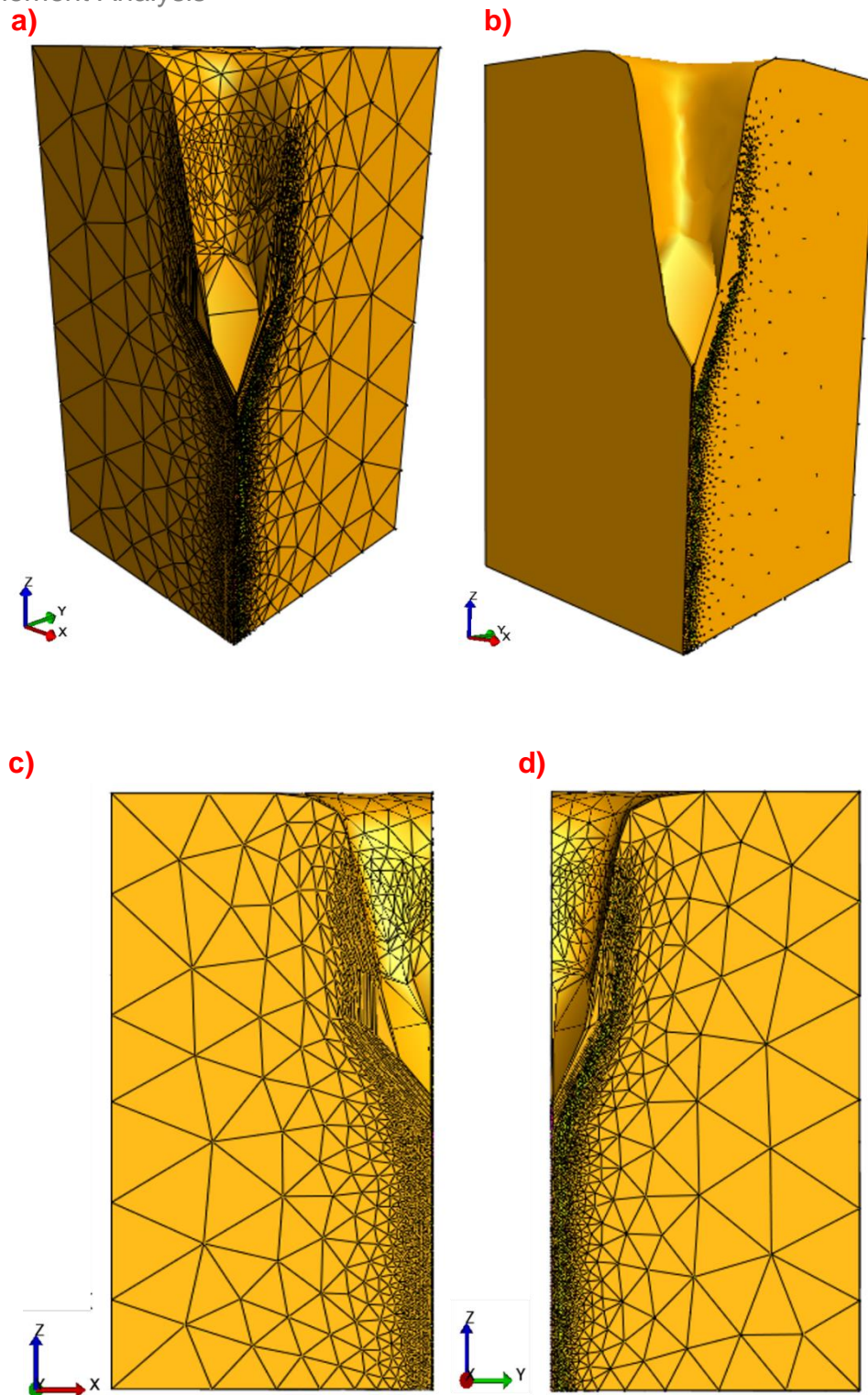


Figure 4-25 - The results from the maximum displacement reached by the dynamic model, of 3.8 mm, showing the instability of the mesh and needle placement. The isometric view of just the silicone with the mesh a) and without the mesh b). The front view without the needle c) and the side view without the needle d)

## Finite Element Analysis

The components of displacement were exported from FEBio to view the displacement fields at the maximum point of indentation displacement observed in this model. The original model was created as a quarter, so to visualise the model as a half, a mirror plane was used within FEBio for the X and Z components, given the needle's symmetry in the X plane. Figure 4-26 show these displacement fields. The X component displacement field shows a region of high strain around the silicone surface near the needle edge, with a minimum -0.8067 mm. in comparison, the Y component has a maximum of 0.7069 mm behind the needle. The Z component, illustrated in Figure 4-26 c), shows a more symmetrical displacement around the full needle to silicone surface contact, with a minimum of -4.099 mm around the needle tip.

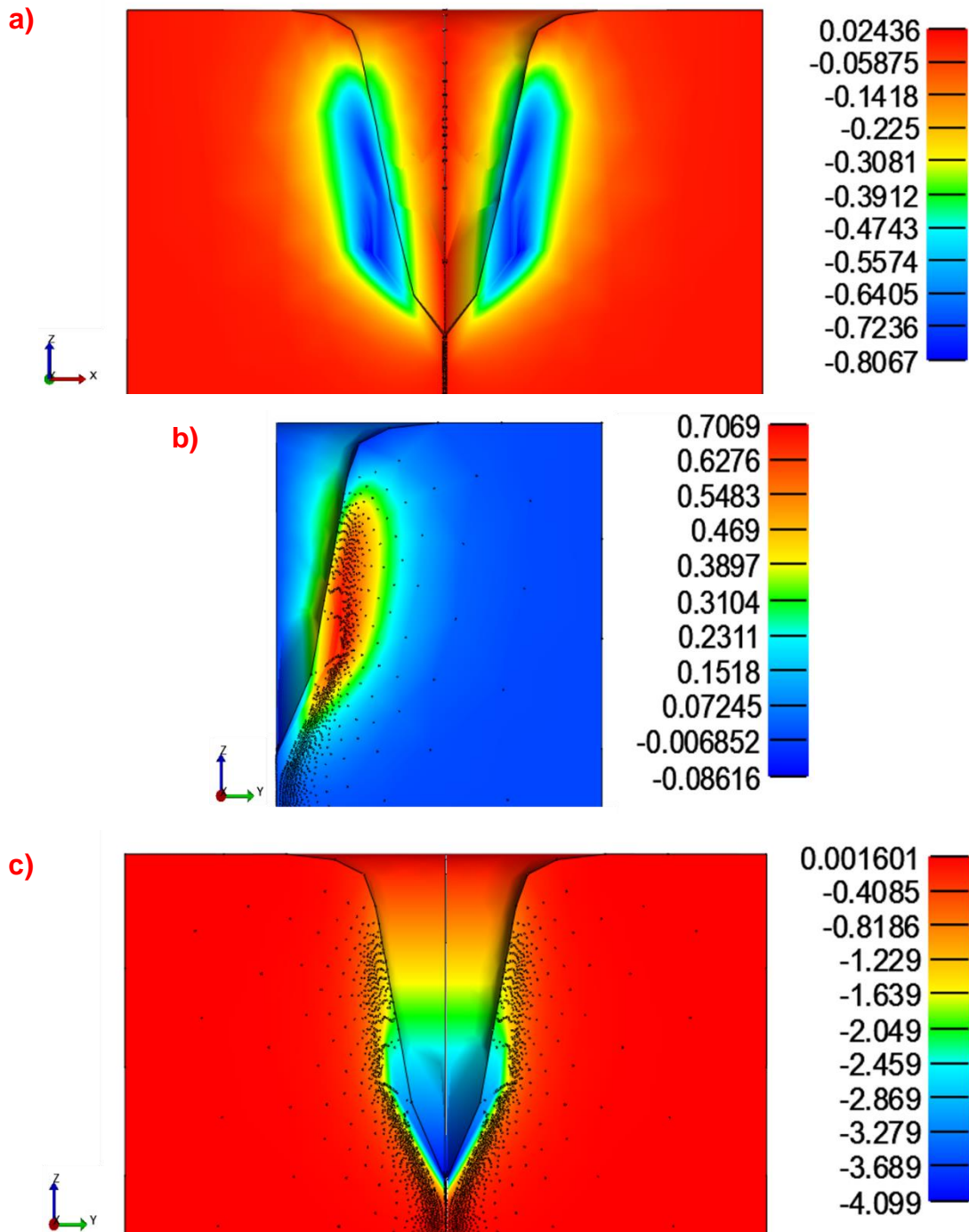


Figure 4-26 - The components of displacement maps for the dynamic model at the maximum needle displacement of 3.8mm, with a mirrored view along the plane of needle symmetry. X component a) Y component b) Z component c)

The next step in validating this model was the comparison with the puncture experiment. This dynamic model successfully ran to 0.38 mm of displacement, so the experimental data was similarly truncated for comparison. As shown in Figure 4-27,

## Finite Element Analysis

the initial load-displacement characteristics were overestimated; however, as the needle displacement increased, the load-displacement curve began to align with the experimental data. Despite this, the mesh dependence became evident around 2mm of displacement. This dependence is reflected in the jagged nature of the load-displacement curve, and is highly likely to have caused the model to fail to converge further to the full 8 mm displacement set for the simulation.

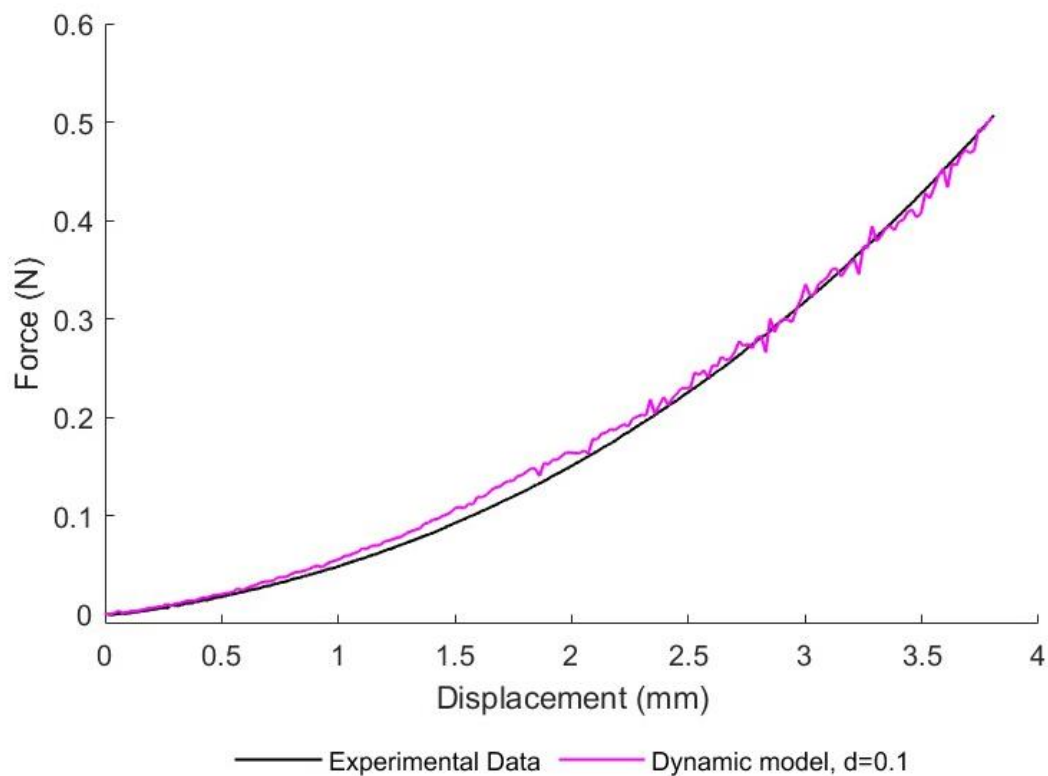


Figure 4-27 - The load-displacement curve of the dynamic model with the silicone density of  $0.1 \text{ kg/m}^3$  used, and the experiment data

Table 4-10 shows the error analysis calculations between the dynamic model and experimental puncture data for both displacement and force. The RMSE for the displacement outputs was 1.0467 mm whilst for the force outputs, it was 0.1604 N. Similarly, the overall MAE was 0.9097 mm for the displacement and 0.1257 N for the force. These errors may be attributed to the jagged load-displacement curve observed in Figure 4-27.

Table 4-10 - Table showing the RMSE, MAE for the results in Figure 4-27, comparing the experimental displacement and force with the dynamic model to 3.8 displacement magnitude

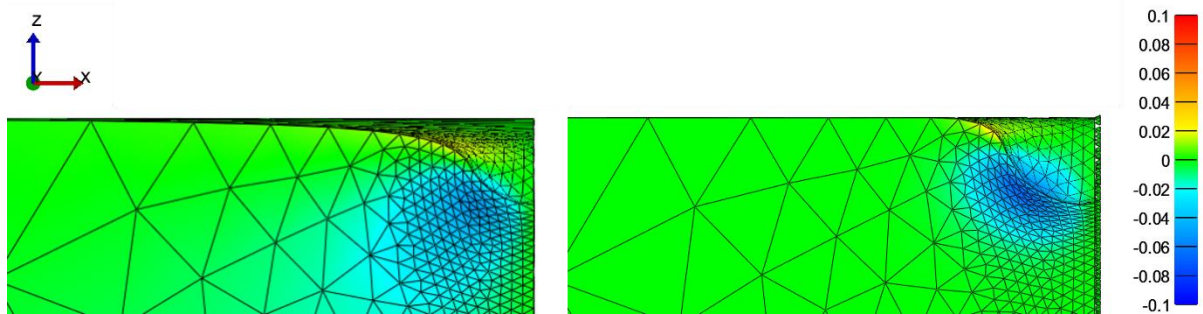
<b>Input data 1</b>	<b>Input data 2</b>	<b>RMSE</b>	<b>MAE</b>
<b>Dynamic model displacement</b>	Experimental displacement	1.0467 mm	0.9097 mm
<b>Dynamic model force</b>	Experimental force	0.1604 N	0.1257 N

#### 4.7.4 Comparison of static and dynamic models

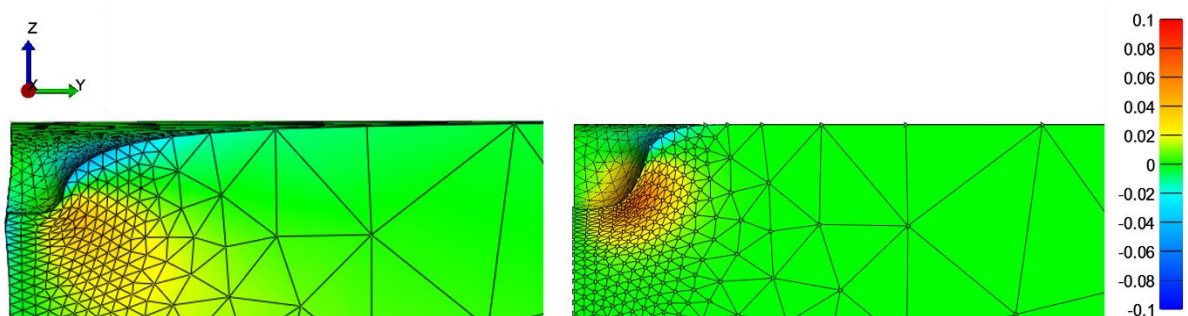
To compare the dynamic model to the static model, the components of displacements at the closest step to the experimental displacement magnitude (0.38 mm) were outputted. As detailed in Section 4.7.3, a mirror plane was used to facilitate comparison of the displacement fields for the X and Z components. Figure 4-28 a) shows the X component of displacement, which ranges from 0.02765 mm, at the needle tip edge, to -0.06699 mm, at the silicone surface. The Y component, Figure 4-28 b)], displays a main cluster of displacement at the back of the needle tip, with a maximum displacement of 0.06289 mm and a minimum of -0.03106 mm at the silicone surface. The Z component, shown in Figure 4-28 c), exhibits symmetry along the Z plane with a displacement of -0.38 mm directly beneath the needle tip, indicating that the Z component is primarily responsible for the vertical compression of the silicone.

## Finite Element Analysis

a)



b)



c)

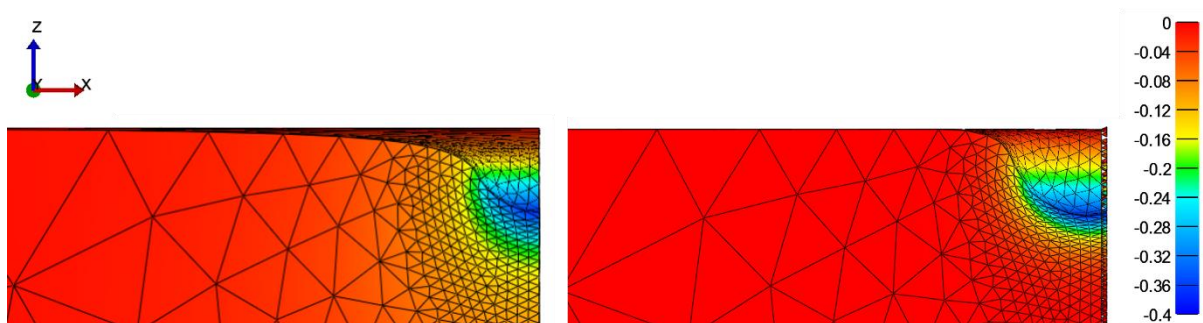
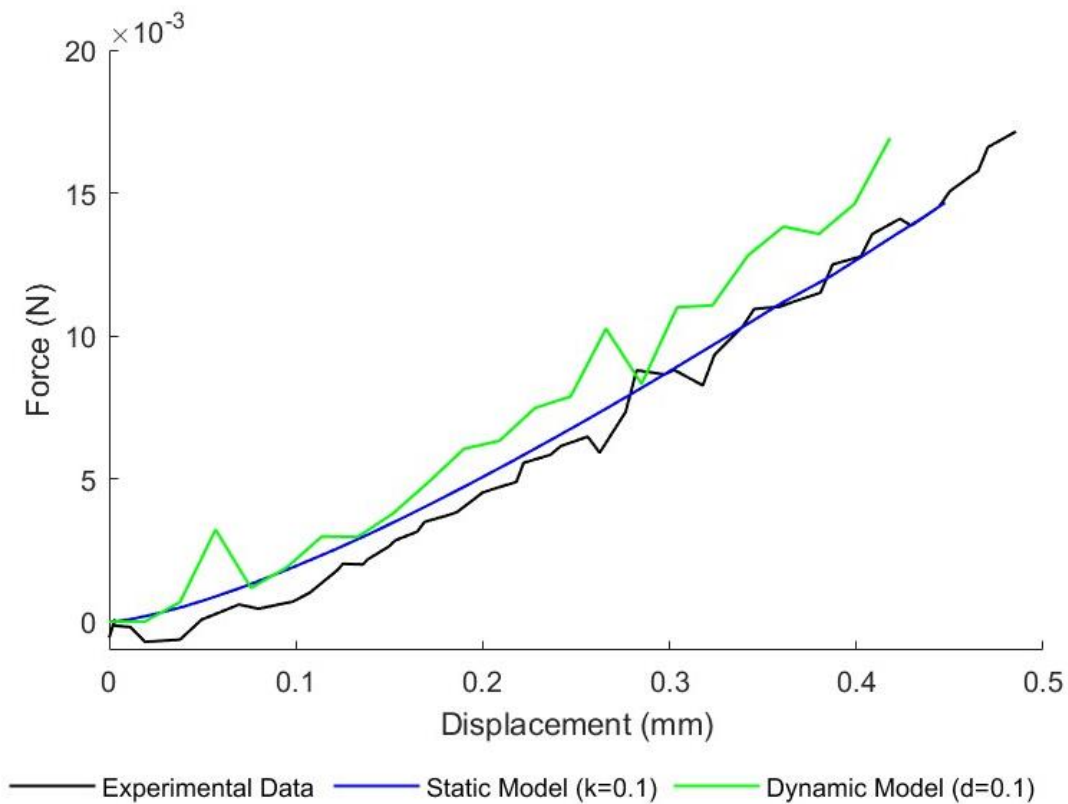


Figure 4-28 - The component of displacement fields for the static and dynamic model (left and right respectively) at the needle displacement of 0.38 mm, similar to that of the static model needle displacement. X component a) Y component b) Z component c)

Lastly, to highlight the differences between the static model, dynamic model, and the experimental puncture results, the load-displacement curves for all three were plotted on Figure 4-29. The static model, represented by the blue line, shows an almost linear load-displacement curve which matches the experimental data reasonably well from approximately 0.2 mm onward. In contrast, the dynamic model, the green line,

## Finite Element Analysis

overestimates the load-displacement behaviour, with the exception of one point at around 0.275 mm where it briefly aligns with the experimental data.



*Figure 4-29 - The load-displacement curves for the final static and dynamic models used within this study*

To calculate the error between the load-displacement outputs observed in Figure 4-29, the RMSE, MAE, and percentage error for the force and displacement data between the static model, dynamic model, and experimental puncture results are presented in Table 4-11. The static model compared to experimental data has an RMSE of 0.1008 mm and an MAE of 0.0733 mm for displacement, while the force shows an RMSE of 0.0043 N and an MAE of 0.0034 N. The experimental to dynamic results show increased RMSE and MAE values for displacement, at 0.1462 mm and 0.1372 mm, respectively. The force results also exhibit higher errors, with an RMSE of 0.0072 N and an MAE of 0.0063 N. When comparing the static and dynamic models, the displacement errors are 0.0998 mm for RMSE and 0.0986 mm for MAE, with force errors of 0.0049 N and 0.0046 N. Overall, the lowest error is for the experimental and

static model displacement, while the dynamic and experimental results show the highest error for the force data.

*Table 4-11 - Table showing the RMSE, MAE for the results in Figure 4-29, comparing the experimental displacement and force with the static model, the dynamic model, and the comparison between the two models*

<b>Input data 1</b>	<b>Input data 2</b>	<b>RMSE</b>	<b>MAE</b>
<b>Experimental displacement</b>	Static model displacement	0.1008 mm	0.0733 mm
<b>Experimental force</b>	Static model force	0.0043 N	0.0034 N
<b>Experimental displacement</b>	Dynamic model displacement	0.1462 mm	0.1372 mm
<b>Experimental force</b>	Dynamic model force	0.0072 N	0.0063 N
<b>Static model displacement</b>	Dynamic model displacement	0.0998 mm	0.0986 mm
<b>Static model force</b>	Dynamic model force	0.0049 N	0.0046 N

## 4.8 Discussion

This study focuses primarily on the computational modelling of needles, which could potentially aid in the development of clinically available MNs. This area of research is growing in popularity, with numerous approaches to needle puncturing being published. However, despite extensive research, a common theme in these publications is the recognition of limitations that remain widespread, as discussed in Chapter 2.6. In this study, a prospective experimental validation for computational modelling is outlined in Chapter 5, and, therefore, a simple, low-strain model was designed as a proof of concept. As discussed later in Chapter 5.2.4, certain elements of this model, such as the needle and silicone mesh, were also used in parts of the data processing for the DVC, including the interpolation of the raw DVC results, so that the data could be directly compared with the models created within this chapter.

The geometry of the silicone was created in SolidWorks and meshed within Salome. The silicone geometry was used for both the static and dynamic models discussed in this chapter, with the mesh chosen in Section 4.2.2 similarly applied to both models. The main difference with the silicone geometry was that a full silicone block was used for the static model, where as the dynamic model benefitted from modelling only a

quarter of the block. This was due to computational limitations and allowing for the fracture boundary conditions to be incorporated without excessive computational demand. The needles were both derived directly from the CT scans conducted in Section 3.4.6. Segmenting the needle geometry from the scans, instead of using the original SolidWorks files, allowed the needles to reflect the exact dimensions observed and facilitated alignment with the DVC data, as explained in Section 5.2.

Additionally, a further similarity between both models was the contacts used between the needle and the silicone. A simple facet-on-facet sliding contact was employed to enforce a non-penetration constraint in the model, with the penalty factor set to 100 for the static model and 10,000 for the dynamic model.

The material properties were experimentally determined in Chapter 3.4. This utilised the Ogden material model, with the parameters outlined in Table 4-1. The static model is not density-dependent, so the density was left at the default of 1 kg/m<sup>3</sup>, with the bulk modulus at 47.26 MPa. However, when comparing this model's load-displacement curve to the experimental data, as shown in Figure 4-18, the discrepancy is quite significant. Therefore, a small parameter investigation was conducted to identify the property that the model is dependent on and how that parameter needed to be adjusted. As shown in Figure 4-19, the static model was dependent on the bulk modulus of the silicone, with a reduction to 0.1 MPa allowing the load-displacement curve to accurately fit the experimental data, at least at low strains. The choice to adjust the bulk modulus, rather than the shear modulus, was intended to reduce the material's overall stiffness in the model to compensate for the inherent stiffness of the mesh. This adjustment allowed for the displacement and strain fields to be visually inspected, allowing for further comparison with the DVC data in Chapter 5.3.

The components of the displacement fields, illustrated in Figure 4-20, show distinct patterns radiating through the silicone from the tip of the needle to the body of the silicone. The X component has a maximum of 0.04807 mm, while the Y component has a maximum of 0.03829 mm, indicating that the static FEA shows greater deformation in the X direction, which is attributed to the asymmetrical shape of the needle used, which has a slope which influences how the strain is distributed through the silicone. This is also visible in the shape of the deformation around the needle in

these figures. The deformation can also be described in terms of the normal and shear strains shown in Figure 4-21 and Figure 4-22. These are discussed in relation to DVC comparison in Chapter 6.

The  $E_{xx}$  and  $E_{yy}$  strain fields exhibit noticeable symmetry around the needle tip, indicating relatively uniform deformation in these directions in tension. Additionally, as the regions of maximum strain for  $E_{zz}$  are radiating further from the needle tip, it suggests that the silicone is compressed directly beneath the needle tip, predominantly in the Z direction. The shear strains also show a clear symmetry around the needle tip, indicating a uniformity of shear strain distribution with balanced regions of compression and tension. The bands of tension and compression around the edge of the needle further highlight that the needle edges influence the indentation. However, as the shear strain magnitudes are lower than the normal strain, this suggests that, while shear strain is present during the deformation, it plays a secondary role to the normal strains and compression mechanisms. It also suggests that the asymmetry of the needle leads to a non-uniform shear stress distribution for  $E_{yz}$  and  $E_{xz}$ . Visually, these bands of compression and tension can be observed in the DVC images further discussed in Chapter 5.4.

While the creation of a simpler static model allowed for the analysis of the material's deformation under steady-state conditions in a computationally efficient manner, it could not capture the tearing behaviour that occurs during needle penetration. Static models are generally suitable for slow processes or steady-state conditions, but the high deformation and instability associated with tearing require a more specialised approach. Therefore, a dynamic model incorporating a cohesive zone method, initially developed by M. Potts at Cardiff University, was investigated. This model is not intended to simulate traditional dynamic effects like inertia or time-dependent mass damping. Instead, the explicit solver in this model enables stable simulation of larger deformations and material tearing by adjusting certain parameters, such as density, to reduce the stiffness and minimise instabilities. To justify these parameter adjustments, comparisons were made between static and explicit dynamic models, showing consistent deformation patterns. This approach allows the model to better represent silicone behaviour at larger deformations, even though realistic dynamic parameters such as actual material density were not directly applied. The deformation behaviours

can then be initially compared with the outcomes of the second set of  $\mu$ -CT scans in Section 5.1, to evaluate the effectiveness of this approach over static modelling.

The development of this cohesive zone method, which incorporates the WoF experimental outputs from the tear tests completed in Section 3.4.5, allows for an additional set of material characteristics to be added to the fracture plane, accounting for more realistic material behaviour than methods such as element deletion. Published FEAs by Chen [20], Kong [28], and Shu [19], while using experimental load-displacement data to influence the needle insertion, delete elements within the material based on a von Mises stress criterion, resulting in a non-realistic representation of the needle insertion process. This process is outlined by Oldfield [17] and Davis [10], and is said to have at least one phase of indentation before the material tears to allow needle penetration. While the length of this first phase depends on the material's properties and size, as well as the needle size, these element deletion FEMs shorten this phase. In addition, due to the nature of the element deletion criterion used, the needle could puncture before the expected insertion point, with little to no indentation phase, leading to an overestimation of needle insertion criteria such as Von Mises stress, skin strain or the prevention of needle penetration [17], [19], [20], [26], [27], [28], [204].

However, the dynamic model developed in this study is still in its infancy and this study represents an early-stage attempt to capture the behaviour of silicone under large deformations. Whilst it has been useful in providing initial insights, there are fundamental limitations with using FEM to simulate extreme deformations accurately, especially those approaching material failure. As deformations become large, FEM models face issues such as mesh distortion, numerical instability and convergence challenges that can increase when tearing or puncture behaviour is introduced. For complete validations against DVC data, further development and refinement is required. However, it is likely that a purely finite element approaches may never fully capture such large-scale deformations. Alternative approaches, such as combining FEM with mesh-free methods or adaptive remeshing could offer more realistic results.

As a result, the FEM can currently be examined in three ways: first, by comparing the output data to the static model and the DVC data at small displacements and strains;

## Finite Element Analysis

second, by assessing the stability of the FEM up to its current maximum displacement; and finally, by exploring how it could be improved to achieve a displacement of 8 mm. Finally, as the maximum displacement reached is 3.8 mm, and the first step of the  $\mu$ -CT scans was 3 mm, the initial states of the FEM can be validated.

The comparison of the needle displacement to 0.375 mm for the dynamic model, as used for the static model to observe low deformations, shows a good similarity of displacement fields through the silicone. The fields for each component of displacement are positioned in the same locations and focused on the same points of the needle at the final displacement step. For example, in the X component, both models show an area of tension around the edge of the needle tip radiating through the silicone, and a small area of compression at the rounded, deformed edge of the silicone. However, there is a large numerical difference between the maximum and minimum displacements of the two models, at a 42.5% and 39.6% difference, respectively. Similarly, the Z component of displacement shows the same areas of positive and negative displacements around the needle tip and rounded silicone edge, with differences of 60.1% and 34.6%, respectively. However, the static model noticeably radiates the displacement fields through the silicone, a behaviour not seen in the dynamic model. While the fields are equally symmetrical in both models, the static model suggests that elements at least double the distance from the needle tip, compared to the dynamic model, are displacing around -0.15 mm. This could be due to the implicit solver, which determines the stable configuration by accounting for all forces at once, leading to broader displacement propagation compared to the dynamic solver.

Another reason for the differences could be due to the changes in material model properties. Initially, the dynamic model was run with a density of 1 kg/mm<sup>3</sup>, as used in the static model. The bulk modulus was also set to 0.1 MPa, as determined by the parameter study for the static model. However, with these parameters, it was found that the dynamic model exhibited significant differences in the load-displacement curve compared to the static model and experimental data. Therefore, another material model parameter study was conducted, this time adjusting the density. The density was changed because, during the initial adjustment of the bulk modulus, it was found that the FEM was not dependent on the bulk modulus. When the density was

## Finite Element Analysis

reduced to  $0.1 \text{ kg/mm}^3$ , there was a slight overestimation of the load-displacement when compared to the experimental data, as shown in Figure 4-23. However, further reducing the density to  $0.01 \text{ kg/mm}^3$  significantly underestimated the load-displacement characteristics after 0.15 mm.

While there are some visual differences, Figure 4-29 shows the differences in the load-displacement curves of the static and dynamic models compared to the puncture experiment. The static model shows a smooth curve, while both the dynamic and experimental curves are jagged. Experimentally, this could suggest some noise artefacts, especially at the low loads measured, this could be mitigated by using a smaller load cell than the 10 N load cell used in the puncture experiments. Computationally, there could be several reasons for the non-linear load-displacement curve compared to the static model. The most likely cause is the mesh and contacts used, with bumps introduced due to the flat elements being pulled around the curved edges of the needle. Overall, though, both models show good agreement at low displacements.

As previously stated, this has achieved a maximum indentation displacement of 0.38 mm, just under half of the experimental displacement to which the needle was found to indent. Due to this, only initial comparisons with the raw DVC data can be made, as the first DVC step was to 3.5 mm. When comparing the load-displacement characteristics of the dynamic model and experimental data, as shown in Figure 4-27, the dynamic model initially slightly overestimated, but after around 2.5 mm, a better agreement between the two datasets was observed. However, by 2 mm, the dynamic model became unstable. This instability is also evident in Figure 4-25, which show the silicone deformed with and without the mesh. With the mesh, it is clear that the elements near the needle tip are excessively stretched and distorted to the point where they no longer deform around the needle. This also means that the contact between the needle and silicone is no longer functioning properly. This suggests that the overall convergence issues are caused by mesh dependencies, irregular contact conditions, and material properties (such as inertia or damping).

Visually, the displacement field components show similarities in field placement, as observed at smaller displacements. The X and Y components have concentrated

displacements around the needle edges, with decreased displacements in these planes under the needle tip. However, this could be due to the mesh instability identified earlier. The Z component of displacement still shows symmetry around the needle tip and edges. These displacement fields can then be compared visually with the DVC data at 3.5 mm (the first scan step). Numerical comparisons could provide initial insights into the accuracy of this model, but due to the limitations of the mesh, it would not be ideal to rely on the displacement outputs at this displacement for now.

The dynamic model developed in this study successfully captures the initial indentation stage of the needle, which is a critical aspect of the needle insertion process. Unlike previous studies, such as the work by Oldfield, which also used a skin substitute (gelatin), this study addressed the challenges of modelling the initial deformation phase which Oldfield's cohesive zone approach struggled to capture. They concluded that their method could not prevent the needle from penetrating, thereby failing to accurately represent the first stage of needle insertion, which is the initial deformation [10]. Similarly, while Amiri used a similar cohesive zone method to model the insertion force of MNs and focused on post-penetration deformation when the skin begins to close around the MN, it did not address the initial stages of deformation [29]. This model improves on that presented by Oldfield and Amiri by successfully simulating the material's behaviour through the initial stage of indentation and early deformation stages.

However, the dynamic model still has its limitations, particularly with the materials tearing behaviour and how it is represented beyond the initial indentation. Despite this, the dynamic model has demonstrated its potential in accurately capturing some key aspects of MN penetration, especially the early deformation process. This offers a solid foundation for future work that can refine the model and address the challenges in representing material tearing and the full penetration process.

The nature of computational modelling is fundamentally challenging but fortunately ever-evolving. Future iterations of this model could include continued research into the potential for adaptive mesh refinement algorithms or advanced adaptive meshing techniques. This could improve the accuracy of the indentation phase by incorporating dynamic meshing tools that track changes in geometry and material deformation.

Given the high strain that the model experiences before failing to converge, it appears highly dependent on the mesh used. However, implementing these dynamic meshing tools would require adaptations to the cohesive zone model, as the method proposed in this study relies on the surface mesh and node numbers.

Another adaptation that could prove useful would be to explore not only the geometry dependence of the model but also the modelling of multiple needles, similar to the study conducted by Potts [9]. This would also require further  $\mu$ -CT testing and continued DVC development.

## 4.9 Conclusion

This chapter has demonstrated the use of two variations of models for specific applications, initially utilising the parameters obtained from Chapter 3.4, and subsequently adapting them to fit the experimental load-displacement data from Section 4.7. The correlation between the static and dynamic model load-displacement data has illustrated how different models can be sensitive to parameters such as bulk modulus or density. While the dynamic model failed to converge to the requested displacement magnitude, it serves as a promising foundation for developing a more realistic insertion model. The innovative cohesive zone method, developed by M. Potts, integrates realistic work of fracture experimental results whilst working to maintain the model's stability—something other cohesive zone method models have struggled to achieve. The inclusion of a realistic material toughness before tearing demonstrates the level of deformation prior to material tearing that is excluded from most published puncture methods, such as element deletion methods.

Ultimately, computational modelling has not yet reached its full potential to create completely realistic simulations that incorporate all necessary parameters. However, these models have provided a baseline for initial validation with DVC and have identified areas for improvement in the experimental validations, which are explored further in Chapter 5. The models also highlight potential methodologies that, although not yet fully operational, address factors that have been overlooked in previous studies, such as the extended indentation phase. Additionally, they have successfully

## Finite Element Analysis

avoided premature penetration, an issue that other studies have acknowledged as a limitation.

Future work could focus on adapting the models with remeshing algorithms to reduce the mesh dependencies observed in the dynamic model. Other important considerations include introducing time-dependent behaviours in dynamic modelling, which would allow the incorporation of velocity during needle penetration into soft materials—a factor that was beyond the scope of this project. When adapting these models for use with human skin, it will be crucial to account for skin layer thickness, fibre orientation, and the varying mechanical properties of each layer, such as the Ogden material model parameters.

# ***CHAPTER 5***

---

## **EXPERIMENTAL MEASUREMENTS OF NEEDLE PENETRATION**

### **5.1 Introduction**

The accuracy and reliability of MN computational models depend on the validation techniques used to describe the complex phenomena of needle insertion and skin deformation biomechanics. To date, imaging techniques for MN insertion have primarily focused on post insertion microchannel tracking or the resultant needle damage. While methods like DIC have been applied to measure skin surface deformation and strain, these approaches are limited in scope. They are unable to capture complete, volumetric deformation during needle penetration, as the needle tip often falls outside the field of view provided by the standard two or three camera set up .

This chapter describes the image collection process, an experimental protocol for imaging MN indentation. This protocol used  $\mu$ -CT to capture both small and large deformations, presenting a novel approach towards FEA validation. The measurement

## Experimental Measurements of Needle Penetration

of displacements and strains during the indentation (pre puncture) at varying deformation levels, aimed to enhance the understanding of biomechanics of MN insertion. This method was designed to later be transferable to porcine and human skin.

The initial validation process investigated for needle penetration tracking is also presented. By using imaging techniques that have yet to be applied to dynamic needle imaging due to their inherent challenges, this study provides the first published results on imaging the pre-puncture process. To date there are no published results on imaging the whole needle penetration process. This approach allows key parameters such as volumetric displacement and strains to be measured, facilitating their use in FEA validation. All axes discussed in relation to DVC can be referenced from the FEA Figure 4-4.

## 5.2 Method

### 5.2.1 *Image collection*

To accurately capture the indentation phase of needle penetration, a detailed image collection process was developed. This section outlines the imaging methodology using  $\mu$ -CT, with a focus on tracking the needle deformation for low and high deformations.

#### 5.2.1.1 Method 1 – initial scans (Versa scanner)

An initial needle indentation experiment was set up at the University of Southampton nXCT lab to assess small deformations and resolution settings. Material C was used, with the sample cut to dimensions 10 x 10 x 10 mm, with the corners cut to minimise attenuation through the sample. Trimming the corners ensured the path length for the X-rays remained consistent at all angles during scanning, improving image accuracy and reducing artefacts. This sample was then  $\mu$ -CT scanned at 110 kVp 10W using a 160 kVp Zeiss Xradia Versa 510 (Carl Zeiss GmbH, Germany) at 2  $\mu$ m voxel resolution [Figure 5-1, Figure 5-2, and Figure 5-3].

## Experimental Measurements of Needle Penetration

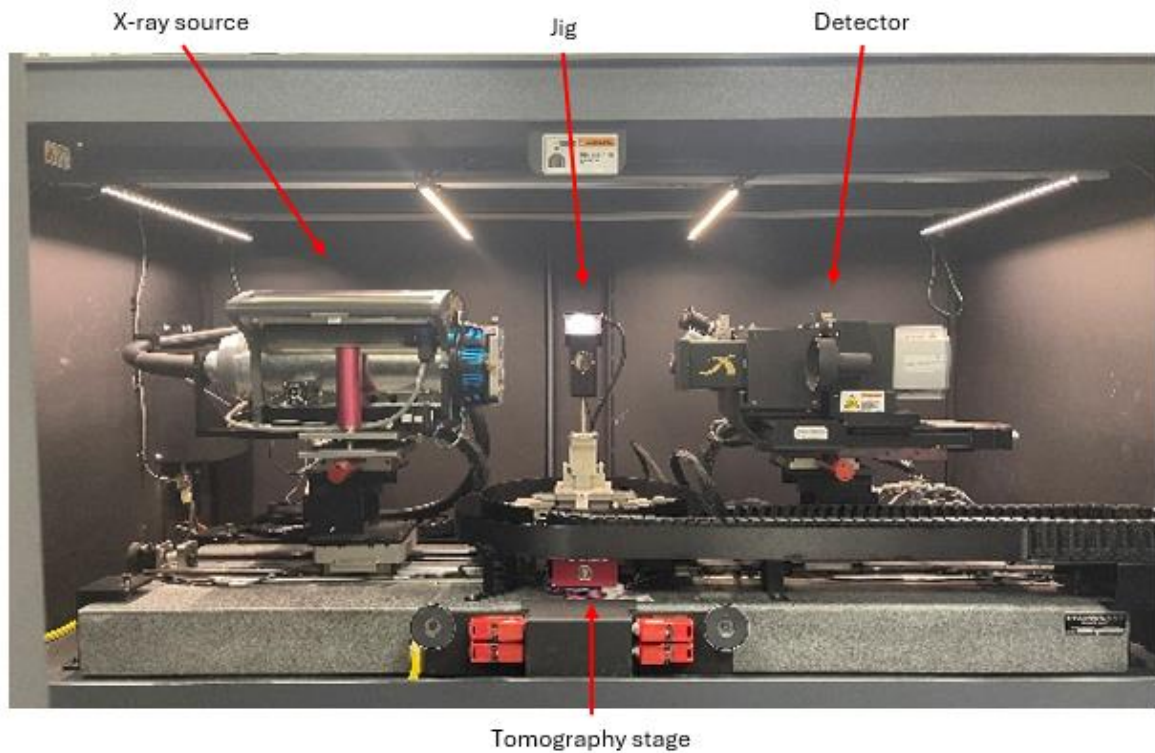


Figure 5-1 - Versa CT machine used for the first set of scans, showing the X-ray source, detector, tomography stage, and the custom jig

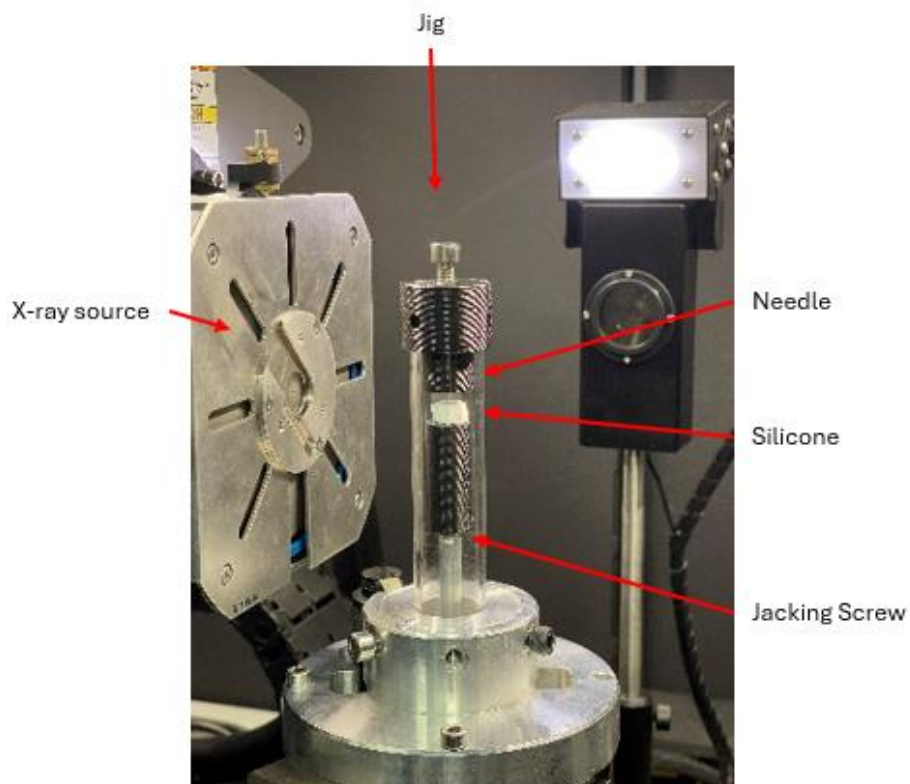
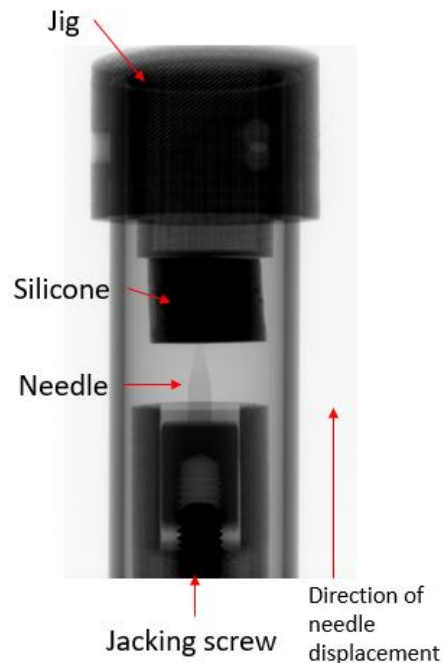


Figure 5-2 – The custom jig used for first set of scans, with silicone moving upwards

## Experimental Measurements of Needle Penetration



*Figure 5-3 – The custom jig used in both experiments is shown, featuring the jacking screw, Perspex needle, and silicone. In the second experiment, this setup was used with the silicone held stationary while the needle was displaced; in the first experiment, the configuration was reversed, with the needle fixed and the silicone moving upwards.*

For DVC, a maximum pixel displacement of 5% is desirable. At time steps of  $100\ \mu\text{m}$ , this would correspond to a movement of 50 voxels. Time steps of  $75\ \mu\text{m}$  were chosen, which with a 1000-pixel FoV gives 3.75 % voxel scope, is under the required 5 %. Starting from 0mm, the first scan was  $100\ \mu\text{m}$  (the reference image), and the remaining six scans were taken at  $75\ \mu\text{m}$  step sizes finishing with a maximum displacement of 0.375mm. Once the needle was displaced, the silicone was left to rest for 20 minutes before the scan began to ensure there was no movement of the silicone during the scan; this time was recommended by the lab technicians. Due to the silicone moving upwards, with the needle static, rigid body displacement (RBD) scans were also required at each displacement step to assess any extra movement. These scans are different from the standard scans as they specifically capture any rigid body motion of the silicone, isolating it from the deformation caused by the needle displacement. The overall scan time was roughly 4 hours.

Reconstructed volumes of each scan were processed in Fiji/ImageJ [226] for particle distribution assessment and to check the resolution and field of view used. The original files were 8 bit little-endian byte order,  $1.998\ \mu\text{m}$  resolution  $998 \times 1013 \times 993$  pixels in

## Experimental Measurements of Needle Penetration

width (X), height (Y), slices (Z) respectively. This was resliced within ImageJ to change the perspective, as the initial view shown in Figure 5-4 a) is through the z axis, ending with 1013 x 993 x 988 [Figure 5-4 b)].

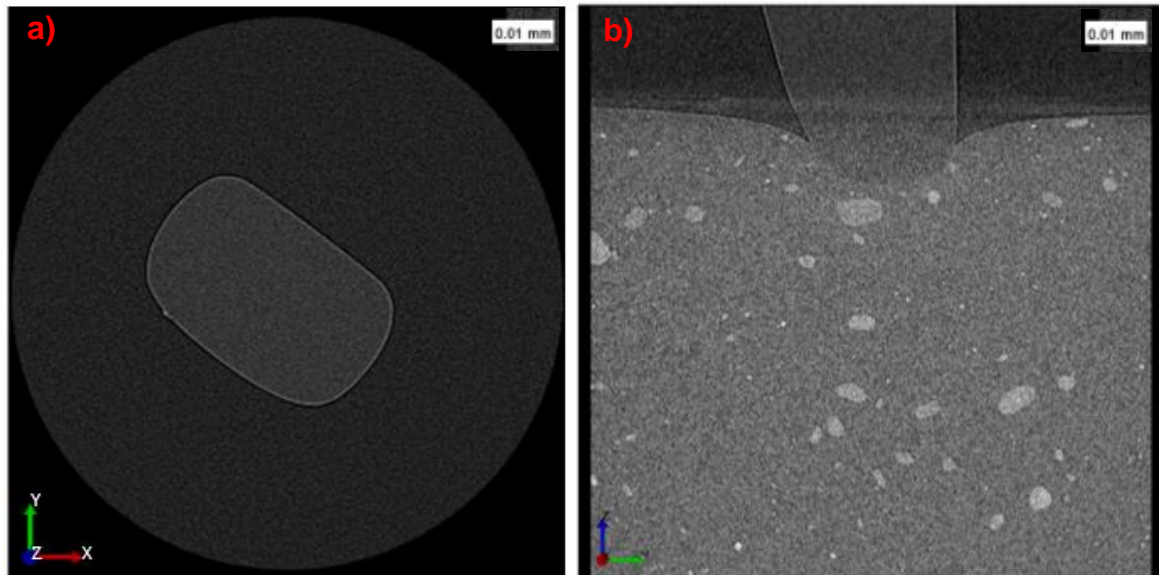


*Figure 5-4 - Top view of CT scan through Z plane a) side view through X plane b)*

### 5.2.1.2 Method 2 – second scans (Diondo)

Another set of scans were taken around the predicted penetration point, 8 mm, the penetration test completed in Section 3.3.3.1 and the results of this experiment are in Section 3.4.3. These scans were completed using the 300 kVp Diondo d5 at a 2.948  $\mu\text{m}$  resolution. The decrease of resolution allowed for the field of view to be increased to 8mm to view the whole needle at the maximum displacement and allowed the scan time to be reduced massively to 1.5 hours, there was no variation of scan time for the different needle displacements. The displacement steps for these six scans were: 0  $\mu\text{m}$ , 350  $\mu\text{m}$ , 650  $\mu\text{m}$ , 700  $\mu\text{m}$ , 750  $\mu\text{m}$  and 800  $\mu\text{m}$ . The jig previously used was adjusted [Figure 5-3 and Figure 5-5] so that the silicone was stationary with the needle moving upwards, this reduced the need for RBD scans however one was still taken to check the scans for additional movement during the image processing.

## Experimental Measurements of Needle Penetration

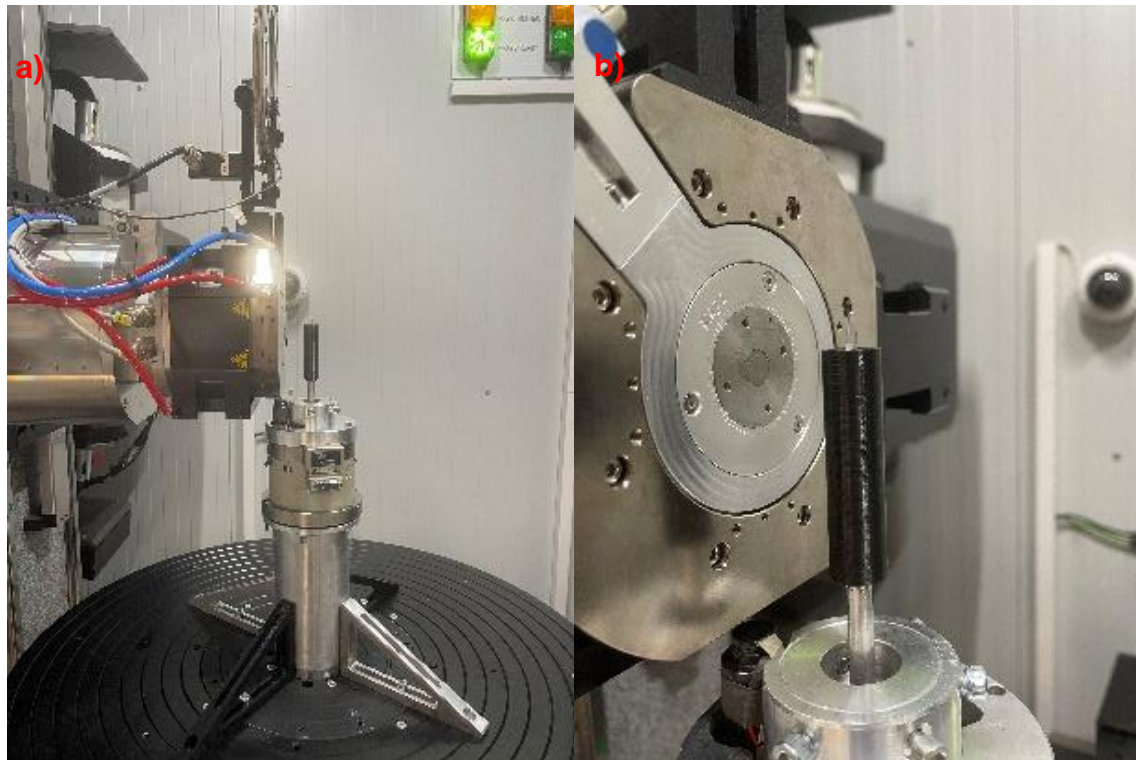


*Figure 5-5 - Diondo CT scanner with Perspex needle in the jig a) and close up of the needle in the jig as needle was moved for the second scans b)*

The original RAW scan details were 8 bit, little endian byte, 3008x3008x2262 pixels in width (X), height (Y), slices (Z) respectively at a resolution of 2.948  $\mu\text{m}$ . This created 8 files (one rigid body scan (RBD), the reference image at 0 mm and the six moving scan images) at 21.8 GB each. This required a large amount of RAM to open just one image in Image J, with this size file also not accepted within DaVis (the software later used in Chapter 5 for DVC). Therefore, the files were reduced within ImageJ. This was completed by grouping the slices in one direction (so every two slices were reduced to one slice), reducing the slices from 3008 to 1504 and 2262 to 1134. This left the size to 1504 x 1504 x 1131 slices. To reduce the files further, the height was reduced by 270 slices, 135 slices either side to remove black slices that are not required for further data processing. The same was done through the slices, where 28 slices were removed from the bottom. This left the file size as 1504 x 1234 x 1103 slices.

## Experimental Measurements of Needle Penetration

As the original files had the same perspective as in Section 5.2.1.1, these files were also resliced to change the perspective to view it through the X direction, to 1504 x 1103 x 1234 slices to allow for consistent axis direction.

### **5.2.2 *Image registration***

DVC analysis was conducted using LaVision DaVis (10.2.0) to extract displacement and strain data from a series of six sequential  $\mu$ -CT scans. The method of capturing these images is detailed in Section 5.2.1, capturing the deformation of the silicone during the indentation process.

The overall process is explained in Figure 5-6, from the image collection to the statistical analysis in MATLAB.

## Experimental Measurements of Needle Penetration

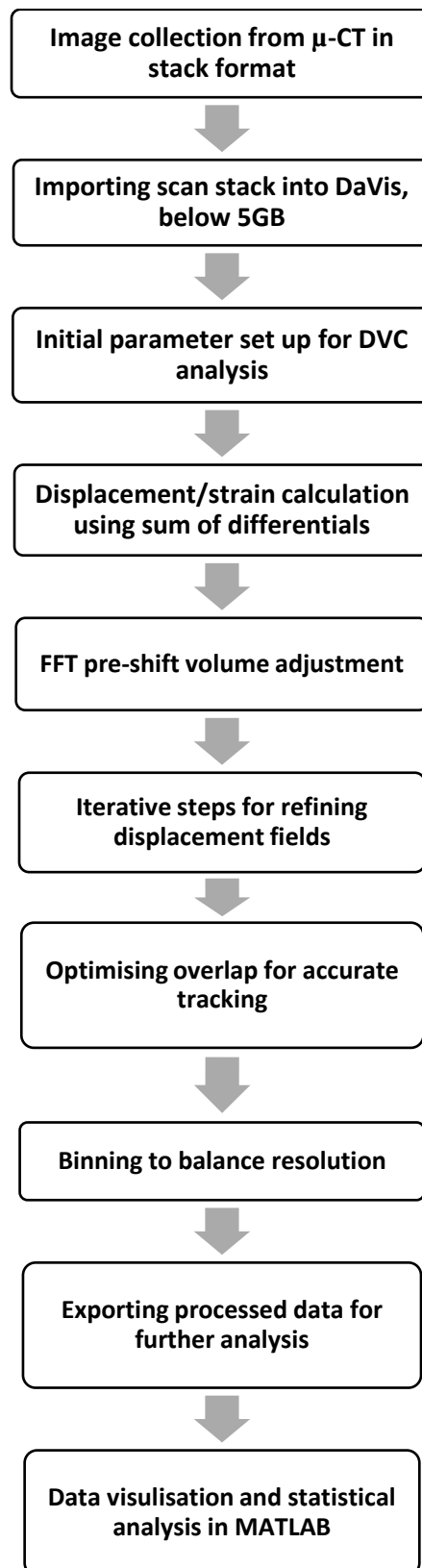


Figure 5-6 - Flow chart of DVC image registration process

## Experimental Measurements of Needle Penetration

The process began with importing the  $\mu$ -CT scans into DaVis for analysis. These scans provide detailed volumetric data on the silicone material at different stages of deformation, enabling the tracking of displacements and deformations within the material over time.

During the DVC analysis in DaVis, several input parameters were specified to optimise the accuracy and reliability of the displacement calculations. These can be adapted based on preference, and for this study the properties below were chosen:

- 1. Sum of Differentials:** The Sum of Differentials method was employed to calculate displacement fields between consecutive  $\mu$ -CT scans. This method was selected because it provides reliable results for the material and imaging conditions used in this study. This method involves comparing voxel intensity values between corresponding regions in successive scans to determine the displacement of material points.
- 2. FFT Pre-Shift Volume:** Fast Fourier Transform (FFT) pre-shift volume size was set to 192 voxels, determining the resolution and accuracy of displacement calculations. This size was chosen to capture subtle deformations within the material while maintaining computational feasibility and noise reduction. A larger pre-shift volume size allows for finer displacement measurements, capturing subtle deformations within the material.
- 3. Iterative step process:** DaVis performs four iterative steps per scan to refine displacement calculations. The process begins with an initial volume size of 128 voxels and gradually reduces to 76 voxels in subsequent steps. This iterative approach helps to improve the accuracy of displacement measurements by refining the spatial resolution of the analysis, ensuring smaller deformations can be accurately resolved by the final steps.
- 4. Overlap:** The overlapping region between consecutive volumes was set to 75% of the total volume, ensuring sufficient spatial coverage for accurate displacement calculations. A higher overlap percentage helps to mitigate errors caused by interpolation and ensures robust tracking of material deformations.

5. **Binning:** Binning, or voxel averaging, is applied during the initial steps of DVC analysis to reduce computational burden while maintaining spatial resolution of the final results. In the first step, binning factors of 4x4x4 were utilised, followed by 2x2x2 in the second step. These factors were chosen to strike a balance between computational efficiency in the early steps and high resolution displacement accuracy in the later steps. Binning is disabled in the subsequent steps to refine displacement calculations and improve accuracy.

The adjustment of any of these parameters can significantly influence the final results. For instance, decreasing the number of voxels may decrease the accuracy of the displacement calculations due to over-averaging. Conversely, smaller voxel sizes can enhance spatial resolution but may increase noise, computational demands, and processing times [173]. It is crucial to balance these parameters to optimise both accuracy and efficiency. Due to time constraints, a trial and error method was implemented to find the most efficient parameters.

Additionally, the choice of parameters depends on the specific material properties and deformation characteristics under study. For example, for small deformations, a coarser resolution might be sufficient because there is less concern about averaging out local deformations. However, for large deformations that require detailed tracking of strain distributions within the material structure, a finer resolution with smaller voxels is necessary to achieve precise measurements of complex deformations [173].

Variations in parameters such as overlap percentage and binning factors can also impact the robustness of the analysis, potentially leading to different interpretations of the material's behaviour. Therefore, a thorough understand of how these parameters interact is essential for accurate and reliable DVC analysis.

As the sum of differentials method was used, one .csv file was created and exported for the first and last step (the middle four are not required for initial processing) along with the displacement and strain differences from all six scans. This data was then imported and manipulated in MATLAB for further processing. The additional processing included general visualisations to explore deformation patterns, statistical analysis and integrating with FEMs for comprehensive evaluations to validate computational models.

### 5.2.3 Image processing and alignment

In the process of correlating the FEA and DVC data using MATLAB, several steps were taken to ensure accurate comparison and validation of experimental and simulated results.

Firstly, the .csv files exported from DaVis were imported into MATLAB. This allowed the extraction of displacement data and the provision of voxel grids from the first and last scans. These voxel grids were then checked to ensure consistency with voxel placements from the DaVis output files, as shown in Figure 5-7.

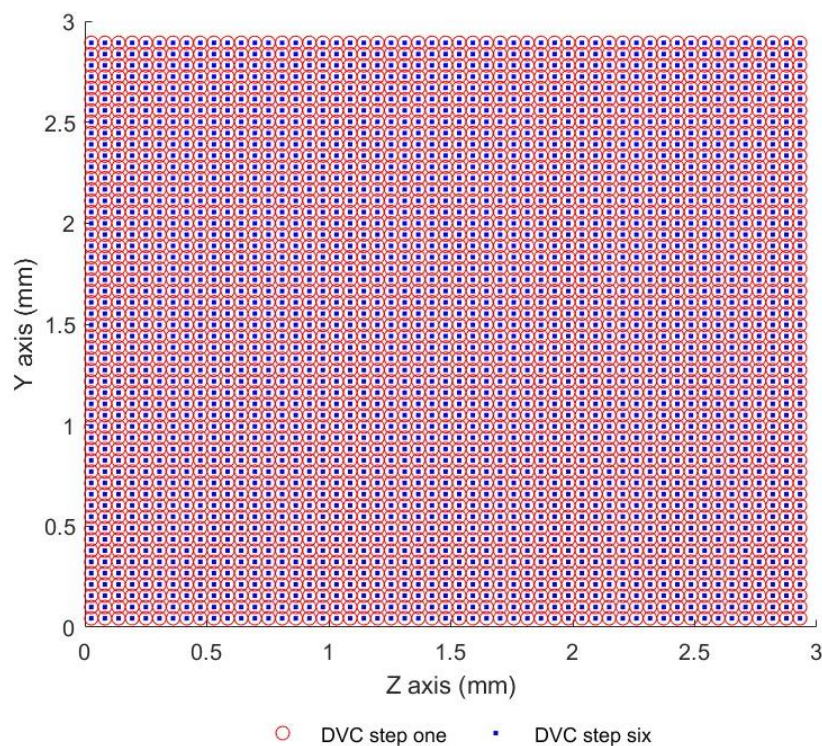


*Figure 5-7 - Comparison of voxel placement for the first and last steps to check for anomalies in the data*

Then, displacement vectors [Figure 5-8] from the final scan were examined to verify correct correlation between voxel positions and displacements. MATLAB's Orthoslicer tool allows for visualisation of displacement components (X, Y, and Z) for each voxel position [Figure 5-9].

## Experimental Measurements of Needle Penetration

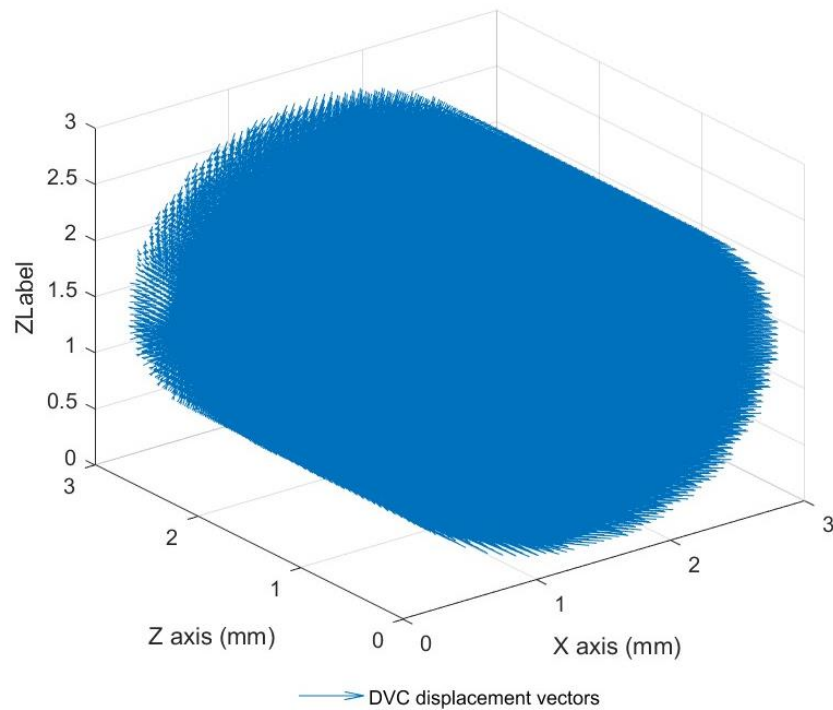


Figure 5-8 – This plot helps check the displacement vectors from the DaVis export file within MATLAB. This can be used to spot any gaps in the plot that may not be showing correctly.

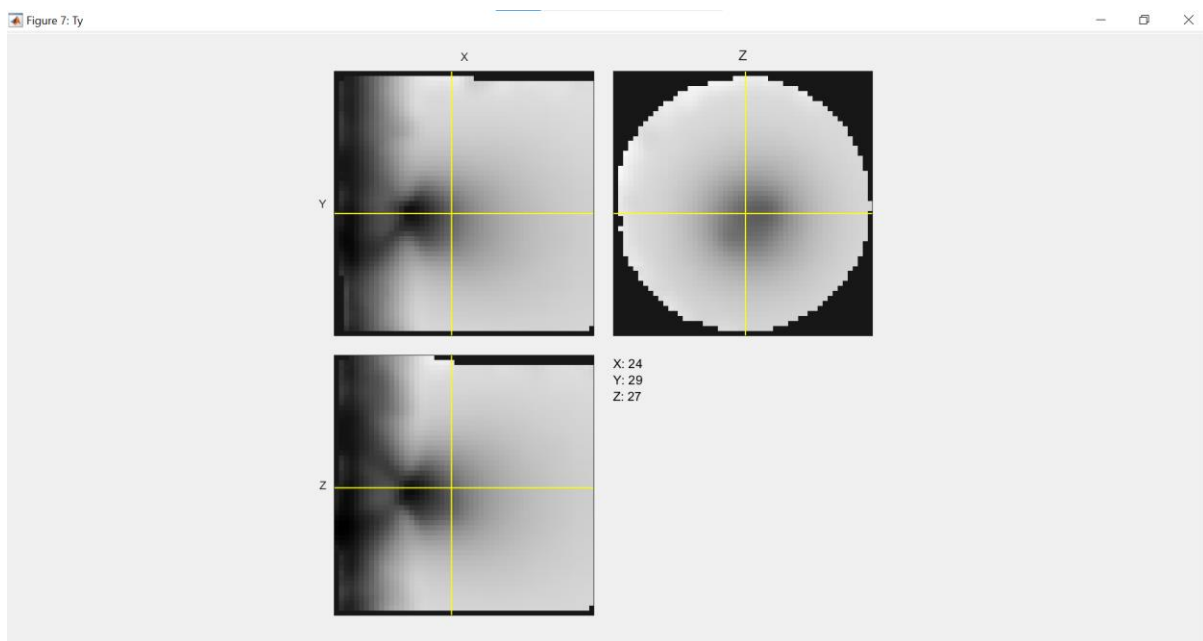
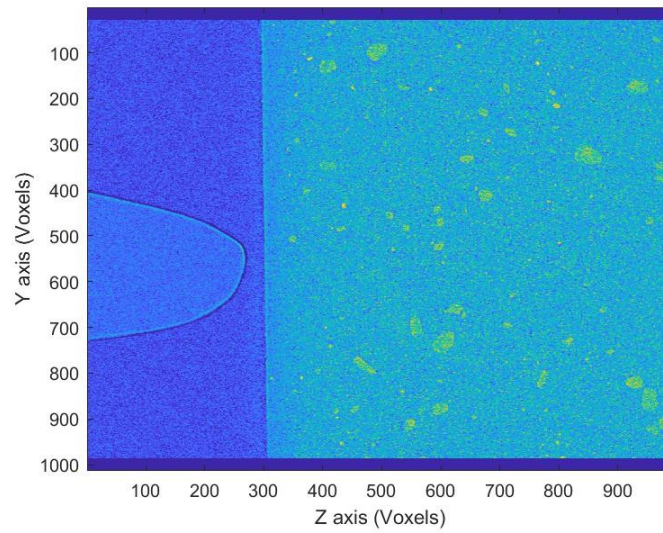


Figure 5-9 - Orthoslicer viewing of the Z component of displacement, which was used to select specific slices for further analysis. This tool allows for interactive viewing of 3D datasets by slicing the volume into 2D sections along different axes, in this case the Z component of displacement was chosen.

## Experimental Measurements of Needle Penetration

The next step was to correlate the experimental data with the model data in Section 4.7.2. Initially, the CT slice was used as a reference [Figure 5-10]. Then the needle mesh from FEBio was imported into MATLAB to ensure alignment, addressing any necessary rotation or translation. Visualisation from different axes allowed for verification of alignment between the needle mesh, silicone, and CT image [Figure 5-11].



*Figure 5-10 - CT scan of the first step to assess needle and silicone placement within MATLAB*

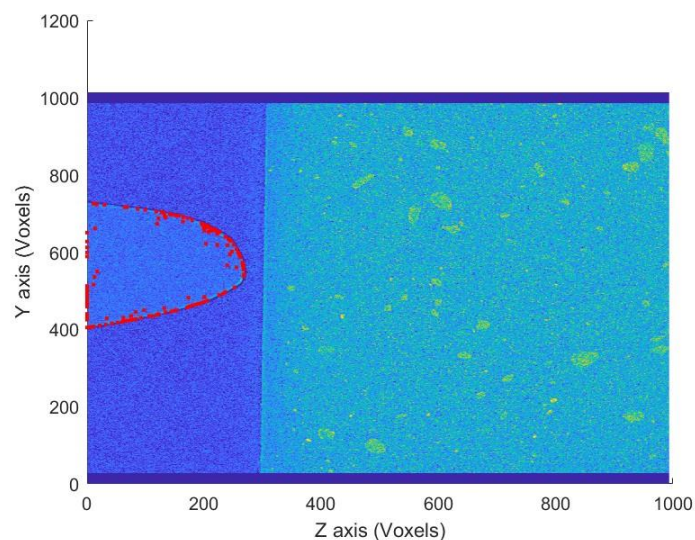


*Figure 5-11 - Overlay of the needle mesh from FEBio (the red dots) onto the CT image to check rotation and translation of the DVC data*

Since the voxel positions from DaVis lack distinguishable features such as the silicone and needle edges, the DVC magnitudes were used instead for validation purposes. The magnitudes were also used because they represent the absolute displacement values, allowing validation of the deformation field even when distinct features like edges are not visible in the voxel positions. The overlay of the segmented needle on DVC magnitude images facilitated orientation checks and ensured the correct alignment between experimental and simulated data [Section 5.3.4]. By aligning and matching these components, an assessment of the experimental and simulated results can be obtained, identifying the maximum and minimum points. The DVC magnitudes can be viewed at any chosen slice, with displacement plots shown within Section 5.3, and strain field plots for all six components of strain then displayed on individual plots. This provides an understanding of the material's deformation behaviour and facilitates the analysis and comparison of strain distribution between experimental and simulated data.

Before starting FEA interpolation onto the DVC data, some checks were made to ensure the FEBio logs were imported correctly and that any rotation, translation, or scaling had been completed. The needle imported into FEBio was segmented from the  $\mu$ -CT scan [Section 4.2.2.1], allowing for direct feature correlation. However, the silicone in FEBio [Section 4.2.2.2] was not segmented from the original CT scans, so it is larger than what is seen on the  $\mu$ -CT scans, which could present challenges when aligning the two data sets. There were three initial checks completed once the FEBio logs were imported into MATLAB: initial mesh check, displacement vector check and displacement magnitude check. These were visually checked before moving onto the interpolation.

The initial FEA mesh check was completed by importing the FEBio mesh node data .txt file [Figure 5-12]. This node data was then split into two: one for the silicone and one for the needle. The second set of information imported from FEBio included the initial and final nodal position, which was used later to match displacements to specific nodes.

## Experimental Measurements of Needle Penetration

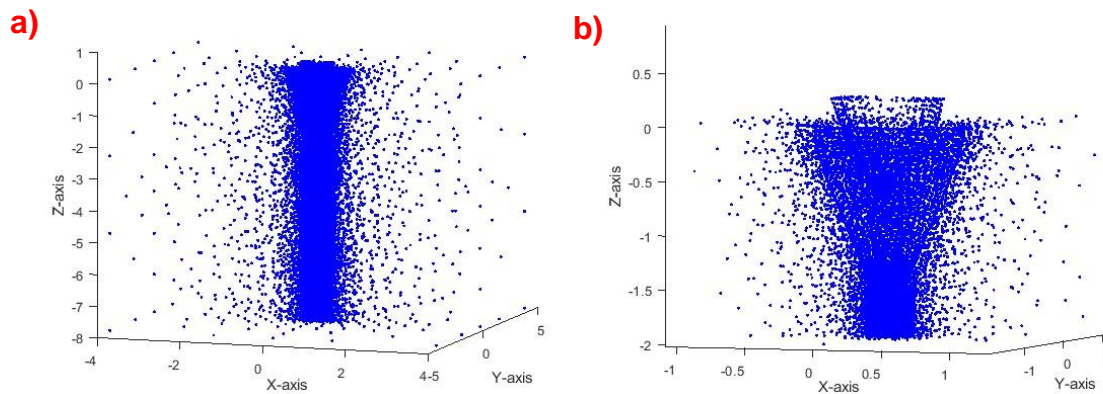


*Figure 5-12 - The whole mesh node position, needle and silicone imported into MATLAB from FEBio (in mm) a) and a close up showing the needle nodes b)*

The second FEA mesh check was calculating the displacement vectors [Figure 5-13]. This was completed by importing the displacement directly from the FEBio log files. This method required matching the displacements to the mesh nodes which made the coding more complex, however useful later on.

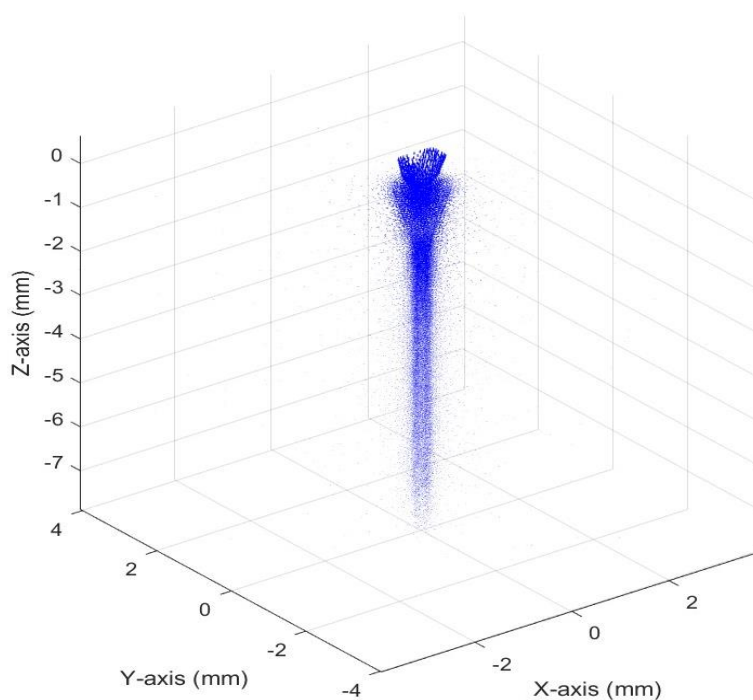


*Figure 5-13 - The displacement vectors show the difference in the initial and final nodal positions.*

## Experimental Measurements of Needle Penetration

Once the displacement vectors were checked, a coloured magnitude plot for the final step, and thus the final displacement, was created. Within FEBio, the needle was instructed to only displace 0.375 mm as this was the same displacement used for the  $\mu$ -CT scans. Initially, all nodes were displayed [Figure 5-14], but most nodes, especially on the outer edges of the silicone, showed zero displacement.

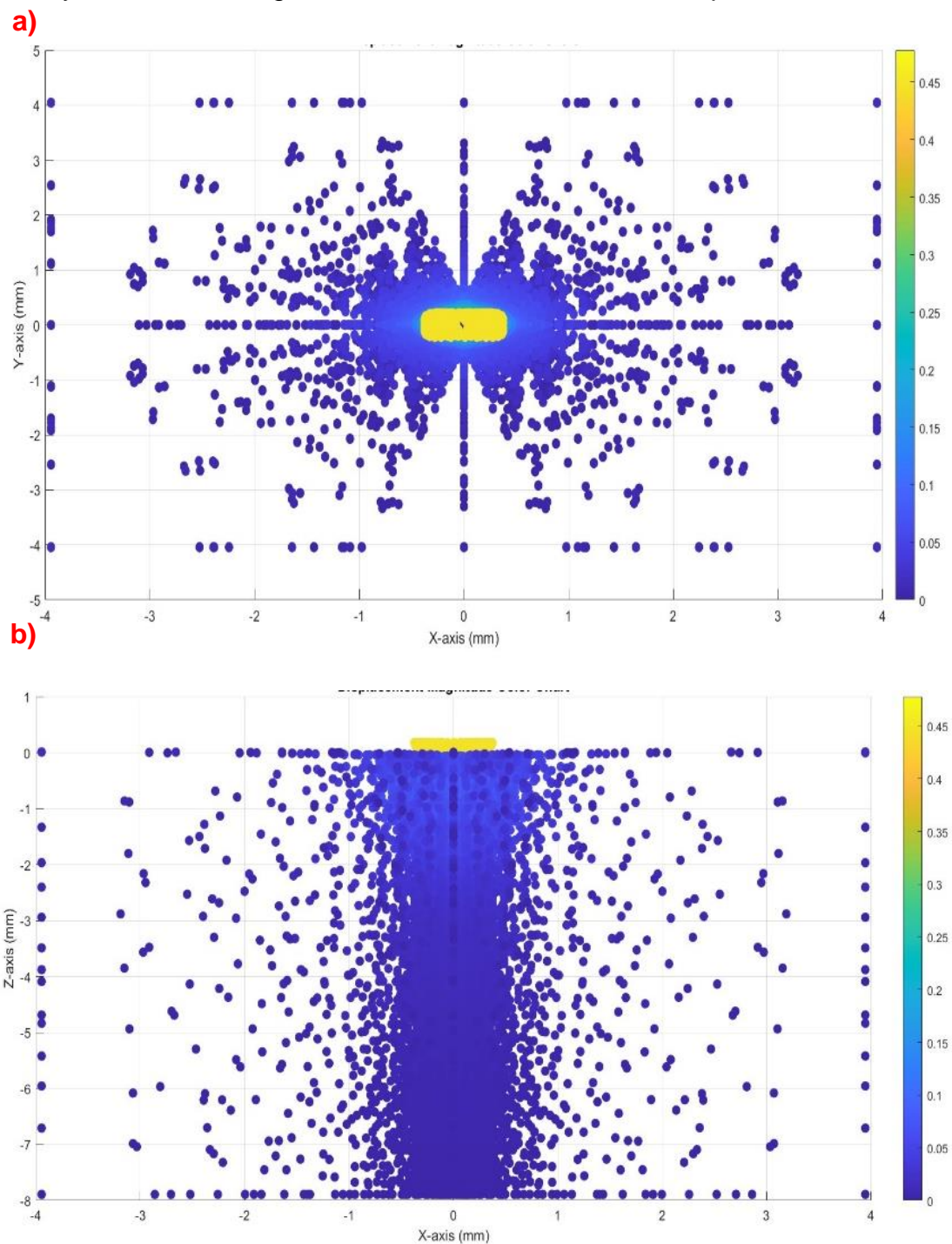
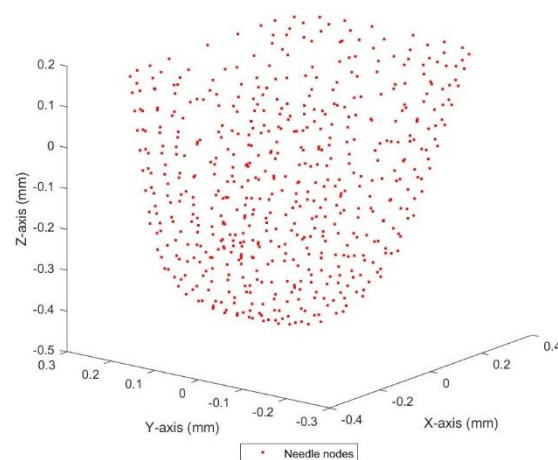


Figure 5-14 - FEBio displacement magnitudes in MATLAB top view a) and side view b)

Once the data sets from the FEM and DVC were verified within MATLAB, the alignment of the two was initialised. This was the final step before interpolation between the two. To start this process, only the needle mesh was used to simplify the determination of rotation and translation matrices [Figure 5-15]. A CT slice from the top view was utilised [Figure 5-16] to assist in finding the rotation matrices, allowing visualisation of the needle base. The DVC mesh matched the size of the CT slices exactly, as the mesh was derived from the slices. Therefore, the DVC mesh was translated to match the CT slice position. The needle was then rotated to match the CT slice [Figure 5-16 b) and c)]. This rotation was subsequently applied to the DVC mesh, as it was decided to keep the final FEA mesh stationary and only move the DVC mesh so that the data could be imported into FEBio. Some discrepancies may be seen in the images due to the CT slice chosen for viewing.



*Figure 5-15 - Needle mesh nodes from FEBio in MATLAB*

## Experimental Measurements of Needle Penetration

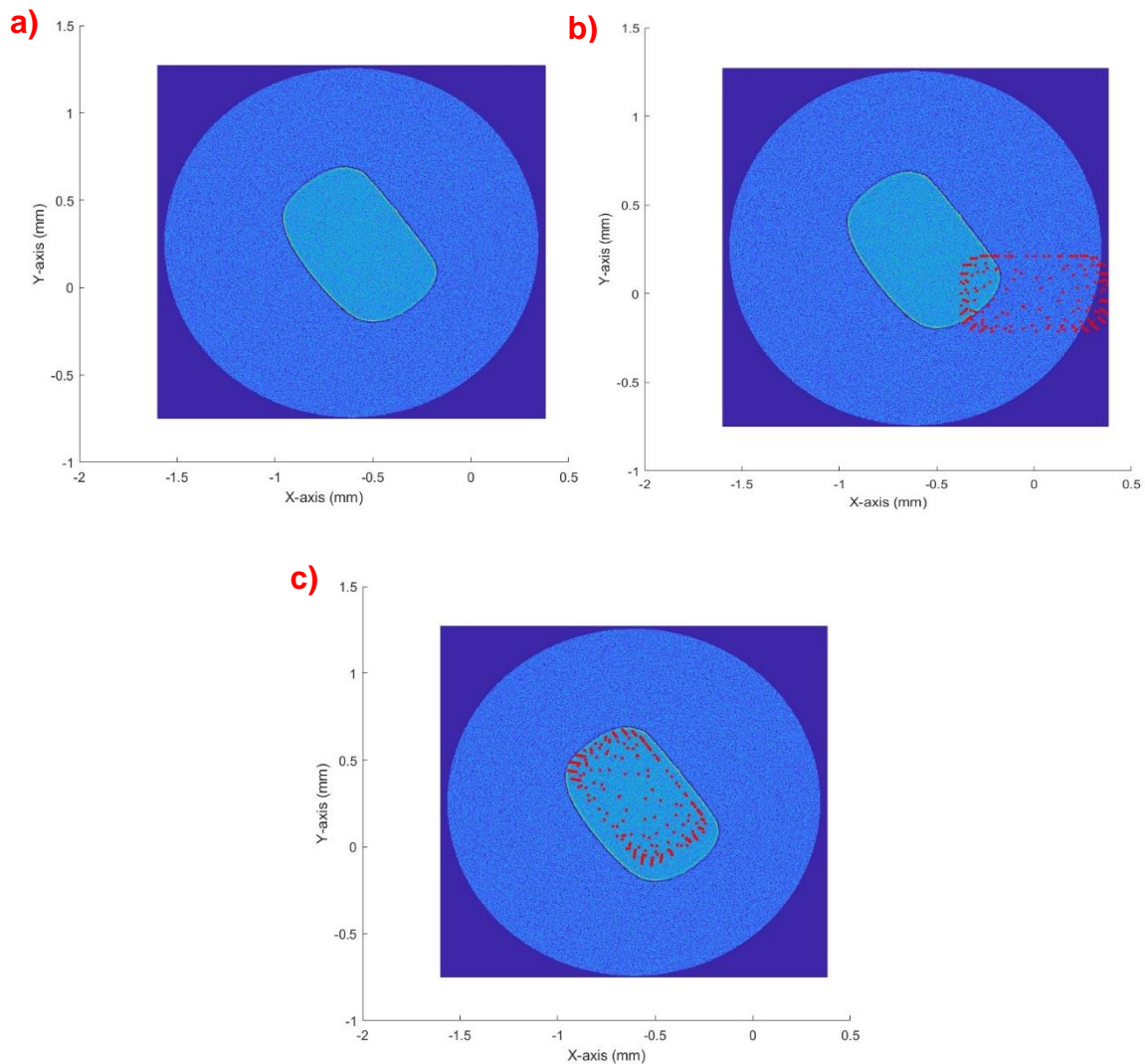


*Figure 5-16 - Translation and rotation of the needle nodes to match the top view of the CT scan. The top view of the CT scan a) the initial placement of the needle mesh b) the rotated and translated needle mesh overlaid onto the CT scan image.*

As an additional alignment check, the DVC mesh was filtered to remove the zero components of displacement [original DVC mesh in Figure 5-17]. By doing this, the lowest areas of displacement magnitude could be matched to the needle tip when the needle rotated. Once this alignment was verified, the entire FEA mesh was then aligned with the now translated and rotated DVC mesh. This alignment was challenging due to the fields of view of the DVC mesh and FEA mesh not matching [Figure 5-18]. Consequently, extra steps were required to ensure an effective alignment.

## Experimental Measurements of Needle Penetration

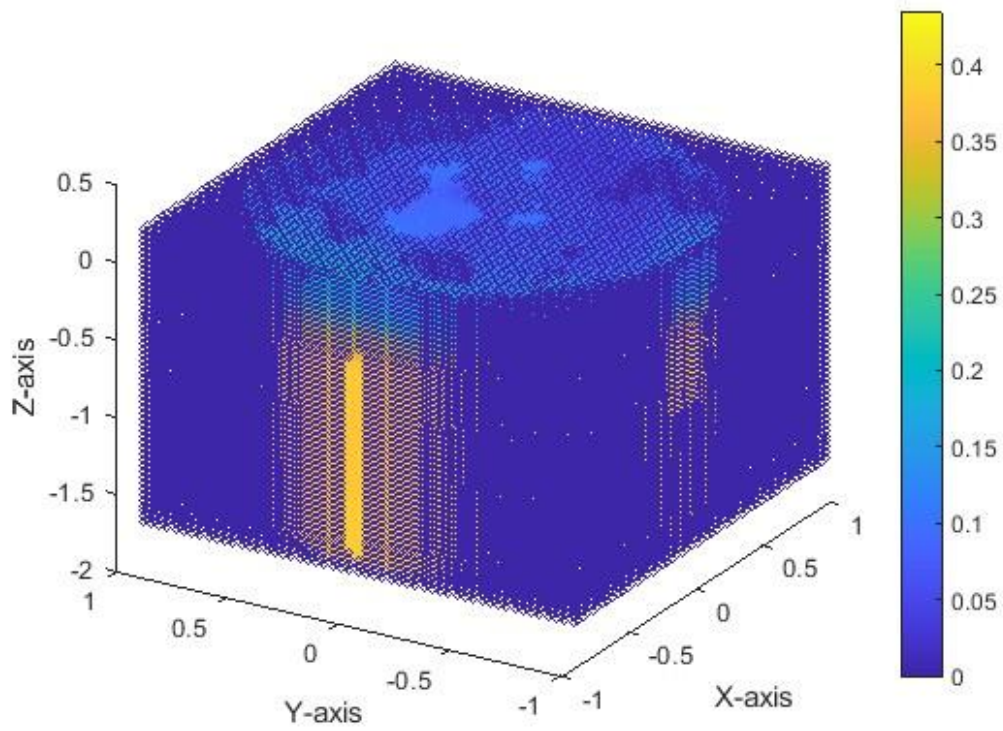


*Figure 5-17 - Displacement magnitudes of the DVC data prior to rotation and translation (in mm)*

## Experimental Measurements of Needle Penetration

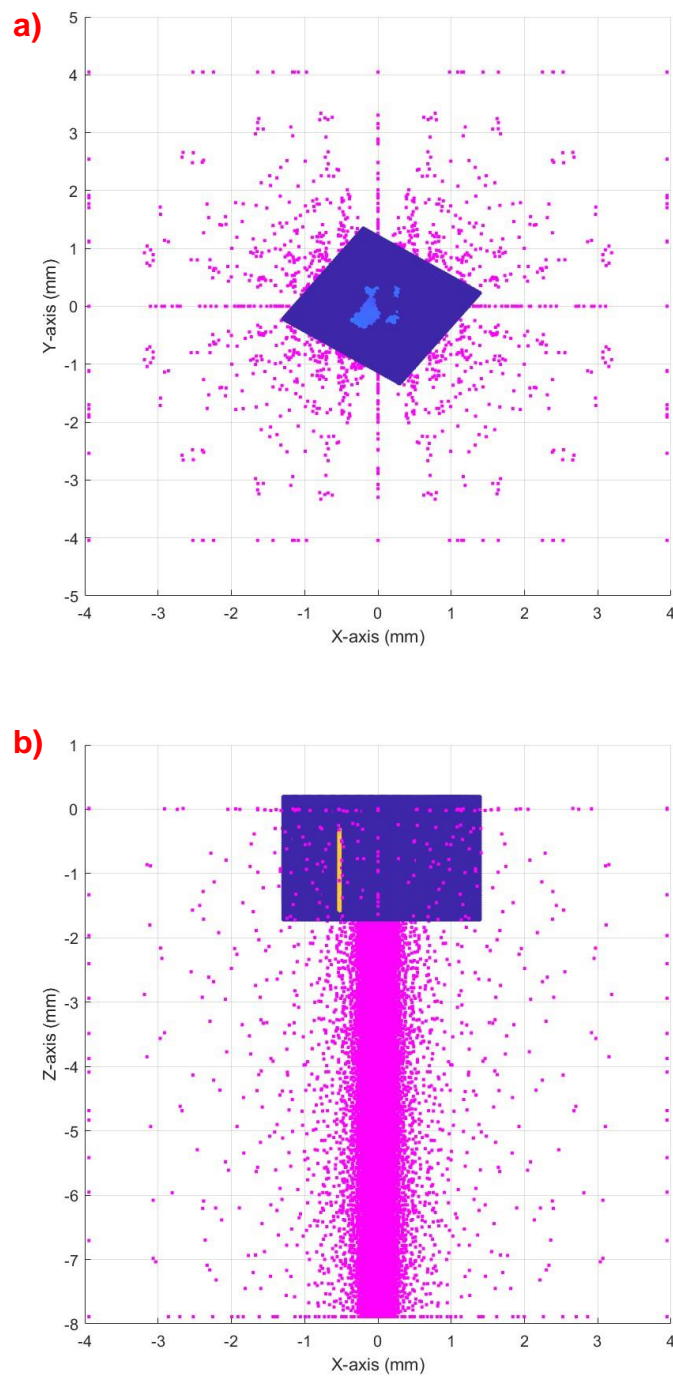


*Figure 5-18 - The DVC data (the blue rectangle) and FEBio mesh nodes (the pink dots) overlaid. The top view a) and side view b) shows the difference in the two data sets FoV*

These steps were then repeated with the second set of scans taken with a larger needle displacement. The needle mesh was imported from FEBio into MATLAB to aid

## Experimental Measurements of Needle Penetration

in the data correlation [Figure 5-19]. Some small discrepancies may be possible due to the slice of needle nodes and CT slice chosen in the image.

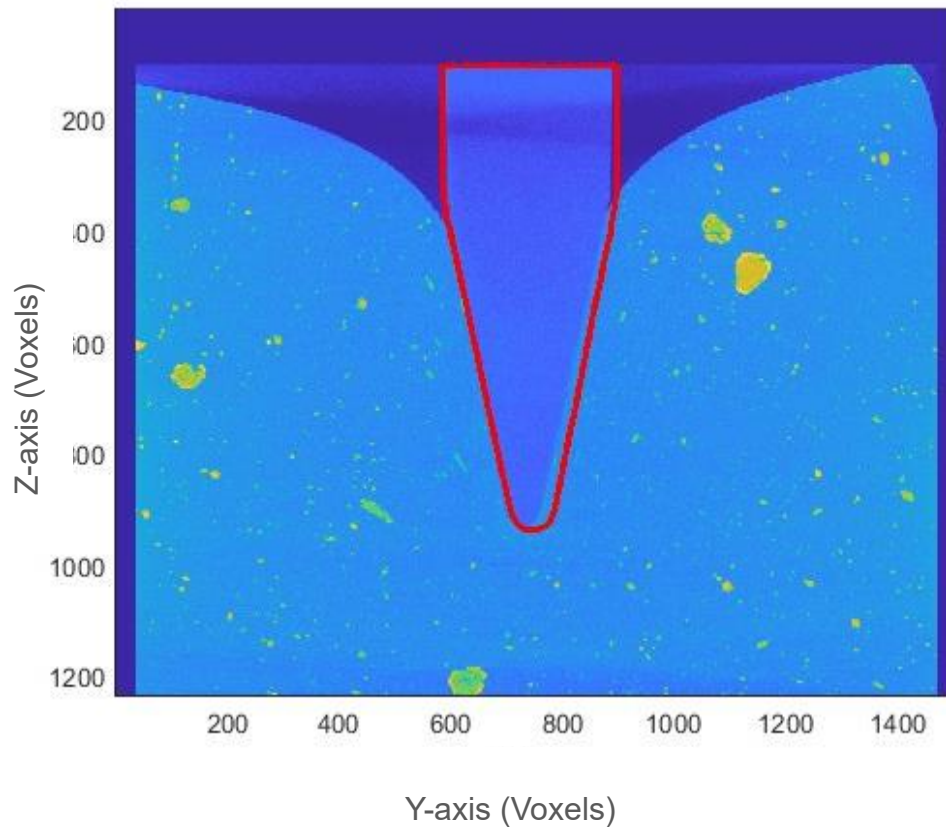


Figure 5-19 - The second set of scans needle mesh placement overlaid onto the CT scan

### 5.2.4 Interpolation of FEA to DVC

The DVC data, which was defined at the voxel positions, was interpolated to find the values at the FEBio node positions. This process effectively changed a high-resolution grid into a lower-resolution node system.

In MATLAB, a weighted sum algorithm with a set range search was employed. The range search was initially set to 1. The algorithm first selects the grid points closest to the nodes, calculates the distance between them (an example is shown in Figure 5-20), and then incorporates this distance into the weighted sum. It also includes some grid points further away from the node to provide a more accurate measurement. This

## Experimental Measurements of Needle Penetration

process ultimately yields the measurement of DVC displacement at the node of the FEBio mesh, which can later be compared to the FEA node displacement.

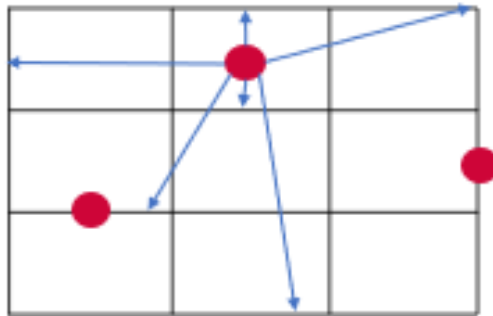


*Figure 5-20 - An example of the search algorithm used to show the nodes placement and the voxel grid*

The field of view (FoV) for the DVC was approximately 2 x 2 x 2 mm (993 x 988 x 1013 pixels at a resolution of 1.996  $\mu\text{m}$ ). In contrast, the FoV of the FEA mesh was over 8 mm in each direction. The alignment of the FEA and DVC meshes is discussed in Section 5.2.3. The FOV determines the search radius used; for example, since the FoV of the DVC is 2 mm, there is no benefit in using a range search beyond this distance. With 53x52x52 voxels, the voxels are approximately 0.04 mm apart. consequently, the range search was then decreased to 0.16 mm after the initial search was completed.

The output consisted of the coordinates of the mesh with the corresponding DVC displacement data, which were input into FEBio to plot the results.

To view all six steps of the interpolated DVC data, the FEA was rerun with 'must' points added. These were predefined time points that FEBio must pass through, ensuring the time stepper evaluates the model at each desired time point. This adjustment changed the number of steps from 17 to 6 to match the experimental displacement steps used in Section 5.2.1.1. Table 5-1 shows the corresponding must points used.

## Experimental Measurements of Needle Penetration

*Table 5-1 - Scan step number with experimental displacement and corresponding FEBio must point time*

<b>Step number</b>	<b>Experimental displacement (mm)</b>	<b>Load controller time (s)</b>
<b>1</b>	0.00	0.0
<b>2</b>	0.075	0.2
<b>3</b>	0.150	0.4
<b>4</b>	0.225	0.6
<b>5</b>	0.300	0.8
<b>6</b>	0.375	1.0

The interpolation code was then adjusted to output a .txt file containing the node numbers and the displacement components for each step, including the zeros for the first step, which served as the reference image. This .txt file was subsequently imported into FEBio Postview into the data section, classified as a node and vec3f (3 fl) type.

### **5.2.5 Parameter study**

Due to the parameters discussed in Section 5.2.3, a parameter study for the DVC results was conducted for both sets of scans. This study enabled a thorough review of the resolution and search radius parameters within DaVis, as this particular method has not previously been used with needle deformation at this level. The parameter changes for the first scans are detailed in Table 5-2, while the parameter changes for the second scans are outlined in Table 5-3. The binning for all tests was 4x4x4 for the first pass, 2x2x2 for the second pass and zero for the third and fourth passes.

Table 5-2 - First scan parameter study test parameters used

Test Number	FFT pre shift window size (Voxel)	Size per pass (voxel)	Overlap (%)	Search Radius (Voxel)	Total Voxels - Y, X, Z (Voxels)
1	104	80,56,48,48	0	4,4,2,2	21,21,21
2	76	56,40,32,32	0	4,4,2,2	32,31,31
3	104	80,56,48,48	50	4,4,2,2	42,41,41
4	192	128,96,80,76	75	8,4,2,2	53,52,52
5	76	56,40,32,32	50	4,4,2,2	63,62,62

Table 5-3 - Second scan parameter study test parameters used

Test Number	FFT pre shift window size (Voxel)	Size per pass (voxel)	Overlap (%)	Search Radius (Voxel)	Total Voxels - Y, X, Z (Voxels)
1	208	152,112,96,88	50	8,4,2,2	34,28,25
2	192	136,104,88,80	50	8,4,2,2	38,31,28
3	128	88,64,56,56	50	8,4,2,2	54,44,39
4	104	80,56,48,48	50	8,4,2,2	63,51,46
5	88	80,52,44,44	50	8,4,2,2	68,56,50
6	64	64,48,32,32	50	8,4,2,2	94,77,69

## 5.3 Results

### 5.3.1 Method 1 – initial scans (versa)

Figure 5-21 shows the centre slice of the six steps of the initial needle indentation scans, from the reference scan (a) at 0 mm to the sixth moving image (f) at 0.375 mm.

## Experimental Measurements of Needle Penetration

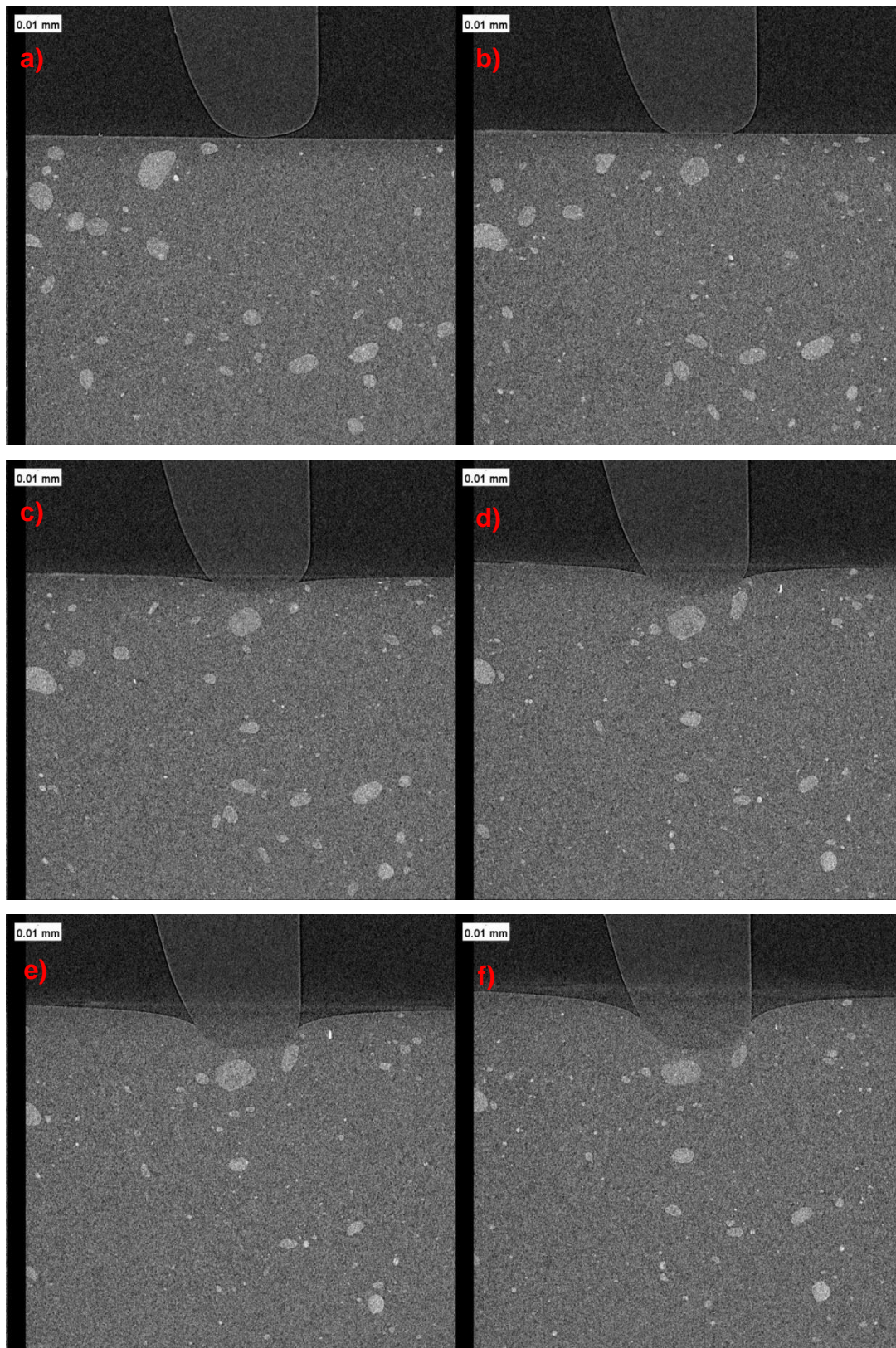


Figure 5-21 -  $\mu$ -CT images of scans one to six a) to f) respectively at the centre slice

**5.3.2 Method 2 – second scans (diundo)**

Figure 5-22 shows the centre slice from the six scans for the second test. (a) is the reference image at 0mm, with (f) as the last moving image at 8mm.

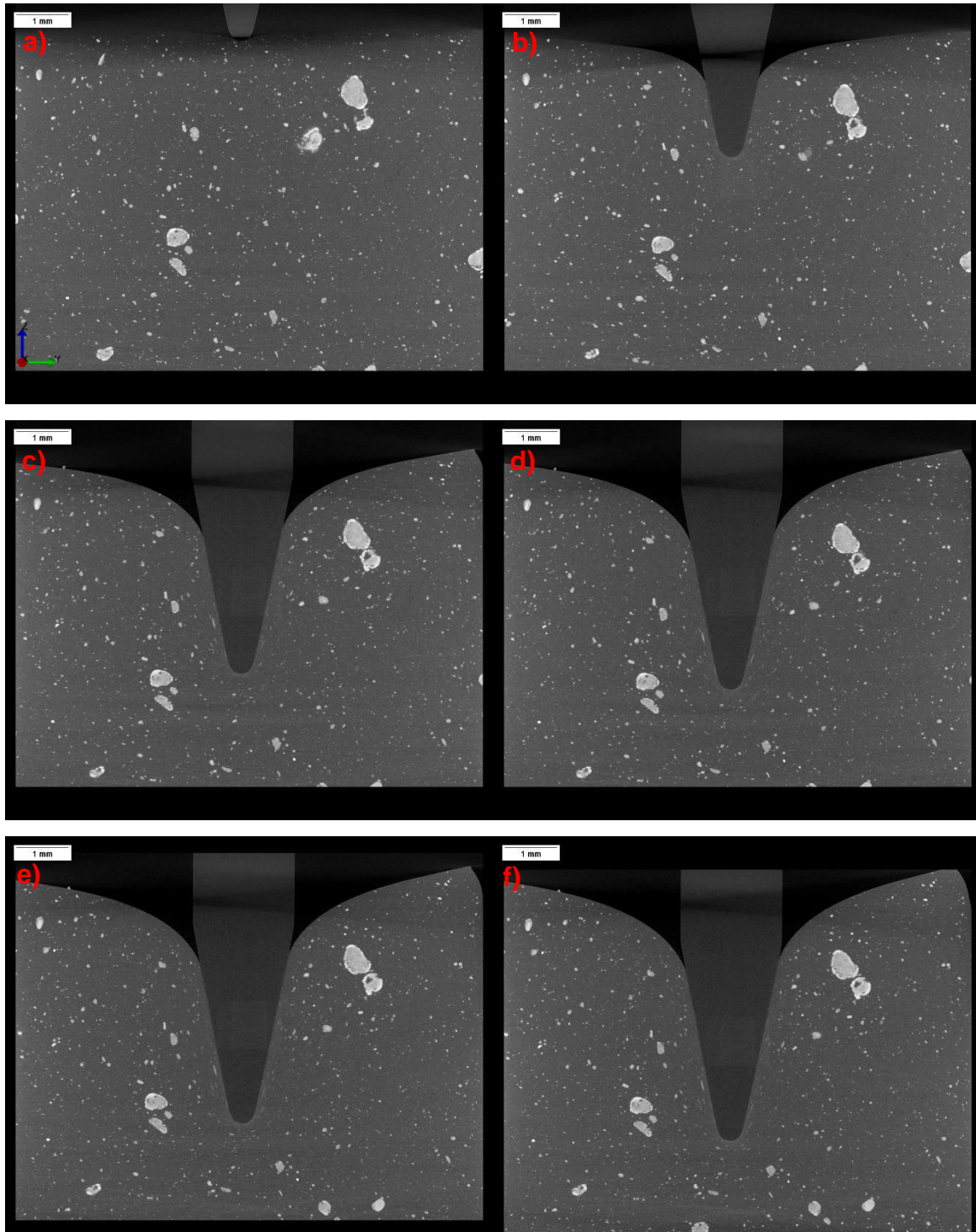


Figure 5-22 -  $\mu$ -CT images of scans one to six a) to f) respectively at the centre slice

### **5.3.3 Parameter study**

To view the differences in parameters within DaVis, four different parameters were chosen. These looked at the initial FFT pre shift window size, the voxel sizes on each step, the overlap percentage on each step, the voxel search radius. The resulting grid points in each axis are detailed in column six in Table 5-2 and Table 5-3. Figure 5-23 shows the difference these parameters make. Increasing the overlap from 0 % to 50 % doubled the number of voxels in each plane. Decreasing the FFT pre shift window from 104 to 76, and decreasing the voxel size per passes at the first pass from 80 to 56, also increased the overall number of voxels.

Figure 5-23 shows the five parameter results studied at the centre slice (where the centre of the needle is assumed to be) showing the Z component ( $T_z$ ) of the displacement through the X direction. It can be seen visually that the displacement fields show very similar shapes. The increase of voxels allows for a greater distinction around the silicone surface. However, this does also increase the amount of noise that can be seen in the background (the dark blue area) of the scans. As the silicone was displaced during the  $\mu$ -CT experiment, as detailed in Section 5.2.1, the silicone shows the greatest overall displacement in yellow, with the silicone that did not displace (the silicone under the needle tip) in dark blue. The increase of the resolution from test one to test five shows the Z displacement magnitude was decreased from 0.05 to 0 mm.

## Experimental Measurements of Needle Penetration

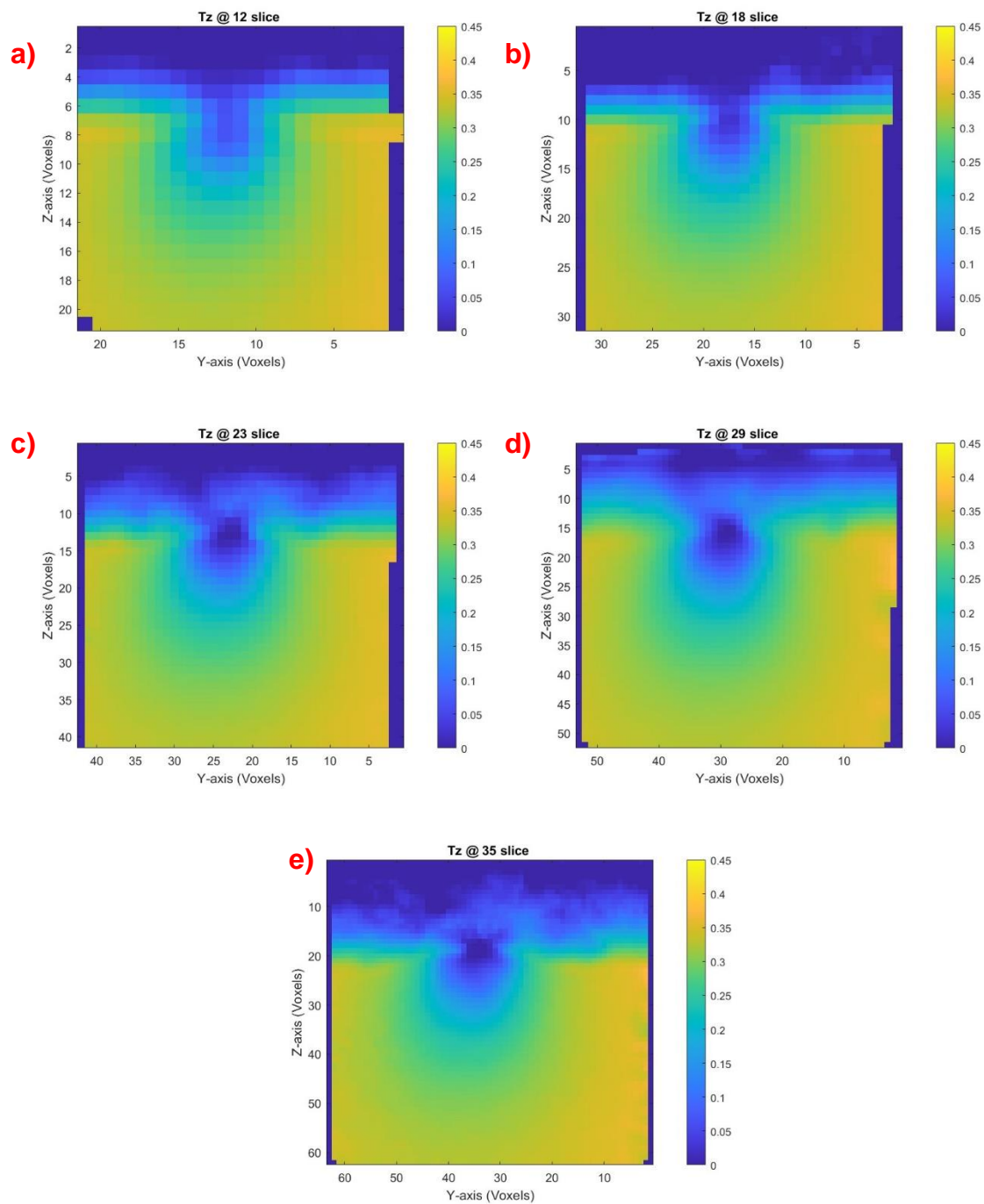


*Figure 5-23 - Parameter study for the first set of scans test 1 a) test 2 b) test 3 c) test 4 d) test 5 e). The resolution of the tests increase as the voxel size per pass and the FFT pre shift window is decreased and increased respectively.*

The second set of scans displaced the needle into the silicone, and a set of six tests were examined to see what difference changing the parameters in Table 5-3 caused on the displacement fields at higher displacements. The overlap was kept at 50 % for

## Experimental Measurements of Needle Penetration

all tests, the binning parameters were also maintained for all tests. Increasing the FFT from 208 to 88 voxels doubled the number of voxels in each plane, increasing the resolution and the displacement range seen around the needle.

Figure 5-24 shows the corresponding tests at the centre slice (where the centre of the needle is presumed to be) for the Z component of the displacement only through the X plane. The number of voxels required to capture the large strains that occur at the final needle displacement steps is a balance. Test 1 and 2, with around 30 voxels in each plane, show smooth displacement maps. Increasing this by 20 voxels starts introducing small amounts of noise (areas where there is no data), and larger areas at the top that don't have any displacement fields. Test 6 had 90 voxels in the Y direction which increased the noise drastically resulting in areas where the needle should be seen instead showing no displacement field. The maximum Z displacement also dramatically decreased as the resolution increased. With tests 1 and 2, -8 mm was the maximum displacement seen, with tests 3, 4 and 5 showing a maximum displacement of -5 to -6 mm. Test 6, however, had too much noise at the centre slice to show a displacement over -4 mm.

## Experimental Measurements of Needle Penetration

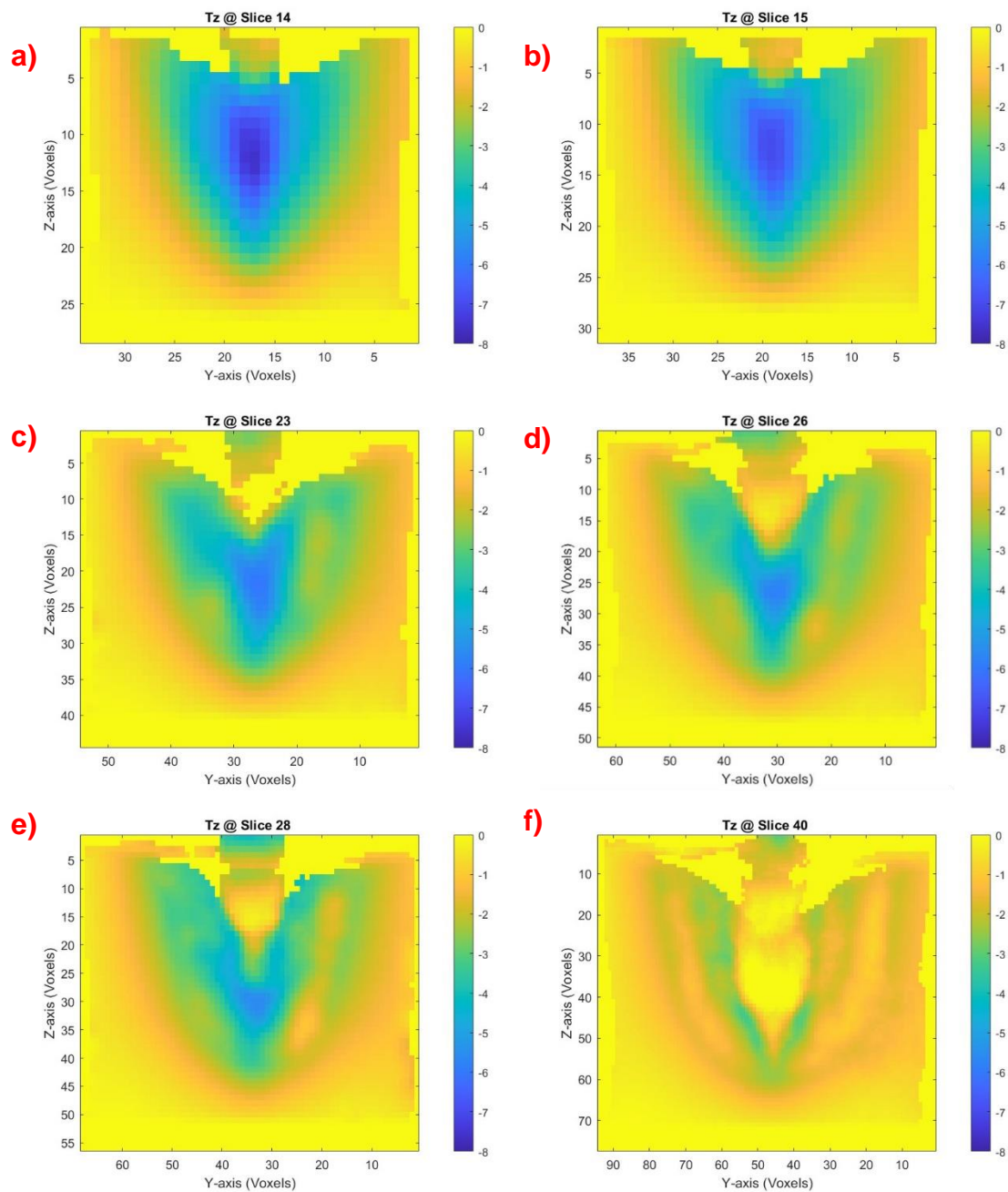


Figure 5-24 - Parameter study for the second set of scans, test 1 a) test 2 b) test 3 c) test 4 d) test 5 e) test 6 f)

### 5.3.4 First scans

The chosen test parameters, detailed in Section 5.2.5, were then examined further. Figure 5-25 shows an approximation of where the needle should be on the centre slice

## Experimental Measurements of Needle Penetration

showing the X, Y and Z components of the displacement. The Z component shows the silicone was displaced to 0.375 mm, with the silicone under the needle tip remaining at 0mm. The Y component of the displacement shows an area of positive and negative on either side of the needle with the centre of the needle tip at 0 mm. The X component of displacement at the centre slice when looking through the X plane shows an almost constant displacement of between -0.16 mm and -0.12 mm.

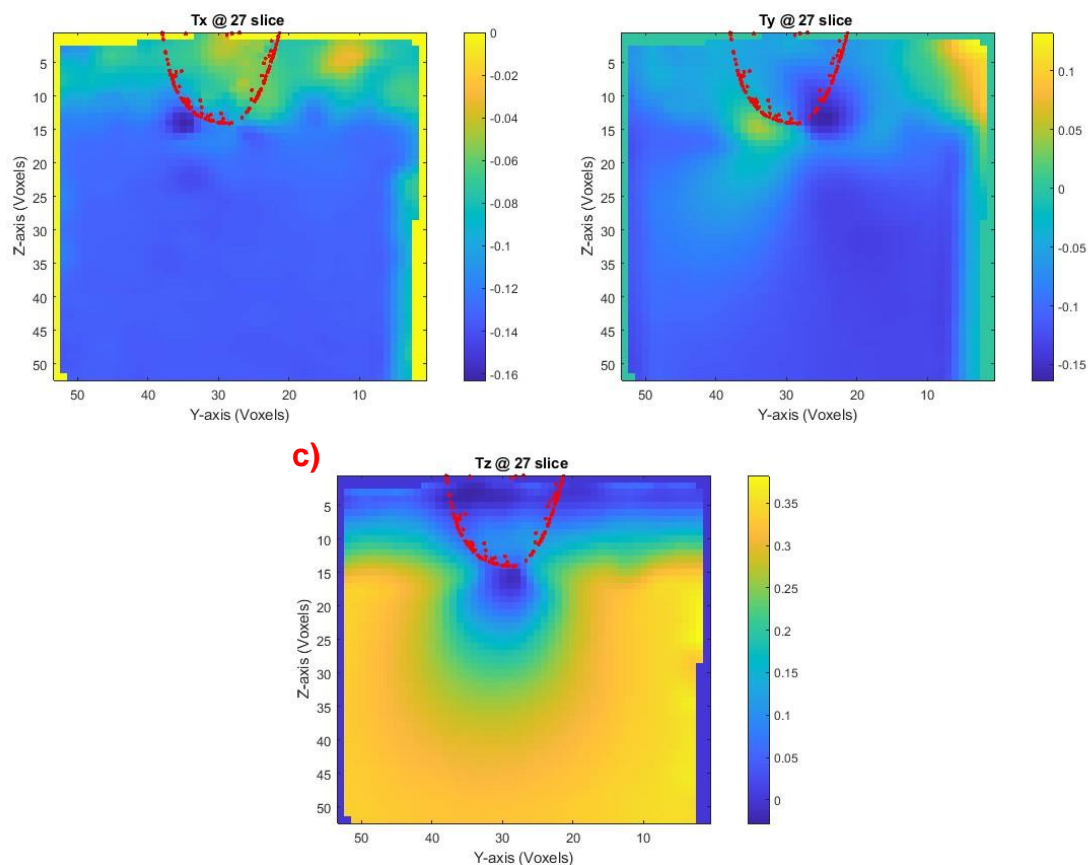


Figure 5-25 - Components of the displacement for test 4, X component a) Y component b) Z component c)

Figure 5-26 shows the six components of the strain for the first set of scans, the normal strain components ( $E_{xx}$ ,  $E_{yy}$  and  $E_{zz}$ ) and the shear strain components ( $E_{xy}$ ,  $E_{xz}$  and  $E_{yz}$ ).

## Experimental Measurements of Needle Penetration

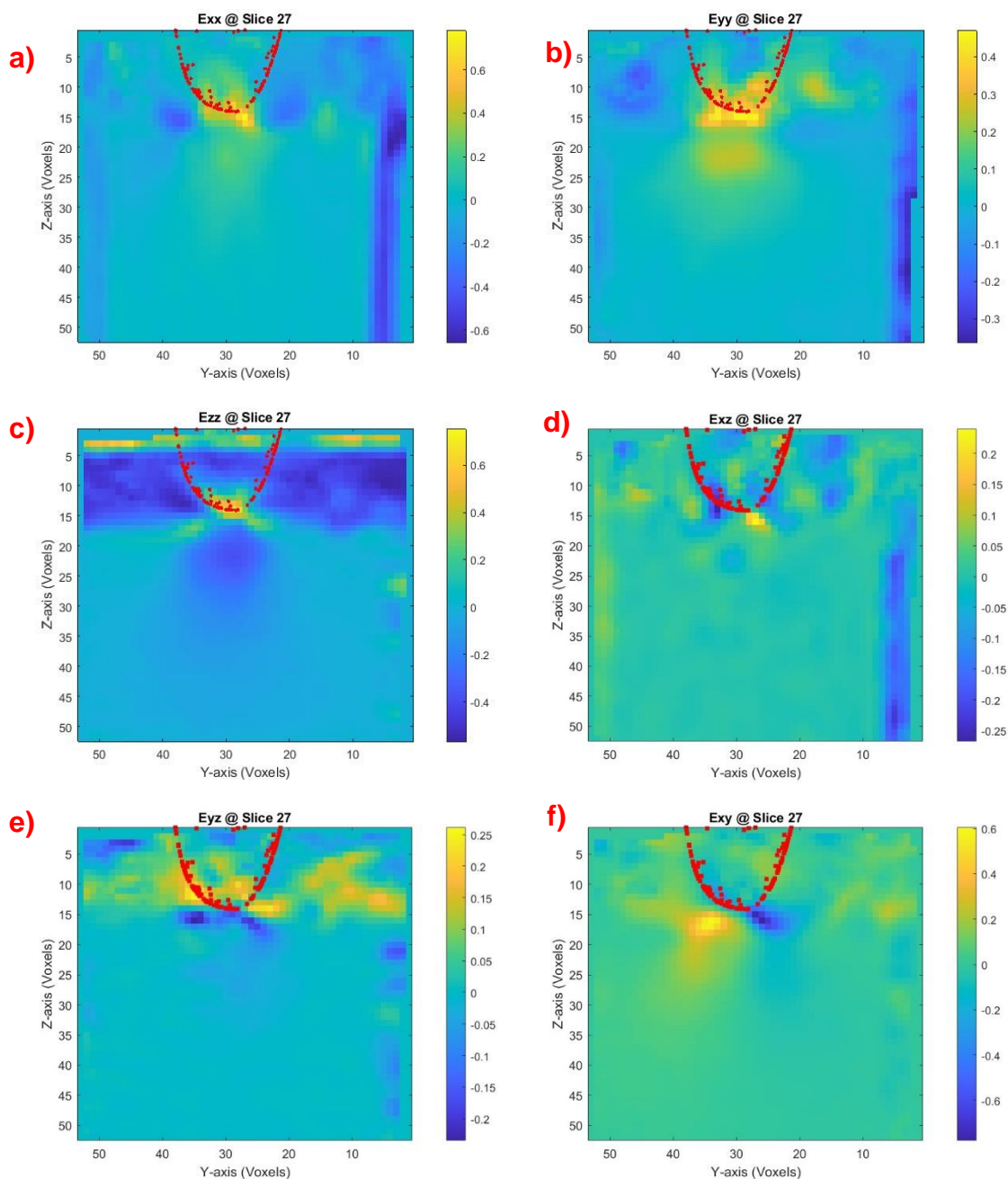


Figure 5-26 - Components of Lagrange normal and shear strain for test 4,  $E_{xx}$  (transverse strain) a)  $E_{yy}$  (axial strain) b)  $E_{zz}$  c)  $E_{xy}$  (shear strain) d)  $E_{xz}$  e)  $E_{yz}$  f)

The normal strain plots show uniformity along the main axes for each component.  $E_{xx}$  has a maximum strain cluster under the needle tip of 0.6 and  $E_{yy}$  has a similar cluster with a maximum of 0.4 with symmetry horizontally along the Y axis.  $E_{zz}$  gradually changes along the Z axes and is symmetrical across the Y, showing the compression of the material with the maximum under the needle tip of 0.6. This shows that there is

## Experimental Measurements of Needle Penetration

a potentially more deformation occurring in the X and Z axis occurring to this centre slice.

The shear strain plots are, as expected, less uniform than the normal strain plots, and regions of maximum and minimum strain is in the area where the needle tip is expected suggesting areas that are under both tensile/compressive and also shear strains. There is significantly higher strain in  $E_{xy}$  with a maximum of 0.6 and minimum of -0.6, than the components  $E_{xz}$  and  $E_{yz}$ , with maximums of -0.25 and minimums of -0.25.

### **5.3.5 Second scans**

The DVC displacement components for the second set of scans, which saw a needle displacement of 8mm, are shown in Figure 5-27 to Figure 5-29. For the centre slice and 10 slices before and after (approximately 3.1 mm) the centre is shown for the final step. Figure 5-27, showing the X component of the displacement, shows maximum displacement of 2 mm under the needle tip and behind the needle, and a minimum displacement of -1.5 mm in front of the needle, showing a symmetry across the Y axis.

## Experimental Measurements of Needle Penetration

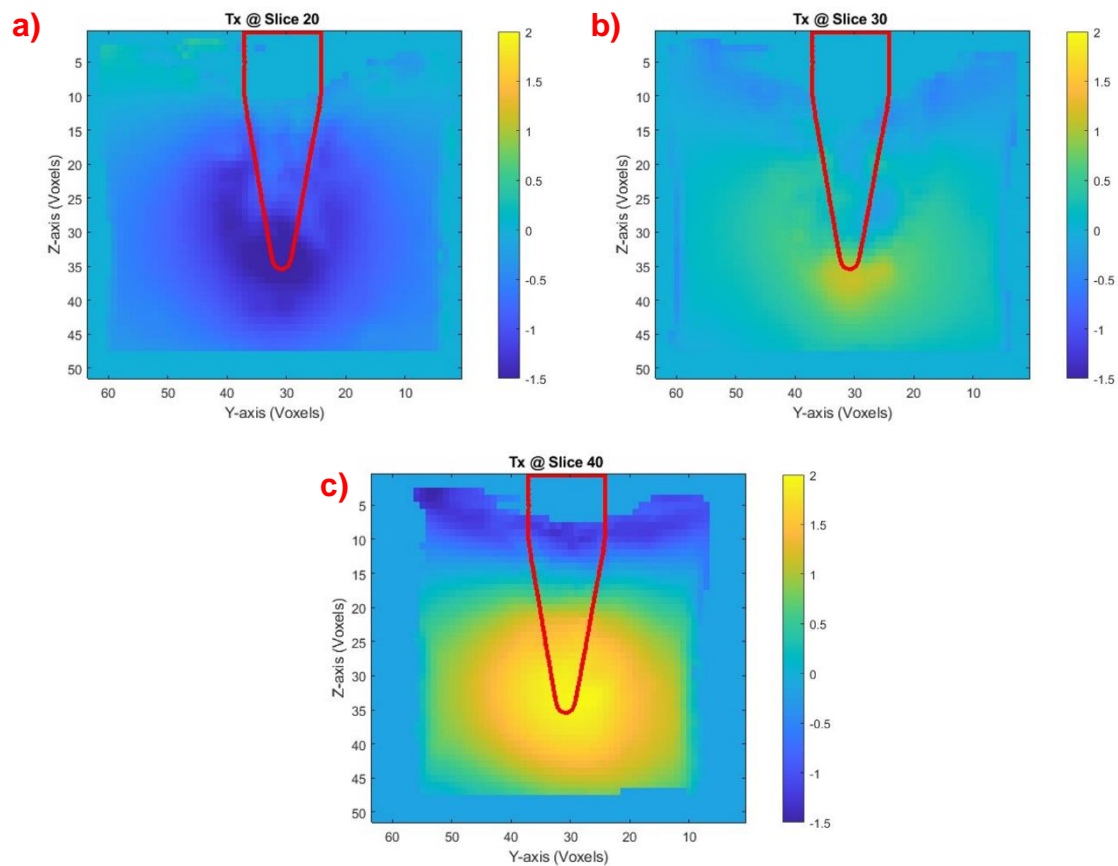


Figure 5-27 - X component of displacement at the centre of the needle and 10 slices before a) and after c) to view the displacement fields

The Y component of the displacement is shown in Figure 5-28. There are areas of compression and tension along the x axis on either side of where the needle is approximately positioned which is relatively symmetrical in front and behind the needle. The Y component also has maximum and minimum regions of 2 and -2 mm respectively likewise to the X component.

## Experimental Measurements of Needle Penetration

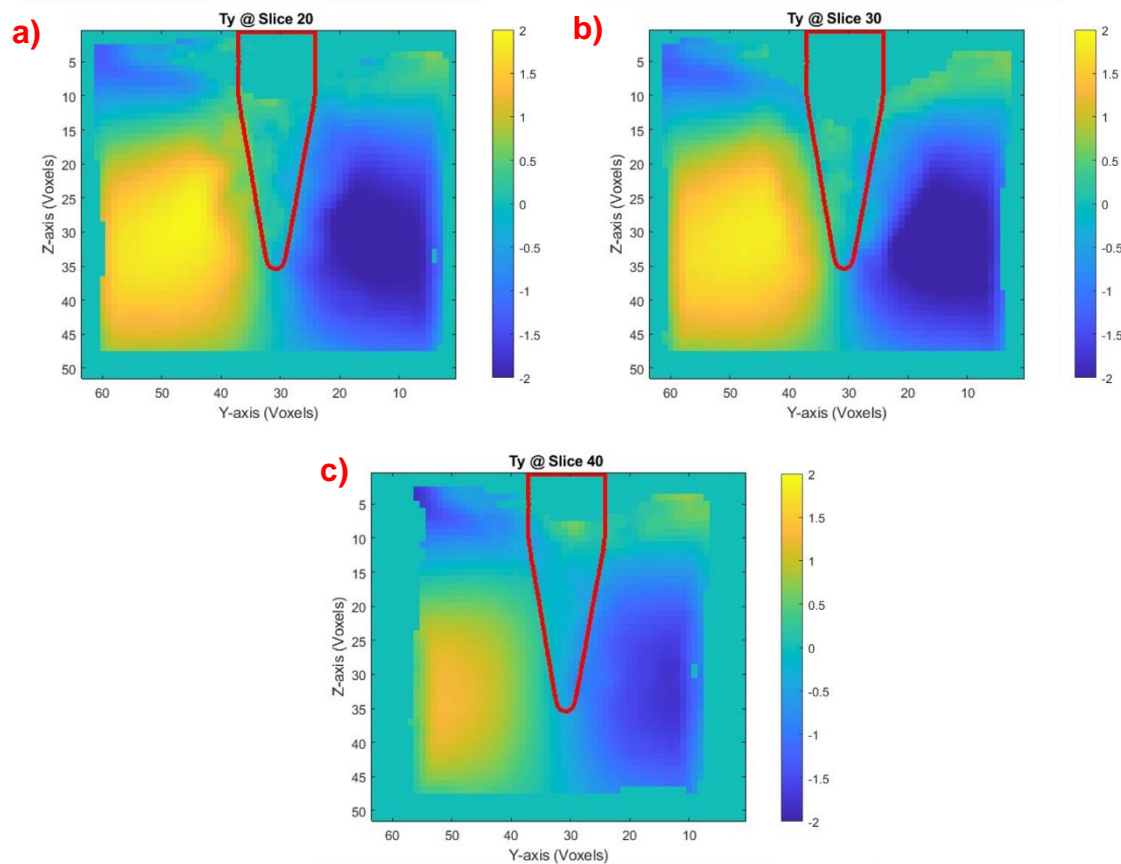


Figure 5-28 - Y component of displacement at the centre of the needle and 10 slices before a) and after c) to view the displacement fields

The Z component of displacement is shown in Figure 5-29 for the same centre and before and after slices as previously referenced. The areas of blue around the needle shows compressive values of up to -5 mm. The centre slice shows a distinctive gradient from the maximum displacement to zero, radiating from the approximate needle placement. Interestingly, the maximum regions of displacement are centred a small distance from the approximate edge of the needle, showing the compression of the silicone is not directly next to the needle edge. This could be due to the needle shape, or the materials resistance to immediate compression near the contact points.

## Experimental Measurements of Needle Penetration

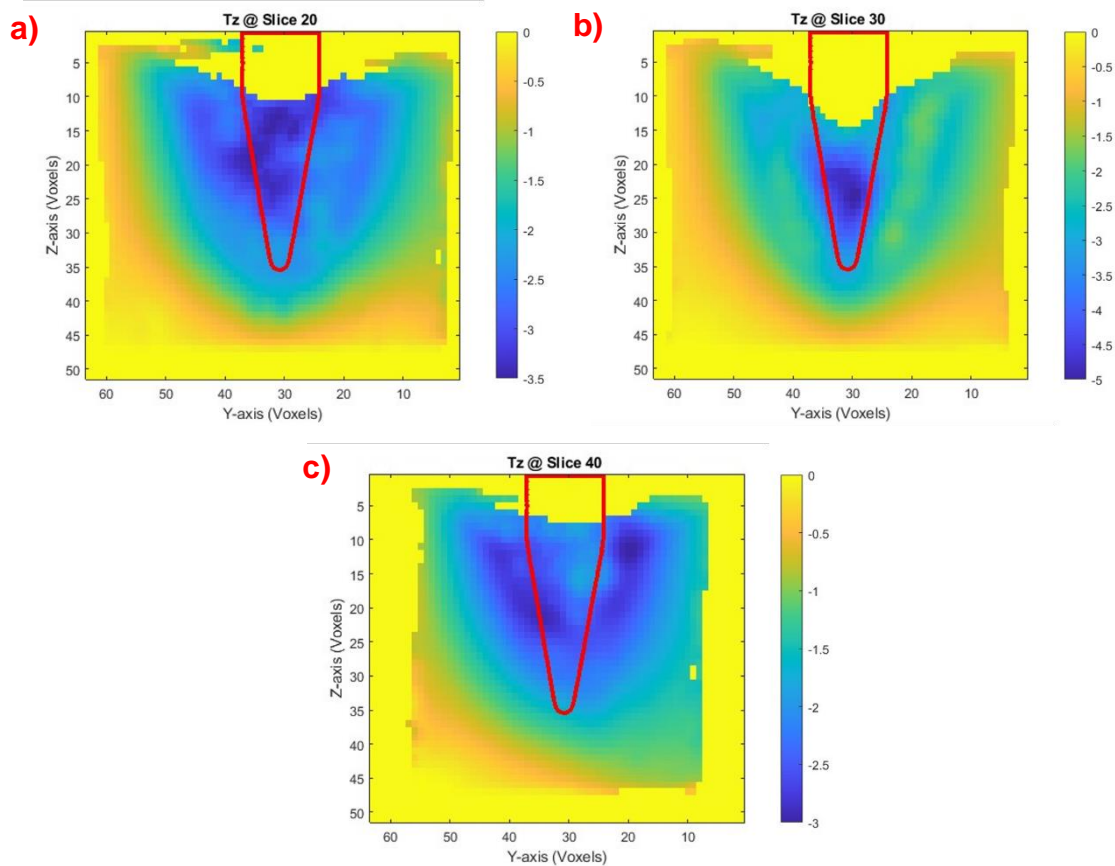


Figure 5-29 - Z component of displacement at the centre of the needle and 10 slices before and after to view the displacement fields

All six components of strain are shown in Figure 5-30, this is the centre slice with the FEA mesh of the needle for approximate needle placement. The normal strain components,  $E_{xx}$ ,  $E_{yy}$  and  $E_{zz}$ , all show clusters of strain maximums of 0.7 around the needle. The needle is not completely symmetrical which could explain the high cluster of yellow maximum of  $E_{xx}$ .  $E_{yy}$  shows a notable compression, yellow, around the needle edges and  $E_{zz}$  shows the compression directly beneath the needle tip and the angle of the needle. The shear strains,  $E_{xy}$ ,  $E_{xz}$  and  $E_{zy}$  shows a more mixed positive and negative regions which is indicative of the complex nature of material shearing and twisting. However, all three show the large amounts of compression expected from the large needle displacement. The maximum and minimum shear strain seen is around 0.2 and -0.2 respectively.

## Experimental Measurements of Needle Penetration

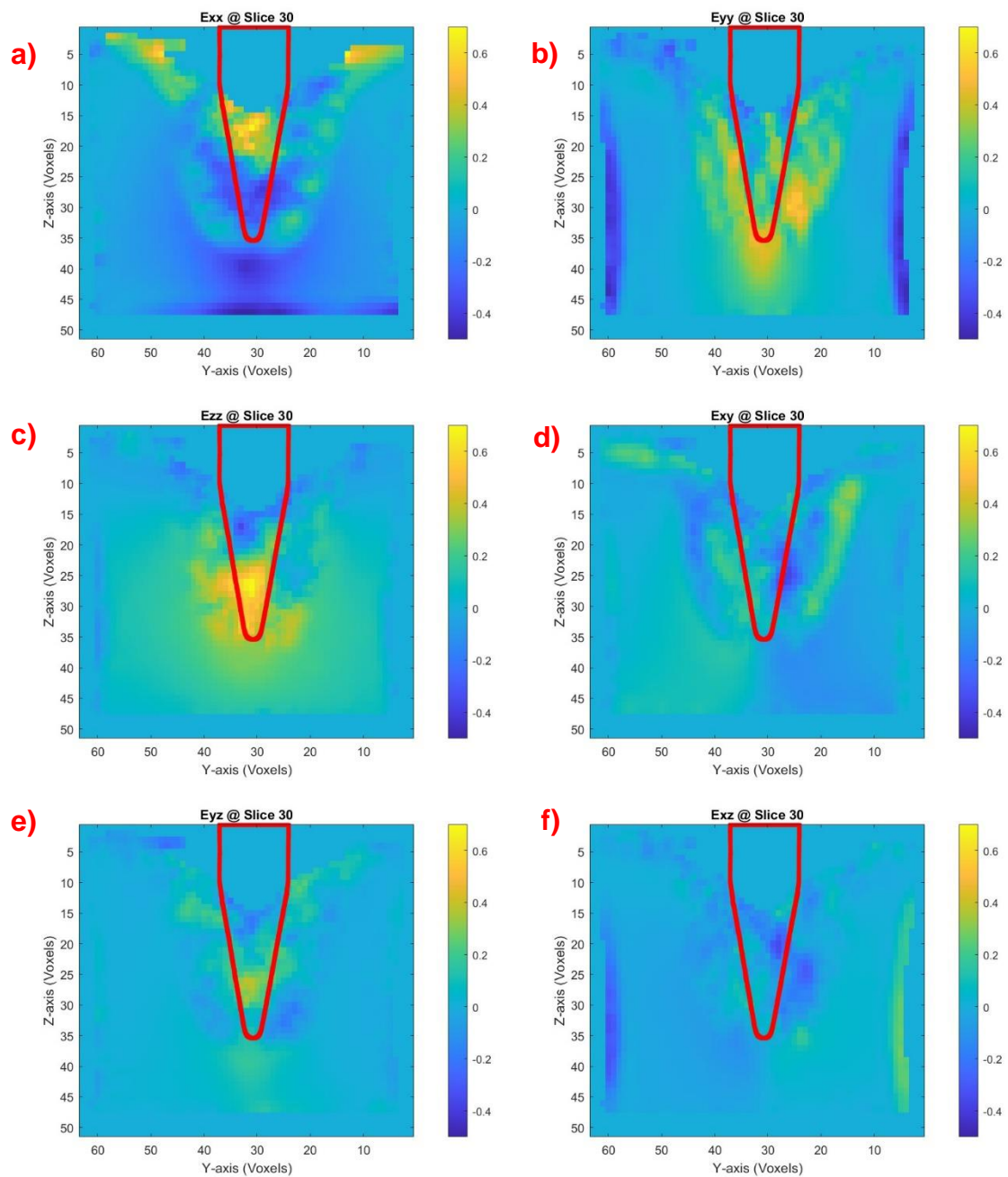


Figure 5-30 - Components of normalised and shear strain for test 4,  $E_{xx}$  a)  $E_{yy}$  b)  $E_{zz}$  c)  $E_{xy}$  d)  $E_{zx}$  e)  $E_{yz}$  f)

For comparison to first step of the FEA, at a displacement of 3.5 mm, the first DVC step is shown in Figure 5-31. The X, Y and Z component at the centre of the needle are shown.

## Experimental Measurements of Needle Penetration

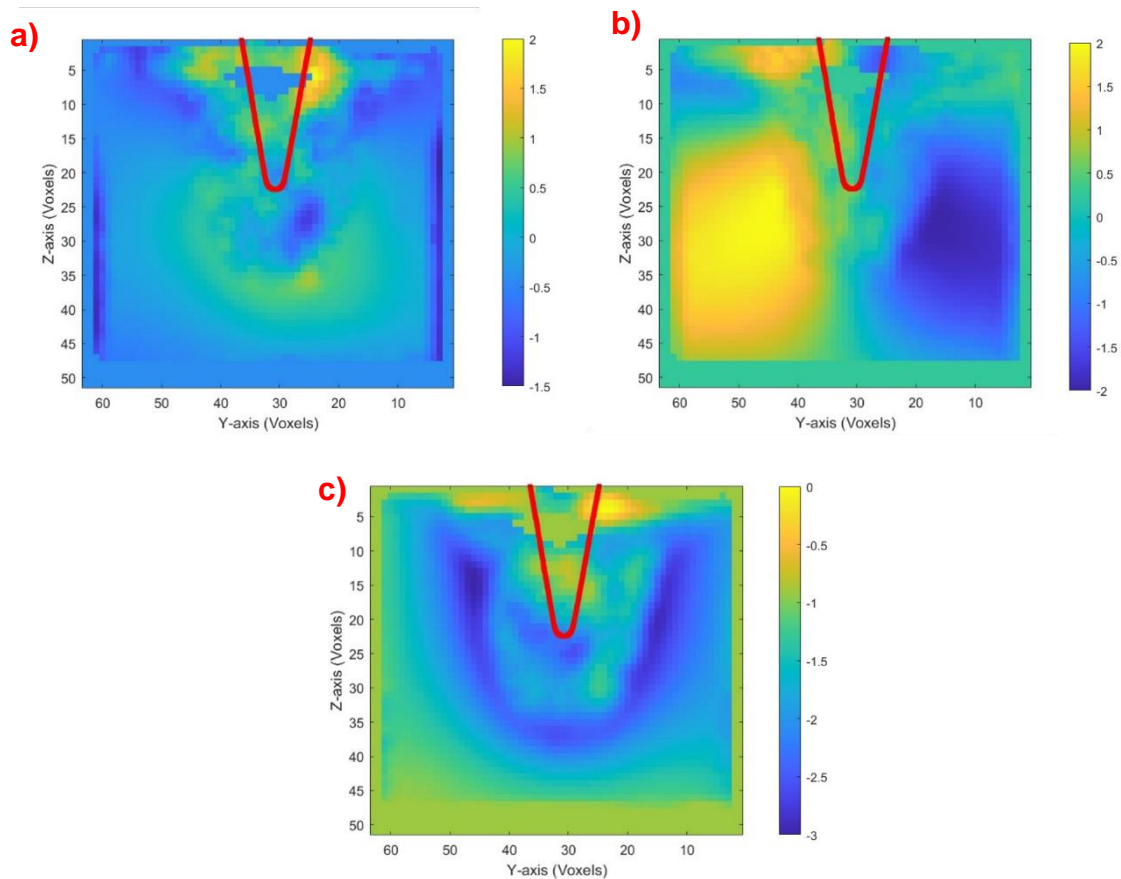
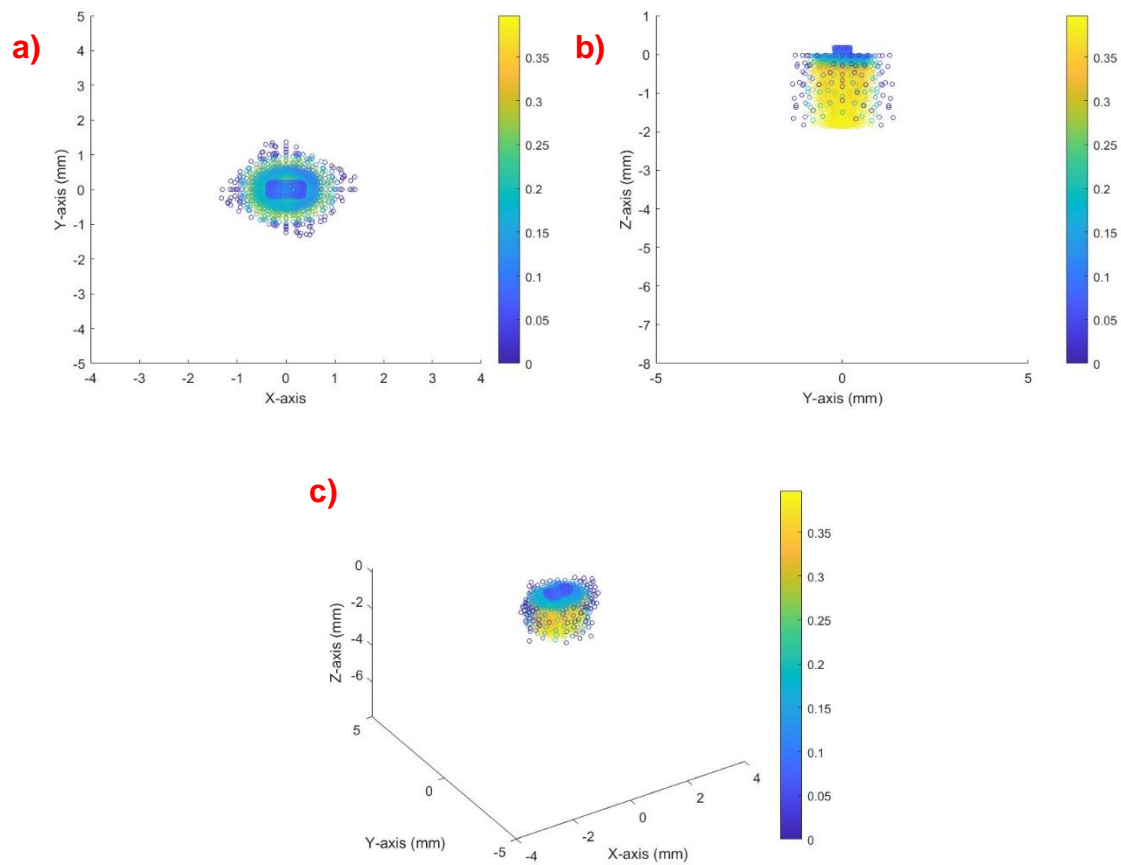


Figure 5-31 - The DVC components of displacement for the first large deformation scan step of 3.5 mm, X component a) Y component b) Z component c)

### 5.3.6 Interpolation

From MATLAB the interpolated DVC data can be seen in Figure 5-32. This is the predicted displacement magnitudes when interpolated onto the FEBio mesh imported, as described in Section 5.2.4. This shows the field of view used for the  $\mu$ -CT scans (approximately 2 mm in each axis). The maximum displacement seen for this interpolated data is around 0.375 mm.

## Experimental Measurements of Needle Penetration



*Figure 5-32 - Interpolated DVC data within MATLAB, showing the displacement magnitude at each mesh node*

As each step was interpolated onto the corresponding FEBio mesh step, and the data imported as explained in Section 5.2.4, the displacement fields can be viewed in FEBio. Figure 5-33 shows the displacement magnitude fields from FEBio.

### Experimental Measurements of Needle Penetration

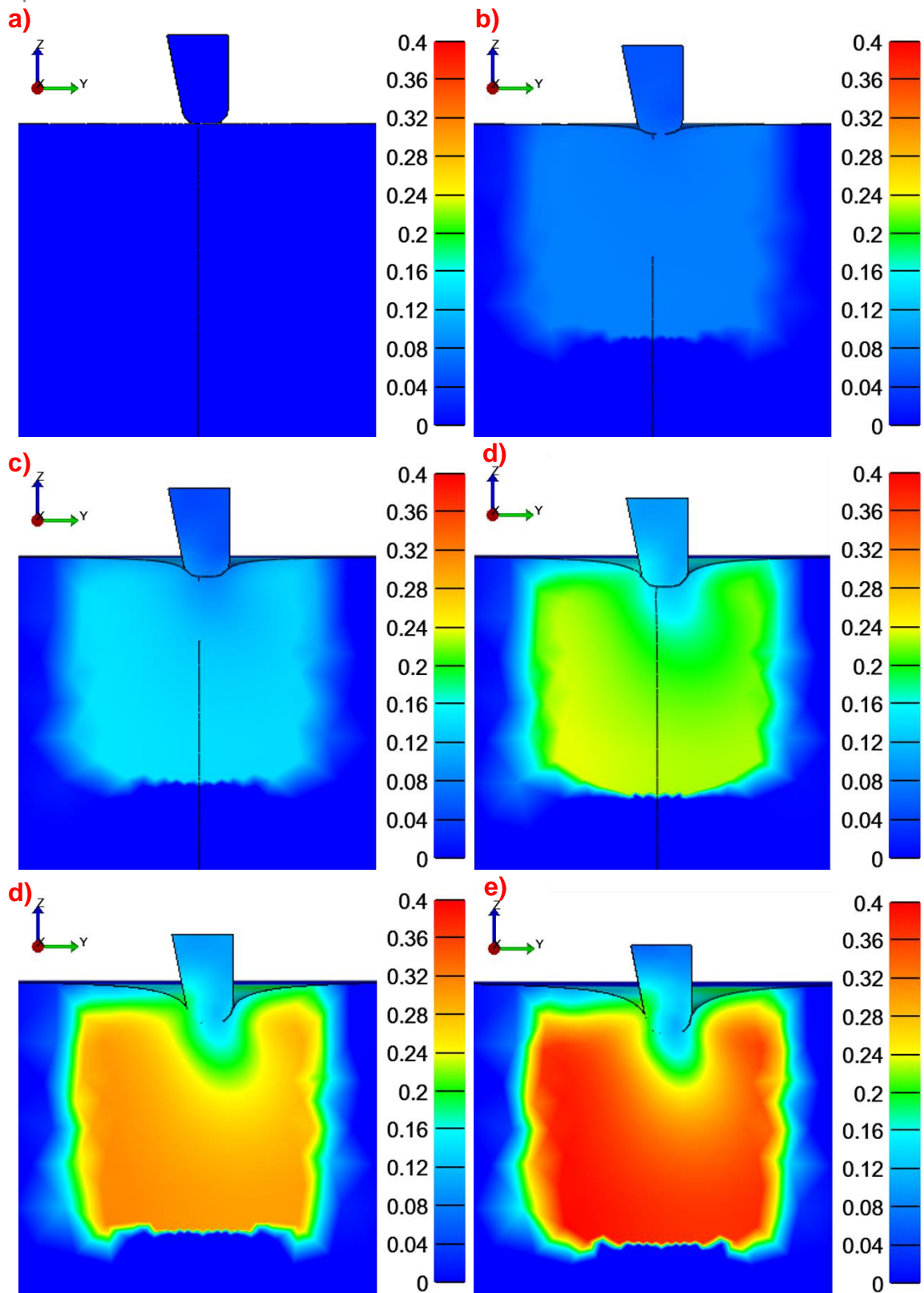


Figure 5-33 - Interpolated DVC data (the displacement magnitudes) imported into FEBio to view each displacement step of the needle

## Experimental Measurements of Needle Penetration

The interpolated data was then compared to the raw DVC data, experimental steps and the FEA displacement magnitudes. For this comparison the original experimental steps outlined in Section 5.2.1 were used. The maximum Z component was then found from the raw DVC data, with the corresponding Y and X components found to calculate the magnitudes. From the interpolated DVC data the maximum Z component was found for the final step, the corresponding node for this component was then used to find the displacement magnitudes for each time step. Finally, the displacement magnitudes for the centre node on the FEM was exported from FEBio. This node theoretically should have displaced the most as it is directly underneath the needle tip. Figure 5-34 shows this data.

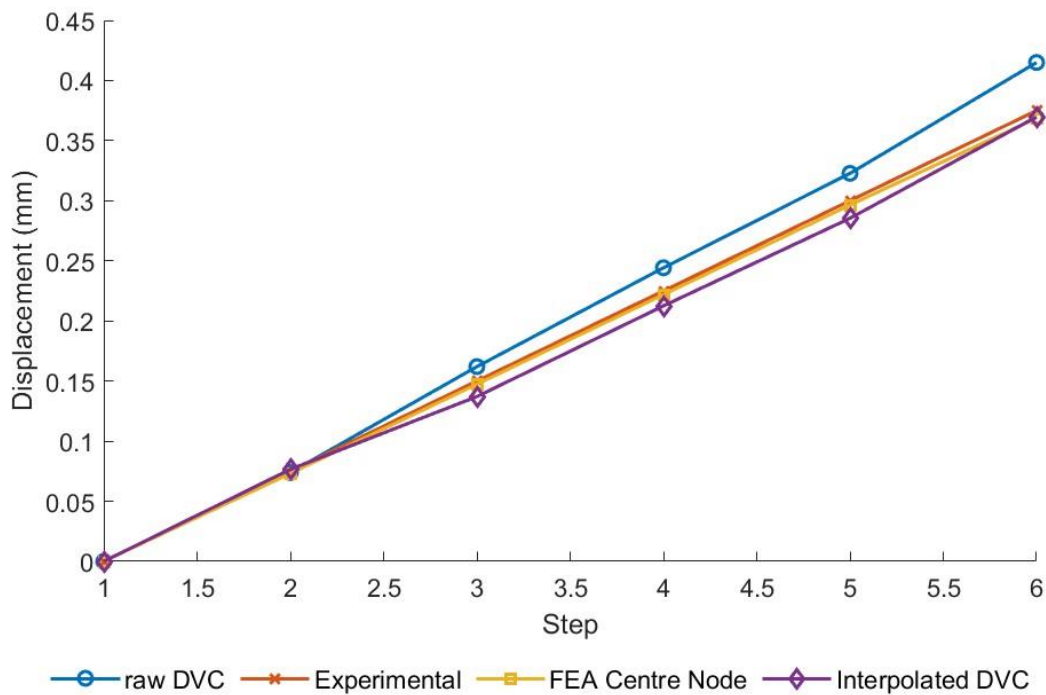


Figure 5-34 - comparison of the experimental steps used for the  $\mu$ -CT scans to the raw DVC data from MATLAB, the interpolated DVC data from MATLAB and the FEA data taken from the centre node

Table 5-4 shows the absolute errors for each step between the first input data set and the second input data set. The overall RMSE and the overall MAE is also shown in the table. RMSE measure the overall magnitude of the error for all six steps, with the MAE

## Experimental Measurements of Needle Penetration

measuring the average magnitude of the error over the six steps. The percentage error is also shown, which is the average percentage error of the first input data set relative to the second input data set. The calculations used for these errors are detailed in Chapter 4.6.

*Table 5-4 - Input comparisons with their absolute errors per step and overall RMSE and MAE for the compared inputs*

Input 1	Input 2	Step absolute error (mm)					Overall RMSE (mm)	Overall MAE (mm)
		2	3	4	5	6		
Raw DVC	Experimental steps	0.0011	0.0120	0.0192	0.0228	0.04	0.0210	0.0158
Raw DVC	Interpolated DVC	0.0026	0.0249	0.0317	0.0373	0.0453	0.0291	0.0236
Raw DVC	FEA centre node	0.0008	0.0146	0.0223	0.0263	0.0462	0.0243	0.0184
Interpolated DVC	FEA centre node	0.0034	0.0103	0.0094	0.0110	0.0010	0.0074	0.0058

It can be seen from Figure 5-34 and Table 5-4 that there is difference between the raw DVC data, interpolated data and FEA centre node to the second step. The absolute error at the fourth step increases to between 0.01 and 0.025 mm. At the fifth and sixth step, the absolute error increases further to over 0.045 mm between the raw and interpolated DVC data. From step three, the raw DVC data overestimates the displacement magnitude when compared to the set experimental steps and the FEA centre node. On the other hand, the interpolated DVC data chosen underestimates the displacement magnitudes, but with the smallest absolute data error at step six at 0.001 mm.

## 5.4 Discussion

A set of scans were performed at larger needle displacements using a Diondo 5 scanner, which offered a larger FoV (8 mm compared to 2 mm) but at a reduced resolution (3  $\mu\text{m}$  instead of 2  $\mu\text{m}$ ). This setup also reduced the scan time to 1 hour per step. While this larger displacement allowed for greater overall needle movement, the increased intervals between steps could introduce challenges during DVC data

## Experimental Measurements of Needle Penetration

processing, potentially causing issues with deformation accuracy between the initial four steps.

Despite the challenges posed by the large deformation scans, these CT scans offer unprecedented insights into the interaction between the needle and silicone. The progressive indentation captured in Figure 5-22 allowed for detailed observation of how the silicone responded under increasing load, close to the approximate point of puncture. Firstly, the deformation of the silicone is observed around the needle tip, which becomes more pronounced with each step. In particular, the top surface of the silicone begins to angle and conform more tightly around the needle's edge. This suggests that the silicone exhibits significant elastic deformation, enabling it to follow the contour of the needle during the initial stages of indentation.

Additionally, as the indentation deepens, particles near the needle tip move due to the material around them stretching and move along the direction of indentation, indicating localised strain. The visibility of these particles in the images enables the tracking of their deformation path. The degree of particle movement near the tip compared to areas further from the needle also highlights strain localisation and could suggest areas where material failure or tearing may initiate if loading continues beyond this point.

Moreover, the shape of the deformed region surrounds the needle tip, particularly the gradual transition from compression to stretching in the silicone, can offer clues about the material's properties. As the indentation deepens, the visible symmetry of the deformation field is maintained, which is a positive indicator that the loading is uniform. However, the scans can only be viewed in one plane direction at a time. Viewing the scans in 3D could provide a more comprehensive understanding of the material behaviour and reveal any experimental imperfections that may be hidden in the current 2D slices. This would be particularly useful in refining future needle designs as it could help identify subtle inconsistencies in deformation or material properties that aren't visible in the current set up.

Digital volume correlation is a powerful technique used to measure 3D displacements and strain fields within materials. In this study, this technique has been employed to evaluate two sets of  $\mu$ -CT experiments: A small deformation study with a needle

## Experimental Measurements of Needle Penetration

displacement of 0.375 mm and a large deformation study with displacements of 8 mm. As discussed in Section 3.5, the use of the silicone Ecoflex-30 as a skin substitute was deemed acceptable, with the addition of TiO<sub>2</sub> particles as fiducial markers within the silicone sample deemed acceptable for DVC tracking. DVC was chosen over traditional imaging processes such as DIC because it allows for the observation of internal deformations, whereas DIC measures only surface displacements.

The image collection process, outlined in Section 5.2.1, required careful selection of key parameters in DaVis to optimise the results. As shown in Table 5-2 and Table 5-3, variations in parameters such as FFT pre-shift voxel size, the number of passes, voxel size, overlap percentage, and search radius were systematically tested to evaluate their effect on the displacement field measurements. The variation in voxel size across the different tests (ranging from 64 to 208 voxels) directly influenced the spatial resolution and noise level in the resulting displacement fields. Larger voxel sizes (such as test 1, Figure 5-23 a)) improved the spatial coverage but at the cost of reduced strain precision, as the smoothing effect of larger voxel sizes can mask small, localised deformations. On the other hand, smaller voxel sizes (such as test 5 for the first scans, and test 6 for the second scans Figure 5-24 b)) provided higher strain precision but increased the risk of noise in the data, leading to less clear deformation patterns and reduced accuracy.

The overlap percentage (0 %, 50 %, 75 %) also had a notable effect on the spatial resolution and strain precision. Higher overlap percentages (e.g. 75 %) tend to enhance spatial resolution, which is crucial for identifying detailed local deformation around critical points, such as near the needle tip. However, this could come at the expense of strain accuracy as an excessive overlap can introduce some redundancy in the data. Redundancy from excessive overlap reduces strain accuracy because highly correlated subsets contain less independent information, which can smooth out true strain gradients and introduce numerical artefacts during correlation.

Lower overlap settings (e.g. 0 %) provide better strain precision but can lead to a less detailed spatial resolution, making it harder to track smaller deformations. Therefore, for the larger deformation scans, it was decided to keep the overlap at 50 % and only increase the voxel sizes for the parameter test to keep a balance between spatial

## Experimental Measurements of Needle Penetration

resolution and strain accuracy. This also allowed the computation strain to be kept at a minimum, as the scans were just under 5 GB each, with four passes per scan the computation effort was already high. The balance between these input parameters can significantly impact the output results, as seen demonstrated by the parameter studies for both the small and large deformation scans [Figure 5-23 and Figure 5-24].

The parameters chosen for the final analysis were selected based on a trade-off between the noise levels and the definition observed in the visual output. For instance, the larger voxel sizes in test 1 for the small deformation scans offered better spatial coverage, which was beneficial for tracking large deformation patterns. However, for these scans the deformation was only 0.375 mm and therefore could use a higher overlap focused on the smaller strain details near the needle tip, such as tests 3 to 6. When observing test 4 and 5, there was better definition of the displacement field due to the number of voxels, so therefore test 4 was chosen. The parameters chosen for the second scans, such as those in test 2 (192 FFT pre-shift voxel size with 50% overlap) provided a good balance between spatial resolution and strain precision, allowing for a stable output. However, decreasing the FFT pre-shift voxel size to 104 voxels allowed for a better level of strain precision around the predicted needle location that is ideal at the larger deformations encountered within these scans.

It is important to note that these parameter studies were limited in scope, and the variation in parameters introduces potential sources of error, particularly in terms of strain localisation and precision. The choice of voxel size and overlap can significantly affect the accuracy of strain measurements, especially in high strain regions like the needle tip, where precise tracking of material deformation is crucial. In the higher deformation scans, larger voxel sizes may smooth out crucial localised strain patterns, while smaller voxel sizes, although more accurate, can introduce higher levels of noise. Additionally, the search radius and overlap settings directly affect how much data is averaged across adjacent voxels. While this can enhance clarity in some regions, it can also obscure critical strain patterns or introduce artefacts that misrepresent the actual deformation fields. Linking back to the material criteria discussed in Section 3.2, the presence and distribution of fiducial markers within the silicone play a key role in the accuracy of displacement tracking.

## Experimental Measurements of Needle Penetration

Several steps were taken for the image alignment process within MATLAB. MATLAB has various toolboxes commonly used in medical and biomedical research with MRI and CT scans, including the Orthoslicer. Figure 5-9 shows the Z component of displacement through Orthoslicer, which allowed for viewing 'slices' through the data to determine which 2D figures to study further. However, a main drawback of using this DVC image processing method was the lack of feature outputs within the data. This necessitated additional steps in the registration process, including the use of the original  $\mu$ -CT scans and components of the FEBio mesh imported into MATLAB [Figure 5-15]. Overlays of the CT scan, needle nodes, and displacement vectors were used to verify the DVC orientation and ensure correct scaling. While the  $\mu$ -CT scanned resolution was  $1.996 \mu\text{m}$ , DaVis scaled the data to a resolution of  $3 \mu\text{m}$ , necessitating the scaling of the exported voxels to match this resolution for accurate visualisation of the FoV. As discussed in Section 5.2.1.1, the initial  $\mu$ -CT images were adjusted within ImageJ to facilitate viewing, resulting in the displacement and strain components in the DaVis data file being in the wrong order.

To determine the image processing parameters for further examination, a parameter study was conducted for both sets of scans. This study focused on the displacement components, primarily the Z component, as the needle displacement was in the Z direction. For the first set of scans, it was found that the main parameter affecting the number of voxels was the overlap percentage. Increasing the overlap from 0 % to a balanced 50 % (tests 1 to 3) doubled the number of voxels, potentially allowing for visualisation of crucial material deformations. However, pairing this with an initial FFT pre-shift window that was too low (i.e. a small initial voxel size) introduced noise into the scans, which could affect the data exported. This observation was supported by the parameter study for the second set of scans.

Increasing the needle displacement from 0.375 mm to 8 mm represents a substantial increase in material deformation, which can significantly affect the required parameters. Small strains would likely benefit from increased spatial resolution to measure finer distinctions and small-scale deformations. For this study, a balance between strain precision and spatial resolution was used, although further investigation is needed into how the overlap affects the data output. Large amounts of noise were noticeable when the FFT pre-shift window was set below 100 voxel size.

## Experimental Measurements of Needle Penetration

However, smaller voxels allowed for a more accurate visual representation of the silicone shape, as seen in the  $\mu$ -CT scans [Figure 5-21 and Figure 5-22].

The initial step in analysing the DVC data was to view the displacement components per voxel for the chosen test parameters (test 4). Figure 5-25 shows the X, Y, and Z components of displacement at the central slice, approximately the centre of the needle. The needle mesh was overlaid onto these displacement fields to approximate where the maximum and minimum displacements were in relation to the needle, as this feature is not visible in the DVC data. This revealed a distinguishable compression field under the approximate needle tip, which is expected since the greatest compression occurs under the needle tip. Additionally, distinct clusters on either side of the needle tip were observed for the Y component of displacement, showing positive and negative areas, similar to the displacement fields observed in the FEA [Figure 4-20]. This is in line with the expected mechanisms of needle penetration, where the needle not only compresses the material directly under the needle tip but also induces lateral deformation such as stretching the sides of the skin.

While the Z component of the DVC data field is visually similar to the Z component of the FEA field and numerically close with maximum values of 0.375 mm and 0.373 mm respectively, the maximum and minimum numerical values of the X and Y components of displacement on the centre slice differ significantly. The DVC Y component shows a maximum of around 0.1 mm and a minimum of -0.15 mm near the needle tip, while the FEA shows a maximum of 0.039 mm and a minimum of -0.047 mm. Similarly, the X component for the DVC has a minimum of -0.16 mm, and as the view is through the X plane, the radiating fields cannot be seen. The DVC results show more significant displacement in the Y direction, which could be attributed to the material's response to lateral forces or the needle asymmetry and orientation. Understanding these displacement fields and the real-world material responses can lead to suggestions on future work of improving the accuracy of directional components, possibly through enhanced meshing or material models within the FEMs.

In contrast, the strain fields for the DVC components match visually, with minimal numerical differences to those seen from the static model [Figure 4-21 and Figure 4-22]. The normalised strains,  $E_{xx}$ ,  $E_{yy}$ , and  $E_{zz}$ , all exhibit similar strain fields with

## Experimental Measurements of Needle Penetration

maxima localised under the approximate needle tip.  $E_{xx}$  and  $E_{zz}$  have maximum strains of 0.7 and minimum strains just over -0.6, with some negative strain appearing as noise in the background space of the scan. In comparison, the maximum strain observed in the FEA is 0.48. Visually,  $E_{zz}$  shows an intriguing strain field with an area of low strain (between -0.2 and -0.4) under the maximum strain, indicating some tension within the material beneath the main compression. This is explained by the shear strain fields, with  $E_{xy}$  and  $E_{yz}$  showing two clusters of high and low strain on either side of the needle tip, indicating material deformation along more than one axis.

Visually, the  $E_{xy}$ ,  $E_{yz}$ , and  $E_{xz}$  strain fields from the FEA resemble those seen in the DVC data. For  $E_{xy}$ , an area of positive and negative strain radiates diagonally away from the needle tip.  $E_{yz}$  displays two bands of positive and negative strain, with positive strain around the needle edge as the material is pushed outward, and negative strain just under the needle tip where the material is primarily pushed downward. This downward change in material deformation is also seen in the cluster of positive and negative strain in  $E_{xz}$ , with strain fields on either side of the needle radiating diagonally downwards. Both the FEA and DVC show larger strains in  $E_{xz}$  than in  $E_{xy}$  and  $E_{yz}$ . However, there are significant numerical differences: DVC's  $E_{xy}$  and  $E_{yz}$  have maximum and minimum strains of 0.25 and -0.25, whereas the FEA values are 0.117 and -0.118 for  $E_{xy}$  and 0.24 and -0.24 for  $E_{yz}$ . Additionally, the DVC's  $E_{xz}$  strain ranges from 0.6 to -0.7, compared to the FEA's 0.23 to -0.22. This indicates that the DVC data shows deformation more dependent on the  $E_{xz}$  component, which is expected as the silicone is moving in the Z direction, while the needle is symmetrical in only one plane. Differences in the FEA could be due to adjustments made to the FEA material models to match the load-displacement curves of the original needle puncture, as discussed in Section 4.4. The reduction of the silicone bulk modulus to 0.1 MPa in the FEA to match the load-displacement also affects the visual appearance of the silicone in  $\mu$ -CT scans and may not fully align with the strain fields derived from the scans.

In addition to the factors already discussed, there are several other potential reasons for the differences between the FEA and DVC strain fields. The boundary conditions used in the FEA model are simplified and therefore might not be a perfect match for the experimental set up. In addition to mitigate the effects of the boundary conditions

## Experimental Measurements of Needle Penetration

on the static model output, it was ensured that the silicone block was sufficiently large enough to ensure no deformation would be close to the block boundaries. The dynamic model was also reduced to a quarter model for computational efficiency, introducing additional boundary condition simplifications that could affect the FEA results. One of these boundary simplifications was the assumption the needle was symmetrical, when the needle is asymmetrical in one direction. Whilst this is assumed not to affect the static model due to the low displacements, where the deformation did not reach the edges where the asymmetry of the needle would influence the deformation, it could have impacted the dynamic model. The asymmetry of the needle, which shows a flat length on one side and a tapered angle on the other, could lead to slight variations in deformation patterns especially during larger displacements. This could be an important factor to address when looking at needle geometry implications to puncture performance.

The FEA models also represented the silicone as a homogeneous material, whilst in the experiment the silicone contained the  $\text{TiO}_2$  particles for DVC tracking. These particles could have influenced the material's local deformation behaviour which are not represented in the FEA leading to different strain distributions. Another factor not considered is the possibility of manufacturing defects with the silicone; the silicone for the experiment was hand cut with a scalpel from a larger material sample, which could have introduced thickness differences not captured within the FEA models. There may have also been slight differences in the experimental set up versus model assumptions. This was minimised by using the needles directly from the CT scans, however subtle misalignments or variation in needle orientation could still be possible due to the lack of distinguishable features in the DVC data. This could affect the strain field recorded by the DVC, in contrast the FEA assumes perfect symmetry and alignment.

On the other hand, the DVC results can be influenced by several factors, including image resolution, the size and spacing of  $\text{TiO}_2$ , and the grid spacing of the displacement data, all of which contribute to discrepancies when comparing the DVC and FEA results. As mentioned previously, the voxel size and overlap can significantly influence the accuracy of the DVC data. With only a small parameter study conducted,

further fine tuning of these parameters could reduce discrepancies in the strain fields or capture finer details in the deformation around the needle tip.

The TiO<sub>2</sub> particles, which were included in the imaging but not the FEA model, introduce more challenges. The size and spacing of these particles affect the tracking capabilities of the DVC and therefore how the displacements and strains are captured. Since these particles are the markers for the DVC, their spacing must be small enough to accurately capture displacements in fine regions, but still random enough in size and distribution. The lack of inclusion in the FEA model means that the simulation does not account for the physical distribution of these markers, however they are included in the material model used so the discrepancies should be minor for these models. The grid spacing of the displacement data also affects the final resolution and ability to see fine detail in low and high strain areas.

The lack of distinguishable features in the DVC data also posed challenges in correlating the 3D data. To address this, two steps were introduced: first, a line of code matched the needle nodes to the minimum area of displacement magnitude. Since the silicone was displaced, voxels with zero (or near-zero) displacement were likely under the needle tip where no movement occurred. The second step involved rotating and translating the needle nodes to match the CT scan viewed through the Z plane. Once these rotation and translation matrices were determined, they were applied to the DVC data [Figure 5-18]. It was decided not to move the FEA mesh nodes within MATLAB, as the additional steps could introduce uncertainties and potential errors.

While MATLAB offers valuable coding capabilities, it lacks the data manipulation features found in FEBio, such as easily adjusting field plots, adding multiple plane splits, and removing components. To compare displacements at nodes rather than whole voxels, interpolation was required. It was decided to interpolate the higher-resolution DVC data to match the lower-resolution FEBio mesh and import the interpolated DVC data back into FEBio. The interpolation algorithm used within MATLAB was a weighted sub-algorithm with a range search. Given the FoV of the DVC was 2 mm and voxel placement was approximately 0.04 mm apart, the range search was set to 0.16 mm. To analyse differences between interpolated DVC data

and FEA output, each scan step used for the  $\mu$ -CT was interpolated to assess errors at each step rather than just the final step.

Figure 5-32 illustrates the interpolation of the DVC displacement data onto the FEBio mesh along with the node placement within MATLAB. In contrast, Figure 5-33 presents this interpolated DVC displacement data within FEBio. However, discrepancies were noted between the maximum displacement magnitudes observed in MATLAB and those in the interpolated FEBio data. To evaluate these inconsistencies, the maximum Z displacement component for the raw data was identified at each scan step, and the corresponding X and Y components were used to check displacement magnitudes. Similarly, the maximum Z component for the interpolated DVC data was determined, and the displacement magnitude at each step for the corresponding node was assessed. These two datasets were then compared to the experimental steps used for the  $\mu$ -CT scans, specifically the displacement magnitude for the centre node of the FEBio mesh, which should exhibit the greatest displacement as it is directly under the needle tip.

The FEBio node displacement matched exactly with the experimental steps. However, the raw DVC data showed an overestimation of displacement magnitudes from the 3rd to 6th step, whereas the interpolated DVC data underestimated these magnitudes. The raw DVC data had an overall percentage error of 7.25 % and 8.48 % compared to the experimental and FEA steps, respectively. In contrast, the interpolated DVC data exhibited a smaller percentage error of 3.97 % relative to the FEA data, with an absolute error of only 0.001 mm at step 6. This indicates that errors occurred during the interpolation process as the DVC data was estimated to fit the node placement. The closer alignment of interpolated data with the experimental steps suggests that the raw DVC data contained some processing errors, potentially due to noise or inaccuracies in the maximum data selection, with errors increasing from 0.012 mm to 0.04 mm from step 2 to step 4. Additionally, the lack of distinguishable features in the raw DVC data may have led to slight inaccuracies in rotation and translation.

The field maps for each displacement component for the second set of scans are shown in Figure 5-27 and Figure 5-29. These figures display the centre slice of the DVC data, where the needle's centre is located, along with 10 slices before and after

## Experimental Measurements of Needle Penetration

the centre. This visualisation allows for a detailed view of the complex Y and X components of displacement. In the FEM for the static model, the X and Y components exhibit radiating fields away from the needle along their respective axes. This pattern is evident in the large deformation scan DVC fields as well. The X component of displacement shows a significant area of tension through the silicone on one side of the needle, a large area of compression on the other side of the needle, and compression mainly under the needle tip. Similarly, for the Y component, areas of tension and compression are found on either side of the needle, with minimal movement under the needle tip. The Z component demonstrates the primary silicone movement around the edges of the needle, indicating that the needle is pushing the silicone away and downward during deformation. The maximum Z component is around -5 mm, which is less than the needle's displacement of -8 mm.

The strain fields for the large deformation scans, the second set of scans, visually resemble those from the small deformation scans, the first set. For instance, the Eyy strain component displays large clusters of strain radiating away from the needle's edge, particularly around the needle tip. The shear strain components also show similar patterns. Exy exhibits positive and negative strain patterns on either side of the needle, diagonally pushing through the silicone, which aligns with the needle's angle. Eyz shows similar positive and negative clusters as in the small deformation scans, with compression near the tip and tension further up the needle, likely due to the needle's slight angle in that plane.

Unfortunately, the dynamic model described in Chapter 4.2.6 did not reach the final displacements used in the  $\mu$ -CT steps for the large displacement scans, so a direct comparison and validation of the FEM with experimental data is not possible. However, some notable publications can provide context. One key study is by Oldfield, which used an adapted DIC method to examine displacements and both normal and shear strains during needle insertion through gelatin [163]. Oldfield's experiments, where the needle was punctured to 20 mm, provide a basis for numerically validating previous work using the cohesive zone method and material toughness. While this study did not focus on Von Mises stress distribution, it offers valuable insights into stress distribution similar to what is seen around the needle's edge in Oldfield's

findings. This similarity in deformation patterns and positive and negative fields on either side of the needle supports the relevance of Oldfield's findings.

The methodologies developed in this study can be adapted for MNs with careful adjustments for scale, taking into account the smaller size and finer resolution requirements. The key challenges would be ensuring the image resolution is sufficient to capture the smaller deformations typical of MNs, which may require refining the voxel size in the  $\mu$ -CT scans, adjusting the FoV, and ensuring the fiducial markers are sufficiently small. This may require a change of particle material from  $\text{TiO}_2$ , which would require retesting the silicone material properties for the material models, or acquiring  $\text{TiO}_2$  particles with a smaller average particle size.

Future work with  $\mu$ -CT and DVC could focus on observing the tearing mechanism during needle penetration through soft materials. The use of synchrotron, which can acquire images very quickly at high resolution, could be the next step to observing tearing due to needle penetration through soft materials, and in particular skin. Unlike traditional  $\mu$ -CT, synchrotron imaging offers the ability to capture real-time deformation, addressing the limitations of static imaging techniques, such as machine setup and scan time. Additionally, adapting  $\mu$ -CT imaging to observe needle indentation or puncture in skin would involve significant method adjustments, particularly given the issues of skin dehydration and the need for fiducial markers—which DVC relies on for volumetric displacement and strain tracking. Synchrotron could mitigate some of these issues, providing higher resolution images with faster acquisition times, allowing for better tracking of volumetric displacements and strains without significant skin dehydration. This adaptation would also necessitate changes to the parameters used in DaVis; however, the methods described in this chapter can serve as a baseline for coding requirements.

## 5.5 Conclusion

This study successfully used  $\mu$ -CT to measure the deformation of silicone around the needle in detail, in 3D, something that, to the authors' knowledge, has never previously been done. This represents a significant step forward in understanding the

## Experimental Measurements of Needle Penetration

mechanisms of needle penetrations and providing new insights into the material deformation and failure processes. The ability to capture internal deformation in soft materials during puncture, rather than just surface-level or post insertion analysis (as is typical with techniques like DIC and OCT), gives a much more comprehensive view of the needles interaction with material. this is critical for refining needle design and improving insertion efficiency, especially for MNs or needles.

The successful use of low-deformation  $\mu$ -CT scans enabled a second set of high-deformation scans, bringing the imaging closer to the estimated puncture point of the needle used in this study. The volumetric imaging obtained through low and high deformation scans enabled the identification of high strain areas around the needle. More specifically, the areas around the needle edges and tips, which are more prone to rupture or tearing. This insight is valuable in the context of improving needle performance as it challenges the traditional view that material failure is predominantly directly under the needle tip. Understanding how material failure progresses along the sides of the needle could lead to more efficient needle designs.

While the experiments in this chapter were performed using a scaled needle as proof of concept for  $\mu$ -CT as an imaging technique, the methodologies developed can be easily adapted for MNs, with minor adjustments for scale. Furthermore, these experiments can also be adapted to skin with considerations for the fiducial markers required for the DVC tracking and precautions to prevent dehydration of excised skin. While  $\mu$ -CT offers advantages over other image collection techniques, it also has limitations. These limitations are carried over into the image processing techniques used. For instance, voxel smoothing, which can occur during processing, may obscure areas of high stress and strain, making it more difficult to identify critical regions.

This chapter has initiated the connection between DVC and FEA, using DVC as a potential validation method. It utilised the two model variations discussed in Chapter 4 where a low-deformation static model was developed to serve as a proof of concept for  $\mu$ -CT as an image collection method, and DVC as an image processing technique. Unfortunately, due to the challenges encountered with the high-deformation dynamic model, highlighted in Section 0 , only the first step of the high-deformation DVC results could be compared to the FEA. This comparison is discussed further in Chapter 6.

# ***CHAPTER 6***

---

## **MAIN DISCUSSION**

The literature reviewed across these various topics has demonstrated the significant progress in MN development over the years. From the initial patent in 1976 [227] to more recent advancements in biodegradable MNs [50], [79], [87], research continues to grow, yet the production of a safe and effective biodegradable MNA remains a challenge. MNs are still undergoing development for a variety of applications, such as API delivery and vaccine administration. Historically, MN design has been largely focused on experimental, manufacturing and pharmaceutical drug viability [2] with limited feedback from computational models. This is primarily due to the complexity involved in accurately representing skin and the MN insertion process. Skin is a multi-layered structure with each layer having unique mechanical properties, and oversimplifying these properties in FEMs could have significant implications for the design of needles and therefore their performance in clinical settings. Furthermore, the investigation into the biomechanics of skin tearing and puncturing has been limited, with most studies comparing skin to rubber-like materials that share similar deformation characteristics [103], [138], [194]. In the context of layered skin modelling,

## Main Discussion

the intricacies of its structure and complex mechanical properties add significant challenges to accurately modelling these interactions [23], [65], [194], [195], [198].

Modelling in MN design has seen increasing interest over the past decade, but it still represents a relatively small portion of the available research [2]. Many of the published models fail to capture the full range of MN insertion biomechanics, particularly under high-strain conditions, because they rely heavily on experimental data from low-strain scenarios [17], [19]. This limits the applicability of these models in representing the real-world performance of MNs [10], [17]. In particular, element deletion methods have been widely critiqued for providing unrealistic representations of material behaviour. In these models, elements are prematurely deleted, failing to recreate the high deformations observed within soft materials prior to puncture, and necessitating higher stress conditions to compensate for their rapid removal [19], [20], [26], [27], [28], [204]. This leads to unrealistic stress-strain responses, especially in the case of soft tissues like skin, where material failure is not accurately predicted [19].

This study aimed to enhance our understanding of MN penetration and the biomechanics surrounding this process. To achieve this, a FEM was developed using a cohesive zone method, initially introduced by M. Potts at Cardiff University and adapted for this research. This method utilises tetrahedrons fused at identified crack surfaces to recreate the tearing characteristics of soft materials while maintaining stability in the model. This model, whilst in its infancy and yet to be fully validated, shows potential to function as a versatile design tool, particularly for soft materials where the work of fracture is known. With further development and refinement, it could be used as a versatile design tool to provide insights into material behaviour during needle penetration, and currently during the early stages of needle indentation.

To validate the completed model,  $\mu$ -CT and subsequent DVC were hypothesised to enable visualisation of the needle during the initial steps of penetration (dubbed by Davis and Oldfield as the first phase, 'indentation'). This first phase is often missed by most published models, which rely only on load-displacement, post-puncture needle analysis, or surface displacement and strain fields. Digital Volume Correlation (DVC), which tracks volumetric data through a material via a series of images, offers insights beyond just surface tracking. This method has not yet been fully utilised in the

## Main Discussion

experimental or computational validation of MNs. DVC was chosen over Digital Image Correlation (DIC), which would only allow for surface tracking, limiting data collection in the area directly under the needle tip. Similarly, OCT (Optical Coherence Tomography) has limitations in resolution and dynamic imaging, reducing its ability to provide comprehensive volumetric data.

The experimental setup for DVC had to be divided into multiple sections. Human skin presents numerous experimental challenges, such as dehydration and the current lack of knowledge regarding natural fiducial markers. For example, it is unclear whether staining will highlight markers of the correct size in skin (e.g. collagen fibres) to be scanned at a micron level, or which stains will not affect the mechanical properties of the skin. Therefore, a material criterion for a skin substitute was outlined in Chapter 3.2. This allowed the selection of a skin substitute that could potentially allow this proof of concept to be applied to skin at a later date. Using a skin substitute required several experimental procedures to ensure its characteristics aligned with published skin properties.

In this study, Ecoflex-30 was identified as a reasonable skin substitute due to its close correlation to skin's Young's modulus (0.0659 MPa reported for skin) and shear modulus (0.0396 MPa reported for skin) when TiO<sub>2</sub> markers were added as fiducial markers for DVC (0.0970 MPa and 0.0323 MPa respectively). The stiffness of all six materials tested did not fully match the in situ skin stiffness range reported by Groves et al. (0.9665 to 7.2526 N/mm compared to 0.04431 N/mm for skin). However, the shear modulus of 0.0323 for Ecoflex-30 with TiO<sub>2</sub> and was deemed acceptable [23]. In addition, the one parameter Ogden material model investigated showed  $\mu$  in the range of 0.035 to 0.78 MPa which is just outside the range highlighted by Shergold (0.1 to 2.5 MPa) [148]. The range noted for  $\alpha$  was 2.5 for skin and 9 for silicone, with Ecoflex-30 with TiO<sub>2</sub> achieving an average of 2.75. While these discrepancies do not pose a significant issue for the current model using silicone, since silicone eliminates the variability in material properties commonly observed in skin testing by providing a consistent and repeatable sample to test on, it could present challenges if the FEM were adapted to model real skin in the future. Additionally, although variation in skin properties is widely reported in literature (Section 2.2.1), the mechanical properties of the tested silicone materials still fall within the broader range of those reported for skin.

## Main Discussion

To better contextualise the variability, values for Young's modulus of human skin reported in literature range from 0.007 MPa to over 100 MPa, depending on testing method and anatomical site [148],[96]. This wide range supports the assertion that the silicone materials tested fall within a physiologically relevant window.

If actual skin properties were to be introduced into the model, certain parameters within the FEM, such as damping and viscoelastic properties, might need to be adjusted. The model was initially calibrated for silicone, and differences in material behaviour, such as the way skin responds to dynamic loading or deformation, would require changes in how damping and other time-dependent properties are simulated. This is important because silicone and skin have different viscoelastic responses, and without proper adjustment, the model could misrepresent how skin behaves under similar conditions, particularly during needle insertion. Additionally, skin has a more complex structure with multiple layers with varying mechanical properties. Its anisotropic behaviour, driven by fibres within the dermis, would need to be accounted for. This could be achieved by changing the material model to the Holzapfel-Ogden-Gasser model, which accounts for the hyperelasticity of tissue as well as the anisotropic, fibre-reinforced nature of tissues. Therefore, transitioning to skin modelling would necessitate recalibrating these parameters to ensure accuracy in predicting strain, deformation, and puncture dynamics as well as the incorporation of a more complex three layer structure. It could also increase the pressure on the computational load already considered too high.

Despite eliminating the challenges of using excised skin by incorporating a skin substitute, such as dehydration and poroelastic movement,  $\mu$ -CT still has its limitations. For instance, scan times can range from one to four hours depending on the required resolution, field of view, and the machine used. As a result, it was decided to limit the study to six displacement steps for the two sets of scans. Furthermore,  $\mu$ -CT is a static imaging method, so material movement during the long scan times must be considered. Rigid body movement scans were required to minimise this risk. Unfortunately, using a faster imaging method, such as a synchrotron, was not feasible for this study and is discussed later in Chapter 8.

## Main Discussion

The initial scans, as shown in Figure 5-21, were used as a proof of concept and demonstrated that the chosen fiducial markers were effective in visualising small displacements. When processed through DaVis, the outputs were generated smoothly and showed good visual agreement between the DVC and FEA results.

Since the initial scans captured a displacement of only 0.375 mm, a simple static indentation model was developed using the needle geometry segmented from the  $\mu$ -CT scans, discussed previously in Section 4.2.2.1. This model was expected to demonstrate the feasibility of the image registration process at low deformations and align with the DVC data through interpolation, facilitating further investigation. Furthermore, comparing the material models used in this low-deformation static model with experimental results highlighted areas that need modification for modelling larger deformations and strains. Initially, the load-displacement data from the static model, which employed the Ogden material model with experimental material constants derived from tensile tests in Section 3.4.4, was compared to the experimental puncture test. The static model overpredicted the load-displacement characteristics, as shown in Figure 4-18, leading to a reduction in the bulk modulus from 47.62 MPa to 0.1 MPa. The initial bulk modulus was determined by multiplying the  $\mu$  value by 1000, in line with the published results from Groves et al. [23].

Given that the bulk modulus is not easily measured, this initial value was varied based on comparisons with experimental puncture results, allowing for iterative adjustments until a more accurate representation was achieved at 0.1 MPa. However, it is acknowledged that this approach results in a bulk modulus much lower than the realistic value for soft tissues. Although this adjustment provided good initial alignment, it is unclear whether the same alignment would hold at higher strains, as only the initial load-displacement curve (up to 0.375 mm) was matched, not the higher displacements near the puncture point (8 mm). The reduction in bulk modulus could also explain the numerical misalignment observed in the X and Y displacement components between the FEA and DVC. However, visually, the displacement fields in both methods show strong similarities, indicating that the model is reasonably accurate in these early stages, or that both approaches share similar limitations as they rely on many of the same geometry, mesh, and underlying assumptions.

## Main Discussion

For the X component, the displacement fields in both the FEA and DVC exhibit a symmetrical pattern around the needle tip, with both methods capturing similar deformation behaviours. In the Y component, both the FEA and DVC display similar spread of displacement along the Y-axis, with regions of positive and negative displacement radiating from the needle tip. The differences in magnitude between the two results has a deviation of approximately 60% (-0.404779 mm for the static model and -0.16 mm for the DVC) might stem from simplifications in the FEA model's material properties, which may not fully account for the viscoelastic and nonlinear behaviour of the silicone during deformation. Another reason for the differences could be the higher compressibility or lower Poisson's ratio of the FEA material model than the actual silicone used.

The Z component shows the highest displacement concentration directly under the needle tip. Both the FEA and DVC results display similar compression patterns and numerical alignment, suggesting the main misalignment of the FEA is with the X and Y components. This suggests that the FEA's bulk modulus and compressive behaviour align well with experimental behaviour, and therefore the lateral deformation is more sensitive to the material model parameters such as Poisson's ratio and shear modulus. Whilst there are some numerical discrepancies between the FEA and DVC results, the visual alignment of displacement fields across all components suggests that the model captures the overall behaviour accurately. Further refinements of the material properties and boundary conditions in the FEA may be necessary to improve the numerical agreement and ensure better alignment with the experimental data as larger strains are introduced.

While these small-deformation scans may not provide insight into the tear mechanics of the silicone, the combination of FEA and DVC results allows for a detailed view of how the material behaves in 3D during the initial stages of needle penetration. For example, the strain fields highlight how the material deforms around the needle tip in all three directions (X, Y, Z). Typically, displacement magnitude is the primary focus of simple load-displacement tests. However, this analysis offers a more complete picture of the strain localisation and anisotropy of the material than what is usually obtained from DIC surface strain measurements alone. Additionally, most imaging techniques used in recent years have focused on post-penetration imaging to predict

## Main Discussion

the needle pathway and resulting shape, without examining the deformation during the indentation stage. This has led to attempts to predict how the material tears, influencing FEMs, but without knowing the exact causes—details that are difficult to capture in simple experiments such as puncture or compression tests.

As discussed in Section 5.3.6, a small error was observed when comparing the raw DVC data from MATLAB to the interpolated DVC data imported into FEBio (0.0291 mm RMSE and 0.0236 MAE), and the FEA centre node results (0.0243 mm RMSE and 0.0184 MAE). These differences can arise due to several factors, including the experimental setup, the parameters used in DaVis, and the configuration of the static model. The most notable discrepancy occurred between the interpolated and raw DVC data, likely due to the estimation process involved when interpolating voxel data to node coordinates, shown in Figure 5-33 and Figure 5-34.

During interpolation, the voxel-based DVC data (which is grid-based) is translated into node coordinates for use in FEBio and the FEA model. This process involves approximating displacement data for nodes that may not directly correspond to the original voxel locations. As a result, the interpolated data may introduce some smoothing effects or artificial gradients, which can lead to reduced accuracy in regions with high strain gradients or complex deformations, such as near the needle tip. This is a common issue when converting from volumetric (DVC) to nodal (FEA) data formats, as there is an inherent trade-off between retaining detailed local data and creating a smoother dataset for analysis.

Another potential source of error lies in the processing parameters used within DaVis. Parameters such as voxel size, search radius, and overlap settings can influence the accuracy of the DVC data. The optimisation of these parameters for the specific deformation fields being studied is a critical step in refining the accuracy of the results. If these parameters are not optimised for the specific deformation fields being studied, artefacts or noise may remain in the raw DVC data, affecting both the raw and interpolated results. For example, a larger search radius can introduce averaging over larger regions, which may mask localised strain effects that are critical for accurate needle penetration analysis. Achieving optimal settings involves balancing computational efficiency with measurement accuracy using parameters such as voxel

## Main Discussion

sizes and noise, and the current settings have been refined to ensure the best possible results. However, future optimisation may be necessary for subsequent analyses or changes in methodology. These differences are discussed more thoroughly in Chapter 5.2.

In addition, any unresolved noise or artefacts in the raw DVC data would be carried over into the interpolated data, further contributing to the differences observed. While interpolation helps to smooth out some of these effects, it may not eliminate them entirely, leading to slight discrepancies when comparing the results to the FEA model. In this case, the averaging of the search range seems to have minimised some of these errors, as shown by the reduction in percentage error from 8.48 % in the raw DVC data to 3.97 % after interpolation in Table 5-4.

Finally, the differences could also arise from the FEA model setup itself. The FEA is built on assumptions about material behaviour (e.g., using the Ogden material model) and boundary conditions that may not perfectly match the real-world deformation observed in the DVC scans. For instance, the bulk modulus used in the FEA was reduced to match the load-displacement curve in Figure 4-19, this could lead to a mismatch in the displacement and strain fields, contributing to the observed error (and RMSE of 0.0243 mm and MAE of 0.0184 mm). Moreover, the simplifications made in the FEA model (such as ignoring certain behaviours or boundary effects) could lead to differences when compared with the experimental DVC data, which captures the full 3D deformation of the material.

Following the low-deformations images, a second set of scans was taken closer to the approximate puncture point, identified through a needle insertion test. For the needle used in this study, the approximate puncture point was determined to be just over 8mm [Figure 3-15]. Therefore, the scans were conducted in five steps (3.5 mm, 6.5 mm, 7 mm, 7.5 mm and 8 mm) to avoid accidentally tearing the material, which would have caused an image collection failure. This approach allowed for the investigation of higher strain levels through DVC processing. However, several limitations were identified with these higher deformation scans, including the introduction of noise disturbance in the DVC data processed via DaVis. This may be attributed to the initial properties used in DaVis, such as the pre shift voxel size, the initial voxel size for each

## Main Discussion

step employed for each scan, or the overlap that was investigated. The noise could also be attributed to the larger displacement steps used in the high deformation scans, which could have affected the accuracy of the results. Whilst DaVis removes rigid body movement from the scans as an added feature, smaller displacement steps might reduce noise by providing more gradual changes, resulting in a better correlation between scans. Alongside this, further investigations are required into the rigid body scans to determine the noise between the reference and initial images, which could improve this methodology. This could help identify the noise levels resulting from scan conditions, material creep or other factors that influence the accuracy of displacement measurements. Despite these issues, the overall the image processing in MATLAB enabled visualisation of the silicone interaction around the needle for each component of displacement, as well as for each normal and shear strain component.

In Section 5.3.5, the figures for the final step of the 8 mm indentation are presented. These include the centre slice, where the centre of the needle is approximated, as well as slices 10 voxels before and after this point. This setup provides a comprehensive view of the displacement fields in the silicone, both in front of and behind the needle. Across all components of displacement, the fields appear symmetrical in the respective planes, indicating uniform deformation of the silicone. This symmetry suggests a predictable and controlled deformation pattern, which could serve as a valuable baseline for the development of computational models or design tools that aim to replicate similar uniformity in indentation parameters. Uniformity, or consistent deformation patterns, could allow for more accurate prediction of material behaviour under specific conditions and inform the development of design tools that replicate such uniformity.

As anticipated, the Z component shows maximum displacement beneath the needle tip, but there is a mismatch between this maximum displacement and the experimental 8 mm indentation. This discrepancy could stem from several factors, including the initial parameters used in DaVis. In earlier tests (Figure 5-24), the displacement reached the 8 mm mark, but the excessive smoothing from a larger voxel size obscured important features, which led to this test being excluded. This suggests that further exploration of parameters such as voxel size, overlap, and pre-shift settings within DaVis may be necessary to improve the discrepancy in Z displacement.

## Main Discussion

Refining these aspects could lead to better alignment between the actual experimental displacement and the DVC results, especially for larger deformations. Adjusting the DVC processing parameters—such as search radius and voxel size—might also provide clearer visualisation of the full displacement range, helping to improve model fidelity and providing a more accurate reflection of the material's behaviour under indentation.

The normal and shear components, shown in Figure 5-26, reveal an intricate strain field within the silicone, highlighting regions under tension and compression. Areas of high strain (yellow regions) may indicate where the material is likely to rupture or tear, potentially initiating the needle puncture phase. Understanding the puncture mechanics of silicone suggests that the high  $E_{xx}$  and  $E_{yy}$  values could identify locations where the silicone is prone to failure. The  $E_{xy}$  component, which shows shear strain between the X and Y planes, provides insight into how the material twists or slides relative to these axes. High  $E_{xy}$ ,  $E_{xz}$  and  $E_{yz}$  values near the needle tip suggest significant shearing forces in the silicone in response to both the downward force of the needle and the lateral stretching. This behaviour along the sides of the needle suggests where the material might tear as the needle advances.

High shear strains could enhance needle efficiency by promoting material failure and tearing making the insertion smoother, lowering the insertion force required, and improving overall performance. However, it should be considered that reducing shear strains could also impact the required insertion force; if the needle tip geometry is optimised to distribute strain more evenly, it might necessitate higher displacement to puncture effectively, or it could reduce the strain to such an extent that rupture does not occur. One approach to achieve this could be through optimising the needle tip geometry to a sharper needle point, or even sharpening the sides of the needle, decreasing excessive stretching but also increasing the strain concentration around the needle. Sharpening refers to reducing the radius of curvature at the needle tip or refining the edges along the sides, creating a more pointed or blade-like geometry, which lowers insertion resistance and focuses strain into a smaller region of the material. Further in-depth investigations into needle geometries and insertion processes, similar to studies by Römgens [15], [63] or Potts [9], using the methods introduced in this study, would be necessary to develop such optimisations.

## Main Discussion

The high-deformation DVC investigation was introduced to help validate the dynamic model using the cohesive zone method. However, with the dynamic model only reaching a displacement magnitude of 3.8 mm due to computational limitations, the model can only be partially compared to the DVC results. The computational issues that arose with the dynamic model highlighted the advances in both computational power and software that are still required to produce a more realistic puncture model. The model experienced convergence problems, primarily related to mesh dependencies and unrealistic deformations around the needle tip. Conducting a dynamic analysis also introduced challenges with damping and inertia, making the model density dependent. This required the material density of the FEM to be reduced from  $1 \text{ kg/m}^3$  to  $0.1 \text{ kg/m}^3$  [Figure 4-23] to produce load-displacement outputs similar to the experimental results. This material density reduced the inertia through the silicone and alleviated some of the convergence issues initially observed. However, the model still could not simulate the full 8 mm indentation due to extensive element stretching under the needle tip. Reducing this element stretching would require the implementation of a remeshing algorithm, which has been utilised in some published studies [228], [229], [230]. However, this was outside the scope of the current project and its timeline. A remeshing algorithm would allow for mesh adjustments, particularly by refining the mesh in areas where it becomes overly dependent on mesh density to maintain accuracy.

However, despite being in its early stages, the model did reach a displacement magnitude of 3.8 mm, which allowed for an initial comparison with the first DVC step of 3.5 mm. The X, Y, and Z components of displacement for this first displacement step are shown in Figure 5-31 -. While capturing the initial stages of deformation, the 3.5 mm DVC grid exhibits similar deformation patterns to those observed in X, Y, Z components of displacement from the 8 mm DVC grids. However, there is a significant amount of noise in the X and Y displacement components, which could be attributed to the large first step of displacement used. In contrast, the 8 mm scans utilised five points of reference to calculate the final displacement maps, leading to smoother results.

The Z component reveals a ring of high strain in the silicone, located some distance away from where the needle is expected to be. This may be due to strain redistribution

## Main Discussion

through the material, where compression occurs further from the actual needle-silicone boundary. This observation highlights that deformation does not only occur locally but also affects regions further from the point of indentation. Examining each scan step could help identify how the material transitions from elastic deformation to potential failure

When comparing the deformation data, along the Y plane the X component shows quite a bit of noise. However, the areas of tension and compression are still seen with highs of 2 mm and lows of 1 mm. When comparing this to the FEA data, with a maximum of 0.02436 mm and minimum of -0.8067 mm numerically there is quite a difference. For the Y component, the strain pattern is visually similar, but numerically very different, with a maximum of 0.7068 mm compared to the DVC maximum of 2 mm. Numerically, the Z component is similar with a minimum displacement around the needle tip of -4.1 mm for the FEA and -3 mm for the DVC. However, the maximum Z displacements are not viewed around the needle tip, this could be due to the slice viewed

This is most likely due to the limitations already discussed for this dynamic model, where the silicone is not deforming as realistically as it could do, and most likely due to the high density and inertia of the silicone. For example, there is only a slight curve of the silicone around the needle edge, where in the CT scans, Figure 5-22, this curve is more pronounced and stretches across at least half the silicone surface at the first step. This means the components of displacement are more localised to just the needle edge. Another limitation is the mesh, with the elements stretching too much there will be an overestimation of the displacement and strain components seen.

The differences in the dynamic model to the DVC data could be attributed to several factors. One potential reason is the adjustments made to the material properties based on the load-displacement experimental data. These properties were only validated at low deformations, and the material's behaviour at higher strains was not fully considered, as the model did not run beyond 3.8 mm displacement magnitude. Additionally, the boundary conditions used for the quarter model may have underestimated the experimental conditions. The assumption of symmetry in the silicone's behaviour could also be inaccurate, as the needle itself is only symmetrical

## Main Discussion

in one plane, which may lead to inaccuracies in the predicted material response. Furthermore, the smoothing effects of the DVC parameters chosen in DaVis could have attributed to underestimating displacements and strain. The voxel size, overlap, and search radius settings may have dampened finer details of the displacement fields, especially near the needle edges, leading to discrepancies when comparing the DVC data with the dynamic model. Since these will always be considerations when choosing DVC, the only effective way to reduce these potential errors is by adapting the initial image acquisition techniques. This could include optimising parameters such as FoV, machine choice, initial binning, and resolution (the number of slices taken) during the image capture process.

The main consideration throughout this study was the implications for future design tools and the biomechanics of needle puncture. Previous publications have largely focused on the behaviour of skin at low displacements or strains, and then used these material models within high-strain FEMs [18], [20], [24], [163]. As noted by Groves et al., material models derived from low-strain tensile tests are often extrapolated to high-strain conditions in FEMs of skin, potentially underrepresenting localised failure mechanisms. This limitation highlights the importance of validating material models against observed deformation and fracture behaviour.

Using material properties derived from low-strain observations can lead to design issues, such as unsafe puncturing due to underestimation of puncture forces, ineffective needle penetration, and wasted materials. If detachable MNs fail to puncture efficiently, especially when used by untrained professionals, it could lead to a range of safety concerns. Inadequate puncture could cause increased risk of injury, such as skin irritation, improper drug delivery, or even infection, as the MNs may not penetrate the skin deep enough to reach the desired tissue or release the required dosage. Additionally, when MNs remain attached to the patch rather than detaching properly, they may pose disposal issues. The remaining needles could cause harm if not properly disposed of, creating risk of injury or contamination. For non-detachable MNs, similar concerns arise if they do not puncture effectively. If the needles fail to reach the correct depth or do not deliver the intended dose, there is a risk of insufficient therapeutic effect, irritation or needle fracture.

## Main Discussion

The experimental work within this study utilised a silicone skin substitute, which was identified as being behaviourally similar to skin. However, there are still fundamental differences, particularly due to the inherent challenges in replicating the complex mechanical properties of skin. For example, skin is both poroelastic and viscoelastic, meaning it exhibits time-dependent deformation behaviour and allows water to move in and out of its structure when compressed or stretched. Silicone, on the other hand, lacks this dynamic fluid interaction and primarily behaves as an elastic material. In Section 2.2, it was noted that skin properties can vary depending on factors such as age, environment, hydration, and anatomical location. Therefore, it is unlikely that there will ever be a completely accurate skin substitute. Furthermore, even tests conducted on *ex vivo* skin can yield data that differs significantly from *in vivo* conditions.

Adaptations to the high-deformation model could include the introduction of time-dependent behaviour, such as incorporating viscoelasticity to simulate the dynamic response more accurately. This would aid in the development of a more realistic time-dependent model, introducing variables such as needle puncture velocity into dynamic modelling, rather than focusing solely on static load-displacement variables.

The needle used in this study was a scaled-up version of a 1.1 mm needle, with a length of 11.1 mm. In the puncture test discussed in Section 3.4.3, it was observed to indent to roughly 8 mm at 3.2 N. This indentation represents around 72% of the needle's total length. Needle design will need to take this depth into account. When considering MNs, if the needle is scaled down by a factor of 10 and indents 0.8 mm the force would most likely scale with the area to 0.032 N, a distinctly higher insertion force than considered in other publications [67]. This suggests that reducing the needle tip diameter could be an important design factor to minimise the force required. Similarly, the needle slope (its taper) is a crucial design aspect. These findings align with the results published by Römgens, who noted that the force required for needle insertion increased linearly with the needle tip diameter, with the smallest needle tip (5  $\mu\text{m}$ ) achieving the smoothest insertion. Larger needle tips, in contrast, caused more skin indentations prior to puncture [15]. Davis, however, investigated larger needle tips (ranging from 60 to 160  $\mu\text{m}$ ) and reported on the relationship between the force at the insertion point and the needle tip diameter being linear [10]. Boonma also observed

## Main Discussion

that the insertion force for MNs decreased with the sharpness of the needle tip, with their blunt needle failing to penetrate within the 2 mm displacement used in the study [67]. The DVC and FEA results both revealed strain concentrations along the edges and beneath the needle tip, indicating that material failure could occur in these areas. This failure is essential for creating a pathway for the needle as it advances, particularly along the sides of the needle where the material must tear to enlarge the hole. A reduced needle angle could help decrease this strain, as suggested in publication [15], [67].

Understanding the material's strain distribution (both normal and shear) at high deformation allows for the optimisation of needle geometry, minimising tissue damage while ensuring successful puncture. By incorporating realistic strain data into design tools, manufacturers can optimise needle length, tip sharpness, and arrangement to balance force application with minimal tissue trauma. A verified design tool could ensure that MAPs meet safety standards, such as puncture force requirements and tissue response thresholds, even before they enter clinical testing.

Further refinement of the model could be centred around exploring MN geometry and design, particularly optimising tip and side sharpness, length, and array spacing to maximise efficacy. The flexibility of the approach to accommodate variations in MN architecture should also be evaluated, ensuring that it support rapid design iterations. Expanding the FEM to MNAs rather than single needles would provide more realistic representation of clinical application, although this would depend on the computational limits of array size and depth of puncture that can be modelled. Additionally, the model's ability to represent larger scale interactions, such as the tearing and strain distribution in multi-needle configurations, should be assessed.

In pharmaceutical design, the focus is on creating products that are clinically safe and effective. Although most designs progress beyond the modelling stage quickly, modelling tools are still valuable during the early stages of prototyping. Validating a computational model could remove the ethical concerns surrounding the use of animal or human skin, offering an efficient way to evaluate different MN designs (e.g., geometry, patch shape, needle array spacing) without requiring immediate testing on skin. This study forms a foundation for a design aid, but to become a fully practical

## Main Discussion

tool, further validation with skin, refinement of material properties, and the incorporation of time-dependent responses like viscoelasticity are necessary. While it may not yet be ready for direct implementation in the pharmaceutical industry, it is on the right path, particularly with further refinement of strain models and validation techniques.

In terms of adapting the experiments from this study to work with skin, several considerations must be taken into account. Skin is a complex, multi-layered structure with varying mechanical properties across the epidermis, dermis, and subcutaneous layers. Key differences between silicone and skin include viscoelasticity, anisotropy, and heterogeneity. Simple ex vivo tensile experiments, like those published by Ottenio [22], must also account for the rapid dehydration of skin once it is excised. The mechanical properties of skin can vary significantly based on fibre orientation and anatomical location, making it difficult to generalise results.

While tension tests cannot be conducted in vivo, mechanical properties in vivo are typically obtained through compression or torsion tests, which can be ethically approved. However, these tests don't take into account the high strain tearing mechanisms of skin. If DVC were adapted for use with skin, it would need to accommodate the lack of fiducial markers for tracking. Staining could be used to highlight known characteristics such as fibres or collagen, allowing for tracking during DVC imaging. Another challenge would be the time required for  $\mu$ -CT scans. The excised skin would need to remain hydrated throughout the scanning process, which can take hours. While synchrotrons can speed up the process, they might still not be fast enough to capture the required resolution efficiently. Furthermore, using in vivo skin introduces ethical concerns due to the radiation exposure from X-rays, which would limit the use of live participants in such tests.

Finally, the scanning of dynamic tearing has not been included in this study. It was assumed that a static imaging technique might not be capable of capturing the dynamic failure of skin quickly enough. Future studies should consider how dynamic imaging techniques or other methods might capture these rapid failure events more effectively.



# ***CHAPTER 7***

---

## **MAIN CONCLUSION**

In recent years, the modelling and simulation of MNs have gained traction as valuable tools in their design and optimisation. These computational approaches aim to accurately predict puncture mechanics and refine MN geometry and material properties. By leveraging modelling techniques, the reliance on physical prototyping and early-stage clinical trials can be reduced. However, understanding skin biomechanics remains a significant challenge due to various limitations.

The aim of this thesis was to further investigate needle puncture mechanics using a skin substitute, thereby avoiding the limitations associated with excised human and pig skin. Human skin, presents significant ethical challenges, including compliance with health and safety standards and adhering to the Human Tissue Act. Furthermore, practical limitations arise during experimental procedures, such as extended u-CT scan times leading to tissue dehydration, the requirement of staining for DVC, and subsequent changes to the mechanical properties. Given these challenges, the use of a skin substitute offers a more controlled and replicable environment for studying puncture mechanics. This study involved characterising the mechanical properties of

## Main Conclusion

potential substitute and employing a material selection criteria that aligns with published in vivo and ex vivo skin results.

Several objectives were established in Chapter 1.2 to achieve the aims of this thesis. The first objective, "Identify suitable skin substitutes", focused on understanding soft material behaviour and suggesting appropriate substitutes. Chapter 3.2 details the material criteria based on published in vivo and ex vivo skin properties. Experimental protocols were used to investigate the mechanical response of various materials, including compression, tension, puncture and tear tests. After testing against the material criteria, Ecoflex-30 was identified as having the closest properties to skin. With the addition of TiO<sub>2</sub> for DVC tracking, the material properties changed slightly but remained within an acceptable range. Specifically, the addition of the TiO<sub>2</sub> increased the stiffness from 0.0263 to 0.0323 N/mm, and the Youngs modulus from 0.0788 to 0.0979 MPa. Despite these changes, Excoflex-30 with TiO<sub>2</sub> was selected as the most appropriate material to continue with.

Following the selection of the skin substitute, two FEA models were developed to simulate small and large deformations. The small deformation model was suitable for static analysis, matching the needle displacement in the first  $\mu$ -CT scans. However, mechanical testing showed that the initial Ogden parameters overestimated the needle's load-displacement characteristics, prompting a parameter study where the bulk modulus was reduced from 47.26 MPa to 0.1 MPa.

For large deformations, a cohesive zone method using tetrahedrons created in Rhino Grasshopper was developed to incorporate the work of fracture data and simulate crack propagation during needle insertion. The method improved model stability and allowed for larger deformation prior to material fracture, which was a limitation in previous cohesive zone models, and in approaches such as element deletion. Unfortunately, the dynamic model failed to converge beyond 3.8 mm, falling short of the target 8 mm indentation displacement and full insertion. This limitation hindered full validation using the second set of DVC scans, but the model still demonstrated dependencies on density and mesh.

The final objective was to use advanced imaging techniques to validate the FEA models. Chapter 5.2.1 outlines the image collection process, which included using  $\mu$ -

## Main Conclusion

CT to image both small (0.375 mm) and large deformations (8 mm). The large deformation DVC scans offered insights into strain concentrations around the needle edges, highlighting areas susceptible to rupture as the needle continues to penetrate. These strain concentrations are significant as they highlight regions where the material is most likely to fail and facilitate tearing. Interestingly, these areas are not confined to the needle tip, but extend along the sides of the needle, suggesting sharper needle sides are a consideration for needle design to reduce resistance and improve insertion efficiency.

Additionally, the strain patterns provide clues about how the material deforms under loading. For example, the distribution and magnitude of strains near the needle edges may help identify optimal wall angles and tip shapes to minimise indentation and achieve a cleaner puncture. The results also suggest that needles with greater sharpness at both the tip and sides could reduce the required force while limiting the extent of surrounding tissue damage. Furthermore, these observations can inform designs that improve the consistency of puncture mechanics, such as balancing the needle's ability to penetrate efficiently while maintaining structural integrity to avoid buckling or bending under higher loads. As previously reported, reducing the tip diameter and optimising the wall angle reduces the indentation prior to needle penetration. Therefore, designing needles with a sharp needle tip and near parallel walls could enhance insertion efficiency after puncture while mitigating unnecessary material deformation.

However, the dynamic FEA model's failure to converge beyond 3.8 mm prevented a full comparison with these scans. Despite these limitations, the study demonstrates DVC's potential as a validation tool, particularly as a technique to track needle-induced volumetric deformation rather than just surface or post-puncture evaluation.

Overall, the three objectives set out in this thesis were integral to achieving its main aims. Through the comprehensive material analysis and the development of advanced image collection and processing methods, significant insights have been gained that contribute to a deeper understanding of needle puncture mechanics. While the needle's actual puncturing into soft material was not observed due to the static nature of  $\mu$ -CT, the large deformations near the material failure point provided valuable

## Main Conclusion

information about strain concentration zones that could lead to material failure. This study also uncovered areas of strain concentration around the needle, not just at the tip but along the edges, which are critical to needle tearing. These findings challenge the traditional view that penetration is primarily driven by the sharpness of the needle tip. These insights suggest that needle designs with sharper edges or closer to parallel sides could enhance penetration efficiency, as the sides contribute to material failure and allow the needle to move deeper into the tissue at a reduced force.

Although the dynamic model is not yet fully validated for high strain and large deformation scenarios, it has laid essential groundwork for further FEA optimisation. This includes addressing the indentation phase, which is often noted in needle puncture analyses but is frequently overlooked in FEMs. The FEA has provided key insights into the distribution of forces during puncture and highlighted dependencies on static and dynamic properties, as well as the need for improving mesh algorithms. Future improvements will require further optimisation of needle geometry, such as tip sharpness, length, and angle. The insights gained from this research also highlight the importance of MN geometry and the necessity of model adaptations for use with porcine or human skin.

The final objective was to use advanced imaging techniques to validate the finite element models. The study employed DVC to validate both small and large deformation scans, providing an important proof of concept for integrating imaging techniques with FEA. The DVC data for low deformations aligned well with the static model, although minor numerical differences were noted (an overall RMSE of 0.0243 mm), likely due to assumptions made during both modelling and imaging. These findings underscore the potential for refining static models and highlight the importance of considering factors such as voxel smoothing and resolution limitations during high-deformation scans. Although the dynamic model could not be fully validated with DVC due to mesh-related challenges, the study has established a promising baseline for using DVC as a tool to validate needle indentation and identify areas of potential material failure.

In conclusion, this research has provided valuable insights into the mechanical interactions between needles and soft materials, particularly by highlighting strain

## Main Conclusion

distributions and puncture forces during different stages of needle insertion. The findings emphasise the importance of optimising needle geometry to minimise puncture force and improve safety and efficacy. Ultimately, while the study has not yet resulted in a fully viable design tool for clinical applications, it provides a strong foundation for future work. Further refinement of FEA models and DVC techniques will be essential for optimising MN designs and ensuring successful validation with in vivo or ex vivo skin models.

# ***CHAPTER 8***

---

## **FUTURE WORK**

The challenges and limitations observed in this study have highlighted key areas of further research and development to advance MN design tools. These are identified below:

### **Experimental work on ex vivo skin**

The experimental methods used in this study would require significant adaptations to work effectively with skin. One key challenge is the reliance on fiducial markers for DVC, which are easier to incorporate into synthetic materials like silicone but more difficult to apply to biological tissues. Research into the staining properties of skin, such as using collagen or fibre markers, could provide a way to track volumetric deformation without altering the tissue's mechanical behaviour.

Additionally, the dehydration of skin during experiments poses another problem, as it can affect the mechanical properties of the tissue. Techniques to mitigate this, such as hydration chambers or more rapid imaging methods such as a synchrotron, are necessary to maintain skin integrity throughout the scanning process. Given the viscoelastic nature of skin, another consideration is the potential movement of the

## Future Work

tissue during imaging and creep. Reducing  $\mu$ -CT scan time would also allow for the imaging of more dynamic needle indentation properties, making it possible to capture real-time needle-tissue interactions. Finally, imaging the tearing mechanisms in skin could provide critical insights into material failure, helping to refine finite element models and improve the accuracy of puncture predictions.

### **Experimental work on array patches and optimising needle designs**

While this study offers a good foundation for understanding needle puncture mechanics, it did not explore the impact of different needle geometries or the effects of array patch design, such as needle spacing. Variations in needle length, tip sharpness, or diameter could significantly alter the insertion forces and strain distribution in the material. In practical applications, needle array spacing is crucial for ensuring uniform puncture, dosage control, and minimal tissue trauma. Future experimental work could focus on testing different MNAs to determine how these variables influence mechanical behaviour, with the ultimate goal of optimising patch design for both safety and efficacy in clinical applications.

### **Refinement of experimental work**

This study successfully demonstrated the proof of concept for using DVC as a validation tool for FEA models in needle indentation and investigating needle mechanics. However, there remains a need for further refinement, particularly in differentiating between static (specific points) and dynamic (real-time) imaging. Static imaging, as used here, is useful for understanding deformation in controlled environments but does not capture the real-time dynamics of needle puncture, especially in soft, complex tissues like skin. Refining the DVC properties, such as improving the voxel size and overlap parameters, will be necessary for capturing high-resolution strain fields at large deformations. Additionally, improvements in image acquisition techniques could help reduce noise and increase the accuracy of strain localisation, offering a more reliable basis for model validation.

### **Refinement of puncture model**

The dynamic FEA model developed in this study showed promise but encountered challenges due to mesh distortion, particularly at higher displacements. One potential improvement is the introduction of remeshing algorithms that adjust the mesh dynamically as the model deforms, allowing for greater accuracy and convergence stability. Alternatively, a more segmented approach could be taken, where one model simulates the indentation up to the point of material tearing, and a second model picks up after the tear starting with a predefined crack. This method, as used by Fregonese and Bacca [66] could bypass the challenging phase where skin suddenly fails. Such techniques could significantly reduce mesh distortion and dependency, allowing the model to simulate larger indentations without convergence failures. The goal would be to model the needle's behaviour all the way to material tearing, offering a more realistic simulation of the puncture process.

### **Dynamic model incorporating skin layers and properties**

To create a more realistic model for needle puncture into skin, the dynamic model must be adapted to account for the layered structure of skin, which includes the epidermis, dermis, and subcutaneous tissue and crucially, the stratum corneum. Each of these layers has unique mechanical properties that need to be represented in the model, particularly their varying responses to compression and shear forces. The stratum corneum, for example, is tougher and more resistant to puncture due to its dense structure, while the underlying dermis and subcutaneous tissue are more compliant and respond differently to compression and shear forces. Additionally, fibre orientation and anisotropic behaviour should be incorporated, as these factors significantly influence skin's response to needle insertion. By adapting the model to include these properties, the finite element model would offer a more accurate simulation, improving the design and safety of MAPs for use in clinical settings.

## REFERENCES

---

- [1] W. Montagna, *The Structure and Function of Skin*, 3rd ed. Elsevier, 2012.
- [2] P. R. Yadav, T. Han, O. Olatunji, S. K. Pattanayek, and D. B. Das, "Mathematical modelling, simulation and optimisation of microneedles for transdermal drug delivery: Trends and progress," Aug. 01, 2020, *MDPI AG*. doi: 10.3390/pharmaceutics12080693.
- [3] G. S. Kwon and D. Y. Furgeson, *Biodegradable polymers for drug delivery systems*. Woodhead Publishing Limited, 2007. doi: 10.1533/9781845693640.83.
- [4] R. U. Jaman and M. F. Samad, "Design and analysis of a reservoir-based controllable microneedle for transdermal drug delivery applications," *Drug Deliv Transl Res*, vol. 14, no. 3, pp. 812–825, Mar. 2024, doi: 10.1007/s13346-023-01438-0.
- [5] H. K. Makadia and S. J. Siegel, "Poly Lactic-co-Glycolic Acid (PLGA) as biodegradable controlled drug delivery carrier," *Polymers (Basel)*, vol. 3, no. 3, pp. 1377–1397, Sep. 2011, doi: 10.3390/polym3031377.
- [6] D. D. Zhu, X. P. Zhang, C. B. Shen, Y. Cui, and X. D. Guo, "The maximum possible amount of drug in rapidly separating microneedles," *Drug Deliv Transl Res*, vol. 9, no. 6, pp. 1133–1142, Dec. 2019, doi: 10.1007/s13346-019-00658-7.
- [7] C. J. Ke *et al.*, "Multidrug release based on microneedle arrays filled with pH-responsive PLGA hollow microspheres," *Biomaterials*, vol. 33, no. 20, pp. 5156–5165, Jul. 2012, doi: 10.1016/j.biomaterials.2012.03.056.
- [8] L. K. Vora *et al.*, "Microneedle array systems for long-acting drug delivery," *European Journal of Pharmaceutics and Biopharmaceutics*, vol. 159, pp. 44–76, Feb. 2021, doi: 10.1016/j.ejpb.2020.12.006.

## References

- [9] M. R. Potts, S. L. Evans, R. Pullin, S. A. Coulman, J. C. Birchall, and H. Wyatt, "An analysis of the relationship between microneedle spacing, needle force and skin strain during the indentation phase prior to skin penetration," *Comput Methods Biomech Biomed Engin*, vol. 26, no. 14, pp. 1719–1731, 2023, doi: 10.1080/10255842.2022.2136486.
- [10] S. P. Davis, B. J. Landis, Z. H. Adams, M. G. Allen, and M. R. Prausnitz, "Insertion of microneedles into skin: Measurement and prediction of insertion force and needle fracture force," *J Biomech*, vol. 37, no. 8, pp. 1155–1163, Aug. 2004, doi: 10.1016/j.jbiomech.2003.12.010.
- [11] A. M. Okamura, C. Simone, and M. D. O'Leary, "Force modeling for needle insertion into soft tissue," *IEEE Trans Biomed Eng*, vol. 51, no. 10, pp. 1707–1716, Oct. 2004, doi: 10.1109/TBME.2004.831542.
- [12] O. Olatunji, D. B. Das, M. J. Garland, L. Belaid, and R. F. Donnelly, "Influence of array interspacing on the force required for successful microneedle skin penetration: Theoretical and practical approaches," *J Pharm Sci*, vol. 102, no. 4, pp. 1209–1221, 2013, doi: 10.1002/jps.23439.
- [13] S. D. Gittard *et al.*, "The effects of geometry on skin penetration and failure of polymer microneedles," *J Adhes Sci Technol*, vol. 27, no. 3, pp. 227–243, 2013, doi: 10.1080/01694243.2012.705101.
- [14] A. Davidson, B. Al-Qallaf, and D. B. Das, "Transdermal drug delivery by coated microneedles: Geometry effects on effective skin thickness and drug permeability," *Chemical Engineering Research and Design*, vol. 86, no. 11, pp. 1196–1206, Nov. 2008, doi: 10.1016/j.cherd.2008.06.002.
- [15] A. M. Römgens, D. L. Bader, and J. A. Bouwastra, "Monitoring the penetration process of single microneedles with varying tip diameters," vol. 40, pp. 397–405, 2014, doi: 10.1016/j.jmbbm.2014.09.015.
- [16] S. A. Coulman *et al.*, "In vivo, in situ imaging of microneedle insertion into the skin of human volunteers using optical coherence tomography," *Pharm Res*, vol. 28, no. 1, pp. 66–81, Jan. 2011, doi: 10.1007/s11095-010-0167-x.
- [17] M. Oldfield, D. Dini, G. Giordano, and F. Rodriguez y Baena, "Detailed finite element modelling of deep needle insertions into a soft tissue phantom using a cohesive approach," *Comput Methods Biomech Biomed Engin*, vol. 16, no. 5, pp. 530–543, May 2013, doi: 10.1080/10255842.2011.628448.
- [18] H. Mohammadi, H. Mohammadi, and N. Maftoon, "A Validated Cohesive Finite Element Analysis of Needle Insertion into Human Skin," 2021. [Online]. Available: <https://www.researchgate.net/publication/351919580>
- [19] W. Shu, H. Heimark, N. Bertollo, D. J. Tobin, E. D. O'Cearbhaill, and A. N. Annaidh, "Insights into the mechanics of solid conical microneedle array insertion into skin using the finite element method," *Acta Biomater*, vol. 135, pp. 403–413, Nov. 2021, doi: 10.1016/j.actbio.2021.08.045.
- [20] S. Chen, N. Li, and J. Chen, "Finite element analysis of microneedle insertion into skin," *Micro Nano Lett*, vol. 7, no. 12, pp. 1206–1209, Dec. 2012, doi: 10.1049/mnl.2012.0585.

## References

- [21] T. Gambichler, R. Matip, G. Moussa, P. Altmeyer, and K. Hoffmann, "In vivo data of epidermal thickness evaluated by optical coherence tomography: Effects of age, gender, skin type, and anatomic site," *J Dermatol Sci*, vol. 44, no. 3, pp. 145–152, Dec. 2006, doi: 10.1016/j.jdermsci.2006.09.008.
- [22] M. Ottenio, D. Tran, A. Ní Annaidh, M. D. Gilchrist, and K. Bruyère, "Strain rate and anisotropy effects on the tensile failure characteristics of human skin," *J Mech Behav Biomed Mater*, vol. 41, pp. 241–250, Jan. 2015, doi: 10.1016/j.jmbbm.2014.10.006.
- [23] R. B. Groves, S. A. Coulman, J. C. Birchall, and S. L. Evans, "Quantifying the mechanical properties of human skin to optimise future microneedle device design," *Comput Methods Biomech Biomed Engin*, vol. 15, no. 1, pp. 73–82, Jan. 2012, doi: 10.1080/10255842.2011.596481.
- [24] C. Radhika and B. K. Gnanavel, "Finite element analysis of polymer microneedle for transdermal drug delivery," *Mater Today Proc*, no. xxxx, 2020, doi: 10.1016/j.matpr.2020.05.549.
- [25] S. M. Amin, M. H. Ramlee, H. F. Mohd Latip, H. S. Gan, and M. R. A. Kadir, "Finite Element Analysis of Needle Insertion Angle in Insulin Therapy," *Int. J. Automot. Mech. Eng.*, vol. 16, pp. 7512–7523, 2019, doi: 10.15282/ijame.16.4.2019.21.0555.
- [26] L. Jiang *et al.*, "Research on Insertion Process of Medical Needle," in Proc. 3rd Int. Conf. Mater. Eng., Manuf. Technol. Control (ICMEMTC), 2016.
- [27] W. Assaad, A. Jahya, P. Moreira, and S. Misra, "Finite-element modeling of a bevel-tipped needle interacting with gel," *J Mech Med Biol*, vol. 15, no. 5, Oct. 2015, doi: 10.1142/S0219519415500797.
- [28] X. Q. Kong, P. Zhou, and C. W. Wu, "Numerical simulation of microneedles' insertion into skin," *Comput Methods Biomech Biomed Engin*, vol. 14, no. 9, pp. 827–835, 2011, doi: 10.1080/10255842.2010.497144.
- [29] Y. Amiri and B. Vahidi, "Three dimensional simulation of the microneedle penetration process in the skin by finite element method," in *2019 26th National and 4th International Iranian Conference on Biomedical Engineering, ICBME 2019*, Institute of Electrical and Electronics Engineers Inc., Nov. 2019, pp. 70–74. doi: 10.1109/ICBME49163.2019.9030385.
- [30] W. Yu *et al.*, "Fabrication of biodegradable composite microneedles based on calcium sulfate and gelatin for transdermal delivery of insulin," *Materials Science and Engineering C*, vol. 71, pp. 725–734, 2017, doi: 10.1016/j.msec.2016.10.063.
- [31] "Needle Gauge Chart | Syringe Needle Gauge Chart | Hamilton." Accessed: May 20, 2021. [Online]. Available: <https://www.hamiltoncompany.com/laboratory-products/needles-knowledge/needle-gauge-chart>
- [32] M. S. Gerstel and V. A. Place, "Drug delivery device - US 3964482 A," *U. S. Patent*, vol. 482, no. 19, 1976.
- [33] Y. Amiri and B. Vahidi, "Three dimensional simulation of the microneedle penetration process in the skin by finite element method," *2019 26th National and 4th International Iranian Conference on*

## References

- Biomedical Engineering, ICBME 2019*, no. November, pp. 70–74, 2019, doi: 10.1109/ICBME49163.2019.9030385.
- [34] M. I. Haq *et al.*, “Clinical administration of microneedles: Skin puncture, pain and sensation,” *Biomed Microdevices*, vol. 11, no. 1, pp. 35–47, 2009, doi: 10.1007/s10544-008-9208-1.
- [35] J. Xu, D. Xu, X. Xuan, and H. He, “Advances of microneedles in biomedical applications,” Oct. 01, 2021, *MDPI*. doi: 10.3390/molecules26195912.
- [36] T. Waghule *et al.*, “Microneedles: A smart approach and increasing potential for transdermal drug delivery system,” Jan. 01, 2019, *Elsevier Masson SAS*. doi: 10.1016/j.biopha.2018.10.078.
- [37] M. Dul *et al.*, “Hydrodynamic gene delivery in human skin using a hollow microneedle device,” *Journal of Controlled Release*, vol. 265, pp. 120–131, 2017, doi: 10.1016/j.jconrel.2017.02.028.
- [38] T. Waghule *et al.*, “Microneedles: A smart approach and increasing potential for transdermal drug delivery system,” *Biomedicine and Pharmacotherapy*, vol. 109, no. September 2018, pp. 1249–1258, 2019, doi: 10.1016/j.biopha.2018.10.078.
- [39] E. Z. Loizidou *et al.*, “Structural characterisation and transdermal delivery studies on sugar microneedles: Experimental and finite element modelling analyses,” *European Journal of Pharmaceutics and Biopharmaceutics*, vol. 89, pp. 224–231, 2015, doi: 10.1016/j.ejpb.2014.11.023.
- [40] M. Y. Kim, B. Jung, and J. H. Park, “Hydrogel swelling as a trigger to release biodegradable polymer microneedles in skin,” *Biomaterials*, vol. 33, no. 2, pp. 668–678, 2012, doi: 10.1016/j.biomaterials.2011.09.074.
- [41] D. D. Zhu, Q. L. Wang, X. B. Liu, and X. D. Guo, “Rapidly separating microneedles for transdermal drug delivery,” *Acta Biomater*, vol. 41, pp. 312–319, 2016, doi: 10.1016/j.actbio.2016.06.005.
- [42] W. Li, R. N. Terry, J. Tang, M. R. Feng, S. P. Schwendeman, and M. R. Prausnitz, “Rapidly separable microneedle patch for the sustained release of a contraceptive,” *Nat Biomed Eng*, vol. 3, no. 3, pp. 220–229, 2019, doi: 10.1038/s41551-018-0337-4.
- [43] D. V Mcallister *et al.*, “Microfabricated needles for transdermal delivery of macromolecules and nanoparticles: Fabrication methods and transport studies,” 2003. [Online]. Available: [www.pnas.org/cgi/doi/10.1073/pnas.2331316100](http://www.pnas.org/cgi/doi/10.1073/pnas.2331316100)
- [44] J. H. Park, M. G. Allen, and M. R. Prausnitz, “Biodegradable polymer microneedles: Fabrication, mechanics and transdermal drug delivery,” *Journal of Controlled Release*, vol. 104, no. 1, pp. 51–66, May 2005, doi: 10.1016/j.jconrel.2005.02.002.
- [45] A. Malek-Khatabi, Z. Faraji Rad, M. Rad-Malekshahi, and H. Akbarijavar, “Development of dissolvable microneedle patches by CNC machining and micromolding for drug delivery,” *Mater Lett*, vol. 330, Jan. 2023, doi: 10.1016/j.matlet.2022.133328.
- [46] I. Xenikakis *et al.*, “Fabrication and finite element analysis of stereolithographic 3D printed microneedles for transdermal delivery of model dyes across human skin in vitro,” *European Journal of*

## References

- Pharmaceutical Sciences*, vol. 137, Sep. 2019, doi: 10.1016/j.ejps.2019.104976.
- [47] Z. Ali, E. B. Türeyen, Y. Karpaz, and M. Çakmakci, "Fabrication of Polymer Micro Needles for Transdermal Drug Delivery System Using DLP Based Projection Stereo-lithography," in *Procedia CIRP*, Elsevier B.V., 2016, pp. 87–90. doi: 10.1016/j.procir.2016.02.194.
- [48] Q. Yang *et al.*, "3D-printed morphology-customized microneedles: Understanding the correlation between their morphologies and the received qualities," *Int J Pharm*, vol. 638, May 2023, doi: 10.1016/j.ijpharm.2023.122873.
- [49] R. Li *et al.*, "3D-printed microneedle arrays for drug delivery," Oct. 01, 2022, *Elsevier B.V.* doi: 10.1016/j.jconrel.2022.08.022.
- [50] N. Elahpour, F. Pahlevanzadeh, M. Kharaziha, H. R. Bakhsheshi-Rad, S. Ramakrishna, and F. Berto, "3D printed microneedles for transdermal drug delivery: A brief review of two decades," Mar. 15, 2021, *Elsevier B.V.* doi: 10.1016/j.ijpharm.2021.120301.
- [51] R. S. J. Ingrole and H. S. Gill, "Microneedle coating methods: A review with a perspective," 2019, *American Society for Pharmacology and Experimental Therapy*. doi: 10.1124/jpet.119.258707.
- [52] K. T. Chang, Y. K. Shen, F. Y. Fan, Y. Lin, and S. C. Kang, "Optimal design and fabrication of a microneedle arrays patch," *J Manuf Process*, vol. 54, pp. 274–285, Jun. 2020, doi: 10.1016/j.jmapro.2020.02.024.
- [53] W. Yu *et al.*, "Fabrication of biodegradable composite microneedles based on calcium sulfate and gelatin for transdermal delivery of insulin," *Materials Science and Engineering C*, vol. 71, pp. 725–734, Feb. 2017, doi: 10.1016/j.msec.2016.10.063.
- [54] Z. Le *et al.*, "Design principles of microneedles for drug delivery and sampling applications," Mar. 01, 2023, *Elsevier B.V.* doi: 10.1016/j.mattod.2022.10.025.
- [55] M. L. Crichton *et al.*, "Characterising the material properties at the interface between skin and a skin vaccination microprojection device," *Acta Biomater*, vol. 36, pp. 186–194, May 2016, doi: 10.1016/j.actbio.2016.02.039.
- [56] M. L. Crichton, A. Ansaldo, X. Chen, T. W. Prow, G. J. P. Fernando, and M. A. F. Kendall, "The effect of strain rate on the precision of penetration of short densely-packed microprojection array patches coated with vaccine," *Biomaterials*, vol. 31, no. 16, pp. 4562–4572, Jun. 2010, doi: 10.1016/j.biomaterials.2010.02.022.
- [57] J. Lim, D. Tahk, J. Yu, D. H. Min, and N. L. Jeon, "Design rules for a tunable merged-tip microneedle," *Microsyst Nanoeng*, vol. 4, no. 1, Dec. 2018, doi: 10.1038/s41378-018-0028-z.
- [58] Y. Wang *et al.*, "Bioimaging of Dissolvable Microneedle Arrays: Challenges and Opportunities," *Research*, vol. 2022, Jan. 2022, doi: 10.34133/2022/9758491.
- [59] M. Pearton *et al.*, "Microneedle delivery of plasmid DNA to living human skin: Formulation coating, skin insertion and gene expression," *Journal of Controlled Release*, vol. 160, no. 3, pp. 561–569, Jun. 2012, doi: 10.1016/j.jconrel.2012.04.005.

## References

- [60] M. Dul *et al.*, “Hydrodynamic gene delivery in human skin using a hollow microneedle device,” *Journal of Controlled Release*, vol. 265, pp. 120–131, Nov. 2017, doi: 10.1016/j.jconrel.2017.02.028.
- [61] J. Birchall *et al.*, “Cutaneous DNA delivery and gene expression in ex vivo human skin explants via wet-etch microfabricated microneedles,” *J Drug Target*, vol. 13, no. 7, pp. 415–421, Aug. 2005, doi: 10.1080/10611860500383705.
- [62] F. Henriquez, D. Celentano, M. Vega, G. Pincheira, and J. O. Morales-Ferreiro, “Modeling of Microneedle Arrays in Transdermal Drug Delivery Applications,” *Pharmaceutics*, vol. 15, no. 2, Feb. 2023, doi: 10.3390/pharmaceutics15020358.
- [63] A. M. Römogens, D. L. Bader, J. A. Bouwstra, and C. W. J. Oomens, “Predicting the optimal geometry of microneedles and their array for dermal vaccination using a computational model,” *Comput Methods Biomech Biomed Engin*, vol. 19, no. 15, pp. 1599–1609, Nov. 2016, doi: 10.1080/10255842.2016.1173684.
- [64] P. Ranjan Yadav *et al.*, “Super-swelling hydrogel-forming microneedle based transdermal drug delivery: Mathematical modelling, simulation and experimental validation,” *Int J Pharm*, vol. 622, Jun. 2022, doi: 10.1016/j.ijpharm.2022.121835.
- [65] K. Moronkeji, S. Todd, I. Dawidowska, S. D. Barrett, and R. Akhtar, “The role of subcutaneous tissue stiffness on microneedle performance in a representative in vitro model of skin,” *Journal of Controlled Release*, vol. 265, pp. 102–112, Nov. 2017, doi: 10.1016/j.jconrel.2016.11.004.
- [66] S. Fregonese and M. Bacca, “Piercing soft solids: A mechanical theory for needle insertion,” *J Mech Phys Solids*, vol. 154, Sep. 2021, doi: 10.1016/j.jmps.2021.104497.
- [67] A. Boonma, R. J. Narayan, and Y. S. Lee, “Analytical modeling and evaluation of microneedles apparatus with deformable soft tissues for biomedical applications,” *Comput Aided Des Appl*, vol. 10, no. 1, pp. 139–157, 2013, doi: 10.3722/cadaps.2013.139-157.
- [68] R. Chumpu, C. L. Chu, T. Treeratanaphitak, S. Marukatat, and S. H. Hsu, “Physics-informed graph neural networks accelerating microneedle simulations towards novelty of micro-nano scale materials discovery,” *Eng Appl Artif Intell*, vol. 126, Nov. 2023, doi: 10.1016/j.engappai.2023.106894.
- [69] R. B. Groves, S. A. Coulman, J. C. Birchall, and S. L. Evans, “An anisotropic, hyperelastic model for skin: Experimental measurements, finite element modelling and identification of parameters for human and murine skin,” *J Mech Behav Biomed Mater*, vol. 18, pp. 167–180, Feb. 2013, doi: 10.1016/j.jmbbm.2012.10.021.
- [70] J. Arya and M. R. Prausnitz, “Microneedle patches for vaccination in developing countries,” *Journal of Controlled Release*, vol. 240, pp. 135–141, Oct. 2016, doi: 10.1016/j.jconrel.2015.11.019.
- [71] I. Menon *et al.*, “Microneedles: A new generation vaccine delivery system,” Apr. 01, 2021, *MDPI AG*. doi: 10.3390/mi12040435.
- [72] J. Halder, S. Gupta, R. Kumari, G. Das Gupta, and V. K. Rai, “Microneedle Array: Applications, Recent Advances, and Clinical

## References

- Pertinence in Transdermal Drug Delivery,” Sep. 01, 2021, *Springer*. doi: 10.1007/s12247-020-09460-2.
- [73] R. Kaur, S. Arora, and M. Goswami, “Advancement in microneedles as minimally invasive delivery system for pharmaceutical and biomedical application: A review,” *Mater Today Proc*, 2022, doi: 10.1016/j.matpr.2022.11.182.
- [74] S. A. Coulman *et al.*, “Microneedle mediated delivery of nanoparticles into human skin,” *Int J Pharm*, vol. 366, no. 1–2, pp. 190–200, Jan. 2009, doi: 10.1016/j.ijpharm.2008.08.040.
- [75] Y. Zhang, J. Yu, A. R. Kahkoska, J. Wang, J. B. Buse, and Z. Gu, “Advances in transdermal insulin delivery,” Jan. 15, 2019, *Elsevier B.V.* doi: 10.1016/j.addr.2018.12.006.
- [76] W. Li *et al.*, “Core-shell microneedle patch for six-month controlled-release contraceptive delivery,” *Journal of Controlled Release*, vol. 347, pp. 489–499, Jul. 2022, doi: 10.1016/j.jconrel.2022.04.051.
- [77] A. J. Guillot, A. S. Cordeiro, R. F. Donnelly, M. C. Montesinos, T. M. Garrigues, and A. Meleró, “Microneedle-based delivery: An overview of current applications and trends,” Jun. 01, 2020, *MDPI AG*. doi: 10.3390/pharmaceutics12060569.
- [78] E. Larrañeta, M. T. C. McCrudden, A. J. Courtenay, and R. F. Donnelly, “Microneedles: A New Frontier in Nanomedicine Delivery,” May 01, 2016, *Springer New York LLC*. doi: 10.1007/s11095-016-1885-5.
- [79] A. F. Moreira, C. F. Rodrigues, T. A. Jacinto, S. P. Miguel, E. C. Costa, and I. J. Correia, “Microneedle-based delivery devices for cancer therapy: A review,” Oct. 01, 2019, *Academic Press*. doi: 10.1016/j.phrs.2019.104438.
- [80] J. Weng *et al.*, “Construction and application of microneedle-mediated photothermal therapy and immunotherapy combined anti-tumor drug delivery system,” *Drug Deliv*, vol. 30, no. 1, 2023, doi: 10.1080/10717544.2023.2232950.
- [81] G. Mužíková, R. Pola, R. Laga, and M. Pechar, “Biodegradable Multiblock Polymers Based on N-(2-Hydroxypropyl)methacrylamide Designed as Drug Carriers for Tumor-Targeted Delivery,” *Macromol Chem Phys*, vol. 217, no. 15, pp. 1690–1703, Aug. 2016, doi: 10.1002/macp.201600097.
- [82] R. H. E. Chong *et al.*, “Gene silencing following siRNA delivery to skin via coated steel microneedles: In vitro and in vivo proof-of-concept,” *Journal of Controlled Release*, vol. 166, no. 3, pp. 211–219, Mar. 2013, doi: 10.1016/j.jconrel.2012.12.030.
- [83] R. Mo *et al.*, “Transdermal drug delivery via microneedles to mediate wound microenvironment,” Apr. 01, 2023, *Elsevier B.V.* doi: 10.1016/j.addr.2023.114753.
- [84] B. Mbituyimana, C. F. Bukatuka, F. Qi, G. Ma, Z. Shi, and G. Yang, “Microneedle-mediated drug delivery for scar prevention and treatment,” Nov. 01, 2023, *Elsevier Ltd*. doi: 10.1016/j.drudis.2023.103801.
- [85] B. H. J. Gowda, M. G. Ahmed, U. Hani, P. Kesharwani, S. Wahab, and K. Paul, “Microneedles as a momentous platform for psoriasis therapy

## References

- and diagnosis: A state-of-the-art review," Feb. 05, 2023, *Elsevier B.V.* doi: 10.1016/j.ijpharm.2023.122591.
- [86] Y. Zhou, L. Jia, D. Zhou, G. Chen, Q. Fu, and N. Li, "Advances in microneedles research based on promoting hair regrowth," Jan. 01, 2023, *Elsevier B.V.* doi: 10.1016/j.jconrel.2022.12.040.
- [87] S. Ruan, Y. Zhang, and N. Feng, "Microneedle-mediated transdermal nanodelivery systems: A review," Dec. 21, 2021, *Royal Society of Chemistry.* doi: 10.1039/d1bm01249e.
- [88] R. Groves, "Quantifying the mechanical properties of skin in vivo and ex vivo to optimise microneedle device design," PhD thesis, Cardiff University, 2012.
- [89] S. A. Coulman *et al.*, "In vivo, in situ imaging of microneedle insertion into the skin of human volunteers using optical coherence tomography," *Pharm Res*, vol. 28, no. 1, pp. 66–81, 2011, doi: 10.1007/s11095-010-0167-x.
- [90] J. Casey and P. M. Naghdi, "A correct definition of elastic and plastic deformation and its computational significance," *Journal of Applied Mechanics, Transactions ASME*, vol. 48, no. 4, pp. 983–985, 1981, doi: 10.1115/1.3157775.
- [91] L. K. Smalls, R. Randall Wickett, and M. O. Visscher, "Effect of dermal thickness, tissue composition, and body site on skin biomechanical properties," *Skin Research and Technology*, vol. 12, no. 1, pp. 43–49, 2006, doi: 10.1111/j.0909-725X.2006.00135.x.
- [92] R. B. Groves, S. A. Coulman, J. C. Birchall, and S. L. Evans, "Quantifying the mechanical properties of human skin to optimise future microneedle device design," *Comput Methods Biomech Biomed Engin*, vol. 15, no. 1, pp. 73–82, 2012, doi: 10.1080/10255842.2011.596481.
- [93] O. Olatunji, D. B. Das, M. J. Garland, L. Belaid, and R. F. Donnelly, "Influence of array interspacing on the force required for successful microneedle skin penetration: Theoretical and practical approaches," *J Pharm Sci*, vol. 102, no. 4, pp. 1209–1221, 2013, doi: 10.1002/jps.23439.
- [94] S. J. Mostafavi Yazdi and J. Baqersad, "Mechanical modeling and characterization of human skin: A review," Jan. 01, 2022, *Elsevier Ltd.* doi: 10.1016/j.jbiomech.2021.110864.
- [95] N. Sasaki, "Viscoelastic properties of biological materials." *Viscoelasticity - From Theory to Biological Applications.* InTech, Nov. 07, 2012. doi: 10.5772/49979.
- [96] F. M. Hendriks, D. Brokken, C. W. J. Oomens, D. L. Bader, and F. P. T. Baaijens, "The relative contributions of different skin layers to the mechanical behavior of human skin in vivo using suction experiments," *Med Eng Phys*, vol. 28, no. 3, pp. 259–266, Apr. 2006, doi: 10.1016/j.medengphy.2005.07.001.
- [97] T. Gambichler, R. Matip, G. Moussa, P. Altmeyer, and K. Hoffmann, "In vivo data of epidermal thickness evaluated by optical coherence tomography: Effects of age, gender, skin type, and anatomic site," *J Dermatol Sci*, vol. 44, no. 3, pp. 145–152, 2006, doi: 10.1016/j.jdermsci.2006.09.008.

## References

- [98] J. F. M. Manschot and A. J. M. Brakkee, "the measurement and modelling of the mechanical properties of human skin in vivo-i. The measurement." *J. Biomechanics*, vol. 19, no. 7, pp. 511–515, 1986. doi: 10.1016/0021-9290(86)90124-7.
- [99] D. L. Bader and P. Bowker, "Mechanical characteristics underlying tissues in vivo of skin." *J. Biomechanics*, vol. 19, no. 7, pp. 511–515, 1986. doi: 10.1016/0021-9290(86)90124-7
- [100] C. Pailler-Mattéi and H. Zahouani, "Analysis of adhesive behaviour of human skin in vivo by an indentation test," *Tribol Int*, vol. 39, no. 1, pp. 12–21, Jan. 2006, doi: 10.1016/j.triboint.2004.11.003.
- [101] C. Pailler-Mattei, S. Bec, and H. Zahouani, "In vivo measurements of the elastic mechanical properties of human skin by indentation tests," *Med Eng Phys*, vol. 30, no. 5, pp. 599–606, Jun. 2008, doi: 10.1016/j.medengphy.2007.06.011.
- [102] A. Pissarenko *et al.*, "Tensile behavior and structural characterization of pig dermis," *Acta Biomater*, vol. 86, pp. 77–95, Mar. 2019, doi: 10.1016/j.actbio.2019.01.023.
- [103] A. Pissarenko *et al.*, "The toughness of porcine skin: Quantitative measurements and microstructural characterization," *J Mech Behav Biomed Mater*, vol. 109, Sep. 2020, doi: 10.1016/j.jmbbm.2020.103848.
- [104] M. Liu, J. Guo, C. Y. Hui, and A. T. Zehnder, "Application of Digital Image Correlation (DIC) to the Measurement of Strain Concentration of a PVA Dual-Crosslink Hydrogel Under Large Deformation," *Exp Mech*, vol. 59, no. 7, pp. 1021–1032, Sep. 2019, doi: 10.1007/s11340-019-00520-4.
- [105] T. K. Tonge, L. S. Atlan, L. M. Voo, and T. D. Nguyen, "Full-field bulge test for planar anisotropic tissues: Part I-Experimental methods applied to human skin tissue," *Acta Biomater*, vol. 9, no. 4, pp. 5913–5925, 2013, doi: 10.1016/j.actbio.2012.11.035.
- [106] R. Panchal, L. Horton, P. Poozesh, J. Baqersad, and M. Nasiriavanaki, "Vibration analysis of healthy skin: toward a noninvasive skin diagnosis methodology," *J Biomed Opt*, vol. 24, no. 01, p. 1, Jan. 2019, doi: 10.1117/1.JBO.24.1.015001.
- [107] S. L. Evans and C. A. Holt, "Measuring the mechanical properties of human skin in vivo using digital image correlation and finite element modelling," *Journal of Strain Analysis for Engineering Design*, vol. 44, no. 5, pp. 337–345, Jul. 2009, doi: 10.1243/03093247JSA488.
- [108] A. Ni Annaidh, M. Destrade, M. Ottenio, K. Bruyere, and M. D. Gilchrist, "Strain rate effects on the failure characteristics of excised human skin." in *Proc. 9th Int. Conf. Mechanics Time Dependent Materials*, Montreal, Canada, May 2014, pp. 1-2. [Online]. Available: hal-01916691.
- [109] F. M. Hendriks, D. Brokken, J. T. W. M. van Eemeren, C. W. J. Oomens, F. P. T. Baaijens, and J. B. A. M. Horsten, "A numerical-experimental method to characterize the non-linear mechanical behavior of human skin," *Skin Research and Technology*, vol. 9, no. 3, pp. 274–283, Aug. 2003, doi: 10.1034/j.1600-0846.2003.00019.x.
- [110] F. M. Hendriks, D. Brokken, C. W. J. Oomens, D. L. Bader, and F. P. T. Baaijens, "The relative contributions of different skin layers to the

## References

- mechanical behavior of human skin in vivo using suction experiments,” *Med Eng Phys*, vol. 28, no. 3, pp. 259–266, 2006, doi: 10.1016/j.medengphy.2005.07.001.
- [111] P. G. Agache, C. Monneur, J. L. Leveque, and J. De Rigal, “Mechanical Properties and Young’s Modulus of Human Skin in Vivo,” *Arch. Dermatol. Res.*, vol. 269, no. 3, pp. 221–232, 1980. doi: 10.1007/BF00406415.
- [112] R. Sanders, “Torsional Elasticity of Human Skin in vivo.” *Pflugers Arch.*, vol. 342, pp. 255–260, 1973. doi: 10.1007/BF00591373.
- [113] M. G. Fernandes, L. P. Da Silva, and A. P. Marques, “Skin mechanobiology and biomechanics: From homeostasis to wound healing,” in *Advances in Biomechanics and Tissue Regeneration*, Elsevier, 2019, pp. 343–360. doi: 10.1016/B978-0-12-816390-0.00017-0.
- [114] C. Pailler-Mattei, S. Pavan, R. Vargiolu, F. Pirot, F. Falson, and H. Zahouani, “Contribution of stratum corneum in determining biotribological properties of the human skin,” *Wear*, vol. 263, no. 7-12 SPEC. ISS., pp. 1038–1043, Sep. 2007, doi: 10.1016/j.wear.2007.01.128.
- [115] C. Pailler-Mattei, S. Bec, and H. Zahouani, “In vivo measurements of the elastic mechanical properties of human skin by indentation tests,” *Med Eng Phys*, vol. 30, no. 5, pp. 599–606, Jun. 2008, doi: 10.1016/j.medengphy.2007.06.011.
- [116] S. Diridollou *et al.*, “In vivo model of the mechanical properties of the human skin under suction,” *Skin Research and Technology*, vol. 6, no. 4, pp. 214–221, 2000, doi: 10.1034/j.1600-0846.2000.006004214.x.
- [117] X. Liang and S. A. Boppart, “Biomechanical properties of in vivo human skin from dynamic optical coherence elastography,” *IEEE Trans Biomed Eng*, vol. 57, no. 4, pp. 953–959, 2010, doi: 10.1109/TBME.2009.2033464.
- [118] Treloar. L R G, “The elasticity of a network of long-chain molecules,” *Transactions of the Faraday Society*, no. 36, pp. 36–41, 1942.
- [119] M. Mooney, “A Theory of Large Elastic Deformation,” *J Appl Phys*, vol. 11, no. 9, pp. 582–592, Sep. 1940, doi: 10.1063/1.1712836.
- [120] R. S. Rivlin, “Large elastic deformations of isotropic materials IV. further developments of the general theory”, doi: <https://doi.org/10.1098/rsta.1948.0024>.
- [121] D. R. Veronda and R. A. Westmann, “Mechanical characterization of skin - Finite deformations,” Pergamon Press, 1970. doi: [https://doi.org/10.1016/0021-9290\(70\)90055-2](https://doi.org/10.1016/0021-9290(70)90055-2).
- [122] R. W. Ogden, “Large Deformation Isotropic Elasticity - on the Correlation of Theory and Experiment for Incompressible Rubberlike Solids.,” *Rubber Chemistry and Technology*, vol. 46, no. 2, pp. 398–416, 1973, doi: 10.5254/1.3542910.
- [123] B. Kim *et al.*, “A comparison among Neo-Hookean model, Mooney-Rivlin model, and Ogden model for Chloroprene rubber,” *International Journal of Precision Engineering and Manufacturing*, vol. 13, no. 5, pp. 759–764, 2012, doi: 10.1007/s12541-012-0099-y.
- [124] T. C. Gasser and G. A. Holzapfel, “A rate-independent elastoplastic constitutive model for biological fiber-reinforced composites

## References

- at finite strains: Continuum basis, algorithmic formulation and finite element implementation,” *Comput Mech*, vol. 29, no. 4–5, pp. 340–360, 2002, doi: 10.1007/s00466-002-0347-6.
- [125] A. C. Vieira, A. T. Marques, R. M. Guedes, and V. Tita, “Material model proposal for biodegradable materials,” *Procedia Eng*, vol. 10, pp. 1597–1602, 2011, doi: 10.1016/j.proeng.2011.04.267.
- [126] L. K. Smalls, R. Randall Wickett, and M. O. Visscher, “Effect of dermal thickness, tissue composition, and body site on skin biomechanical properties,” *Skin Research and Technology*, vol. 12, no. 1, pp. 43–49, 2006, doi: 10.1111/j.0909-725X.2006.00135.x.
- [127] M. Geerligs, L. van Breemen, G. Peters, P. Ackermans, F. Baaijens, and C. Oomens, “In vitro indentation to determine the mechanical properties of epidermis,” *J Biomech*, vol. 44, no. 6, pp. 1176–1181, Apr. 2011, doi: 10.1016/j.jbiomech.2011.01.015.
- [128] M. L. Crichton, B. C. Donose, X. Chen, A. P. Raphael, H. Huang, and M. A. F. Kendall, “The viscoelastic, hyperelastic and scale dependent behaviour of freshly excised individual skin layers,” *Biomaterials*, vol. 32, no. 20, pp. 4670–4681, Jul. 2011, doi: 10.1016/j.biomaterials.2011.03.012.
- [129] D. Broek, *Elementary engineering fracture mechanics*. Dordrecht: Springer Netherlands, 1982. doi: 10.1007/978-94-009-4333-9.
- [130] G. R. Irwin, “Analysis of Stresses and Strains Near the End of a Crack Traversing a Plate,” *J Appl Mech*, vol. 24, no. 3, pp. 361–364, Sep. 1957, doi: 10.1115/1.4011547.
- [131] Griffith Taylor, “VI The Phenomena of Rupture and Flow in Solids,” 1921, doi: <https://doi.org/10.1098/rsta.1921.0006>.
- [132] F. Erdogan and G. C. Sih, “On the Crack Extension in Plates Under Plane Loading and Transverse Shear,” *Journal of Basic Engineering*, vol. 85, no. 4, pp. 519–525, Dec. 1963, doi: 10.1115/1.3656897.
- [133] A. G. Atkins and Y. W. Mai, *Elastic and Plastic Fracture: Metals, Polymers, Ceramics, Composites, Biological Materials*. Halsted Press, Ellis Horwood, 1985.
- [134] T. Yin, T. Wu, J. Liu, S. Qu, and W. Yang, “Essential work of fracture of soft elastomers,” *J Mech Phys Solids*, vol. 156, Nov. 2021, doi: 10.1016/j.jmps.2021.104616.
- [135] Y. -W Mai and P. Powell, “Essential work of fracture and j-integral measurements for ductile polymers,” *J Polym Sci B Polym Phys*, vol. 29, no. 7, pp. 785–793, 1991, doi: 10.1002/polb.1991.090290702.
- [136] T. L. Anderson, *Fracture Mechanics*. CRC Press, 2017. doi: 10.1201/9781315370293.
- [137] G. Cortelli, L. Patruno, T. Cramer, B. Fraboni, and S. De Miranda, “In Situ Force Microscopy to Investigate Fracture in Stretchable Electronics: Insights on Local Surface Mechanics and Conductivity,” *ACS Appl Electron Mater*, vol. 4, no. 6, pp. 2831–2838, Jun. 2022, doi: 10.1021/acsaelm.2c00328.
- [138] R. S. Rivlin and A. G. Thomas, “Rupture of rubber. I. Characteristic energy for tearing,” *Journal of Polymer Science*, vol. 10, no. 3, pp. 291–318, Mar. 1953, doi: 10.1002/pol.1953.120100303.

## References

- [139] K. B. Broberg, "on stable crack growth," *J. Mechanics and Physics of Solids*, vol. 23, no. 3, pp. 215-237, 1975. doi: 10.1016/0022-5096(75)90017-4..
- [140] J. Wu and Y. W. Mai, "The essential fracture work concept for toughness measurement of ductile polymers," *Polym Eng Sci*, vol. 36, no. 18, pp. 2275–2288, 1996, doi: 10.1002/pen.10626.
- [141] M. Oyen-Tiesma and R. F. Cook, "Technique for estimating fracture resistance of cultured neocartilage." *Journal of Materials Science: Materials in Medicine*, vol. 12, no. 4, pp. 327-332, Apr. 2001. doi: 10.1023/A:1011247104621.
- [142] T. Pardoën, Y. Marchal, and F. Delannay, "Essential work of fracture compared to fracture mechanics-towards a thickness independent plane stress toughness." [Online]. Available: [www.elsevier.com/locate/engfracmech](http://www.elsevier.com/locate/engfracmech)
- [143] E. E. Gdoutos, P. M. Schubel, and I. M. Daniel, "Determination of Critical Tearing Energy of Tyre Rubber." *Strain*, vol. 40, no. 3, pp. 119-125, 2004. doi: 10.1111/j.1475-1305.2004.00139.x.
- [144] D. Taylor, N. O'Mara, E. Ryan, M. Takaza, and C. Simms, "The fracture toughness of soft tissues," *J Mech Behav Biomed Mater*, vol. 6, pp. 139–147, Feb. 2012, doi: 10.1016/j.jmbbm.2011.09.018.
- [145] A. Spagnoli, M. Terzano, R. Brighenti, F. Artoni, and P. Stähle, "The fracture mechanics in cutting: A comparative study on hard and soft polymeric materials," *Int J Mech Sci*, vol. 148, pp. 554–564, Nov. 2018, doi: 10.1016/j.ijmecsci.2018.09.013.
- [146] B. Zhang and S. B. Hutchens, "On the relationship between cutting and tearing in soft elastic solids," *Soft Matter*, vol. 17, no. 28, pp. 6728–6741, Jul. 2021, doi: 10.1039/d1sm00527h.
- [147] T. Yin, T. Wu, J. Liu, S. Qu, and W. Yang, "Essential work of fracture of soft elastomers," *J Mech Phys Solids*, vol. 156, Nov. 2021, doi: 10.1016/j.jmps.2021.104616.
- [148] O. A. Shergold and N. A. Fleck, "Experimental investigation into the deep penetration of soft solids by sharp and blunt punches, with application to the piercing of skin," *J Biomech Eng*, vol. 127, no. 5, pp. 838–848, Oct. 2005, doi: 10.1115/1.1992528.
- [149] O. A. Shergold and N. A. Fleck, "Mechanisms of deep penetration of soft solids, with application to the injection and wounding of skin," *Proceedings of the Royal Society A: Mathematical, Physical and Engineering Sciences*, vol. 460, no. 2050, pp. 3037–3058, Oct. 2004, doi: 10.1098/rspa.2004.1315.
- [150] B. P. Pereira, P. W. Lucas<sup>1</sup>, and T. Swee-Hint, "ranking the fracture toughness of thin mammalian soft tissues using the scissors cutting test," *Journal of Biomechanics*, vol. 30, no. 1, pp. 91-94, 1997. doi: 10.1016/S0021-9290(96)00101-7.
- [151] T. Azar and V. Hayward, "Estimation of the fracture toughness of soft tissue from needle insertion," in *Lecture Notes in Computer Science (including subseries Lecture Notes in Artificial Intelligence and Lecture Notes in Bioinformatics)*, 2008, pp. 166–175. doi: 10.1007/978-3-540-70521-5\_18.

## References

- [152] S. Misra, K. B. Reed, A. S. Douglas, K. T. Ramesh, and A. M. Okamura, *Proceedings of the 2nd Biennial IEEE/RAS-EMBS International Conference on Biomedical Robotics and Biomechatronics: Scottsdale, AZ, USA, October 19-22, 2008*. IEEE Xplore, 2009.
- [153] D. Huang *et al.*, “Optical Coherence Tomography HHS Public Access,” *Science*, vol. 254, no. 5035, pp. 1178–1181, Nov. 1991. doi: 10.1126/science.1957169.
- [154] B. I. Gramatikov, “Modern technologies for retinal scanning and imaging: An introduction for the biomedical engineer,” Apr. 29, 2014, *BioMed Central Ltd*. doi: 10.1186/1475-925X-13-52.
- [155] A. F. Fercher, C. K. Hitzenberger, G. Kamp, and S. Y. El-Zaiat, “Measurement of intraocular distances by backscattering spectral interferometry,” *Optics Commun.*, vol. 117, no. 1–2, pp. 43–48, 1995. doi: 10.1016/0030-4018(95)00119-S.
- [156] W. Drexler and J. G. Fujimoto, *Optical Coherence Tomography*. Cham: Springer International Publishing, 2015. doi: 10.1007/978-3-319-06419-2.
- [157] E. Z. Zhang *et al.*, “Multimodal photoacoustic and optical coherence tomography scanner using an all optical detection scheme for 3D morphological skin imaging,” *Biomed Opt Express*, vol. 2, no. 8, p. 2202, 2011, doi: 10.1364/boe.2.002202.
- [158] H. Schreier, J. J. Orteu, and M. A. Sutton, *Image correlation for shape, motion and deformation measurements: Basic concepts, theory and applications*. Springer US, 2009. doi: 10.1007/978-0-387-78747-3.
- [159] F. Hild and S. Roux, “Digital image correlation: From displacement measurement to identification of elastic properties - A review,” May 2006. doi: 10.1111/j.1475-1305.2006.00258.x.
- [160] X. Wang, W. Shi, D. Chen, Y. Zhang, and J. Chen, “In vivo characterization of skin mechanical properties using digital image correlation and finite element modelling: A review,” *Skin Research and Technology*, vol. 27, no. 1, pp. 27–39, 2021.
- [161] B. J. Smith *et al.*, “Digital imaging analysis to assess scar phenotype,” *Wound Repair and Regeneration*, vol. 22, no. 2, pp. 228–238, 2014, doi: 10.1111/wrr.12141.
- [162] M. Palanca, G. Tozzi, and L. Cristofolini, “The use of digital image correlation in the biomechanical area: A review,” 2016, *Taylor and Francis Ltd*. doi: 10.1080/23335432.2015.1117395.
- [163] M. J. Oldfield *et al.*, “Highly resolved strain imaging during needle insertion: Results with a novel biologically inspired device,” *J Mech Behav Biomed Mater*, vol. 30, pp. 50–60, 2014, doi: 10.1016/j.jmbbm.2013.10.016.
- [164] G. N. Hounsfield, “Computerized transverse axial scanning (tomography): Part I. Description of system,” 1973. [Online]. Available: <https://academic.oup.com/bjr/article/46/552/1016/7306149>
- [165] R. A. Ketcham and W. D. Carlson, “Acquisition, optimization and interpretation of X-ray computed tomographic imagery: applications to the geosciences,” *Computers & Geosciences*, vol. 27, pp. 381–400, 2001. doi: 10.1016/S0098-3004(00)00116-3.

## References

- [166] F. Mees, R. Swennen, M. Van Geet, and P. Jacobs, "Applications of X-ray computed tomography in the geosciences," 1982. [Online]. Available: <https://www.lyellcollection.org>
- [167] S. C. Garcea, Y. Wang, and P. J. Withers, "X-ray computed tomography of polymer composites," Mar. 01, 2018, *Elsevier Ltd.* doi: 10.1016/j.compscitech.2017.10.023.
- [168] P. J. Withers, "X-ray nanotomography," *Mater. Today*, vol. 10, no. 12, pp. 26–34, 2007. doi: 10.1016/S1369-7021(07)70305-X.
- [169] E. Z. Loizidou, N. T. Inoue, J. Ashton-Barnett, D. A. Barrow, and C. J. Allender, "Evaluation of geometrical effects of microneedles on skin penetration by CT scan and finite element analysis," *European Journal of Pharmaceutics and Biopharmaceutics*, vol. 107, pp. 1–6, Oct. 2016, doi: 10.1016/j.ejpb.2016.06.023.
- [170] N. Urao, U. A. Okonkwo, M. M. Fang, Z. W. Zhuang, T. J. Koh, and L. A. DiPietro, "MicroCT angiography detects vascular formation and regression in skin wound healing," *Microvasc Res*, vol. 106, pp. 57–66, Jul. 2016, doi: 10.1016/J.MVR.2016.03.006.
- [171] L. A. Walton *et al.*, "Morphological characterisation of unstained and intact tissue micro-architecture by X-ray computed micro- and nano-tomography," *Sci Rep*, vol. 5, May 2015, doi: 10.1038/srep10074.
- [172] L. Vásárhelyi, Z. Kónya, Kukovecz, and R. Vajtai, "Microcomputed tomography-based characterization of advanced materials: a review," Dec. 01, 2020, *Elsevier Ltd.* doi: 10.1016/j.mtadv.2020.100084.
- [173] C. T. Badea, "Principles of Micro X-ray Computed Tomography," in *Molecular Imaging: Principles and Practice*, Elsevier, 2021, pp. 47–64. doi: 10.1016/B978-0-12-816386-3.00006-5.
- [174] B. Pan and B. Wang, "Some recent advances in digital volume correlation," Dec. 01, 2020, *Elsevier Ltd.* doi: 10.1016/j.optlaseng.2020.106189.
- [175] B. K. Bay, "Methods and applications of digital volume correlation," *Journal of Strain Analysis for Engineering Design*, vol. 43, no. 8, pp. 745–760, 2008, doi: 10.1243/03093247JSA436.
- [176] L. Mao, H. Liu, Y. Lei, J. Wu, Y. Ju, and F. P. Chiang, "Evaluation of Global and Local Digital Volume Correlation for Measuring 3D Deformation in Rocks," *Rock Mech Rock Eng*, vol. 54, no. 9, pp. 4949–4964, Sep. 2021, doi: 10.1007/s00603-021-02517-9.
- [177] A. Buljac *et al.*, "Digital Volume Correlation: Review of Progress and Challenges," *Exp Mech*, vol. 58, no. 5, pp. 661–708, Jun. 2018, doi: 10.1007/s11340-018-0390-7.
- [178] F. Xu, "Quantitative characterization of deformation and damage process by digital volume correlation: A review," Mar. 01, 2018, *Elsevier Ltd.* doi: 10.1016/j.taml.2018.02.004.
- [179] J. P. W. Pluim, J. B. A. A. Maintz, and M. A. Viergever, "Mutual-information-based registration of medical images: A survey," Aug. 2003. doi: 10.1109/TMI.2003.815867.
- [180] B. Zitová and J. Flusser, "Image registration methods: A survey," *Image Vis Comput*, vol. 21, no. 11, pp. 977–1000, 2003, doi: 10.1016/S0262-8856(03)00137-9.

## References

- [181] M. Brown and D. G. Lowe, "Automatic panoramic image stitching using invariant features," in *International Journal of Computer Vision*, Aug. 2007, pp. 59–73. doi: 10.1007/s11263-006-0002-3.
- [182] J. Sivic and A. Zisserman, "Video Google: A Text Retrieval Approach to Object Matching in Videos," *Proc. 9th IEEE Int. Conf. Computer Vision*, Nice, France, 2003, pp. 1470–1477, vol. 2. doi: 10.1109/ICCV.2003.1238663.
- [183] S. Klein, M. Staring, K. Murphy, M. A. Viergever, and J. P. W. Pluim, "Elastix: A toolbox for intensity-based medical image registration," *IEEE Trans Med Imaging*, vol. 29, no. 1, pp. 196–205, Jan. 2010, doi: 10.1109/TMI.2009.2035616.
- [184] G. Balakrishnan, A. Zhao, M. R. Sabuncu, J. Guttag, and A. V. Dalca, "VoxelMorph: A Learning Framework for Deformable Medical Image Registration," Sep. 2018, doi: 10.1109/TMI.2019.2897538.
- [185] K. Rankin *et al.*, "Developing an analogue residual limb for comparative DVC analysis of transtibial prosthetic socket designs," *Materials*, vol. 13, no. 18, Sep. 2020, doi: 10.3390/ma13183955.
- [186] J. Fu, F. Pierron, and P. D. Ruiz, "Elastic stiffness characterization using three-dimensional full-field deformation obtained with optical coherence tomography and digital volume correlation," *J Biomed Opt*, vol. 18, no. 12, p. 121512, Dec. 2013, doi: 10.1117/1.JBO.18.12.121512.
- [187] B. K. Bay, T. S. Smith, D. P. Fyhrie, and M. Saad, "Digital Volume Correlation: Three-dimensional Strain Mapping Using X-ray Tomography." *Experimental Mechanics*, vol. 39, pp. 217–226, 1999. doi: 10.1007/BF02323555.
- [188] E. Dall'Ara, D. Barber, and M. Viceconti, "About the inevitable compromise between spatial resolution and accuracy of strain measurement for bone tissue: A 3D zero-strain study," *J Biomech*, vol. 47, no. 12, pp. 2956–2963, Sep. 2014, doi: 10.1016/j.jbiomech.2014.07.019.
- [189] B. C. Roberts, E. Perilli, and K. J. Reynolds, "Application of the digital volume correlation technique for the measurement of displacement and strain fields in bone: A literature review," Mar. 21, 2014, *Elsevier Ltd*. doi: 10.1016/j.jbiomech.2014.01.001.
- [190] D. Christen, A. Levchuk, S. Schori, P. Schneider, S. K. Boyd, and R. Müller, "Deformable image registration and 3D strain mapping for the quantitative assessment of cortical bone microdamage," *J Mech Behav Biomed Mater*, vol. 8, pp. 184–193, Apr. 2012, doi: 10.1016/j.jmbbm.2011.12.009.
- [191] M. Smith, *ABAQUS/Standard User's Manual, Version 6.9*. Providence, RI: Dassault Systèmes Simulia Corp, 2009.
- [192] The MathWorks Inc., "MATLAB version 23.2.0 (R2023b)," 2023, *The MathWorks Inc., Massachusetts: 23.2.0 (R2023b)*.
- [193] S. A. Maas, B. J. Ellis, G. A. Ateshian, and J. A. Weiss, "FEBio: Finite elements for biomechanics," *J Biomech Eng*, vol. 134, no. 1, 2012, doi: 10.1115/1.4005694.
- [194] J. L. Lévêque and B. Audoly, "Influence of Stratum Corneum on the entire skin mechanical properties, as predicted by a computational skin model," *Skin Research and Technology*, vol. 19, no. 1, pp. 42–46, Feb. 2013, doi: 10.1111/j.1600-0846.2012.00664.x.

## References

- [195] N. Sasaki, "Viscoelastic properties of biological materials."
- [196] F. Khatyr, C. Imberdis, P. Vescovo, D. Varchon, and J. M. Lagarde, "Model of the viscoelastic behaviour of skin in vivo and study of anisotropy," *Skin Research and Technology*, vol. 10, no. 2, pp. 96–103, May 2004, doi: 10.1111/j.1600-0846.2004.00057.x.
- [197] C. Flynn and B. A. O. McCormack, "Simulating the wrinkling and aging of skin with a multi-layer finite element model," *J Biomech*, vol. 43, no. 3, pp. 442–448, Feb. 2010, doi: 10.1016/j.jbiomech.2009.10.007.
- [198] D. Pond, A. T. McBride, L. M. Davids, B. D. Reddy, and G. Limbert, "Microstructurally-based constitutive modelling of the skin – Linking intrinsic ageing to microstructural parameters," *J Theor Biol*, vol. 444, pp. 108–123, May 2018, doi: 10.1016/j.jtbi.2018.01.014.
- [199] Y. Zhao, B. Feng, J. Lee, N. Lu, and D. M. Pierce, "A multi-layered model of human skin elucidates mechanisms of wrinkling in the forehead," *J Mech Behav Biomed Mater*, vol. 105, May 2020, doi: 10.1016/j.jmbbm.2020.103694.
- [200] S. L. Evans, "On the implementation of a wrinkling, hyperelastic membrane model for skin and other materials," *Comput Methods Biomech Biomed Engin*, vol. 12, no. 3, pp. 319–332, 2009, doi: 10.1080/10255840802546762.
- [201] A. C. Vieira, A. T. Marques, R. M. Guedes, and V. Tita, "Material model proposal for biodegradable materials," *Procedia Eng*, vol. 10, pp. 1597–1602, 2011, doi: 10.1016/j.proeng.2011.04.267.
- [202] B. Kim *et al.*, "A comparison among Neo-Hookean model, Mooney-Rivlin model, and Ogden model for Chloroprene rubber," *International Journal of Precision Engineering and Manufacturing*, vol. 13, no. 5, pp. 759–764, 2012, doi: 10.1007/s12541-012-0099-y.
- [203] T. Chanthasopephan, J. P. Desai, and A. C. W. Lau, "Modeling soft-tissue deformation prior to cutting for surgical simulation: Finite element analysis and study of cutting parameters," *IEEE Trans Biomed Eng*, vol. 54, no. 3, pp. 349–359, Mar. 2007, doi: 10.1109/TBME.2006.886937.
- [204] S. Singh *et al.*, "Modeling the insertion mechanics of flexible neural probes coated with sacrificial polymers for optimizing probe design," *Sensors (Switzerland)*, vol. 16, no. 3, Mar. 2016, doi: 10.3390/s16030330.
- [205] M. J. Oldfield, D. Dini, T. Jaiswal, and F. Rodriguez Y Baena, "The significance of rate dependency in blade insertions into a gelatin soft tissue phantom," in *Tribology International*, Elsevier Ltd, 2013, pp. 226–234. doi: 10.1016/j.triboint.2012.08.021.
- [206] H. Mohammadi, A. Ebrahimian, and N. Maftoon, "Fracture behaviour of human skin in deep needle insertion can be captured using validated cohesive zone finite-element method," *Comput Biol Med*, vol. 139, Dec. 2021, doi: 10.1016/j.combiomed.2021.104982.
- [207] A. J. Gallagher, A. N. Anniadh, K. Bruyere, M. Otténio, H. Xie, and M. D. Gilchrist, "Dynamic Tensile Properties of Human Skin." *Medicine, Engineering, Materials Science*, 2012.

## References

- [208] “Technovent Silicone page2.” Accessed: May 20, 2021. [Online]. Available: <http://www.technovent.com/technoventsilicones-2.html>
- [209] “Ecoflex™ 00-30 Product Information | Smooth-On, Inc.” Accessed: Oct. 22, 2024. [Online]. Available: <https://www.smooth-on.com/products/ecoflex-00-30/>
- [210] “Ecoflex™ GEL Product Information | Smooth-On, Inc.” Accessed: Oct. 22, 2024. [Online]. Available: <https://www.smooth-on.com/products/ecoflex-gel/>
- [211] “Titanium(IV) oxide, anatase powder, -325mesh, = 99 trace metals 1317-70-0.” Accessed: Oct. 22, 2024. [Online]. Available: [https://www.sigmaaldrich.com/GB/en/product/aldrich/248576?utm\\_source=google&utm\\_medium=cpc&utm\\_campaign=15001183107&utm\\_content=127306761543&gclid=Cj0KCQjwmt24BhDPARIsAJFYKk14jPAq2Md\\_5m3X8Rqn1ccLDucvHrri3MxTcWpm-VN0z4WcyVUv9AoaAI--EALw\\_wcB](https://www.sigmaaldrich.com/GB/en/product/aldrich/248576?utm_source=google&utm_medium=cpc&utm_campaign=15001183107&utm_content=127306761543&gclid=Cj0KCQjwmt24BhDPARIsAJFYKk14jPAq2Md_5m3X8Rqn1ccLDucvHrri3MxTcWpm-VN0z4WcyVUv9AoaAI--EALw_wcB)
- [212] W. C. Hayes, L. M. Keer, G. Herrmann+, and L. F. Mockros, “a mathematical analysis for indentation tests of articular cartilage\*,” PeqamonPress, 1972.
- [213] R. Pattiata “201129432 Pattiata\_Rachel\_1944689\_Final”. Dissertation, Cardiff University, 2023
- [214] M. Wood and S. Evans, “Cutting and Tearing of Soft Materials,” Dissertation, Cardiff University, 2024.
- [215] “Home - MuVIS X-ray Imaging Centre.” Accessed: Oct. 22, 2024. [Online]. Available: <https://muvis.org/>
- [216] “University of Southampton - National X-ray Computed Tomography.” Accessed: Dec. 03, 2024. [Online]. Available: <https://nxct.ac.uk/facilities/university-of-southampton/>
- [217] S. A. Maas, B. J. Ellis, G. A. Ateshian, and J. A. Weiss, “FEBio: Finite elements for biomechanics,” *J Biomech Eng*, vol. 134, no. 1, pp. 1–10, 2012, doi: 10.1115/1.4005694.
- [218] Simpleware, *Simpleware ScanIP Instructions for Software Use*, Version P-2019.09, Aug. 2019. [Online]. Available: <https://www.synopsys.com/content/dam/synopsys/simpleware/datasheet/simpleware-scanip-ifu-2019-09.pdf>. [Accessed: 28 Sept. 2024].
- [219] P. D. . Harvey, *Engineering properties of steel*. American Society for Metals, 1982.
- [220] “Converted document.” Accessed: May 20, 2021. [Online]. Available: [https://help.febio.org/FEBio/FEBio\\_um\\_2\\_9/FEBio\\_um\\_2-9-Subsection-3.13.1.html#prev](https://help.febio.org/FEBio/FEBio_um_2_9/FEBio_um_2-9-Subsection-3.13.1.html#prev)
- [221] “4.6.2.3 Weibull | FEBio User Manual.” Accessed: Sep. 28, 2024. [Online]. Available: <https://help.febio.org/docs/FEBioUser-4-5/UM45-4.6.2.3.html>
- [222] E. Hinton, T. Rock, and O. C. Zienkiewicz, “A note on mass lumping and related processes in the finite element method,” *Earthq Eng Struct Dyn*, vol. 4, no. 3, pp. 245–249, 1976, doi: 10.1002/eqe.4290040305.
- [223] “8.4.2 Explicit Dynamics Solver | FEBio User Manual.” Accessed: Sep. 28, 2024. [Online]. Available: <https://help.febio.org/docs/FEBioUser-4-5/UM45-Subsection-8.4.2.html>

## References

- [224] D. R. Lide, *CRC handbook of chemistry and physics*, vol. 85. CRCpress, 2004.
- [225] R. J. Hyndman and A. B. Koehler, "Another look at measures of forecast accuracy," *Int J Forecast*, vol. 22, no. 4, pp. 679–688, Oct. 2006, doi: 10.1016/j.ijforecast.2006.03.001.
- [226] J. Schindelin *et al.*, "Fiji: an open-source platform for biological-image analysis," *Nature Methods* 2012 9:7, vol. 9, no. 7, pp. 676–682, Jun. 2012, doi: 10.1038/nmeth.2019.
- [227] M. S. Gerstel and V. A. Place, "Drug delivery device - US 3964482 A," *U. S. Patent*, vol. 482, no. 19, 1976.
- [228] P. Alliez, G. Ucelli, C. Gotsman, and M. Attene, "Recent Advances in Remeshing of Surfaces." , in *Shape Analysis and Structuring*, L. De Floriani and M. Spagnuolo, Eds. Berlin, Germany: Springer, 2008, pp. 1–15. doi: 10.1007/978-3-540-33265-7\_2.
- [229] M. Wicke, D. Ritchie, B. M. Klingner, S. Burke, J. R. Shewchuk, and J. F. O'Brien, "Dynamic local remeshing for elastoplastic simulation," in *ACM SIGGRAPH 2010 Papers, SIGGRAPH 2010*, Association for Computing Machinery, Inc, Jul. 2010. doi: 10.1145/1778765.1778786.
- [230] D. Khan *et al.*, "Surface Remeshing: A Systematic Literature Review of Methods and Research Directions," Mar. 01, 2022, *IEEE Computer Society*. doi: 10.1109/TVCG.2020.3016645.

# ***APPENDIX A***

---

## **CONFERENCES**

- 2022 British Society for Strain Measurement, Oxford, England, UK,  
R. Joyce, S. Evans, K. Rankin, M.R. Potts, S.A. Coulman, J.C. Birchall,  
R. Pullin “Measuring micron penetration of skin using DIC and Micro-  
CT” (oral presentation)
- 2023 Computer Methods in Biomaterials and Biomedical Engineering, Paris,  
France  
R. Joyce, M.R. Potts, H. Wyatt, R. Pullin, S.A. Coulman, J.C. Birchall,  
S. Evans “Modelling microneedle indentation and penetration into a  
skin substitute using a cohesive zone method” (oral presentation)  
Microneedles Conference, Seattle, USA
- R. Joyce, M.R. Potts, K. Rankin, S. Evans, H. Wyatt, J.C. Birchall, S.A.  
Coulman, R. Pullin “Evaluating micron scale penetration into a skin  
substitute using micro-focus computed tomography and finite element  
analysis” (poster presentation)
- Cardiff University Engineering Research Conference, Cardiff, Wales,  
UK

## Appendix A– Conferences

R. Joyce, M.R. Potts, K. Rankin, S. Evans, H. Wyatt, J.C. Birchall, S.A. Coulman, R. Pullin “Investigation into micron-scape needle penetration using finite element analysis with experimental validation” (oral presentation)

2024 Cardiff University Engineering Research Conference, Cardiff, Wales, UK

R. Joyce, K. Rankin, R. Pullin, H. Wyatt, J.C. Birchall, S.A. Coulman, S. Evans “Evaluating micron indentation using micro focus computed tomography and digital volume correlation” (oral presentation)

# APPENDIX B

---

## DVC CODE

Strain subplots:

```
clear all
close all
clc
addpath('C:\Users\c1668701\Cardiff University\Rachael Joyce -
DVC_FFT+DirectCorrelation_76x76x76_50%sum_of_differential_2023-04-17_4\Stefano -
Copy\logfiles')

% Reading from CSV the whole spreadsheet
% Make sure to run this function in the same folder where you saved your
% csv files or add the path to the files.
m_all1=readmatrix('Test_40001.csv');
m_all6=readmatrix('Test_40006.csv');

% Do grids of step 1 and 6 coincide?
figure ;hold on
plot3(m_all1(:,1),m_all1(:,2),m_all1(:,3),'ro')
plot3(m_all6(:,1),m_all6(:,2),m_all6(:,3),'b.')
hold off
% Yes!

%% Step = 1
% Voxels are in the first three columns
list_vxls1=m_all1(:,1:3);
% Displacement in the following three columns
list_disp1=m_all1(:,4:6);

% Vector plot of the displacements
figure;
quiver3(list_vxls1(:,1),list_vxls1(:,2),list_vxls1(:,3),...
```

## Appendix B– DVC Code

```
list_disp1(:,1),list_disp1(:,2),list_disp1(:,3),0)

% Finding the number of voxels per dimensions. Not that straightforward as
% I thought, 1 every 38 voxels are saved in the cvs file.
nx=length(unique(list_vxls1(:,1)));
ny=length(unique(list_vxls1(:,2)));
nz=length(unique(list_vxls1(:,3)));

% CAREFUL! 1 every 38 voxels are in the spreadsheet!
max_x=max(list_vxls1(:,1));
max_y=max(list_vxls1(:,2));
max_z=max(list_vxls1(:,3));
disp(['Max voxel position: ' num2str([max_x,max_y,max_z]) ])
disp(['However total voxels: ' num2str([nx,ny,nz]) ])

% Little check if everything looks fine before running reshape
if nx*ny*nz~=size(list_vxls1,1)
    disp('Something's wrong')
end

% Reshape on the individual components, slower but more straightforward.
% From vectors to matrices.
disp_Tx=reshape(list_disp1(:,1),nx,ny,nz);
disp_Ty=reshape(list_disp1(:,2),nx,ny,nz);
disp_Tz=reshape(list_disp1(:,3),nx,ny,nz);
% All components together in a 4D image. It's not needed but might be more
% handy to use
disp_img1=cat(4,disp_Tx,disp_Ty,disp_Tz);

figure
imagesc(disp_img1(:,:,10,3))
% no displacement in step 1!

%% Step = 2
% Same code but for step 6
% Grid is the same, so don't need to re-calculate nx,ny,nz.

list_vxls6=m_all6(:,1:3);
list_disp6=m_all6(:,4:6);

figure;
quiver3(list_vxls6(:,1),list_vxls6(:,2),list_vxls6(:,3),...
        list_disp6(:,1),list_disp6(:,2),list_disp6(:,3),0)

figure;
scatter3(list_vxls6(:,1),list_vxls6(:,2),list_vxls6(:,3),10,...
        sqrt(sum(list_disp6.^2,2)))

disp_Tx=reshape(list_disp6(:,1),nx,ny,nz);
disp_Ty=reshape(list_disp6(:,2),nx,ny,nz);
disp_Tz=reshape(list_disp6(:,3),nx,ny,nz);
disp_img6=cat(4,disp_Tx,disp_Ty,disp_Tz);

figure;subplot 131
imagesc(disp_img6(:,:,27,1));title('Tx @ 27 slice ');colorbar
subplot 132
imagesc(disp_img6(:,:,29,2));title('Ty @ 29 slice ');colorbar
subplot 133
```

## Appendix B– DVC Code

```
imagesc(displ_img6(:,:,27,3));title('Tz @ 27 slice ');colorbar

figure ('Name','Tx')
orthosliceViewer(displ_Tx)
figure ('Name','Ty')
orthosliceViewer(displ_Ty)
figure ('Name','Tz')
orthosliceViewer(displ_Tz)

%%

undef=niftiread('Reslice_of_20221121_VERSA_2948_RJ_step1_100_scaled_recon_1013x993
x988_1996nm_4x_8bit.hdr');
hdr_undef=niftiinfo('Reslice_of_20221121_VERSA_2948_RJ_step1_100_scaled_recon_1013
x993x988_1996nm_4x_8bit.hdr');
undef_med=medfilt3(undef);

undef=flip(undef,2);

%%
% 1) v undef (hdr/img) in indices like febio_mesh.txt
% 2) list_vxl1 (DVC space) [mm], resolution from undef 1.996 microm
m=dlmread('febio_mesh.txt');
m(:,2:4)=m(:,2:4)*1000;

% 1000*1.996 % [microm], 1.996 [mm]
% list_vxls6_indicesSpace=list_vxls6*100;
%
% list_vxls6_indicesSpace=list_vxls6/1996;

% list_vxl in [mm], so it needs to be scaled to indices with some
% resolution
list_vxls6_indicesSpace=list_vxls6/1996; %??

ind_z_dvc=m(:,4)>399 & m(:,4)<401;
ind_z_febio=m(:,4)>399 & m(:,4)<401;
figure;hold on;
plot3(m(ind_z_febio,3),m(ind_z_febio,2),m(ind_z_febio,4),'r.')
imagesc(undef(:,:,400))
%
quiver3(list_vxls6(:,2)/0.003,list_vxls6(:,1)/0.003,list_vxls6(:,3)/0.003,list_dis
p6(:,2),list_disp6(:,1),list_disp6(:,3),10)
% plot3(list_vxls6(:,2)/0.003,list_vxls6(:,1)/0.003,list_vxls6(:,3)/0.003,'g.')
hold off
%% Resolution DaVIs disp 0.003 micron
%% 993 z-dimension

%%
% Extract voxel positions from list_vxls6
x_voxel = list_vxls6(:, 2) / 0.003;
y_voxel = list_vxls6(:, 1) / 0.003;
z_voxel = list_vxls6(:, 3) / 0.003;

% Extract strain components from corrected columns 8, 9, and 10 of m_all6
Exx = m_all6(:, 9); % Corrected index for Exx
Eyy = m_all6(:, 8); % Corrected index for Eyy
Ezz = m_all6(:, 10); % Corrected index for Ezz
```

## Appendix B– DVC Code

```
% Combine strain components into a single matrix
strain_data = [Exx, Eyy, Ezz];

% Calculate the magnitude of the strain vectors
strain_magnitude = sqrt(sum(strain_data.^2, 2));

% Normalize the strain vectors across all slices
normalized_strain_vectors = strain_data ./ max(strain_magnitude);

% Plotting voxel displacement vectors using quiver
quiver3(x_voxel, y_voxel, z_voxel, ...
        list_disp6(:, 2), list_disp6(:, 1), list_disp6(:, 3), 'k');

hold on;

% Overlaying normalized strain vectors using scatter with colormap and
transparency
scatter3(x_voxel, y_voxel, z_voxel, ...
        50, strain_magnitude, 'filled', 'MarkerEdgeColor', 'k', 'MarkerFaceAlpha',
0.7);

% Plotting specific z-slice for reference
ind_z_febio = m(:, 4) > 399 & m(:, 4) < 401;
plot3(m(ind_z_febio, 3), m(ind_z_febio, 2), m(ind_z_febio, 4), 'r.');
```

```
% Plotting undef image
imagesc(undef(:, :, 400));

% Add colorbar for the strain scatter plot
colorbar;

% Adjust the color axis limits for the entire figure
clim([0, max(strain_magnitude)]);

hold off;

% Adding labels or legends
legend('Displacement Vectors', 'Strain Vectors', 'Reference Z-Slice', 'Undef
Image');
title('Voxel Displacement and Strain Vectors');
%% remove zeros

% Extract voxel positions from list_vxls6
x_voxel = list_vxls6(:, 2) / 0.003;
y_voxel = list_vxls6(:, 1) / 0.003;
z_voxel = list_vxls6(:, 3) / 0.003;

% Extract strain components from corrected columns 8, 9, and 10 of m_all6
Exx = m_all6(:, 9); % Corrected index for Exx
Eyy = m_all6(:, 8); % Corrected index for Eyy
Ezz = m_all6(:, 10); % Corrected index for Ezz

% Remove rows with zero strain components
non_zero_indices = any([Exx, Eyy, Ezz] ~= 0, 2);
x_voxel_nonzero = x_voxel(non_zero_indices);
y_voxel_nonzero = y_voxel(non_zero_indices);
z_voxel_nonzero = z_voxel(non_zero_indices);
Exx_nonzero = Exx(non_zero_indices);
```

## Appendix B– DVC Code

```
Eyy_nonzero = Eyy(non_zero_indices);
Ezz_nonzero = Ezz(non_zero_indices);

% Plotting voxel displacement vectors using quiver
quiver3(x_voxel, y_voxel, z_voxel, ...
        list_disp6(:, 2), list_disp6(:, 1), list_disp6(:, 3), 'k');

hold on;

% Plotting strain vectors as scatter with colormap and transparency
scatter3(x_voxel_nonzero, y_voxel_nonzero, z_voxel_nonzero, ...
        50, sqrt(Exx_nonzero.^2 + Eyy_nonzero.^2 + Ezz_nonzero.^2), 'filled',
        'MarkerEdgeColor', 'k', 'MarkerFaceAlpha', 0.7);

% Plotting specific z-slice for reference
ind_z_febio = m(:, 4) > 399 & m(:, 4) < 401;
plot3(m(ind_z_febio, 3), m(ind_z_febio, 2), m(ind_z_febio, 4), 'r.');
```

```
% Plotting undef image
imagesc(undef(:, :, 400));
colorbar;
clim([0, max(sqrt(Exx_nonzero.^2 + Eyy_nonzero.^2 + Ezz_nonzero.^2))]);
hold off;
legend('Displacement Vectors', 'Strain Vectors (Unmodified)', 'Reference Z-Slice',
        'Undef Image');
title('Voxel Displacement and Strain Vectors (Non-Zero Only)');
```

```
%% removing under 1 to visually check

% Extract voxel positions from list_vxls6
x_voxel = list_vxls6(:, 2) / 0.003;
y_voxel = list_vxls6(:, 1) / 0.003;
z_voxel = list_vxls6(:, 3) / 0.003;

% Extract strain components from corrected columns 8, 9, and 10 of m_all6
Exx = m_all6(:, 9); % Corrected index for Exx
Eyy = m_all6(:, 8); % Corrected index for Eyy
Ezz = m_all6(:, 10); % Corrected index for Ezz

% Remove rows with zero strain components
non_zero_indices = any([Exx, Eyy, Ezz] ~= 0, 2);
x_voxel_nonzero = x_voxel(non_zero_indices);
y_voxel_nonzero = y_voxel(non_zero_indices);
z_voxel_nonzero = z_voxel(non_zero_indices);
Exx_nonzero = Exx(non_zero_indices);
Eyy_nonzero = Eyy(non_zero_indices);
Ezz_nonzero = Ezz(non_zero_indices);

% Remove entries with strain magnitude less than 1
magnitude_threshold = 0.5;
high_strain_indices = sqrt(Exx_nonzero.^2 + Eyy_nonzero.^2 + Ezz_nonzero.^2) >
magnitude_threshold;

% Plotting voxel displacement vectors using quiver
quiver3(x_voxel, y_voxel, z_voxel, ...
        list_disp6(:, 2), list_disp6(:, 1), list_disp6(:, 3), 'k');
```

```
hold on;
```

## Appendix B– DVC Code

```
% Plotting strain vectors with magnitude greater than 1 as scatter with colormap
and transparency
scatter3(x_voxel_nonzero(high_strain_indices),
y_voxel_nonzero(high_strain_indices), z_voxel_nonzero(high_strain_indices), ...
    50, sqrt(Exx_nonzero(high_strain_indices).^2 +
Eyy_nonzero(high_strain_indices).^2 + Ezz_nonzero(high_strain_indices).^2),
'filled', 'MarkerEdgeColor', 'k', 'MarkerFaceAlpha', 0.7);

% Plotting specific z-slice for reference
ind_z_febio = m(:, 4) > 399 & m(:, 4) < 401;
plot3(m(ind_z_febio, 3), m(ind_z_febio, 2), m(ind_z_febio, 4), 'r.');
```

```
% Plotting undef image
%imagesc(undef(:, :, 400));

% Add colorbar for the strain scatter plot
colorbar;
clim([0, max(sqrt(Exx_nonzero.^2 + Eyy_nonzero.^2 + Ezz_nonzero.^2))]);
hold off;
legend('Displacement Vectors', 'High Strain Vectors', 'Reference Z-Slice', 'Undef
Image');
title('Voxel Displacement and Strain Vectors (High Strain Only)');
```

```
%% checking the strain directions before transformations

% Extract voxel positions from list_vxls6
x_voxel = list_vxls6(:, 2) / 0.003;
y_voxel = list_vxls6(:, 1) / 0.003;
z_voxel = list_vxls6(:, 3) / 0.003;

% Extract strain components from corrected columns 8, 9, and 10 of m_all6
Exx = m_all6(:, 9); % Corrected index for Exx
Eyy = m_all6(:, 8); % Corrected index for Eyy
Ezz = m_all6(:, 10); % Corrected index for Ezz

% Plotting voxel displacement vectors using quiver
quiver3(x_voxel, y_voxel, z_voxel, ...
    list_disp6(:, 2), list_disp6(:, 1), list_disp6(:, 3), 'k');

hold on;

% Plotting strain vectors as quiver
quiver3(x_voxel, y_voxel, z_voxel, Exx, Eyy, Ezz, 'b');

% Plotting specific z-slice for reference
ind_z_febio = m(:, 4) > 399 & m(:, 4) < 401;
plot3(m(ind_z_febio, 3), m(ind_z_febio, 2), m(ind_z_febio, 4), 'r.');
```

```
% Plotting undef image
imagesc(undef(:, :, 400));

hold off;
legend('Displacement Vectors', 'Strain Vectors (Unmodified)', 'Reference Z-Slice',
'Undef Image');
title('Voxel Displacement and Strain Vectors');
```

## Appendix B– DVC Code

```
%% subplots

list_vxls6 = m_all6(:, 1:3);
list_strain6 = m_all6(:, 8:13); % Extract strain components from corrected columns
8 to 13 of m_all6

% Extract needle positions from the mesh in voxel indices
needle_positions_voxel = m(ind_z_febio, 2:4);

% Rotation matrices
rotation_y = [cosd(90), 0, sind(90); 0, 1, 0; -sind(90), 0, cosd(90)];
rotation_x = [1, 0, 0; 0, cosd(90), -sind(90); 0, sind(90), cosd(90)];

% Rotate needle positions
needle_positions_rotated=(rotation_x * (rotation_y * needle_positions_voxel.')).';

% Dimensions of the strain data voxels (53x52x52)
voxel_dimensions_strain = [53, 52, 52];

% Dimensions of the CT slices voxels (1013x993x988)
voxel_dimensions_CT = [1013, 993, 988];

% Size of the needle in millimeters (adjust this based on your actual needle size)
needle_size_mm = 11;

% Calculate the scaling factors for each dimension
scaling_factors = voxel_dimensions_strain ./ voxel_dimensions_CT;

% Scale down the needle size
scaled_needle_size = needle_size_mm * scaling_factors;

% Display the scaled needle size
disp(['Scaled Needle Size: ' num2str(scaled_needle_size) ' mm']);

% Now, you can use the scaled needle size to adjust the needle positions
accordingly
needle_positions_scaled = needle_positions_rotated .* scaling_factors;

% Extract strain component (Eyy) at the desired slice
desired_slice = 27;
strain_Eyy_slice = reshape(list_strain6(:, 2), nx, ny, nz);
strain_Eyy_slice = squeeze(strain_Eyy_slice(:, :, desired_slice));

% Plot Exx at the desired slice
figure;
imagesc(strain_Eyy_slice);
title(['Eyy @ Slice ' num2str(desired_slice)]);
colorbar;

% Overlay rotated and scaled needle using plot3
hold on;
plot3(needle_positions_scaled(:,3),needle_positions_scaled(:,2),
needle_positions_scaled(:, 1), 'r.', 'MarkerSize', 10);
hold off;

% Plot all strain components and overlay rotated and scaled needle on each subplot
```

## Appendix B– DVC Code

```
figure;

subplot(2, 3, 1);
imagesc(strain_Exx_slice(:, :, desired_slice));
title(['Exx @ Slice ' num2str(desired_slice)]);
colorbar;
hold on;
plot3(needle_positions_scaled(:, 3), needle_positions_scaled(:, 2),
needle_positions_scaled(:, 1), 'r.', 'MarkerSize', 10);
hold off;
xlabel('Z-axis (Voxels)');
ylabel('Y-axis (Voxels)');
zlabel('X-axis (Voxels)');

subplot(2, 3, 2);
imagesc(strain_Eyy_slice(:, :, desired_slice));
title(['Eyy @ Slice ' num2str(desired_slice)]);
colorbar;
hold on;
plot3(needle_positions_scaled(:, 3), needle_positions_scaled(:, 2),
needle_positions_scaled(:, 1), 'r.', 'MarkerSize', 10);
hold off;
xlabel('Z-axis (Voxels)');
ylabel('Y-axis (Voxels)');
zlabel('X-axis (Voxels)');

subplot(2, 3, 3);
imagesc(strain_Ezz_slice(:, :, desired_slice));
title(['Ezz @ Slice ' num2str(desired_slice)]);
colorbar;
hold on;
plot3(needle_positions_scaled(:, 3), needle_positions_scaled(:, 2),
needle_positions_scaled(:, 1), 'r.', 'MarkerSize', 10);
hold off;
xlabel('Z-axis (Voxels)');
ylabel('Y-axis (Voxels)');
zlabel('X-axis (Voxels)');

subplot(2, 3, 4);
imagesc(strain_Exy_slice(:, :, desired_slice));
title(['Exy @ Slice ' num2str(desired_slice)]);
colorbar;
hold on;
plot3(needle_positions_scaled(:, 3), needle_positions_scaled(:, 2),
needle_positions_scaled(:, 1), 'r.', 'MarkerSize', 10);
hold off;
xlabel('Z-axis (Voxels)');
ylabel('Y-axis (Voxels)');
zlabel('X-axis (Voxels)');

subplot(2, 3, 5);
imagesc(strain_Exz_slice(:, :, desired_slice));
title(['Exz @ Slice ' num2str(desired_slice)]);
colorbar;
hold on;
plot3(needle_positions_scaled(:, 3), needle_positions_scaled(:, 2),
needle_positions_scaled(:, 1), 'r.', 'MarkerSize', 10);
hold off;
```

## Appendix B– DVC Code

```
xlabel('Z-axis (Voxels)');
ylabel('Y-axis (Voxels)');
zlabel('X-axis (Voxels)');

subplot(2, 3, 6);
imagesc(strain_Eyz_slice(:, :, desired_slice));
title(['Eyz @ Slice ' num2str(desired_slice)]);
colorbar;
hold on;
plot3(needle_positions_scaled(:, 3), needle_positions_scaled(:, 2),
needle_positions_scaled(:, 1), 'r.', 'MarkerSize', 10);
hold off;
xlabel('Z-axis (Voxels)');
ylabel('Y-axis (Voxels)');
zlabel('X-axis (Voxels)');

%% displacement w needle

figure;
imagesc(disp_img6(:, :, 27, 1)); title('Ty @ 27 slice '); colorbar
colorbar;
hold on;
plot3(needle_positions_scaled(:, 3), needle_positions_scaled(:, 2),
needle_positions_scaled(:, 1), 'r.', 'MarkerSize', 10);
hold off;
xlabel('Z-axis (Voxels)');
ylabel('Y-axis (Voxels)');
zlabel('X-axis (Voxels)');
view(90, 90); % Adjust the view angle

figure;
imagesc(disp_img6(:, :, 27, 2)); title('Tz @ 27 slice '); colorbar
colorbar;
hold on;
plot3(needle_positions_scaled(:, 3), needle_positions_scaled(:, 2),
needle_positions_scaled(:, 1), 'r.', 'MarkerSize', 10);
hold off;
xlabel('Z-axis (Voxels)');
ylabel('Y-axis (Voxels)');
zlabel('X-axis (Voxels)');
view(90, 90); % Adjust the view angle

figure;
imagesc(disp_img6(:, :, 27, 3)); title('Tx @ 27 slice '); colorbar
colorbar;
hold on;
plot3(needle_positions_scaled(:, 3), needle_positions_scaled(:, 2),
needle_positions_scaled(:, 1), 'r.', 'MarkerSize', 10);
hold off;
xlabel('Z-axis (Voxels)');
ylabel('Y-axis (Voxels)');
zlabel('X-axis (Voxels)');
view(90, 90); % Adjust the view angle

%% original
% Extract needle positions from the mesh in voxel indices
needle_positions_voxel = m(:, 2:4);
```

## Appendix B– DVC Code

```
% Rotation matrices
rotation_y = [cosd(90), 0, sind(90); 0, 1, 0; -sind(90), 0, cosd(90)];
rotation_x = [1, 0, 0; 0, cosd(90), -sind(90); 0, sind(90), cosd(90)];

% Rotate needle positions
needle_positions_rotated = (rotation_x * (rotation_y *
needle_positions_voxel.')).';
% Now, you can use the scaled needle size to adjust the needle positions
accordingly
needle_positions_scaled = needle_positions_rotated .* scaling_factors;

[X,Y,Z]=meshgrid(1:size(dispatch_Tz,1),1:size(dispatch_Tz,2),1:size(dispatch_Tz,3));
X=X(1:end);
Y=Y(1:end);
Z=Z(1:end);

figure;hold on
% plot3(X(1:10:end),Y(1:10:end),Z(1:10:end),"r.")
scatter3(X(1:10:end),Y(1:10:end),Z(1:10:end),10,sqrt(sum(list_disp6(1:10:end,:).^2
,2)))
plot3(needle_positions_scaled(:,1),needle_positions_scaled(:,2),needle_positions_s
caled(:,3),"b.")
xlabel('Z-axis');
ylabel('Y-axis');
zlabel('X-axis');
```

### FEA comparison:

```
% Load FEBio mesh nodes for silicone and needle
febio_silicone_nodes = readmatrix('silicone_mesh.txt');
febio_needle_nodes = readmatrix('needle_mesh.txt');

% Load logfile position containing positions of all nodes from final FEBio step
logfile_position_final = readmatrix('x_y_z_final.txt');
febio_all_nodes_position = logfile_position_final(:, 2:4); % Assuming node
positions start from the second column

% Plot FEBio mesh nodes
figure;
plot3(febio_silicone_nodes(:,3), febio_silicone_nodes(:,4),
febio_silicone_nodes(:,5), '.b'); % Silicone nodes
hold on;
plot3(febio_needle_nodes(:,3), febio_needle_nodes(:,4), febio_needle_nodes(:,5),
'.r'); % Needle nodes

% Plot FEBio all nodes
plot3(febio_all_nodes_position(:,1), febio_all_nodes_position(:,2),
febio_all_nodes_position(:,3), 'g. '); % All nodes from logfile
axis equal; % Set equal scaling for all axes
axis tight; % Set the axis limits to the range of the data

xlabel('X-axis');
ylabel('Y-axis');
zlabel('Z-axis');
title('FEBio Mesh Nodes and All Nodes from Logfile');

legend('FEBio Silicone Nodes', 'FEBio Needle Nodes', 'FEBio All Nodes');
```

## Appendix B– DVC Code

```
%% displacement

% Load initial and final node positions
initial_positions = readmatrix('x_y_z_initial.txt');
final_positions = readmatrix('x_y_z_final.txt');

% Compute displacement
displacement = final_positions - initial_positions;

% Load displacement and strain components from FEBio output files
logfile_displacement = readmatrix('ux_uy_uz_final.txt');

% Plot displacement vectors
figure;
quiver3(initial_positions(:,2), initial_positions(:,3), initial_positions(:,4),
...
        displacement(:,2), displacement(:,3), displacement(:,4), 'b');
xlabel('X-axis');
ylabel('Y-axis');
zlabel('Z-axis');
title('Initial position to final position of mesh nodes');
axis equal; % Set equal scaling for all axes
axis tight; % Set the axis limits to the range of the data

%% DVC and FEA

% Load FEBio mesh nodes and displacement data
%febio_silicone_nodes = readmatrix('febio_mesh_silicone.txt');
%febio_needle_nodes = readmatrix('febio_mesh_needle.txt');
%febio_displacement = readmatrix('logfile_disp_final2.txt');

% Display sizes of matrices
%disp('Size of febio_silicone_nodes:');
%disp(size(febio_silicone_nodes));
%disp('Size of febio_needle_nodes:');
%disp(size(febio_needle_nodes));
%disp('Size of febio_displacement:');
%disp(size(febio_displacement));

%%
% Load initial and final displacement data
initial_displacement = readmatrix('ux_uy_uz_initial.txt');
final_displacement = readmatrix('ux_uy_uz_final.txt');

% Extract displacement components
initial_displacement_x = initial_displacement(:, 2);
initial_displacement_y = initial_displacement(:, 3);
initial_displacement_z = initial_displacement(:, 4);

final_displacement_x = final_displacement(:, 2);
final_displacement_y = final_displacement(:, 3);
final_displacement_z = final_displacement(:, 4);

% Calculate displacement vectors
displacement_x = final_displacement_x - initial_displacement_x;
displacement_y = final_displacement_y - initial_displacement_y;
displacement_z = final_displacement_z - initial_displacement_z;
```

## Appendix B– DVC Code

```
% Plot displacement vectors starting from initial node positions
figure;
quiver3(initial_positions(:, 2), initial_positions(:, 3), initial_positions(:, 4),
...
    displacement_x, displacement_y, displacement_z, 'Color', 'k');
xlabel('X-axis');
ylabel('Y-axis');
zlabel('Z-axis');
title('Displacement Vectors');
axis equal; % Set equal scaling for all axes
axis tight; % Set the axis limits to the range of the data

%%
% Calculate displacement magnitude
displacement_magnitude = sqrt(displacement_x.^2 + displacement_y.^2 +
displacement_z.^2);

% Plot color chart
scatter3(febio_all_nodes_position(:, 1), febio_all_nodes_position(:, 2),
febio_all_nodes_position(:, 3), 50, displacement_magnitude, 'filled');
colorbar; % Add color bar to show displacement magnitude scale

xlabel('X-axis');
ylabel('Y-axis');
zlabel('Z-axis');
title('Displacement Magnitude Color Chart');

%% displacement colour plot

% Define the range of cross-sectional x-values
cross_section_x_range = [0.001, 0.0012]; % Adjust this range as needed

% Find indices of nodes within the cross-sectional x-range
cross_section_indices = find(febio_all_nodes_position(:, 1) >=
cross_section_x_range(1) & febio_all_nodes_position(:, 1) <=
cross_section_x_range(2));

if isempty(cross_section_indices)
    error('No nodes found within the specified cross-sectional x-range.');
```

```
end

% Extract the positions and displacement magnitudes of nodes within the cross-
sectional x-range
cross_section_nodes_position = febio_all_nodes_position(cross_section_indices, :);
cross_section_displacement_magnitude =
displacement_magnitude(cross_section_indices);

% Plot cross-sectional view along x-axis
figure;
scatter3(cross_section_nodes_position(:, 1), cross_section_nodes_position(:, 2),
cross_section_nodes_position(:, 3), 50, cross_section_displacement_magnitude,
'filled');
colorbar; % Add color bar to show displacement magnitude scale

xlabel('X-axis');
ylabel('Y-axis');
```

## Appendix B– DVC Code

```
zlabel('Z-axis');
title(['Cross-sectional view along X-axis within range [',
num2str(cross_section_x_range(1)), ', ', num2str(cross_section_x_range(2)), ']']);

%%

% Determine the total number of elements expected after reshaping
expected_num_elements = nx * ny * nz;

% Check if the number of elements in final_displacement_x matches the expected
number
if numel(final_displacement_x) ~= expected_num_elements
    error('Number of elements in final_displacement_x does not match the expected
size after reshaping. ');
end

% Reshape displacement components into 3D arrays
disp_Fx = reshape(final_displacement_x, nx, ny, nz);
disp_Fy = reshape(final_displacement_y, nx, ny, nz);
disp_Fz = reshape(final_displacement_z, nx, ny, nz);

% Concatenate displacement components along the fourth dimension
disp_img_6 = cat(4, disp_Fx, disp_Fy, disp_Fz);

%%
% Convert FEA Nodal Data to Grid Format
% Determine the minimum and maximum coordinates along each axis
min_x = min(final_displacement_x);
max_x = max(final_displacement_x);
min_y = min(final_displacement_y);
max_y = max(final_displacement_y);
min_z = min(final_displacement_z);
max_z = max(final_displacement_z);

% Define a regular grid matching the dimensions of the DVC voxel grid
[x_grid, y_grid, z_grid] = meshgrid(linspace(min_x, max_x, 53), ...
    linspace(min_y, max_y, 52), ...
    linspace(min_z, max_z, 52));

% Interpolate FEA nodal displacement data onto the regular grid
fe_interp_x = interp3(final_displacement_x, final_displacement_y,
final_displacement_z, final_displacement_x, x_grid, y_grid, z_grid, 'linear');
fe_interp_y = interp3(final_displacement_x, final_displacement_y,
final_displacement_z, final_displacement_y, x_grid, y_grid, z_grid, 'linear');
fe_interp_z = interp3(final_displacement_x, final_displacement_y,
final_displacement_z, final_displacement_z, x_grid, y_grid, z_grid, 'linear');

Interpolation :
%% interpolation

% 2mm side of FOV of DVC. 53 vxls per directions. Hence, distance between
% two nearby voxels, 0.04mm.
[Idx_mni, D] = rangesearch(rotated_DVC_positions, febio_all_nodes_position, 0.16);
```

## Appendix B– DVC Code

```
list_disp6_mesh=zeros(size(febio_all_nodes_position));
%[Idx_mni,D]=rangesearch([X,Y,Z],final_mesh',3);
for i_m=1:size(febio_all_nodes_position,1)
    tmp_Vmni=list_disp6(Idx_mni{i_m,1},:);
    weight_i=1./(D{i_m,1})';
    list_disp6_mesh(i_m,:)=sum(repmat(weight_i,1,3).*tmp_Vmni,1)/sum(weight_i);
    disp(i_m/size(list_disp6_mesh,1))
end

figure;hold on; % FEA then DVC
scatter3(febio_all_nodes_position(:,1),febio_all_nodes_position(:,2),febio_all_nod
es_position(:,3),10,sqrt(sum(list_disp6_mesh.^2,2)))
%scatter3(rotated_DVC_positions(:, 1), rotated_DVC_positions(:, 2),
rotated_DVC_positions(:, 3), 10, sqrt(sum(list_disp6.^2, 2)), 'filled');
xlabel('X-axis');
ylabel('Y-axis');
zlabel('Z-axis');
hold off

%%

% Combine node numbers and displacement data
output_data = [logfile_position_final(:, 1), list_disp6_mesh];

% Replace NaN values with 0
output_data(isnan(output_data)) = 0;

% Save the resulting matrix to a file
output_filename = 'febio_node_data.txt';
dlmwrite(output_filename, output_data, 'delimiter', '\t', 'precision', 6);

% Display a message indicating successful file creation
disp(['Output file saved as: ' output_filename]);

%%

% Combine node numbers and displacement data
output_data = [logfile_position_final(:, 1), list_disp6_mesh];

% Replace NaN values with 0
output_data(isnan(output_data)) = 0;

% change the field from positive silicone moe to negative

% Save the resulting matrix to a file
output_filename = 'febio_node_data.txt';
dlmwrite(output_filename, output_data, 'delimiter', '\t', 'precision', 6);

% Display a message indicating successful file creation
disp(['Output file saved as: ' output_filename]);

%%

% Assume logfile_position_final and list_disp6_mesh are already loaded
% Number of rows in your data
num_rows = 44876;

% Create a matrix of zeros with 5 columns and the number of rows
zero_columns = zeros(num_rows, 15);
```

## Appendix B– DVC Code

```
% Combine node numbers, zero columns, and displacement data
% Assuming logfile_position_final(:, 1) and list_disp6_mesh have the same number
of rows
output_data = [logfile_position_final(:, 1), zero_columns, list_disp6_mesh];

% Replace NaN values with 0
output_data(isnan(output_data)) = 0;

% Save the resulting matrix to a file
output_filename = 'febio_node_data.txt';
dlmwrite(output_filename, output_data, 'delimiter', ',', 'precision', 6);

% Display a message indicating successful file creation
disp(['Output file saved as: ' output_filename]);
```

### maximum displacement:

```
% Extract displacement components from DVC data
dvc_disp_x = list_disp6(:, 1);
dvc_disp_y = list_disp6(:, 2);
dvc_disp_z = list_disp6(:, 3);

% Extract displacement components from interpolated FEA data
fea_disp_x = list_disp6_mesh(:, 1);
fea_disp_y = list_disp6_mesh(:, 2);
fea_disp_z = list_disp6_mesh(:, 3);

% Find the index of the maximum Y displacement in DVC data
[max_dvc_disp_y, max_dvc_y_index] = max(abs(dvc_disp_y));

% Corresponding X and Z components for the maximum Y in DVC data
corresponding_dvc_x = dvc_disp_x(max_dvc_y_index);
corresponding_dvc_z = dvc_disp_z(max_dvc_y_index);

% Calculate the magnitude of the displacement vector
dvc_magnitude = sqrt(corresponding_dvc_x^2 + max_dvc_disp_y^2 +
corresponding_dvc_z^2);

% Find the index of the maximum Y displacement in interpolated FEA data
[max_fea_disp_y, max_fea_y_index] = max(abs(fea_disp_y));

% Corresponding X and Z components for the maximum Y in interpolated FEA data
corresponding_fea_x = fea_disp_x(max_fea_y_index);
corresponding_fea_z = fea_disp_z(max_fea_y_index);

% Calculate the magnitude of the displacement vector
fea_magnitude = sqrt(corresponding_fea_x^2 + max_fea_disp_y^2 +
corresponding_fea_z^2);

% Display the results for DVC data
fprintf('DVC Data:\n');
fprintf('Max Y Displacement: %.6f mm\n', max_dvc_disp_y);
fprintf('Corresponding X: %.6f mm, Z: %.6f mm\n', corresponding_dvc_x,
corresponding_dvc_z);
fprintf('Magnitude of Displacement: %.6f mm\n', dvc_magnitude);
```

## Appendix B– DVC Code

```
% Display the results for interpolated FEA data
fprintf('\nInterpolated FEA Data:\n');
fprintf('Max Y Displacement: %.6f mm\n', max_fea_disp_y);
fprintf('Corresponding X: %.6f mm, Z: %.6f mm\n', corresponding_fea_x,
corresponding_fea_z);
fprintf('Magnitude of Displacement: %.6f mm\n', fea_magnitude);

% Optional: Save the results to a text file for record-keeping
comparison_filename = 'displacement_comparison_y_max_5.txt';
fid = fopen(comparison_filename, 'w');
fprintf(fid, 'DVC Data:\n');
fprintf(fid, 'Max Y Displacement: %.6f mm\n', max_dvc_disp_y);
fprintf(fid, 'Corresponding X: %.6f mm, Z: %.6f mm\n', corresponding_dvc_x,
corresponding_dvc_z);
fprintf(fid, 'Magnitude of Displacement: %.6f mm\n\n', dvc_magnitude);

fprintf(fid, 'Interpolated FEA Data:\n');
fprintf(fid, 'Max Y Displacement: %.6f mm\n', max_fea_disp_y);
fprintf(fid, 'Corresponding X: %.6f mm, Z: %.6f mm\n', corresponding_fea_x,
corresponding_fea_z);
fprintf(fid, 'Magnitude of Displacement: %.6f mm\n', fea_magnitude);
fclose(fid);

disp(['Maximum Y displacement comparison saved to: ', comparison_filename]);
```

# GRAPH CODE

Load-displacement static and dynamic model comparisons:

```
% static
data = readmatrix("static model.xlsx");

exp_disp = data(:, 1);
exp_force = data(:, 2);
k_original_disp = data(:, 5);
k_original_force = data(:, 6);

% Create the force vs. displacement graph
figure;
plot(exp_disp, exp_force, '-k', 'LineWidth', 1);
hold on
plot(k_original_disp, k_original_force, '-m', 'LineWidth', 1);
hold on

xlabel('Displacement (mm)');
ylabel('Force (N)');
%title('Force vs. Displacement');
legend('Experimental Data', 'Original Static Model', 'k = 10', 'k = 1', 'k = 0.1');
grid off;

hold off
%% changed static
%force displacement graph

k_10_disp = data(:, 9);
k_10_force = data(:, 10);
k_1_disp = data(:, 13);
k_1_force = data(:, 14);
k_01_disp = data(:, 21);
k_01_force = data(:, 22);

% Create the force vs. displacement graph
figure;
plot(exp_disp, exp_force, '-k', 'LineWidth', 1);
hold on
plot(k_original_disp, k_original_force, '-m', 'LineWidth', 1);
hold on
plot(k_10_disp, k_10_force, '-r', 'LineWidth', 1);
hold on
plot(k_1_disp, k_1_force, '-g', 'LineWidth', 1);
hold on
plot(k_01_disp, k_01_force, '-b', 'LineWidth', 1);
hold on

xlabel('Displacement (mm)');
ylabel('Force (N)');
%title('Force vs. Displacement');
legend('Experimental Data', 'Original Static Model', 'k = 10', 'k = 1', 'k = 0.1');
```

## Appendix B– Graph Code

```
grid off;

hold off

%% dynamic model density change

d_k_0001_disp = data(:, 33);
d_k_0001_force = data(:, 34);
d_d_100_disp = data(:, 37);
d_d_100_force = data(:, 38);
d_d_001_disp = data(:, 42);
d_d_001_force = data(:, 43);
d_d_01_disp = data(:, 47);
d_d_01_force = data(:, 48);

% Create the force vs. displacement graph
figure;
plot(exp_disp, exp_force, '-k', 'LineWidth', 1);
hold on
plot(dynamic_01_disp, dynamic_01_force, '-m', 'LineWidth', 1);
hold on
plot(d_k_0001_disp, d_k_0001_force, '-r', 'LineWidth', 1);
hold on
%plot(d_d_100_disp, d_d_100_force, '-g', 'LineWidth', 1);
%hold on
plot(d_d_001_disp, d_d_001_force, '-b', 'LineWidth', 1);
hold on
plot(d_d_01_disp, d_d_01_force, '-g', 'LineWidth', 1);
hold on

xlabel('Displacement (mm)');
ylabel('Force (N)');
%title('Force vs. Displacement');
legend('Experimental Data', 'k=0.1', 'k=0.001', 'd=0.01', 'd=0.1');
grid off;

hold off

%% dynamic model comparison

% Create the force vs. displacement graph
figure;
plot(exp_disp, exp_force, '-k', 'LineWidth', 1);
hold on
plot(k_01_disp, k_01_force, '-b', 'LineWidth', 1);
hold on
plot(d_d_01_disp, d_d_01_force, '-g', 'LineWidth', 1);
hold on

xlabel('Displacement (mm)');
ylabel('Force (N)');
%title('Force vs. Displacement');
legend('Experimental Data', 'Static Model (k=0.1)', 'Dynamic Model (d=0.1)');
grid off;
```

## Appendix B– Graph Code

hold off

### Comparison of FEA to DVC:

```
% Define the displacement data
dvc_max_z_displacements = [0, 0.073928, 0.161997, 0.244224, 0.322779, 0.415];
experimental_displacements = [0, 0.075, 0.150, 0.225, 0.300, 0.375];
fea_centre_node_displacements = [0, 0.0731531, 0.147401, 0.221919, 0.296465,
0.368792];
node_31335_displacements = [0, 0.076547, 0.137103, 0.212543, 0.285439, 0.369747];

% Perform calculations and save results
calculate_and_save(dvc_max_z_displacements, experimental_displacements,
'DVC_vs_Experimental');
calculate_and_save(dvc_max_z_displacements, fea_centre_node_displacements,
'DVC_vs_FEA_Centre');
calculate_and_save(node_31335_displacements, fea_centre_node_displacements,
'Node31335_vs_FEA_Centre');
calculate_and_save(dvc_max_z_displacements, node_31335_displacements,
'DVC_vs_Node31335');

% Function to calculate errors and save them to a text file
function calculate_and_save(data1, data2, filename)
    % Calculate step-by-step and overall errors
    step_errors = abs(data1 - data2);
    rmse = sqrt(mean(step_errors.^2));
    mae = mean(step_errors);
    valid_idx = data2 ~= 0; % Avoid zero division for percentage error
    perc_error = mean((step_errors(valid_idx) ./ data2(valid_idx)) * 100);

    % Open file to write results
    fid = fopen([filename '.txt'], 'w');

    % Write step-by-step errors
    fprintf(fid, 'Step-by-Step Errors:\nStep\tError (mm)\n');
    for i = 1:length(step_errors)
        fprintf(fid, '%d\t%.4f\n', i, step_errors(i));
    end

    % Write overall error metrics
    fprintf(fid, '\nOverall Error Metrics:\n');
    fprintf(fid, 'RMSE: %.4f mm\n', rmse);
    fprintf(fid, 'MAE: %.4f mm\n', mae);
    fprintf(fid, 'Percentage Error: %.2f%%\n', perc_error);

    % Close the file
    fclose(fid);
end
```

### Error calculations FEA:

```
%% Load Data from Excel Sheets
% Load data from the 'dynamic' worksheet
dynamic_data = readmatrix('dynamic.xlsx');

% Load data from the 'static model' worksheet
static_data = readmatrix('static model.xlsx');
```

## Appendix B– Graph Code

```
% Perform Calculations and Save Results to Text Files
% 1. Dynamic model displacement (column 2) vs experimental displacement (column 5)
calculate_and_save(dynamic_data(:, 2), dynamic_data(:, 5), 'Dynamic Model
Displacement vs Experimental Displacement', 'output_all_results.txt');

% 2. Dynamic model force (column 3) vs experimental force (column 6)
calculate_and_save(dynamic_data(:, 3), dynamic_data(:, 6), 'Dynamic Model Force vs
Experimental Force', 'output_all_results.txt');

% 3. Experimental displacement (column 1 of 'static model') vs static model
displacement (column 21)
calculate_and_save(static_data(:, 1), static_data(:, 21), 'Experimental
Displacement vs Static Model Displacement', 'output_all_results.txt');

% 4. Experimental force (column 2 of 'static model') vs static model force (column
22)
calculate_and_save(static_data(:, 2), static_data(:, 22), 'Experimental Force vs
Static Model Force', 'output_all_results.txt');

% 5. Experimental displacement vs dynamic model displacement (from 'static model'
worksheet, column 47)
calculate_and_save(static_data(:, 1), static_data(:, 47), 'Experimental
Displacement vs Dynamic Model Displacement (Static Model Worksheet)',
'output_all_results.txt');

% 6. Experimental force vs dynamic model force (from 'static model' worksheet,
column 48)
calculate_and_save(static_data(:, 2), static_data(:, 48), 'Experimental Force vs
Dynamic Model Force (Static Model Worksheet)', 'output_all_results.txt');

% 7. Static model displacement vs dynamic model displacement (from 'static model'
worksheet)
calculate_and_save(static_data(:, 21), static_data(:, 47), 'Static Model
Displacement vs Dynamic Model Displacement', 'output_all_results.txt');

% 8. Static model force vs dynamic model force (from 'static model' worksheet)
calculate_and_save(static_data(:, 22), static_data(:, 48), 'Static Model Force vs
Dynamic Model Force', 'output_all_results.txt');

% Function to Calculate, Display, and Save RMSE, MAE, and Percentage Error to a
Single File

function calculate_and_save(data1, data2, description, output_filename)
    % Remove zero, NaN, and Inf values from both data sets
    valid_idx = (data1 ~= 0 & data2 ~= 0 & ~isnan(data1) & ~isnan(data2) &
isfinite(data1) & isfinite(data2));
    data1_valid = data1(valid_idx);
    data2_valid = data2(valid_idx);

    % Check if there are valid elements left after removing zeros, NaNs, and Infs
    if isempty(data1_valid) || isempty(data2_valid)
        error('No valid data points after filtering for %s', description);
    end

    % Calculate RMSE, MAE, and Percentage Error
    rmse_value = sqrt(mean((data1_valid - data2_valid).^2));
    mae_value = mean(abs(data1_valid - data2_valid));
```

## Appendix B– Graph Code

```
% Use the maximum of the two values to avoid large percentage errors when
denominators are small
denominator = max(abs(data1_valid), abs(data2_valid));
perc_error = mean(abs((data1_valid - data2_valid) ./ denominator)) * 100;

% Display the results in the command window
fprintf('Results for %s:\n', description);
fprintf('RMSE: %.4f mm\n', rmse_value);
fprintf('MAE: %.4f mm\n', mae_value);
fprintf('Percentage Error: %.2f%%\n\n', perc_error);

% Save the results to a single text file (append mode)
fid = fopen(output_filename, 'a'); % 'a' for append mode

% Write the description and results to the file
fprintf(fid, 'Results for %s:\n', description);
fprintf(fid, 'RMSE: %.4f mm\n', rmse_value);
fprintf(fid, 'MAE: %.4f mm\n', mae_value);
fprintf(fid, 'Percentage Error: %.2f%%\n\n', perc_error);

% Close the file
fclose(fid);
end
```

### Dynamic comparison:

```
% dynamic
data = readmatrix("dynamic.xlsx");

exp_disp = data(:, 5);
exp_force = data(:, 6);
d_01_disp = data(:, 2);
d_01_force = data(:, 3);

% Create the force vs. displacement graph
figure;
plot(exp_disp, exp_force, '-k', 'LineWidth', 1);
hold on
plot(d_01_disp, d_01_force, '-m', 'LineWidth', 1);
hold on

xlabel('Displacement (mm)');
ylabel('Force (N)');
%title('Force vs. Displacement');
legend('Experimental Data', 'Dynamic model, d=0.1');
grid off;

hold off
```

### Flat indenter compression:

```
% Flat indenter
Data_averages = readmatrix('averages.xlsx'); %open spreadsheet

Material_A_disp = Data_averages(4:end, 1);
Material_A_force = Data_averages(4:end, 2);
```

## Appendix B– Graph Code

```
Material_B_disp = Data_averages(4:end, 4);
Cycle_2_force = Data_averages(4:end, 5);
Material_C_disp = Data_averages(4:end, 7);
Material_C_force = Data_averages(4:end, 8);
Material_D_disp = Data_averages(4:end, 10);
Material_D_force = Data_averages(4:end, 11);
Material_E_disp = Data_averages(4:end, 13);
Material_E_force = Data_averages(4:end, 14);
Material_F_disp = Data_averages(4:end, 16);
Material_F_force = Data_averages(4:end, 17);

% Create the force vs. displacement graph
figure;
plot(Material_A_disp, Material_A_force, '-r', 'LineWidth', 1);
hold on
plot(Material_B_disp, Cycle_2_force, '-m', 'LineWidth', 1);
hold on
plot(Material_C_disp, Material_C_force, '-b', 'LineWidth', 1);
hold on
plot(Material_D_disp, Material_D_force, '-g', 'LineWidth', 1);
hold on
plot(Material_E_disp, Material_E_force, '-k', 'LineWidth', 1);
hold on
plot(Material_F_disp, Material_F_force, '-c', 'LineWidth', 1);
hold on

% Set axis limits to start from 0
xlim([0, max([Material_A_disp; Material_B_disp; Material_C_disp; Material_D_disp;
Material_E_disp; Material_F_disp])]);
ylim([0, max([Material_A_force; Cycle_2_force; Material_C_force; Material_D_force;
Material_E_force; Material_F_force])]);

xlabel('Displacement (mm)');
ylabel('Force (N)');
title('Force vs. Displacement');
legend('Material A Average', 'Material B Average', 'Material C Average', 'Material
D Average', 'Material E Average', 'Material F Average')
grid off;

hold off

%% conical indenter

Data_averages = readmatrix('Conical_averages.xlsx'); %open spreadsheet

Material_A_disp = Data_averages(4:end, 1);
Material_A_force = Data_averages(4:end, 2);
Material_B_disp = Data_averages(4:end, 4);
Cycle_2_force = Data_averages(4:end, 5);
Material_C_disp = Data_averages(4:end, 7);
Material_C_force = Data_averages(4:end, 8);
Material_D_disp = Data_averages(4:end, 10);
Material_D_force = Data_averages(4:end, 11);
Material_E_disp = Data_averages(4:end, 13);
Material_E_force = Data_averages(4:end, 14);
Material_F_disp = Data_averages(4:end, 16);
Material_F_force = Data_averages(4:end, 17);
```

## Appendix B– Graph Code

```
% Create the force vs. displacement graph
figure;
plot(Material_A_disp, Material_A_force, '-r', 'LineWidth', 1);
hold on
plot(Material_B_disp, Cycle_2_force, '-m', 'LineWidth', 1);
hold on
plot(Material_C_disp, Material_C_force, '-b', 'LineWidth', 1);
hold on
plot(Material_D_disp, Material_D_force, '-g', 'LineWidth', 1);
hold on
plot(Material_E_disp, Material_E_force, '-k', 'LineWidth', 1);
hold on
plot(Material_F_disp, Material_F_force, '-c', 'LineWidth', 1);
hold on

% Set axis limits to start from 0
xlim([0, max([Material_A_disp; Material_B_disp; Material_C_disp; Material_D_disp;
Material_E_disp; Material_F_disp])]);
ylim([0, max([Material_A_force; Cycle_2_force; Material_C_force; Material_D_force;
Material_E_force; Material_F_force])]);

xlabel('Displacement (mm)');
ylabel('Force (N)');
title('Force vs. Displacement');
legend('Material A Average', 'Material B Average', 'Material C Average', 'Material
D Average', 'Material E Average', 'Material F Average')
grid off;

hold off

%% material a

%% conical indenter

Data_averages = readmatrix('material a.xlsx'); %open spreadsheet

Cylce_1_disp = Data_averages(:, 1);
Cycle_1_force = Data_averages(:, 2);
Cylce_2_disp = Data_averages(:, 4);
Cycle_2_force = Data_averages(:, 5);
Cylce_3_disp = Data_averages(:, 7);
Cycle_3_force = Data_averages(:, 8);
Cylce_4_disp = Data_averages(:, 10);
Cycle_4_force = Data_averages(:, 11);
Cylce_5_disp = Data_averages(:, 13);
Cycle_5_force = Data_averages(:, 14);
Cycle_avg_disp = Data_averages(:, 16);
Cycle_avg_force = Data_averages(:, 17);

% Create the force vs. displacement graph
figure;
plot(Cylce_1_disp, Cycle_1_force, '-r', 'LineWidth', 1);
hold on
plot(Cylce_2_disp, Cycle_2_force, '-m', 'LineWidth', 1);
hold on
plot(Cylce_3_disp, Cycle_3_force, '-c', 'LineWidth', 1);
hold on
plot(Cylce_4_disp, Cycle_4_force, '-g', 'LineWidth', 1);
```

## Appendix B– Graph Code

```
hold on
plot(Cycle_5_disp, Cycle_5_force, '-b', 'LineWidth', 1);
hold on
plot(Cycle_avg_disp, Cycle_avg_force, '--k', 'LineWidth', 1);
hold on

% Set axis limits to start from 0
%xlim([0, max([Material_A_disp; Material_B_disp; Material_C_disp; Material_D_disp;
Material_E_disp; Material_F_disp])]);
%ylim([0, max([Material_A_force; Cycle_2_force; Material_C_force; Material_D_force;
Material_E_force; Material_F_force])]);

xlabel('Displacement (mm)');
ylabel('Force (N)');
title('Force vs. Displacement');
legend('Cycle 1', 'Cycle 2', 'Cycle 3', 'Cycle 4', 'Cycle 5', 'Cycle Average')
grid off;

hold off
```

### Particle distribution graphs:

```
%particle distribution

particle_averages = readmatrix('Book1.xlsx'); %open spreadsheet

unsieved_size = particle_averages(3:end, 3);
unsieved_volume = particle_averages(3:end, 2);

sieved_size = particle_averages(3:end, 13);
sieved_volume = particle_averages(3:end, 12);

% Create the graph
figure;
semilogx(unsieved_size, unsieved_volume, '-r', 'LineWidth', 1);
hold on
semilogx(sieved_size, sieved_volume, '-m', 'LineWidth', 1);
hold on

% Set axis limits to start from 0
xlim([0, max([unsieved_size; sieved_size])]);
ylim([0, max([unsieved_volume; sieved_volume])]);

xlabel('Size (microns)');
ylabel('Volume (%)');

legend('Unsieved TiO2 average', 'Sieved TiO2 average ')
grid off;

hold off
```

### Puncture test:

```
puncture = readmatrix('combined.xls'); %open spreadsheet
```

## Appendix B– Graph Code

```
disp_1 = puncture(2:end, 3);
force_1 = puncture(2:end, 5);

disp_3 = puncture(2:end, 9);
force_3 = puncture(2:end, 11);

disp_5 = puncture(2:end, 15);
force_5 = puncture(2:end, 17);

% Create the force vs. displacement graph
figure;
plot(disp_1, force_1, '-r', 'LineWidth', 1);
hold on
plot(disp_3, force_3, '-m', 'LineWidth', 1);
hold on
plot(disp_5, force_5, '-b', 'LineWidth', 1);
hold on

% Set axis limits to start from 0
xlim([0, max([disp_1; disp_3; disp_5])]);
ylim([0, max([force_1; force_3; force_5])]);

xlabel('Displacement (mm)');
ylabel('Force (N)');

legend('0.1 mm/s speed', '0.3 mm/s speed', '0.5 mm/s speed')
grid off;

hold off

WoF:
%import data
sample_1=readmatrix('titanium4.xlsx');

%force and displacement variables
disp_1=sample_1(:,3)
force_1=sample_1(:,4)

disp_2=sample_1(:,8)
force_2=sample_1(:,9)

disp_3=sample_1(:,13)
force_3=sample_1(:,14)

disp_4=sample_1(:,18)
force_4=sample_1(:,19)

% Remove zeros and NaNs from disp_1 and force_1
valid_indices_1 = ~(isnan(disp_1) | isnan(force_1) | disp_1 == 0 | force_1 == 0);
disp_1 = disp_1(valid_indices_1);
force_1 = force_1(valid_indices_1);

% Remove zeros and NaNs from disp_2 and force_2
valid_indices_2 = ~(isnan(disp_2) | isnan(force_2) | disp_2 == 0 | force_2 == 0);
disp_2 = disp_2(valid_indices_2);
```

## Appendix B– Graph Code

```
force_2 = force_2(valid_indices_2);

% Remove zeros and NaNs from disp_1 and force_1
valid_indices_3 = ~(isnan(disp_3) | isnan(force_3) | disp_3 == 0 | force_3 == 0);
disp_3 = disp_3(valid_indices_3);
force_3 = force_3(valid_indices_3);

% Remove zeros and NaNs from disp_1 and force_1
valid_indices_4 = ~(isnan(disp_4) | isnan(force_4) | disp_4 == 0 | force_4 == 0);
disp_4 = disp_4(valid_indices_4);
force_4 = force_4(valid_indices_4);

%plot graphs
plot(disp_1, force_1)
hold on
plot(disp_2, force_2)
hold on
plot(disp_3, force_3)
hold on
plot(disp_4, force_4)
hold off

% Adjust plot axes
%axis equal; % Set equal scaling for all axes
axis tight; % Set the axis limits to the range of the data

xlabel('Displacement (mm)');
ylabel('Force (N)');
title('Sample: Ecoflex with Titanium dioxide 4');

% Adding legends
legend('Crack 1', 'Crack 2', 'Crack 3', 'Crack 4');

%calculating areas
area_1=trapz(disp_1/1000, force_1)
area_2=trapz(disp_2/1000, force_2)
area_3=trapz(disp_3/1000, force_3)
area_4=trapz(disp_4/1000, force_4)

%input variables
thickness = 1.57/1000
crackgrowth_i = 24.74/1000
crackgrowth_1 = 28.43/1000
crackgrowth_2 = 5.66/1000
crackgrowth_3 = 4.54/1000
crackgrowth_4 = 3.86/1000

%% crack one WoF

% 1. calculate crack growth
crackgrowth_1
```

## Appendix B– Graph Code

```
% 2. calculate area of crack
area_of_crack_1 = crackgrowth_1 * thickness;

% 3. calculate area of graph corresponding to crack growth
work_done_1 = area_1

% 4. work of fracture = area of graph / area of crack
work_of_fracture_1 = work_done_1 / area_of_crack_1
%% crack two WoF

% 1. calculate crack growth
crackgrowth_2

% 2. calculate area of crack
area_of_crack_2 = crackgrowth_2 * thickness;

% 3. calculate area of graph corresponding to crack growth
work_done_2 = area_2

% 4. work of fracture = area of graph / area of crack
work_of_fracture_2 = work_done_2 / area_of_crack_2
%% crack three WoF

% 1. calculate crack growth
crackgrowth_3

% 2. calculate area of crack
area_of_crack_3 = crackgrowth_3 * thickness;

% 3. calculate area of graph corresponding to crack growth
work_done_3 = area_3

% 4. work of fracture = area of graph / area of crack
work_of_fracture_3 = work_done_3 / area_of_crack_3

%% crack four WoF

% 1. calculate crack growth
crackgrowth_4

% 2. calculate area of crack
area_of_crack_4 = crackgrowth_4 * thickness;

% 3. calculate area of graph corresponding to crack growth
work_done_4 = area_4

% 4. work of fracture = area of graph / area of crack
work_of_fracture_4 = work_done_4 / area_of_crack_4

%% Wof is the average of all four

work_of_fracture_avg = mean([work_of_fracture_1, work_of_fracture_2,
work_of_fracture_3, work_of_fracture_4]);
```